*Author:*
**Dickenson, Andrew C**

*Title:*
**Measurement and simulation of ion energy distributions in a reactive ion etcher.**

*Measurement and Simulation of Ion Energy Distributions*

*In a Reactive Ion Etcher.*

*by*

*Andrew C. Dickenson*

A thesis submitted to the University of Bristol in accordance with the requirements for the degree of Doctor of Philosophy in the Faculty of Science, Department of Chemistry.

May, 1994.

## Abstract

The ion energy distribution (IED) of ions impacting semiconductor surfaces plays a central role in the production of microelectronic circuits. It remains to be understood exactly how the IED is affected by changes in the process conditions. This study is concerned with the measurement and simulations of IEDs.

IEDs have been measured at the anode of a reactive ion etcher using a retarding field analyser (RFA) that has been developed from a similar instrument used in fusion plasma studies. SIMION studies show that even at the highest sheath voltages the analyser is only expected to induce 6% error in the measurement of ion energies. Measurements were performed for Ar, He, Xe, $CO_2$, $N_2$, $CF_4/8\%O_2$, $SF_6$, $CF_3Cl$ and $CCl_4$ discharges for a variety of process conditions. Results show that all the IEDs exhibit some degree of RF modulation as characterized by a double peaked distribution where the peak splitting, $\Delta E$, is typically 10 eV. The degree of this RF modulation is found to depend strongly upon discharge conditions. As the voltage is increased in electropositive gas discharges the degree of RF modulation decreases as evidenced by a decrease of $\Delta E$ of $\sim 2$ - 5 eV; this is attributed to a sheath thickness that increases with applied RF voltage. For these same discharges the degree of RF modulation is found to increase when the discharge pressure is increased as similarly indicated by an increase of $\Delta E$ of $\sim 2$ - 5 eV; this is attributed to a decrease in the sheath thickness. Electronegative discharges exhibit less change in the degree of RF modulation of the IED as process conditions are altered. It is proposed that this is due to the discharge being better confined between the electrodes leading to a more stable sheath.

IEDs have also been measured for Ar where the anode to cathode area ratio was increased. Values of $\Delta E$ up to 25 eV were observed. The previously observed changes in the IED due to changes in the degree of RF modulation were progressively removed with increasingly large area ratios. This is attributed to the presence of a sheath whose thickness does not change significantly due to the discharge being better confined between the electrodes.

Simulation of Ar IEDs were performed using a Monte Carlo computer program. Where the plasma potential was described as a rectified sinusoid a full fit to the experimental data was not possible. It is demonstrated that improved agreement of simulation and experiment, using the sheath thickness as a fitting parameter, can be achieved when the Bohm criterion is included and the plasma potential expression altered to describe a sinusoid. This suggests that the plasma potential in the reactor is sinusoidal. Cathode IEDs have also been calculated using the fitting parameters derived from anode IEDs; these are directly relevant for the process engineer.

## Desiderata

Ξ Go placidly amid the noise and haste, and remember what
peace there may be in silence. As far as possible without
surrender be on good terms with all persons. Speak your
truth quietly and clearly; and listen to others, even the dull
and ignorant; they too have their story. Ξ Avoid loud and
aggressive persons, they are a vexation to the spirit. If you
compare yourself with others you may become vain and
bitter; for always there will be greater and lesser persons
than yourself. Enjoy your achievements as well as your
plans. Ξ Keep interested in your own career, however
humble; it is a real possession in the changing fortunes of
time. Exercise caution in your business affairs; for the world
is full of trickery. But let this not blind you to what virtue
there is; many persons strive for high ideals; and everywhere
life is full of heroism. Be yourself. Especially do not feign
affection. Neither be cynical about love; for in the face of all
aridity and disenchantment it is perennial as the grass.
Ξ Take kindly the counsel of the years, gracefully
surrendering the things of youth. Nurture strength of spirit to
shield you in sudden misfortune. But do not distress yourself
with imaginings. Many fears are born of fatigue and
loneliness. Beyond a wholesome discipline, be gentle with
yourself. You are a child of the Universe, no less than the
trees and the stars; you have a right to be here. And whether
or not it is clear to you, no doubt the Universe is unfolding
as it should. Ξ Therefore be at peace with God, whatever you ·
conceive Him to be, and whatever your labours and
aspirations, in the noisy confusion of life keep peace with
your soul. Ξ With all its sham, drudgery and broken dreams,
it is still a beautiful world. Be careful. Strive to be happy. Ξ

**Anon. Found in Old S$^{t.}$ Pauls Church, Baltimore.
Dated 1692.**

# ACKNOWLEDGMENTS

## Memorandum

The research described in this thesis was carried out by the author in the Department of Chemistry at the University of Bristol under the supervision of Dr. D. Field and Dr. D.F.Klemperer.

The work reported herein is original to the author, except where acknowledged by reference. No part of this work has been submitted previously for any degree.

# CONTENTS

## Chapter 1 - Introduction.

## Chapter 2 - Experimental

## Chapter 3 - Measurement of
## Ion Energy Distributions

## Chapter 4 - Calculation of
## Ion Energy Distributions

## Chapter 5 - Concluding Remarks
## and Further Work

# CHAPTER 1

# INTRODUCTION

.
.

# 1.1 INTRODUCTION

Integrated circuits, ICs, have become increasingly commonplace in all manner of applications. Demand for faster computers requires that the manufacturing process of the IC is tightly controlled. A critical step in the process is the etching of a semiconductor in order to build up circuit elements. Etching is normally carried out using a radio frequency (RF) gas discharge. The energy distribution of ions from the discharge is critical in determining the etch profile and thus the performance of the final device. The main aim of this work is to measure ion energy distributions (IEDs) and to compare the experimental results to theoretical calculations.

# 1.2 SEMICONDUCTORS[1]

In order to understand the importance of the reactive ion etching process we first examine semiconductors to show why their electrical properties are of technological interest.

## 1.2.1 Conduction In Solids

In a solid the atomic orbitals are very close in energy and it is convenient to think of these orbitals as forming a continuous band. The orbitals will, however, continue to be quantized so that the bands formed are *virtually* continuous. Solids form two such bands which are referred to as the valence band and the conduction band. In general, the valence band will consist of bonding orbitals and the conduction band of anti-bonding orbitals. Electrical conduction will occur where electrons can move from the top filled level into unoccupied orbitals where they give rise to a net motion of charge. The electrical conductivity of a solid thus depends upon the energy gap between the valence band and the conduction band and on the number of electrons occupying the bands. The energy difference between bands is referred to as the band gap.

The ability of solids to conduct electricity to any extent or not leads to their classification as either a metal, an insulator or a semiconductor.

**Metals:** In a metal the valence and conduction bands overlap so the band gap is zero. The resulting single continuous band is not completely filled with electrons so very
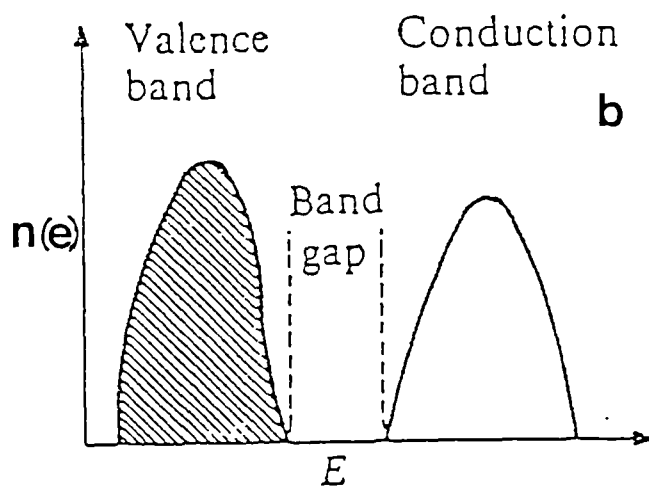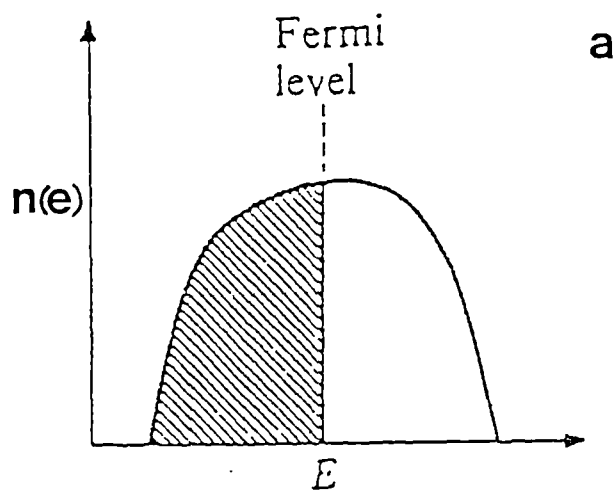
**Figure 1.1** Densities of states in a) metal and b) insulator. After Cox[1].

little energy is required for an electron to move from the highest filled level to the next higher level and so move through the solid. Metals are consequently good conductors of electricity. A density of states diagram, which shows the number of allowed energy levels, is shown in figure 1.1a for a metal.

**Insulators:** In an insulator the band gap is quite substantial, often several eV, so electrons cannot gain enough energy to be promoted into the conduction band. Additionally, the valence band is full so there is no possibility of conduction by a valence electron moving to a nearby unoccupied valence orbital. Insulators cannot, therefore, conduct electricity. Figure 1.1b shows the density of states diagram for an insulator.

**Semiconductors:** Semiconductors are non-metallic solids that conduct due to the thermal excitation of electrons across the band gap. They have a conductivity that lies between that of metals and insulators. This is a reflection of their band gap, which at $\sim$ 1 eV, is between that of a metal and an insulator. At absolute zero the valence band is full and the solid will behave as an insulator. At other temperatures there will be some electrons with sufficient thermal energy to reach the conduction band and thus respond to an applied electric field. Conductivity also occurs in the valence band when it is not completely filled. It is most convenient in this case to ignore the electrons in the valence band and think of the small number of vacancies. These are referred to as holes and behave as positively charged particles. The number of electrons excited at a given temperature is governed by the *Fermi-Dirac distribution*. The *Fermi level* in a material corresponds to the top filled level in a band. At absolute zero the Fermi level, $E_F$, is a sharp cut off between the filled levels and empty levels. At higher temperatures the Fermi-Dirac distribution is smeared out and the Fermi level can be thought of as being the energy at which the probability of an electron occurring is 1/2. The Fermi-Dirac distribution for an intrinsic semiconductor (one with equal numbers of electrons and holes) is shown in figure 1.2a. Non-intrinsic semiconductors where the numbers of electrons and holes are not equal can be formed by the incorporation of small amounts of impurities into the lattice in a process known as doping.

4
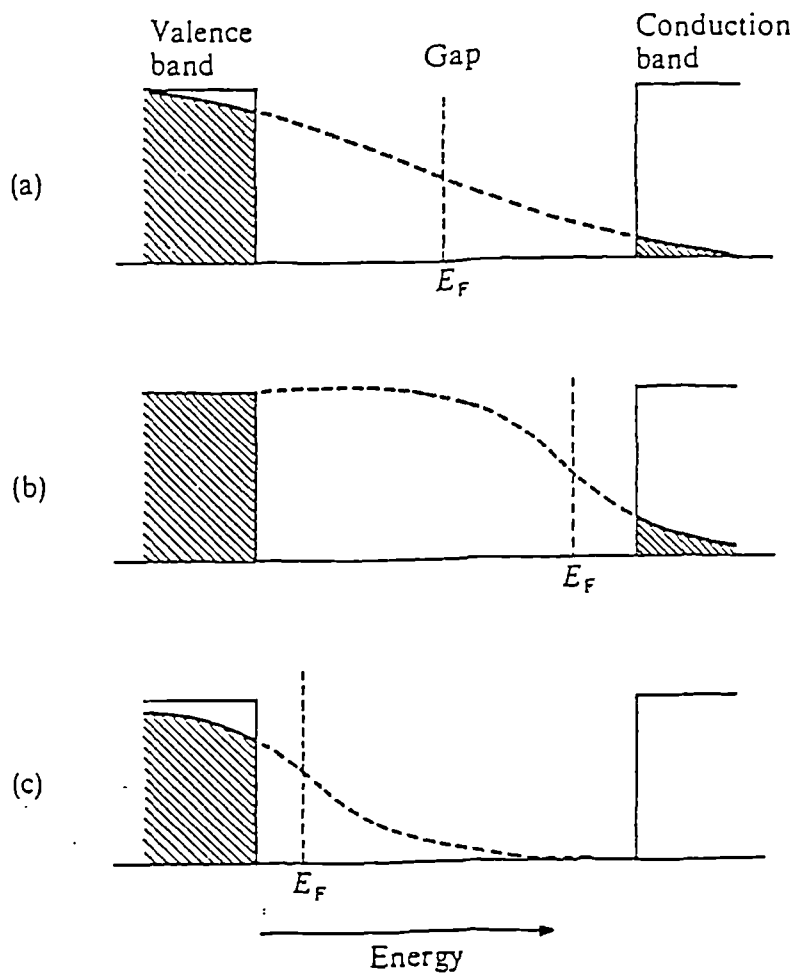
**Figure 1.2** Fermi-Dirac distribution in a semiconductor. a) intrinsic semiconductor, b) n-type semiconductor and c) p-type semiconductor. After Cox[1].

5

**Doped Semiconductors:** Doped semiconductors may be one of two types, either *n-type* or *p-type*. An n-type semiconductor is formed when a Group V element, such as phosphorous, is doped into the silicon lattice as a substitutional defect. Si atoms have four valence electrons, which hold the lattice together, and so the valence band is full. Phosphorous atoms have five valence electrons and so the extra electrons go into the conduction band. Here they are free to move throughout the solid thereby allowing the Si to conduct electricity more readily. The Fermi-Dirac distribution of electrons in an n-type semiconductor is shown in figure 1.2b.

P-type semiconductors are formed when silicon atoms are substituted by a Group III element such as aluminium. In this case there is one less valence electron which results in a reduction in the number of electrons in the valence band. The charge carriers here are then the positively charged holes. The Fermi-Dirac distribution of electrons for a p-type semiconductor is shown in figure 1.2c.

## 1.2.2 The P-N Junction and Transistors

The most basic component of solid state devices that uses doped semiconductors is the p-n junction. This may be formed by diffusing a dopant of one type into a semiconductor of the other type. The junction cannot be in equilibrium unless the Fermi levels in each material are the same. For this to be so some electrons from the n-type region move into holes in the p-type region. A *depletion layer*, where there are no charge carriers, is formed between the two regions. The electrons leave behind a positive charge in the n-type region and a negative charge develops in the p-type region. The potential barrier that develops opposes the further migration of electrons and eventually an equilibrium is reached. At this point the Fermi levels become equal. Figure 1.3a illustrates a p-n junction.

A p-n junction is the solid state equivalent of an electric diode. When a positive potential is applied to the n-type side more charge carriers are removed, increasing the depletion layer and the energy barrier (figure 1.3b). When the voltage is reversed the energy barrier at the junction is decreased and more carriers may flow through the junction (figure 1.3c).
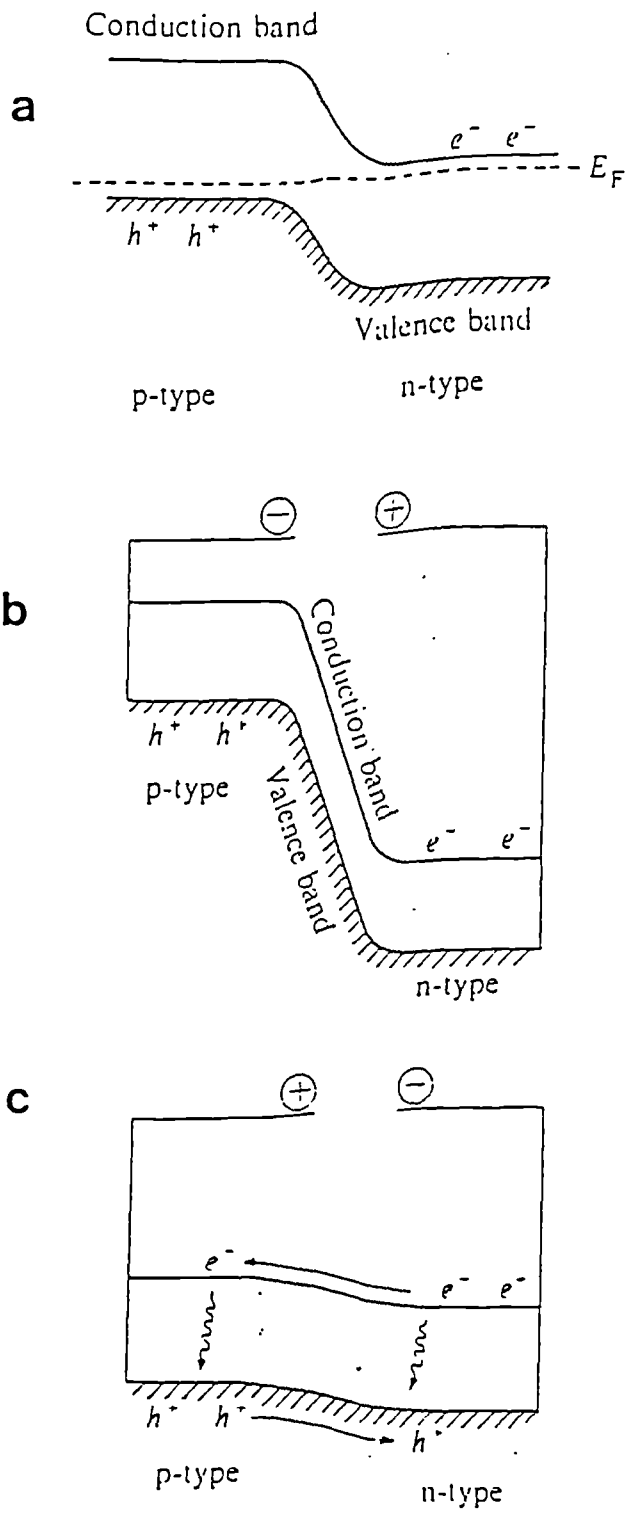
**Figure 1.3** p-n junction a) Fermi levels equal b) reverse bias causing increase in energy barrier and c) forward bias showing decrease of energy barrier. After Cox[1].

7
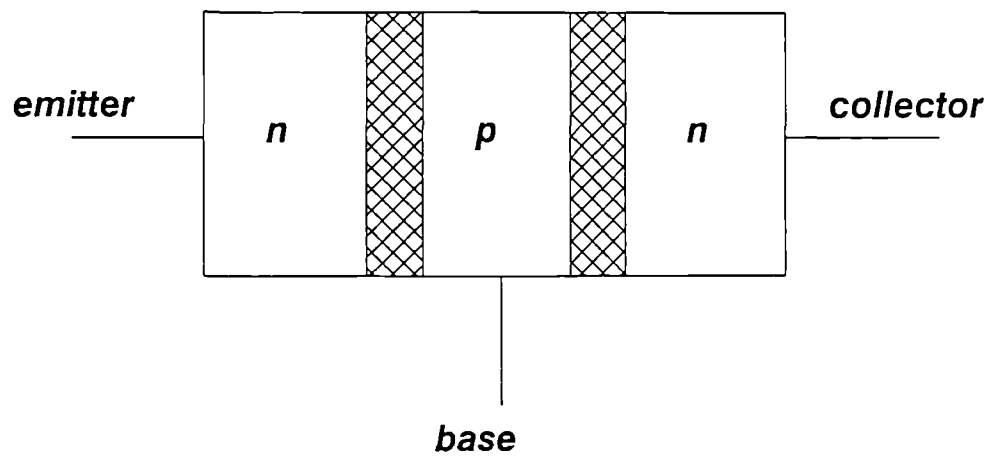
**Figure 1.4** npn junction formed by the combination of two
pn junctions.

Combinations of *pn* junctions can be used to form transistors in the same piece of semiconductor material. Figure 1.4 shows two adjacent *pn* junctions that comprise an *npn* transistor. Electrons from the n-type layers migrate and recombine with holes in the p-type region, forming depletion layers. A potential difference applied between the *emitter* and *collector* will cause only a small current to flow due to the potential barrier in the *base*. If a small potential is applied to the base however, then the electrons that form this potential barrier are depleted and an increased current can flow between emitter and collector. An *npn* transistor relies on the flow of electrons across the base region. Transistor action can also be found with a *pnp* junction. This is dependent upon the flow of holes across the base region.

Transistors have two properties which makes their fabrication out of solid materials desirable:

i) Transistors can act as amplifiers since a small current is used to control a larger one.

ii) A transistor can also function as a very fast switch. Coupling of transistors in a logic array leads to digital electronics and computers.


Many electronic components can be formed in the same piece of semiconductor material. These devices can then be connected together, into an integrated circuit, so that they perform specific functions.


## 1.3 INTEGRATED CIRCUITS[2,3]

Many electronic devices, such as those described above, can be formed simultaneously within the same substrate or wafer. These devices can then be suitably connected together so that the finished circuit performs a specific useful function. The finished circuit is known as an integrated circuit (IC). The major production method for ICs is the *planar process*. In this process many layers of semiconducting materials, with different electrical properties, are arranged one on top of the other. The layers are patterned to form all the various circuit elements required for the IC and the elements connected together with a patterned conducting layer (the interconnect).

Fabrication of an IC may involve up to 200 processing steps with as many as 15 layers being formed.

The planar process involves four main steps for each patterned layer in the integrated circuit: film production, doping, lithography and etching. Repetition of these steps allows complex multilayered structures to be formed. Each of these steps will be examined in detail in the following section to illustrate where the etch process, our main area of interest, fits into the overall process. First, however, we consider how the wafers of starting material can be formed.

## 1.3.1 Starting Materials

Silicon and gallium arsenide based ICs are both formed on single crystal wafers. Silicon is purified from raw silica in a *zone refining* process. This produces silicon that is chemically purified but polycrystalline. Single crystal ingots are grown by the *floating zone* or *Czochralski* methods[4]. The ingots are then sawn into wafers which are lapped (smoothed), polished and finally chemically cleaned to produce a mirror finish. Wafer size can be up to 200 mm diameter, allowing many circuits to be formed on the same substrate.

Gallium arsenide ingots are grown by *liquid encapsulated Czochralski* or *Horizontal Bridgman methods*. The resulting wafers are usually only up to 75 mm diameter due to difficulties in the production method.

## 1.3.2 Process Steps[2,4,5]
### 1.3.2.1 Film Formation

Each cycle in the IC process involves the formation of a thin film on the wafer surface. For this film to be useful it requires the following characteristics:

a) Good interlayer adhesion

b) Uniformity of thickness

c) Controlled composition

d) Compatibility with subsequent steps

e) Unreactivity to adjacent layers

10

f) Durability, if permanent, or ease of lift off if temporary.

There are many methods of film growth used in the IC fabrication process. Only a few are mentioned briefly here. Standard texts[2,4] give more detailed accounts.

## a) Oxidation

This is one of the most basic of all the steps in the fabrication process. $SiO_2$ is grown by reaction of silicon in either an oxygen or steam atmosphere. $SiO_2$ is used as a protective coating over surfaces and as an insulator between layers of the IC.

## b) Spin on and Spray on Processes

These methods are mainly used for applying photoresist coatings to wafers. In the spin on process a drop of the photoresist reagents, in a carrier solvent, is placed on the wafer. The wafer is spun at high speed to spread the photoresist and help drive out the solvent. This creates a uniform coating of the photoresist at the surface. In the spray on process finely controlled spray guns travel over the wafer surface to produce a uniform photoresist coating.

## c) Chemical Vapour Deposition (CVD)

The CVD technique is the most commonly used method for producing thin films. As the name suggests, the procedure involves gas phase reactants, often diluted with an inert carrier gas, forming a thin solid film at the wafer surface. Often the surface is heated to drive the reaction. The constituents of the gas can be independently varied in concentration allowing accurate control of the film stoichiometry. CVD can be used to deposit amorphous, polycrystalline and epitaxial layers with a high degree of purity. CVD can take place at low pressures, 0.1 - 1 torr, (LPCVD) or at.atmospheric pressure (APCVD). Plasma Enhanced CVD (PECVD) has recently been developed, where the energy source for the reaction is the RF power supply. This allows much lower substrate temperature, which is sometimes desirable, while achieving acceptable growth rates.

## d) Sputtering

In this process the material that is to be deposited is used as the cathode in an inert gas glow discharge at low pressure. High energy ions are accelerated on to the cathode causing sputtering of the target material. The sputtered atoms will then condense on nearby surfaces which includes substrate wafers placed at the anode. The sputtering process is most often used for the deposition of metal films.

## e) Evaporation[6]

This is another frequently used method to produce metallic films. It is a comparatively simple method in which a pellet of the material to be deposited is placed in a crucible in a vacuum chamber. Direct heating, or electron bombardment, of the pellet causes atoms to leave the surface from where they can condense on to a nearby substrate. Alloys can be formed by the simultaneous evaporation of materials from a number of crucibles.

## f) Molecular beam epitaxy (MBE)

In this technique very thin films, down to monolayers, can be formed of elements, compounds and alloys. MBE involves the reaction of multiple molecular beams with a heated substrate target under UHV conditions. The films formed are epitaxial i.e. the film adopts the same crystal structure of that of the underlying substrate rather than its own usual structure or an amorphous layer.

## 1.3.2.2 Doping

Fabrication of the circuit elements requires a method of ensuring that specific regions of the substrate have the correct electrical characteristics i.e the correct concentrations of holes or electrons. This is achieved by the process of doping. Two techniques for doping have been commonly used:

## a) Diffusion.

In this method the dopant atoms are placed on the surface either by a gas phase

deposition step or by the face to face placing of wafers containing the dopant to the substrate wafers. This is followed by drive in diffusion in which the substrate is heated to $\sim 1000^{\circ}$C. The heat causes the impurities to diffuse into the substrate. The distribution of the dopant will depend on the temperature used, the length of diffusion time and the method of placing the dopant near the surface.

## b) Ion implantation.

Diffusion methods have now been largely replaced by ion implantation techniques. This offers greater control over doping concentrations thus allowing low concentrations of dopant in the substrate. Also since diffusion occurs laterally as well as vertically the device size is limited with the diffusion process to a few microns. Ion implantation by contrast allows the formation of shallow abrupt junctions where the doping levels can be very well controlled. Additionally, the process is carried out at low temperatures.

Ion implantation involves the dopant atoms being ionised and accelerated to high energies. The ions are mass separated to remove unwanted species and the resulting beam is directed at the surface. The high energy ions lose energy by collision with target atoms and finally come to rest in the substrate. The dopant profile is controlled by the ion energy while the ion current allows precise control over the dopant concentrations. One disadvantage of ion implantation is that it causes lattice damage which requires an annealing step to repair the lattice. This is done at a temperature below that of a typical diffusion step to keep diffusion of the dopants to a minimum. More recently laser annealing has been developed where the substrate is heated to a very high temperature for a short time (100 s to ns). This allows repair of the lattice without allowing significant dopant diffusion.

## 1.3.2.3 Lithography

In this step of the fabrication process a pattern is transferred from a mask to a photoresist covering on the wafer, from where it will be subsequently transferred to

13

the substrate in an etch process. Several steps are required for the transfer of a pattern. First, masks are made from large scale drawings which are reduced in size by cameras to produce a real size template. Photoresist is applied to the wafer and the wafer is softbaked to remove the solvents and partially harden the resist. The mask containing the pattern is then overlaid on to the surface and the wafer exposed to UV light to print the pattern. The resist is then developed by placing the wafer in contact with a solvent that will selectively attack either the exposed regions, leaving a positive image of the mask behind, or the unexposed regions in which case a negative image is formed. The wafer is then post baked to harden the resist further and to drive out moisture before the etch process.

In the microfabrication process the drive is towards ever smaller linewidths. Current lithography techniques use UV light to develop the photoresist. There is however a lower limit to the achievable linewidth, which is approximately twice the wavelength of the radiation, beyond which diffraction occurs. A commonly used wavelength is the 436 nm line of the mercury lamp which produces a lower limit of 0.87 $\mu$m linewidth. Recently the trend has been towards using the mercury i-line at 365 nm with a consequent improvement in resolution. With developments of techniques such as phase shift masking optical lithography could be capable of 0.2 $\mu$m resolution[7]. Beyond this other lithographic techniques are being developed. These include electron and ion beam lithography, x-ray lithography and the use of excimer lasers. Scanning electron beam lithography is capable of sub 0.1 $\mu$m resolution. Although it suffers from problems of wafer throughput this problem is being overcome[8]. Each of these lithographic methods requires a unique photoresist material.

### 1.3.2.4 Etching

Once a pattern is defined by the photoresist layer the next step in a process is to transfer that pattern to the substrate. This involves an etch step where the material not covered by the photoresist is removed. Two types of etching are commonly employed in the fabrication process: wet etching and dry etching. The main requirements of the etch process are:

a) removal of surface atoms

b) good selectivity towards any surfaces that are not to be removed

c) accurate transfer of the pattern in the resist to the substrate

d) removal of etch residues i.e the process is clean.

The processes of wet and dry etching are now considered in detail to examine the relative merits of each.

## 1.3.2.4.1 Wet Etching

Wet etching is used extensively in the fabrication process for the removal of films from a surface, for cleaning and for pattern transfer for large scale features. It is a simple process where the wafer is immersed in a chemical solution for an appropriate length of time to allow etching to occur. The wafer is usually agitated to ensure a fresh supply of the etchant to the surface. Since it requires little sophisticated equipment it is also very cheap and highly reliable. An important feature of wet etching is that it exhibits a high degree of selectivity and will remove only the specified material. The major drawback to wet etching is that it is isotropic i.e. it proceeds in all directions equally. Thus, etching a 1 $\mu$m thick film will cause the mask to be undercut by 1 $\mu$m also. Where the feature to be etched is large > 10 $\mu$m this is not a problem but when linewidths and feature sizes of < 3 $\mu$m are required this rapidly becomes unacceptable. Figure 1.5a illustrates an etch profile that will be obtained using wet etching techniques.

## 1.3.2.4.2 Dry Etching

In direct response to the problem of isotropy caused by wet etching techniques other methods have been developed to allow high resolution pattern transfer. The techniques of dry etching allow linewidths to be etched that are about the same width as the film thickness. Dry etching involves the reaction of a gaseous compound or compounds, the process gas, with the surface to form a volatile compound that then leaves the surface. The main advantage of the dry etch process is the highly directional etch profile, achieved by ion bombardment perpendicular to the surface, but it also

15
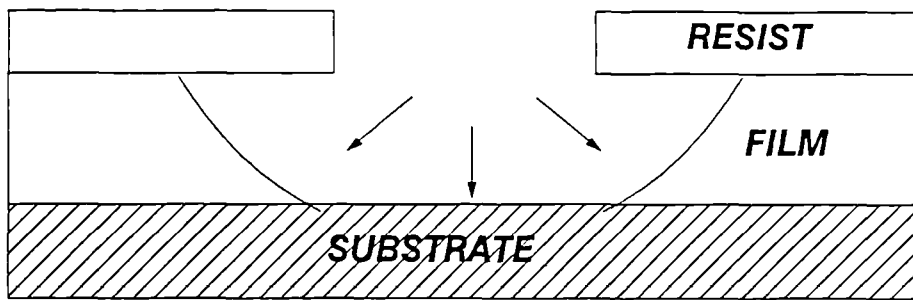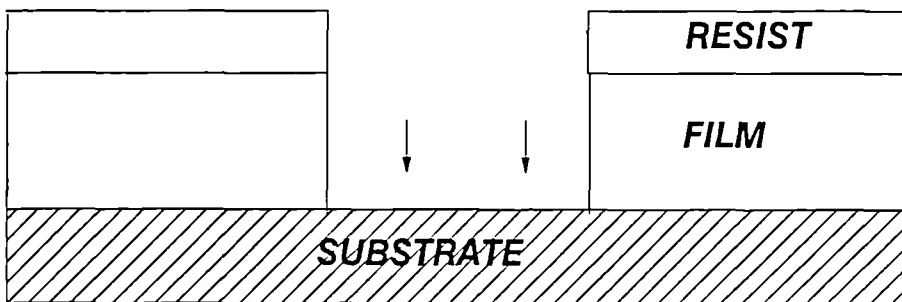
**Figure 1.5** Etch profiles obtained by a) wet etching and b) dry etching. Arrows indicate the direction of etch.

allows greater cleanliness and can be easily automated. However, dry etching does suffer from several disadvantages. These include poor selectivity to different layers, high equipment costs and the possibility of lattice damage in the substrate. There are several types of dry etching processes in use that can be classified according to the relative amounts of chemical and physical etching occurring. Since the main aim of this thesis is increased understanding of the dry etching process detailed descriptions of the various methods now follow.

### a) Ion Beam and Sputter Etching

These techniques are closely related and rely solely on physical methods to remove the surface atoms. In ion beam etching inert gas ions, usually $Ar^+$, are formed by an ion gun and accelerated towards the substrate using collimators. Sputter etching uses a low pressure RF discharge to produce ions that are then accelerated towards the surface by the sheath potential. Both of these techniques produce ions with several hundred eV energy that are incident at or near perpendicular to the wafer surface at the pressures normally employed. Bombardment of the surface causes energy to be transferred to the surface atoms which, if it is sufficient, can cause the atoms to leave the surface in a process known as sputtering. The high directionality of the ions leads to etching in only the direction of ion incidence and thus the problem of anisotropy associated with wet etching is overcome. Figure 1.5b shows an ideal anisotropic etch profile.

Although highly directional, sputter etching does have some disadvantages that restricts its usefulness. These include the tendency for all substrate films, and indeed resists, to sputter at approximately the same rate. End point detection is thus very difficult which makes run to run reproducibility unreliable. Also the high energy bombardment can cause ion implantation rather than etching as well as damage to the substrate lattice. For these reasons sputter etching is rarely used in IC fabrication.

### b) Plasma Etching

This is a largely chemical technique that involves the creation of a discharge
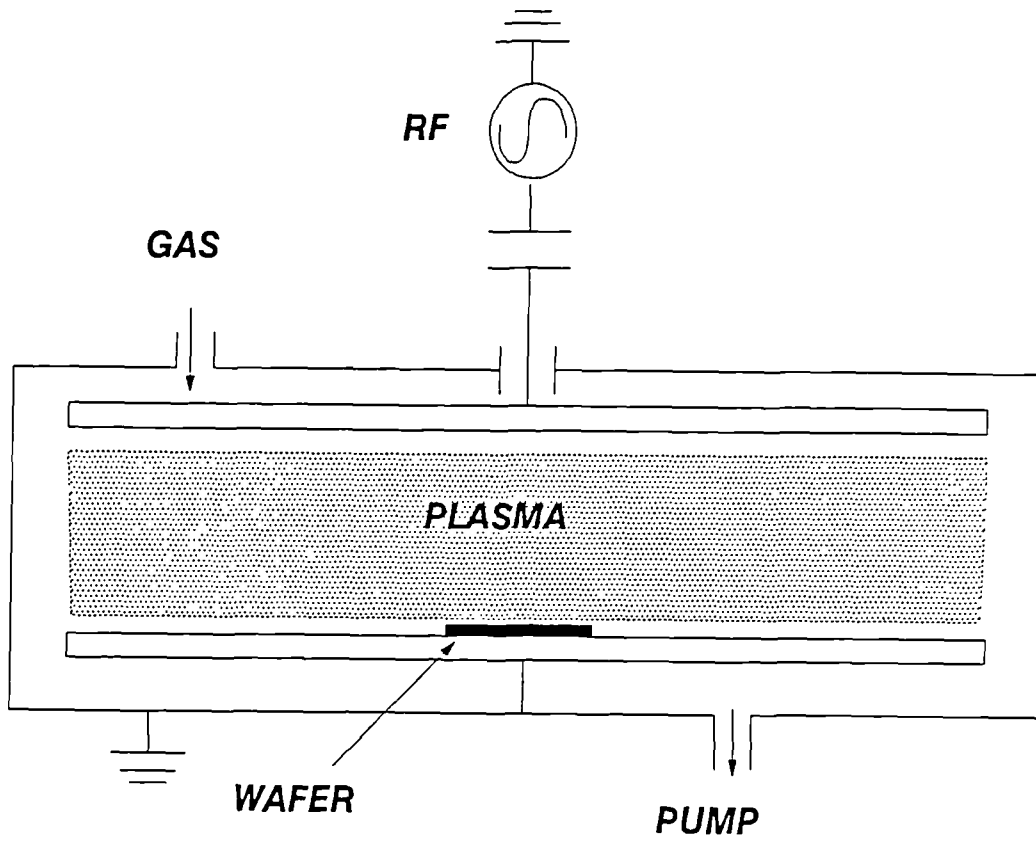
**Figure 1.6** Schematic diagram of a parallel plate etcher used in plasma etching.

between two parallel plates. The discharge consists of atoms, radicals, ions and neutrals. The wafer to be etched is placed on the lower of the two plates which is grounded while the upper plate is connected to an RF supply. The chamber is maintained at a pressure of, typically, a few hundred mTorr. A typical parallel plate plasma etcher is illustrated in figure 1.6.

The reactive species that are formed in the discharge diffuse to the surface where they can react to form volatile compounds. These desorb from the surface and are pumped away. The primary advantage of plasma etching is that very reactive species can be introduced to the surface. For example a $CF_4$ discharge will produce F and $CF_x$ (x = 1 to 3) all of which have much higher sticking probabilities than $CF_4$ and will readily react with the surface. The geometry of the etcher is such that the ions will only experience limited ion bombardment and so sputter etching is minimal. Consequently the etch profiles obtained tend to be isotropic although anisotropic profiles can be achieved. The process is also quite selective, due to its low energy, and introduces little damage to the wafer.

## c) Reactive Ion Etching

In this method the etch process proceeds by a combination of both physical and chemical etching. The geometry of the etcher is such that the areas of the electrode are very different. The smaller electrode, on which the wafer is placed, is connected to an RF supply, typically at a frequency of 13.56 MHz. An RIE reactor is illustrated in figure 1.7. The small electrode acquires a negative bias (see section 1.4.6) which causes the sheath potential to reach several hundred volts. Ions produced in the discharge are accelerated on to the wafer surface where both physical sputtering and chemical etching mechanisms are initiated. The pressure in the discharge is low, < 100 mTorr, to avoid excessive collisions of the ions crossing the sheath which would otherwise reduce their directionality and energy.

The aim of reactive ion etching is to combine the advantages of plasma etching (high selectivity, low damage) with those of sputter etching (anisotropic profiles, fast etch rates). This is the ideal case and many process engineers spend much time trying

19
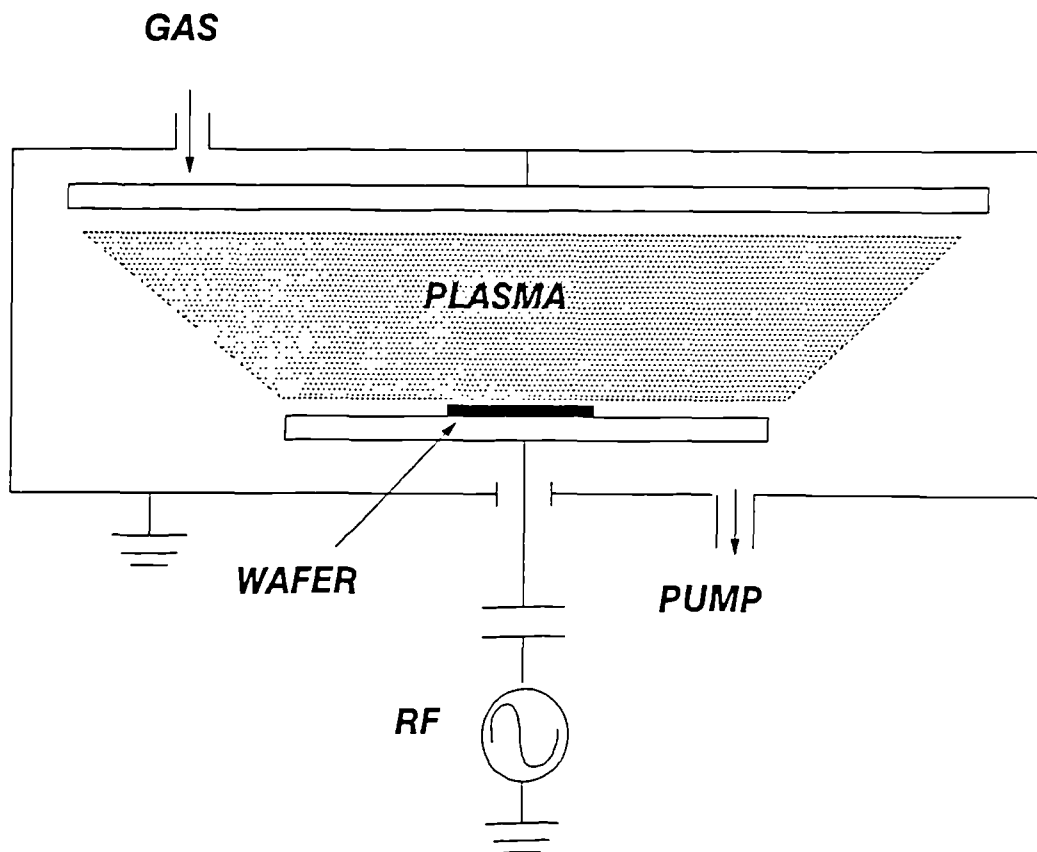
**Figure 1.7** Schematic diagram of a reactive ion etcher.

to achieve these conditions. Reactive ion etching has now become the standard technique used for etching in the semiconductor industry, although the precise mechanisms, especially the role of energetic ions, that occur during an etch are not well understood. It is this lack of understanding that is the motivation behind the work contained in this thesis.

## d) Miscellaneous Dry Etch Techniques

Other dry etch techniques are currently being developed[9] for the next generation of etchers. Electron Cyclotron Resonance (ECR) is a technique that is now quite well developed. It involves a magnetic field containing an RF or microwave discharge. The electrons are forced to follow spiral trajectories and so undergo many ionising collisions. The degree of ionisation is much higher than in RF reactors and the process can therefore operate at pressures as low as 1 mTorr. Consequently a high degree of anisotropy is easily achieved, together with good etch rates and little damage to the substrate. Other systems which contain these attributes have also recently become available. These include inductively coupled plasmas (ICP), M = 0 resonant induction (MORI) and helical resonators. As yet none of these systems has been sufficiently characterized for it to be clear whether any will be the basis for future production applications.

## 1.3.3 Fabrication Example[3]

Having outlined all the relevant steps in the fabrication process an example of a pn diode process is now presented to illustrate the overall procedure. All four of the processes outlined above i.e. film formation, lithography, etching and doping are involved. The steps are shown in figure 1.8 a) to f).

 a) A film of $SiO_2$ is grown by oxidation on the silicon substrate

 b) Photoresist is applied and a mask laid down on the wafer. Exposure to UV light is followed by developing which transfers the required pattern.

 c) The developed resist is removed leaving a photoresist pattern on the wafer.

 d) Etching of the $SiO_2$ layer takes place, stopping at the silicon layer. The

UV

PHOTORESIST

SiO2 | SiO2

n | n

(a) | (b)

ION ETCH

PR | PR | PR | PR

SiO2 | SiO2

n | n

(c) | (d)

METALLIZATION
LAYER

ION IMPLANTATION

SiO2 | SiO2

p | p

n | n

(e) | (f)
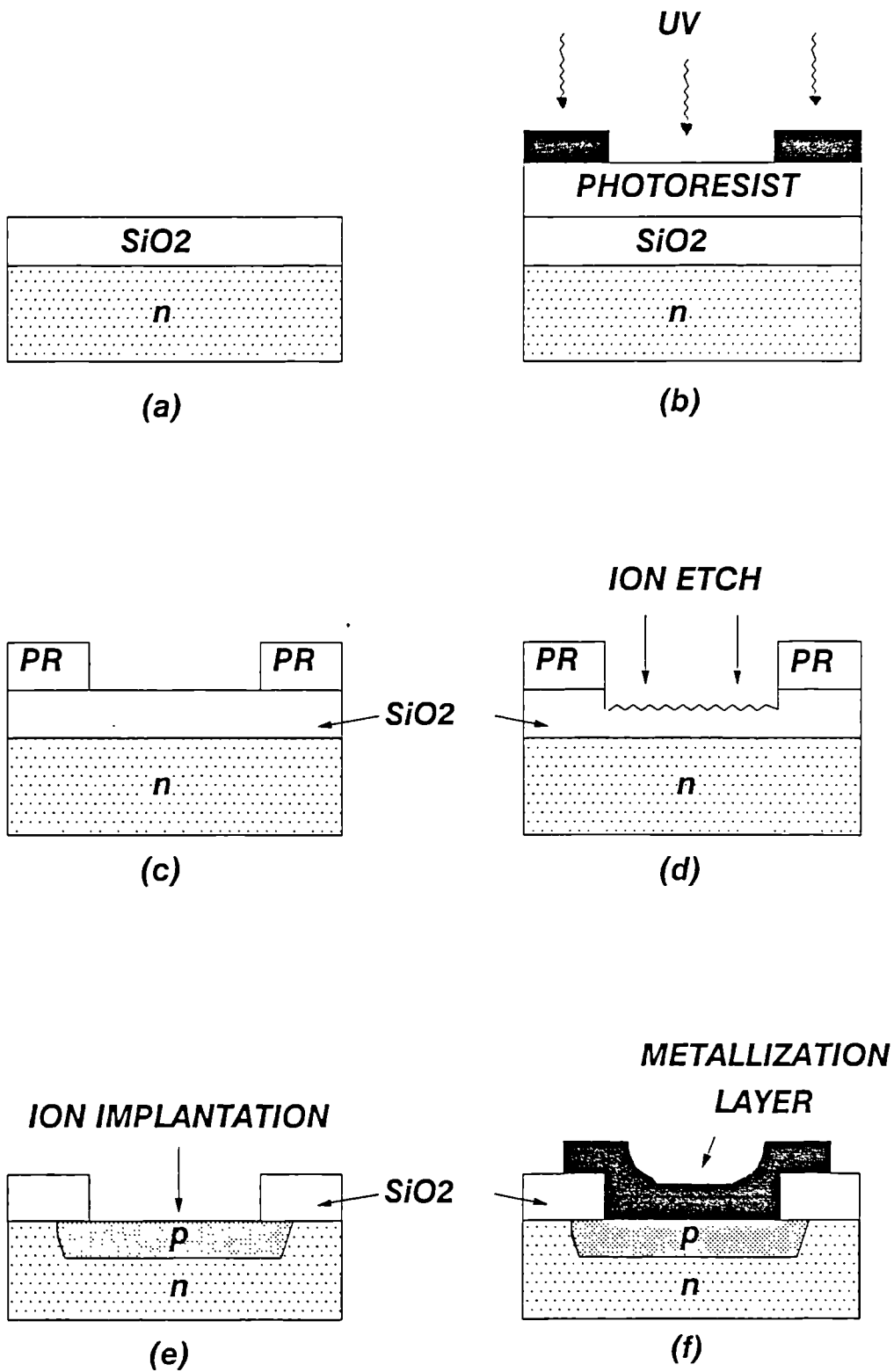
**Figure 1.8** Typical process sequence for production of a pn diode. See text for details of each step.

22

remaining resist is also removed after etching is completed.

e) Doping of the n type silicon with boron produces a region of p type silicon.

f) Metallization of the exposed p type silicon is carried out for later contact to other components.


This procedure only produces one layer of the multi-layer structure. Subsequent steps will isolate components, etch contact holes and join separate transistors together to produce the finished device. Detailed descriptions of fabrication processes on silicon can be found in Elliott[2].


## 1.4 PLASMA PHYSICS[10-12]

We now consider some of the basic physics of the discharge. First of all it is useful to have a definition of a plasma. Chen[13] has provided the following:


'A plasma is a quasi-neutral gas of charged and neutral

particles which exhibits collective behaviour'.


In an ordinary gas the molecules are electrically neutral and move about until they collide, almost elastically, with another molecule. The situation in a plasma is different since the gas is partially ionised and therefore contains neutrals (atoms and molecules), electrons, positive and negative ions and photons. The charges that are present will cause regions of positive and negative charge, leading to electric fields, current flow and induced magnetic fields. These fields will affect the motion of other charged particles by long range Coulomb interactions. It is the Coulomb force that causes the collective behaviour referred to by Chen, i.e. it is not only local conditions that can affect the motion of a particle but the status of remote parts of the plasma also. Despite containing many charged particles the plasma has overall charge neutrality - hence the use of the term quasi-neutral.

Plasmas are used in a great variety of applications. It is their use in the microfabrication process with which this work is concerned. The physics of low

pressure RF gas discharges is now considered in the following sections.

## 1.4.1 Initiation and Maintenance of the Discharge

The plasmas that are formed in a reactive ion etcher are weakly ionised, the degree of ionisation being typically $10^{-4}$. Thus the bulk of the plasma consists of neutral molecules and radicals. The discharge is initiated by the release of an electron in one of two ways:

a) photoionisation of a neutral species by cosmic rays or background radiation or

b) field emission caused by strong electric field about a sharp point on the electrode surface.

The released electron is then accelerated by the applied electric field, eventually gaining sufficient energy to ionise a neutral in an inelastic collision. The released electron is also accelerated in the field and a cascade effect is rapidly set up with other gas molecules being ionised in subsequent collisions.

This process does not of course continue indefinitely. Electrons are lost from the plasma at the chamber walls, by recombination with positive ions and by electron attachment reactions. To sustain the plasma electrons must be generated at a rate sufficient to offset their rate of loss. The major mechanism for producing electrons, and therefore in sustaining the plasma, is thought to be the release of secondary electrons from electrode surfaces by ion bombardment[14]. A second sustaining mechanism can occur in plasmas where the frequency of the applied voltage is > 1 MHz. The field fluctuation in the body of the plasma accelerates electrons which subsequently collide with gas molecules. Although most of the electrons will have insufficient energy to cause an ionising reaction there will be some in the high energy tail of the distribution that will attain energies of tens of eV. These electrons will be able to cause ionisation and help sustain the plasma. However, this mechanism only accounts for a few percent of the total electron population.

24

## 1.4.2 RF and DC Discharges

Only discharges powered by RF are currently used in dry etching systems. The frequency of the supply is upwards of 50 kHz. The reason for using high frequency is that it removes the necessity for drawing direct current through the system, as would be required in a DC discharge. This allows for the etching of insulators, such as $SiO_2$. If a DC discharge were to be used to try to etch an insulator the surface of the insulator would charge up and rapidly cause the discharge to extinguish. In an RF discharge the negative charge built up on one half cycle can be neutralised by ion bombardment in the following half cycle. If the frequency of the applied voltage is greater than a few kHz then the discharge can be continuously sustained.

## 1.4.3 Temperature of Electrons, Ions and Neutrals

The species in a plasma all receive their energy either directly or indirectly from the applied electric field. For a system at thermal equilibrium the energies of an assembly of particles will be described by the Maxwell-Boltzmann distribution. The plasma is not an equilibrium system and so the Maxwell-Boltzmann distribution may not be expected to apply. We find however that the energy distributions are closely approximated by a Maxwellian type distribution and so we can consider the species to have a temperature. The temperature, T, is usually quoted in Kelvin or may be converted to eV using

$$kinetic\ energy = (3/2)\ kT/e \qquad \textbf{(1.1)}$$

where k = Boltzmann constant and e = electronic charge.

The three main species types within a plasma have different effective temperatures. These are now considered separately below

**Electrons.** The bulk of the plasma region is at equipotential and is therefore considered to be field free. The edges of the plasma oscillate with the applied RF. Interaction of charged particles with the RF results in the particles gaining energy. Electrons gain energy very efficiently from the field fluctuations due to their small mass. Secondary electrons are also emitted from the surface by ion bombardment

25

gaining very high energies by acceleration through the entire sheath potential. Finally, electrons can also gain energy by reflection off the moving plasma-sheath boundary. These factors combine to produce a high average electron temperature of $\sim 20,000$ K ($\sim 2$ eV) in an electropositive plasma and usually much higher in an electronegative discharge.

**Ions.** Ions receive energy from the electric field far less efficiently than electrons due to their greater mass. Consequently their temperature is much lower, typically only just above thermal i.e. $\sim 400$ K ($\sim 0.05$ eV).

**Neutrals.** Neutral gas molecules gain energy inefficiently, usually via collisions with ions. Their temperature is very close to ambient i.e. $\sim 300$ K ($\sim 0.04$ eV).

## 1.4.4 The Electron Energy Distribution

It was stated above that the energies of particles in the plasma can be approximated by a Maxwell-Boltzmann type distribution, but this is only applicable to an assembly of particles in thermal equilibrium. The non-equilibrium nature of the plasma means that deviations from the Maxwellian distribution may occur. The relatively massive ions and neutrals are in fact well approximated by a Maxwellian distribution but the lighter electrons may have a distorted distribution. In order to investigate this possibility Druvestyn and Penning[15] calculated a theoretical distribution for electrons moving in a weak electric field that predicted a Maxwellian curve with the high energy tail depleted. Other workers[16,17] predict similar distributions. Experimental evidence[18-22], usually in Langmuir probe systems, shows that the electron distribution is far more Maxwellian than these theories predict. However, the exact form of the distribution has been shown to be strongly dependent on plasma conditions[23,24]. Clearly, the exact form of the EED is uncertain.

## 1.4.5 Sheath Formation and Floating Potential

One of the most important features of a discharge is the formation of a sheath region surrounding any surface in contact with the plasma. It is the nature of this region that causes positive ion bombardment at the surface. We now consider the

formation of the sheath in detail.

An electrically isolated substrate placed in the discharge will initially be struck by positive ions and electrons. The flux of any singly charged species to the surface is given by:

$$J = \frac{en\bar{c}}{4} \tag{1.2}$$

where e = electronic charge, n = density and $\bar{c}$ is the mean speed of the species given by:

$$\bar{c} = \sqrt{\frac{8kT}{\pi m}} \tag{1.3}$$

where k = Boltzmann's constant, T = temperature and m = mass of the species.

There is a large difference in temperature (and therefore velocity) between electrons and ions and consequently a much larger flux of electrons will reach the surface than ions. The surface thus begins to charge negatively, repelling further electrons and attracting ions. This causes a region of positive space charge to arise about the substrate. This region is known as the *sheath*. The potential which the substrate attains is known as the *floating potential*, since it automatically acquires this potential, or 'floats' up to it.

The typical extension of the sheath in space is usually small and is characterised by the electron Debye length. However, this typical case has a fundamental complication that was first identified by Bohm[25]. Due to the distortion of the ion distribution in the sheath by losses to the wall (or substrate) the shielding of the negatively charged wall from the plasma is not possible unless the *Bohm criterion* is met. This condition states that ions must enter the sheath with a velocity somewhat higher than thermal. For this to occur ions must be accelerated before they reach the sheath. Physically, the Bohm criterion can be thought of as the sheath decaying in a quasi-neutral region as illustrated in figure 1.9. The Bohm criterion requires that the energy of the ions when they enter the sheath be at least $\frac{1}{2}kT_e$ which corresponds to

*I* *max*

*plasma*     *quasi-neutral*
*transistion*
*region*

*electrode*

*positive*
*space*
*charge*
*region*
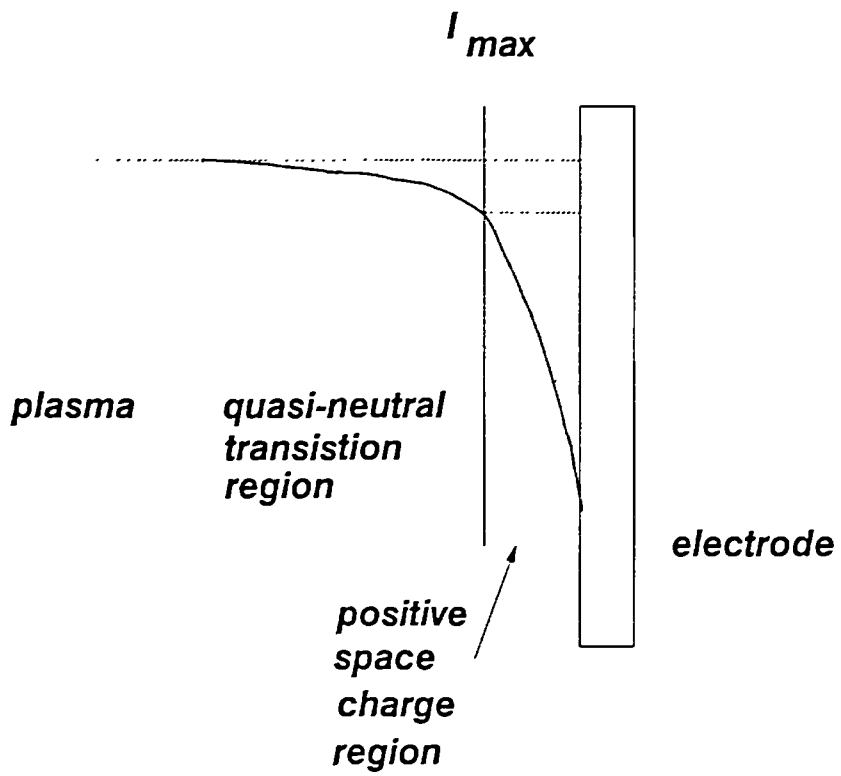
**Figure 1.9** Potential variation near a negative electrode. After Chapman[11].

a potential in the pre-sheath region of at least $\frac{1}{2}kT_e/e$.

There is some debate as to the validity of the Bohm criterion in RF discharges[26,27]. The conditions for which it was derived (monoenergetic cold ions, completely absorbing walls) do not apply to plasma-sheath boundaries in the discharge. We discuss the validity of the Bohm criterion in section 4.2.

The potential to which an isolated substrate will float, taking into account the Bohm criterion, is given by[11]:

$$V_p^0 = -\frac{kT_e}{2e} \ln \frac{m_i}{2.3m_e} \qquad (1.4)$$

where $T_e$ = electron temperature, $m_i$ = ion mass, $m_e$ = electron mass, $k$ = Boltzmann's constant and $e$ = electronic charge.

A further consequence of the high mobility of electrons in relation to ions is that electrical disturbances in the bulk plasma are small. The bulk plasma therefore resides at equipotential. This is termed the *plasma potential*, $V_p(t)$ and this oscillates with the applied RF voltage $V_0(t)$. The potential difference between the plasma potential and the floating potential is defined as the *sheath potential*. This is the potential over which an ion is accelerated on to a floating substrate.

The sheath is a region of positive space charge, i.e. the electron density here is lower here than in the bulk plasma. Thus, there are less electron impact excitation reactions in the sheath and consequently reduced fluorescent emission from excited species. The sheath is therefore dark compared to the bulk plasma . The substrate is then surrounded by a *dark space* and, if it is sufficiently thick, can be viewed in the reactor.

## 1.4.6 Voltage Distributions in RF Reactors

In an RIE reactor surfaces are not floating but are either grounded (anode) or powered (cathode). This affects the sheath potentials at the electrodes. At the anode

the sheath potential simply becomes equal to the plasma potential while at the cathode the sheath potential is the difference between the plasma potential and the voltage on the electrode. This can be extremely large due to the contribution of the applied voltage and the *DC bias*.

The DC bias arises as a consequence of the unequal electrode areas and the presence of a blocking capacitor between the cathode and power source. This introduces the constraint that there can be no net charge transport across the discharge in one RF cycle. Thus the net total charge flow to the anode and cathode in one RF cycle must sum to zero. Most etchers used in plasma processing have unequal electrode areas. The grounded area or anode, $A_a$, in an etcher is usually larger than that of the powered area or cathode, $A_c$. For the requirement of zero net current flow to be met the cathode charges negatively to reduce the electron current to the surface. This produces a large negative DC offset between the cathode and the plasma. This is referred to as the DC bias, $V_{dc}$. This can be of the order of several hundred volts depending on the relative areas of the anode and cathode[28].

Song et al have derived a relationship between the electrode areas and the sheath potentials for an RIE etcher. The expressions developed fit experimental data well and the theory has proved to be more reliable than older theories[29]. The theory of Song et al also provides expressions for the DC bias and the plasma potential which depend, importantly, only on readily measurable plasma parameters. The expressions derived for the fundamental potentials in the plasma are:

$$V_{dc} = V_0 \sin \frac{\pi}{2} \frac{1-A_e}{1+A_e} \qquad (1.5)$$

$$V_e(t) = V_0 \sin(\omega t) - V_{dc} \qquad (1.6)$$

$$V_p(t) = \frac{kT_e}{e} \ln \left( \frac{1 + A_e \exp \frac{eV_e(t)}{kT_e}}{1 + A_e} \right) + V_p^0 \qquad (1.7)$$

where $V_0$ = applied RF voltage, $A_e = A_c/A_a$, $\omega$ = frequency of RF.

Figure 1.10 shows the relation between $V_{dc}$ and $V_0$ for a typical RIE reactor. For the majority of the RF cycle the cathode sheath potential is negative and electrons are excluded from the sheath. Only during the small fractions of the RF cycle where the potential is positive can electrons reach the cathode. In this way the criterion for no net current flow in one cycle can be met.

The time variation of the sheath potentials at both the anode and cathode are shown in figure 1.11. Note that the anode sheath potential is identical to the plasma potential since the electrode is at ground. The cathode sheath potential is the difference between the plasma potential and the electrode potential and so the magnitude of the sheath potential at the cathode is far greater than at the anode. A further consequence of the unequal electrode areas is that the cathode sheath potential is greater than the minimum value for a large part of the RF cycle. The anode potential is in anti-phase to the cathode potential and so for the majority of the cycle is at the minimum potential. The time averaged potentials in the chamber are shown in figure 1.12. This figure demonstrates that the plasma potential is the most positive potential in the chamber.

## 1.4.7 Spatial Variation Of The Sheath Potential

The variation of the sheath potential with distance x into the sheath is not accurately known for RF discharges. There have been many different forms suggested[11] such as the Child-Langmuir potential, linear fields, ion-mobility limited potentials and modifications to any of these. The most satisfactory potential, derived in Chapman[11], is the Child-Langmuir potential given by:

$$\frac{4}{3} V^{\frac{3}{4}} = \left(\frac{4J}{\epsilon_0}\right)^{\frac{1}{2}} \left(\frac{m_e}{2e}\right)^{\frac{1}{4}} x \qquad (1.8)$$

where J = electron flux, $m_e$ is the mass of the electron, $\epsilon_0$ is the permittivity of free space and x is the distance into the sheath.
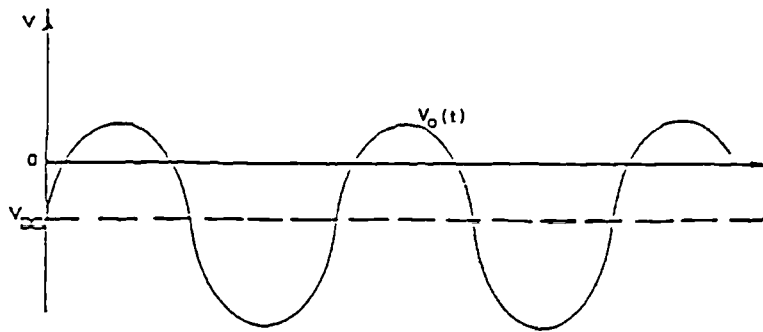
**Figure 1.10** Variation of $V_0$ with time for an RIE system
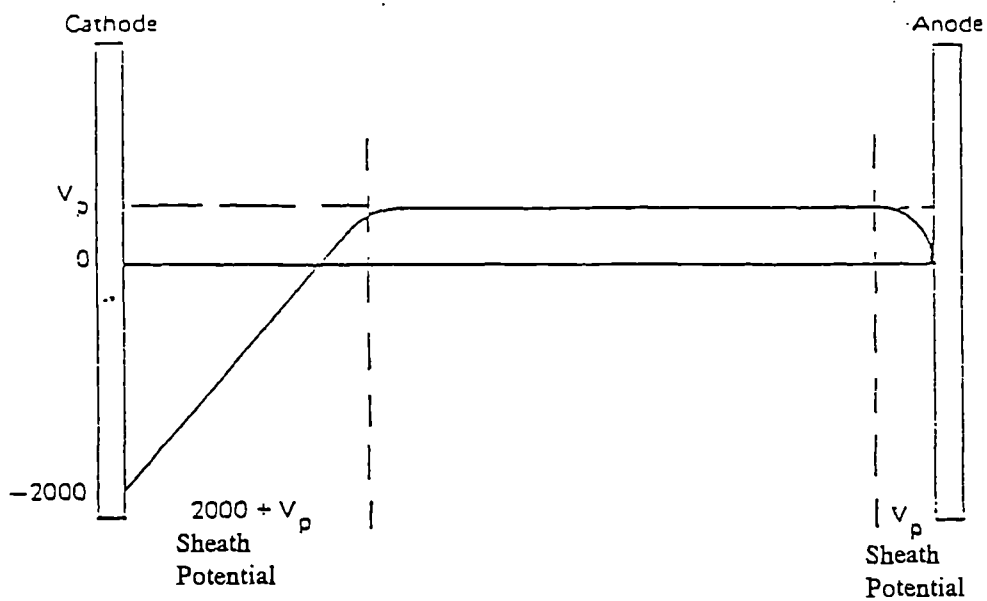


**Figure 1.12** Time averaged sheath potential versus location in an RIE reactor. After Chapman[11].
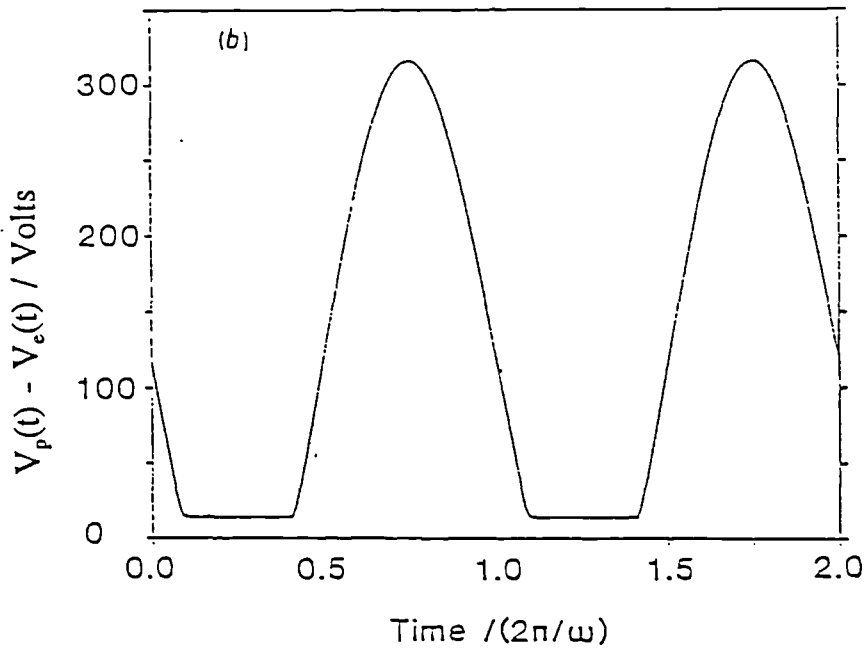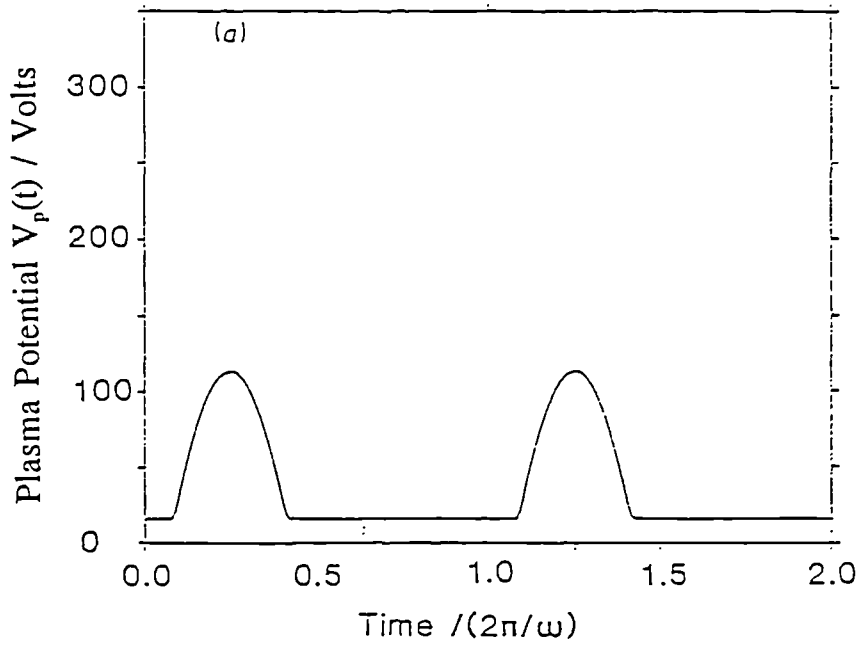
**Figure 1.11** Variation of sheath potential for a) the anode and b) the cathode for a 13.56 MHz RIE plasma. After Song et al [28].

## 1.4.8 Origin of The Ion Energy Distribution

Ions enter the sheath region with energies that are, on average, slightly above thermal. As they cross the sheath they are accelerated by the potential that is present and arrive at the electrode surface with greatly increased energies. Ions incident on the anode surface have energies of tens of eV while those at the cathode can reach hundreds of eV.

Ions gain energy due to acceleration by the sheath potential which is oscillating on an RF timescale. Field et al[30] have used the theory of Song et al to derive equations for the maximum and minimum sheath potentials at both the cathode and the anode of a reactor. These equations are:

Cathode:

$$V_{pe,max} = V_0 + V_{dc} + V_p^0 - \frac{kT_e}{e} \ln (1+A_e) \qquad (1.9)$$

$$V_{pe,min} = V_p^0 + \frac{kT_e}{e} \ln \frac{A_e}{1+A_e} \qquad (1.10)$$

Anode:

$$V_{pe,max} = V_0 - V_{dc} + V_p^0 + \frac{kT_e}{e} \ln \frac{A_e}{1+A_e} \qquad (1.11)$$

$$V_{pe,min} = V_p^0 - \frac{kT_e}{e} \ln (1+A_e) \qquad (1.12)$$

To gain an insight into the form of the IED that arises we consider a square wave that oscillates between two extremes, $V_{pe,min}$ and $V_{pe,max}$ where $V_{pe}$ = voltage between plasma and electrode (i.e. the sheath potential). This situation is shown in figure 1.13a. At this point we introduce the concept of a plane of origin that

corresponds to the maximum spatial extent of the sheath. If an ion crosses the plane of origin when the sheath is expanded it immediately experiences an acceleration and will reach the electrode with energy of $E_{max} = eV_{pe,max}$. Similarly, ions that cross the plane of origin when the sheath is at its minimum extent (and potential) will not experience an acceleration until they encounter the minimum sheath boundary. These ions have resulting energies of $E_{min} = eV_{pe,min}$. This situation would give rise to two single peaks in the IED as shown in figure 1.13b. In reality, however, the sheath potential varies sinusoidally - or as a rectified sinusoid. The effect of this is to produce a saddle shaped IED positioned between $E_{max}$ and $E_{min}$ as shown in figure 1.13c.

An ion can only attain energy of $E_{max}$ where it can cross one *full* sheath potential before the sheath contracts about it leaving it travelling towards the electrode with constant velocity. Ions that do not experience the full potential will not gain the maximum energy. Thus we can identify the *ion transit time* across the sheath as being an important parameter in determining the energy an ion can attain. Factors which affect the ion transit time, and consequently the IED, are:

a) **Frequency of applied RF.**

At a low frequency the sheath potential varies only slowly relative to the ions transit time across the sheath. An ion can easily cross the sheath in one cycle or less. At higher frequencies the sheath will contract about the ion leaving it travelling towards the electrode at a constant velocity. The ion may then impact on the electrode before the sheath again envelops it or it may experience one or more further cycles of acceleration and constant velocity. In either case the ion will receive less energy than $E_{max}$.

At very high frequencies an ion will experience many cycles of acceleration and constant velocity periods. Here the ion will attain an energy much less than $E_{max}$. Also, no ions will be able to cross the sheath region from the plane of origin to the minimum sheath boundary before the sheath expands to envelop and accelerate the ion. Consequently there will be no ions present with the minimum energy, $E_{min}$. In the extreme case where all ions experience many cycles of sheath expansion and contraction the IED will consist of a single peak corresponding to the average sheath
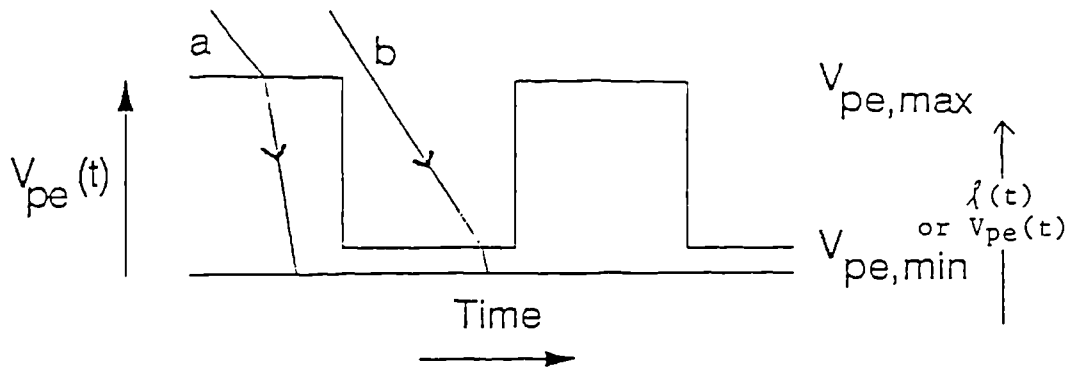
**Figure 1.13a** Diagram showing ion trajectories for a square wave sheath potential of low frequency. Ion a) experiences the maximum potential, $V_{pe,max}$ while ion b) experiences only the minimum value, $V_{pe,min}$.
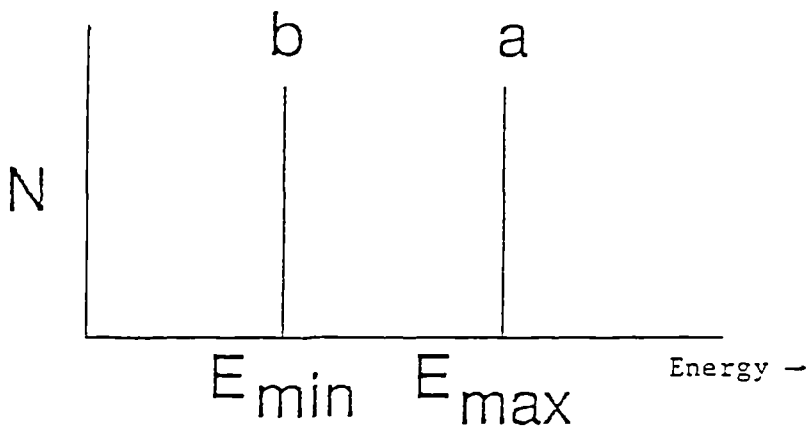


**Figure 1.13b** IED that would arise from the trajectories in figure 1.13a.
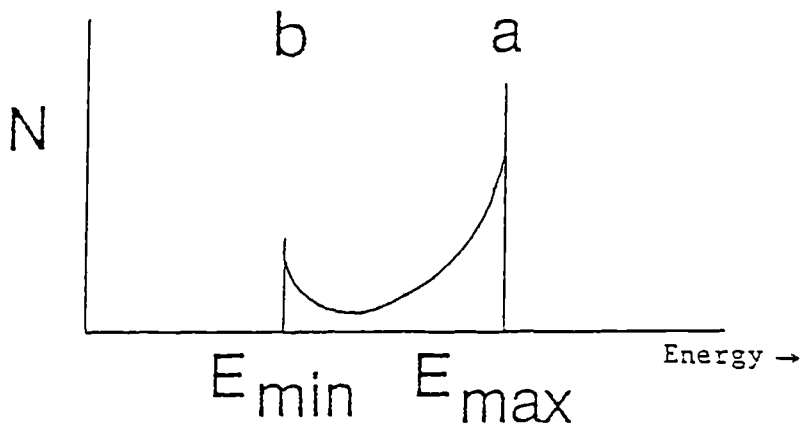


**Figure 1.13c** IED expected from a plasma where the sheath potential varies as a rectified sinusoid.

potential.

## b) Sheath Thickness.

If a thick sheath is present at the electrode surface then an ion can take many RF cycles to cross the sheath. The situation is then analogous to the effect of high frequency as described above and we are likely to observe a distribution that is a single peak, or is two peaks very close together. A thin sheath is analogous to the low frequency effect and an IED with well separated peaks will result.

## c) Ion Mass.

Heavy ions cross the sheath more slowly than light ions. Thus, given all other parameters in the discharge equal, the IED obtained with light ions will be more spread out than with heavy ions.

## d) Ionic Charge.

Doubly charged ions are accelerated by the sheath potential to higher energies than singly charged ions. Thus the transit time across a sheath for doubly charged ions is less than that for singly charged ions across the same sheath. The IED of doubly charged ions will therefore be narrower than a singly charged species of the same ion. It will also appear at a different energy.

The width of an IED is therefore dependent on the ions' transit time. Ions that cross the sheath in only a few RF cycles, or less, produce double peaked distributions. This is referred to as *RF modulation* of the IED[31]. RF modulation is apparent even in cases where the ion transit time is greater than ~ 5 RF periods[32]. Vallinga[33] has derived an expression for the width of the collisionless IED that has been empirically modified by Field et al[30].

$$\Delta E = 0.889 \frac{[eV_{pe,max}]^{\frac{3}{2}}}{\pi \, e \, \omega \, l_{max} \sqrt{2m_i}} \tag{1.13}$$

Where e = electronic charge, $V_{pe,max}$ = maximum sheath potential, $\omega$ = frequency of

applied RF voltage, $l_{max}$ = maximum sheath thickness and $m_i$ = mass of ion.

Note that this equation assumes that the ions are singly charged. The splitting, $\Delta E$, is an indicator of RF modulation and the magnitude of $\Delta E$ a sign of the degree of that modulation.

The above discussion applies to ions that suffer no collisions as they cross the sheath. Ion neutral collisions resulting in momentum and energy transfer will significantly alter the IED from that found in a collisionless sheath. Whether a collision occurs or not depends on the sheath thickness and the discharge pressure. Most studies to date of collisional sheaths have focused on argon plasmas. Effects observed in these discharges are elastic scattering and charge exchange. The effect of elastic scattering is to redirect a portion of the ions velocity away from perpendicular to the electrode. This results in a smearing of the IED towards lower energies. Charge exchange involves the creation of a new ion, with thermal energy, at some point in the sheath. The new ion is then accelerated towards electrode by the sheath potential. It does not experience the full potential that an ion entering the sheath at the plane of origin would. Consequently sharp peaks at energies lower than the main IED may be observed. Figure 1.14 shows a typical IED from a collisional sheath.

## 1.5 PLASMA CHEMISTRY
### 1.5.1 Reactions in the Plasma

Having discussed the physics of plasmas we now consider the chemical reactions that can occur within an etch reactor. A full discussion of the possible chemical reactions is beyond the scope of this study and therefore we only concentrate on processes that are relevant to the present work. Plasmas consist of a complex mixture of neutrals, ions, electrons, free radicals and photons. The relative concentrations of these species will be closely interrelated and complicated reaction schemes for specific processes have been proposed[34]. Typically, these reaction schemes include both gas-phase and gas-surface interactions. Detailed descriptions of the chemistry of plasmas can be found in many textbooks[11,35] and other sources[34,36].

The reactions that are of interest in this study are basically only those that
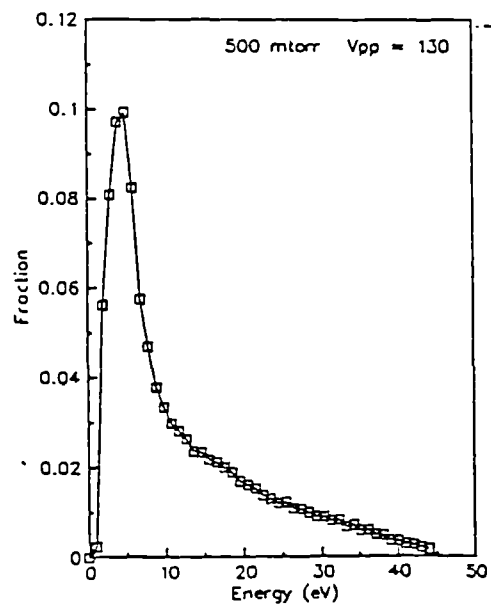
**Figure 1.14** Ar IED from a collisional sheath. After Liu
et al[67].

produce and remove ions from the plasma, since these determine the species that will be incident at the electrode. However, there are many other reactions that occur and these will affect the kinetic energies of particles. This in turn affects the measured IED through such factors as:

i) Ion transit time across the sheath.

ii) Average electron temperature (see equations 1.9 - 1.12)

The fundamental reactions that occur within a low density plasma, such as is considered in this thesis, are[11,12]:

### (a) Electron Impact Reactions

Excitation (electronic, vibrational or rotational)

$$e + A_2 \rightarrow A_2^* + e \qquad (1.14)$$

$$e + A \rightarrow A^* + e \qquad (1.15)$$

Dissociative Attachment

$$e + A_2 \rightarrow A^- + A \qquad (1.16)$$

$$e + A_2 \rightarrow A^- + A^* \qquad (1.17)$$

Dissociation

$$e + A_2 \rightarrow 2A + e \qquad (1.18)$$

Ionisation

$$e + A_2 \rightarrow A_2^+ + 2e \qquad (1.19)$$

Dissociative Ionisation

$$e + A_2 \rightarrow A^+ + A + 2e \qquad (1.20)$$
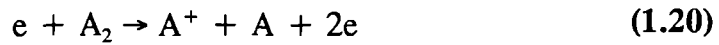
### b) Inelastic Collisions between heavy particles

Penning Dissociation

$$M^* + A_2 \rightarrow 2A + M \qquad (1.21)$$

Penning Ionisation

$$M^* + A_2 \rightarrow A_2^+ + M + e \qquad (1.22)$$

Charge Transfer

$$M^+ + A_2 \rightarrow A_2^+ + M \qquad (1.23)$$
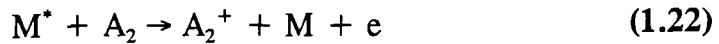
Collisional Detachment

$$M + A_2^- \to A_2 + M + e \qquad (1.24)$$
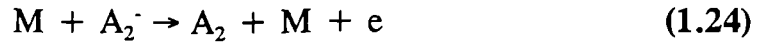
Associative Attachment

$$A^- + A \to A_2 + e \qquad (1.25)$$

Electron-Ion Recombination

$$e + A_2^+ \to 2A \qquad (1.26)$$

$$e + A_2^+ + M \to A_2 + M \qquad (1.27)$$

Atom Recombination

$$2A + M \to A_2 + M \qquad (1.28)$$

Atom Abstraction

$$A + BC \to AB + C \qquad (1.29)$$

Atom Addition

$$A + BC + M \to ABC + M \qquad (1.30)$$

**C) Heterogeneous Reactions** (Where S = surface in contact with plasma)

Atom Recombination

$$S\text{-}A + A \to S + A_2 \qquad (1.31)$$

Metastable De-excitation

$$S + M^* \to S + M + h\upsilon \qquad (1.32)$$

Atom Abstraction

$$A + S\text{-}B \to S + AB \qquad (1.33)$$

Sputtering

$$S\text{-}A + M^* \to S + A + M \qquad (1.34)$$
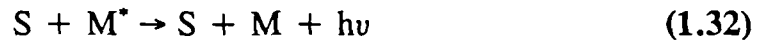
In all these reactions an asterisk indicates an excited state, while M is some third body.

## 1.5.2 Electronegative and Electropositive Plasmas

Whether or not an electron attaches to a neutral and forms a negative ion determines the electronegativity of the plasma. Plasmas are usually classified in to one of two types according to their degree of electronegativity. May[12] has calculated the

41

electron attachment cross section for some common process gases which can be arranged in order of increasing electronegativity. The following series is found:

$$Ar \leq N_2 < CF_4 < CF_2Cl_2 < Cl_2 < CFCl_3 < SF_6 < CCl_4.$$
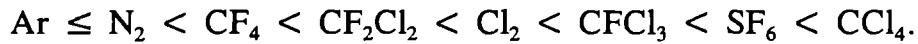
Since our work involves both electropositive and electronegative plasmas we shall now look at each type in more detail.

## a) Electropositive Plasmas

These plasmas are formed by those gases that do not have a particularly large electron attachment cross section i.e. they do not easily form negative ions. Such gases include the noble gases and some unreactive gases e.g. nitrogen. The number of positive ions formed is almost exactly equal to the number of electrons in the plasma. Since there is a large number of electrons these plasmas are generally easy to initiate and sustain. Typical electron temperatures in these plasmas are around 2-5 eV[37]. An electron energy distribution (EED) for an $N_2$ plasma is shown in figure 1.15a.

## b) Electronegative Plasmas

These plasmas have a high electron attachment cross section and negative ions are formed more easily. Consequently the number of free electrons in the plasma is much reduced by comparison to an electropositive discharge. The number of positive ions can outnumber the electrons by up to 100 times. Overall charge neutrality is achieved by the large numbers of negative ions. The relative dearth of electrons means that the transfer of power from the applied electric field to the plasma is somewhat inhibited. Thus electronegative plasmas require high powers to sustain them and can be difficult to initiate. Gases which form electronegative plasmas include the common fluoro- and chlorocarbon process gases e.g. $SF_6$, $CCl_4$ etc. The average electron temperature in these plasmas is often much higher than that found in electropositive discharges. This is because the low energy electrons are removed by the attachment collisions and also due to the fact that energy put into the plasma is distributed between fewer electrons, with a consequent increase in the average energy. Typical electron temperatures may be 5 - 10 eV[37]. An EED from a $CCl_4$ plasma is shown in figure 1.15b.
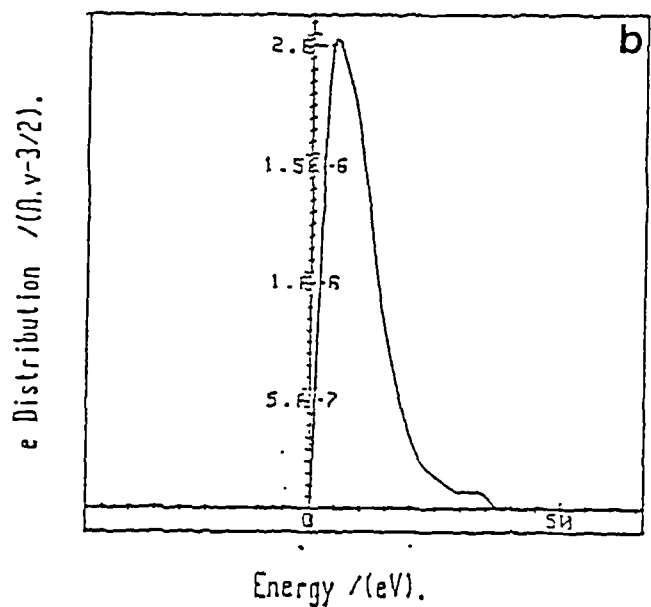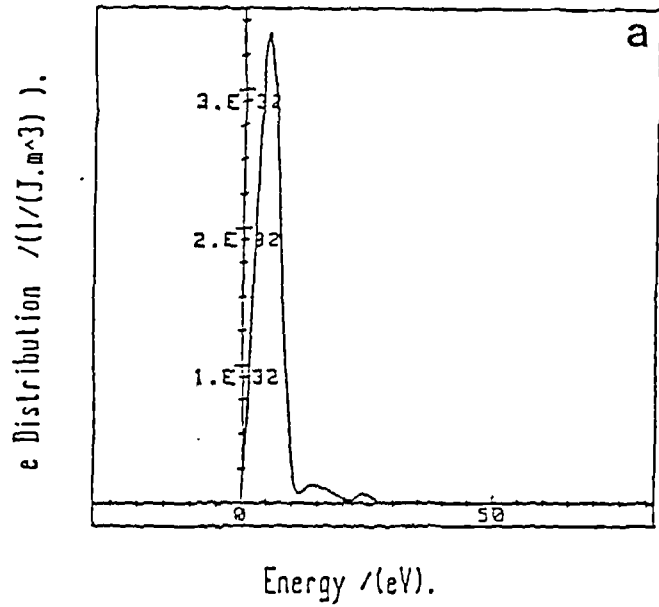
**Figure 1.15** Electron energy distributions from a) $N_2$ plasma and b) $CCl_4$ plasma. After Welch[37].

## c) Intermediate Plasmas

There is of course no unequivocal division between electronegative and electropositive plasmas. There are some gases which have small but non zero electron attachment cross sections. These gases form some negative ions but the numbers formed do not exceed the number of free electrons in the plasma. Such gases include $H_2$, $O_2$, $CH_4$ and also $CF_4$. $CF_4$ forms substantial numbers of negative ions but not as many as in a truly electronegative gas such as $SF_6$. The intermediate type gases form discharges with characteristics between that of electronegative and electropositive plasmas.


## 1.6 PROCESS DIAGNOSTICS[38]

To understand better the mechanisms of plasma processes many diagnostic techniques have been developed. It is hoped that an increased understanding of these mechanisms will lead to more efficient, faster processes and improved reactor design. We can identify two ways in which processes are broadly monitored. These are, firstly, the study of the actual process itself and, secondly, the post process investigation of the substrate. We now consider some of the widely used techniques in each of these areas in turn.


### 1.6.1 Plasma Diagnostics
### 1.6.1.1 Optical Techniques
### a) Emission Spectroscopy.

This has been one of the most popular techniques used to study plasmas since it is non-intrusive, i.e. it does not affect the process, and also it is relatively easy to implement. The technique allows the observer to study emission from electronically excited species and thus identify constituents of the discharge. The formation of bright and dark regions in the plasma also enables study of the effect of the spatially varying fields on ion and electron motion. Emission spectroscopy is usually carried out in the ultra-violet and visible regions.

## b) Laser Induced Fluorescence (LIF).

This method uses a laser to excite a resonance between a ground state and a level in the electronically excited state. The consequent fluorescence allows the concentration of ground state species to be studied in a non-invasive manner. LIF is extremely selective and is also highly sensitive, being able to detect species at densities $\sim 10^8 cm^{-3}$ (cf neutral density of plasma $\sim 10^{14} cm^{-3}$). LIF is also capable of temporal and three dimensional spatial resolution[39].

## c) Fabry-Perot Interferometry[12,40]

This is a technique that has recently been used in this laboratory to examine emission lines with ultra high resolution. This allows the kinetic energies of species to be determined by the measurement of Doppler linewidths.

## d) Ellipsometry[41,42]

This is a technique that allows changes in film thickness during an etch or deposition process to be monitored. It is sensitive to changes in thickness of $< 30$ Å. It relies on the change of polarization of light when reflected at non-normal incidence from a surface. The degree of polarization change can be related to the surface film thickness. Ellipsometry has also been successfully applied to the study of film growth mechanisms where nuclei of $\sim 30 - 70$ Å were seen to coalesce and form a continuous film[43].

## 1.6.1.2 Mass Spectrometry

Mass Spectrometry is a technique used to identify and determine the concentrations of gas phase molecules. It has been used in numerous studies of etch processes[44-48]. Although there are many types of mass spectrometer the most commonly used in the plasma processing environment is the quadrupole mass spectrometer due to the convenient size of the instrument. Two basic methods have been used in studying plasmas. One of these involves placing the mass spectrometer at some point downstream from the plasma, where it is non-intrusive to the process.

However, this technique has the disadvantage that it can be difficult to relate the results to the plasma composition in the chamber. Most species will have taken part in gas phase reactions during the process of being pumped to the analyser. The second basic technique involves sampling directly from the plasma to avoid this uncertainty. Here, the sampling is often achieved by drilling a small aperture in the electrode and allowing species to effuse through to the analyser. Alternatively, a capillary probe has been used to sample directly from the centre of the plasma[49,50].

Mass spectroscopy when used in conjunction with other techniques, such as emission spectroscopy[34] or ellipsometry[51], can be valuable tools in unravelling complex chemical pathways in plasma processing.

### 1.6.1.3 Langmuir Probes

In their simplest form Langmuir probes consist of a bare wire inserted into the plasma. They measure the electrical current, which depends upon their bias voltage in relation to the plasma potential. As the voltage on the probe is altered, so the current to the probe changes. This I-V characteristic can be related to plasma parameters such as the electron temperature, electron density and time averaged plasma potential. Probe techniques have been reviewed by Swift and Schwar[52] and Kushner[53].

Langmuir probes suffer from the problem that there is RF modulation of the signal due to the oscillating plasma potential. In order to eliminate this effect several workers[23,24,54] have tried feeding a voltage from the generator back to the probe, thus forcing the probe to follow the fluctuation of the plasma. However, this assumes that the plasma potential varies sinusoidally. This is open to some debate as we shall show in section 4.6.

### 1.6.1.4 Electrostatic Energy Analysers

The analysis of the energies of ions at the electrode surface yields information about the nature of the ion trajectory across the sheath. The subject of ion energy analysis is reviewed in section 1.7.

## 1.6.2 Post-Process Diagnostics

### 1.6.2.1 Etch Rate Measurement

This is perhaps the simplest of all methods for determining data on the process. The substrate to be etched is weighed before and after the process. Given the known exposed surface area of the wafer the etch rate can be simply calculated. Alternatively, a slightly more sophisticated method is to use a profilometer. This is a stylus that is dragged across the surface, passing over etched features. The movement in the stylus is recorded and the amount of material removed determined. Profilometers are sensitive to changes down to 10 Å.

### 1.6.2.2 Scanning Electron Microscope (SEM).

In this technique a beam of electrons is rastered over the surface of a sample that is enclosed in a vacuum chamber. The secondary electron emission is detected and an image of the surface formed. Resolutions of ~ 100 nm are possible, making this method ideal for examining etch profiles and developing new processes. Another major use is to examine defects at the surface caused by the etch process.

### 1.6.2.3 Surface Analysis

After etching the substrate can be examined to identify the chemical composition and environment of the surface layers. Most of the surface analytical techniques involve directing a probe beam at the surface and detecting either a change in the reflected beam or particles that are released as a result of stimulation by the probe. Commonly used techniques include Auger Electron Spectroscopy (AES), X-ray Photoelectron Spectroscopy (XPS), Secondary Ion Mass Spectroscopy (SIMS) and Ion Scattering Spectroscopy (ISS). The first two of these, AES and XPS, both detect electrons that are characteristic of the element of origin, thus revealing surface composition. SIMS and ISS use ion beams as probes for the surface. In ISS the energy of backscattered probe ions is detected and from this the mass of the surface target atom can be deduced. This technique is similar to Rutherford Backscattering (RBS) but uses lower energy incident ions and is consequently more sensitive to the surface

layers. SIMS analysis involves detecting the energies and yields of ions ejected from the surface by ion bombardment, thus revealing surface composition. SIMS is highly surface sensitive since the secondary ions released originate from depths of only $\sim 5\text{Å}$.

Surface techniques are complementary and no one method provides full information. Recent instruments combine several techniques in the one apparatus to gain the benefits each has to offer.

## 1.6.3 Miscellaneous Diagnostic Techniques

There are many other diagnostic techniques that have been employed for the study of plasmas. Some of these are now briefly mentioned.

**a) Actinometry** A drawback of the OES technique is that it does not allow a direct measure of the ground state concentration of a species. In actinometry a small known amount of an inert tracer gas eg Ar is added to, say, a $CF_4$ discharge[55]. The emission from both species is observed and the concentration of F can be determined from the ratio of line intensities.

**b) Macroscopic Discharge Parameters** e.g. pressure, DC bias or substrate temperature can sometimes be used as indicators of etch end-points.

**c) Transmission Electron Microscopy** is used to study defects in the crystalline lattice of the substrate. A few Å resolution can be achieved.

**d) Infrared Spectroscopy** has been used in the study of deposited films[56].

**e) Titration** Gas phase titration is occasionally used to study concentrations e.g. F atom concentration has been determined downstream from a $CF_4 + O_2$ plasma using $Cl_2$[57].

## 1.7 ION ENERGY ANALYSIS

Our work is concerned with the analysis of ion energies incident at the surfaces of an RF reactor. Therefore we now present a brief review of the topic of ion energy analysis. Studies of IEDs have been carried out at both the anode and the cathode of etch reactors. Measurements at the anode are more numerous in the literature. This technique allows one an insight into ion trajectories in the sheath region without the

48
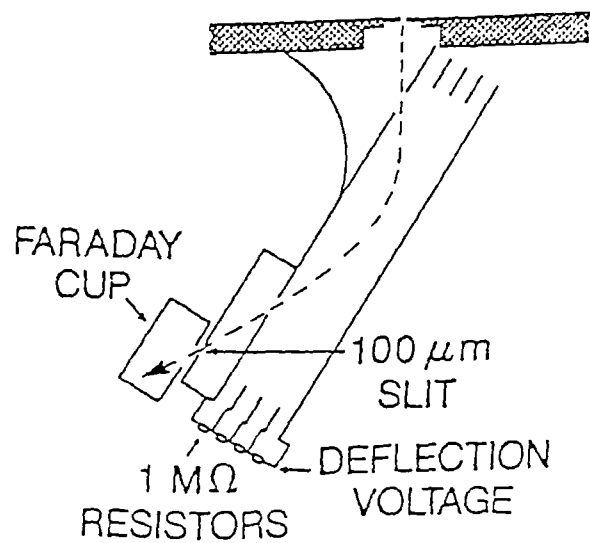
**Figure 1.16** Schematic view of a parallel plate electrostatic analyser. After Manenschijn[58].

experimental difficulties encountered in a study at the cathode. This is the philosophy adopted in this study. Experimental anode IEDs can be compared to theoretically derived distributions, allowing refinement of the theoretical model and, more importantly, prediction of cathode IEDs.

We shall now consider the various techniques that have been used to study ion energies, before going on to consider some of the more important studies that have been carried out by workers. Finally we shall consider the theoretical studies of ion energies that have been proposed.

## 1.7.1 Instrumentation

Experimental ion energy analysis essentially involves creating a small aperture in the electrode through which a sample of the incident ions pass. These ions are then energy, and occasionally mass, analysed. The ion analysis system employed is usually one of the following techniques:

a) **Retarding Field Analyser (RFA)** In this method of analysis an electrostatic field is used to retard incoming ions. The energy of an incident ion is deduced from the potential barrier it can just surmount. Retarding fields can be applied to the collector or to a grid situated in front of the collector. The most commonly used RFA is the parallel grid analyser and is the design used in our study. A full discussion of the theory of operation of this analyser is presented in section 2.3.

b) **Parallel Plate Analyser** Energy analysis by this technique involves ion deflection. It uses a pair of parallel plates with a potential maintained between them as shown in figure 1.16[58]. The ions enter at an angle and are deflected along a parabolic path to a collector. The degree of deflection depends on the voltage between the plates. Varying the voltage allows ions of different energies to be focused on the detector.

c) **Cylindrical Analyser** This is also an ion deflection technique and has often been combined with mass analysis to produce mass and energy resolved IEDs. The energy analysis is carried out by an electric field created between two cylindrical plates bent over an angle, often chosen to be 90°. The angle over which an incident ion is bent depends on its kinetic energy and charge. Thus only ions with a particular

50
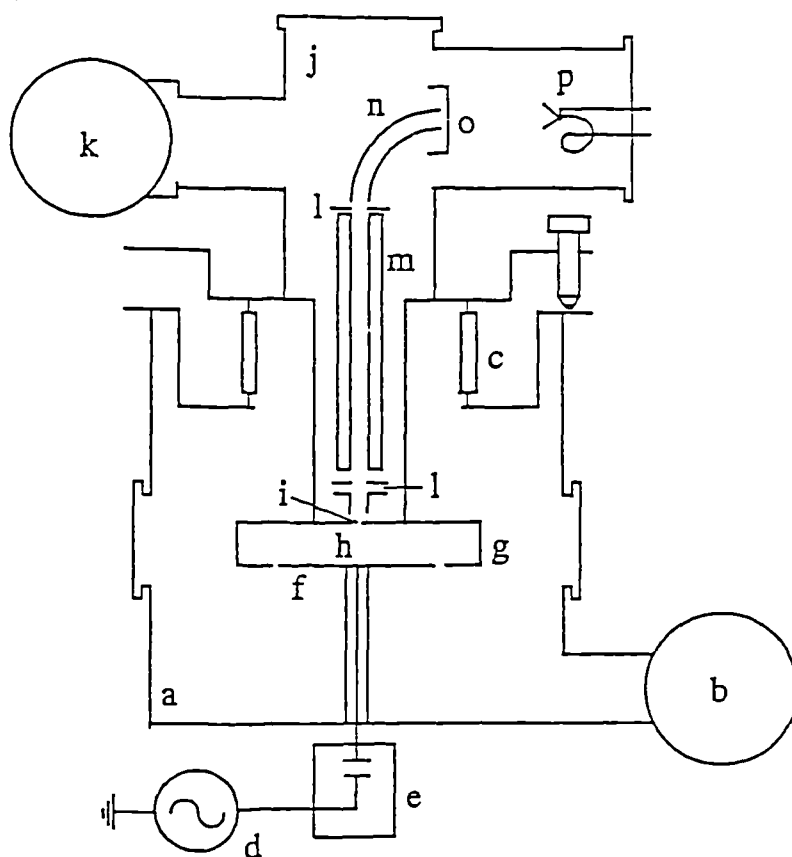
**Figure 1.17** Schematic view of a cylindrical analyser combined with quadropole mass analysis. a) reactor vessel, b) pump, c) bellows, d) RF generator, e) matching network, f) RF electrode, g) grounded electrode, h) plasma cavity, i) sample hole, j) detection chamber, k) pump, l) ion lens, m) quadropole mass selector, n) energy selector, o) exit slit, p) channeltron. After Snijkers[59].

pass energy reach the detector and are analysed. Figure 1.17 shows a recent experiment[59] that uses a cylindrical analyser in conjunction with a quadrupole mass selector. This analyser has often been referred to as cylindrical mirror analyser (CMA). It is actually a cylindrical sector field analyser while a CMA is another deflection analysis technique.

It is important to recognise the limitations of these techniques. The electrostatic deflection analyser, as used by Manenschijn et al[58], has the disadvantage that the sensitivity is proportional to the ion energy. Thus, the IED is attenuated in the low energy region. Additionally, this makes any comparison with theory more difficult. Cylindrical analysers have similarly low sensitivity at energies of less than 5 to 10 eV. To the authors knowledge there is only one paper that directly compares energy analysers applied to RF discharges[60]. Comparison of an RFA and a cylindrical mirror analyser shows large differences in the low energy part of the distribution. The RFA shows ions with all energies between 0 and 15 eV while the CMA distribution consists of just one peak at 7 eV. The authors conclude that results from the CMA are erroneous.

There are many other of these techniques for the analysis of ion beams, but few of these have been applied to IED measurements in a plasma system. A full review of energy analysers may be found in reference 61.

## 1.7.2 Experimental Ion Energy Distributions

The first measurement of energy distributions in an RF discharge was carried out by Coburn and Kay[31] using a cylindrical analyser and quadrupole arrangement. These IEDs showed the double peaked form that is now familiar. Coburn and Kay showed that $\Delta E$, the peak splitting, is proportional to $M^{-1/2}$, where M is the ion mass, although there was some deviation at high ion masses.

Most IED measurements that have followed this initial work have been performed at the anode of the reactor using inert gas plasmas[62-70]. Liu et al[67] have recently measured angularly resolved IEDs at the anode of a reactor using a modified RFA. Instead of using parallel plates to retard the incoming ions concentric spherical

grids were employed, as shown in figure 1.18. The collector is a series of electrically isolated annular rings that allows ~4.5° resolution. Their data shows that at a pressure of 10 mTorr the majority of ions are incident near normal to the electrode. At 500 mTorr, however, ions are incident at all angles. The ion angular distribution (IAD) is seen to peak at around 11°. Other workers have studied the IEDs from gases that are used in actual processes. Thompson et al[71] have studied electronegative plasmas such as $SF_6$, $CFCl_3$, and $CF_3Br$ while Bisschops[72] has studied a $CF_4$ plasma.

The difficulty of measuring IEDs at the cathode in a reactive ion etcher arises because of the rapidly oscillating RF voltage that is present there. This means that the potential of the whole analyser must follow the RF signal, i.e. the 'ground' to which grid voltages are referenced must oscillate with the RF. This has been proved to be possible as shown by Kuypers and Hopman[73], Manenschijn[74] and recently Janes et al[75-77]. Janes et al have measured angularly resolved IEDs for a variety of gases, including some 'real' process gases such as $CF_4$. However, these experiments at the cathode require techniques, such as data transmission via optical fibres, that are complicated by comparison to measurement at the anode. Hence the preference of most workers to study anode IEDs.

Other solutions to the measurement of cathode IEDs have been developed. Otsubo and Ohara[78] have used an analyser that is referenced to ground but is situated behind the cathode. This creates a field between the analyser and the cathode that will affect the ions motion. To overcome this Otsubo and Ohara calculated the equation of motion of an ion in this field and the error that will be introduced in any measurement. They show that any error in the ion energy is inversely proportional to the distance between the analyser and electrode. They conclude that ion energy analysis is possible without any error when the analyser and cathode are more than 20 mm apart. The few results which they present, of $Cl^+$ ions from a $CCl_4$ plasma, show a double peaked distribution.

Wild and Koidl[79] have demonstrated an elegant way of measuring cathode IEDs without using complex techniques. In their experiment they have simply inverted the geometry of the etcher so that the larger electrode, usually grounded, is connected to
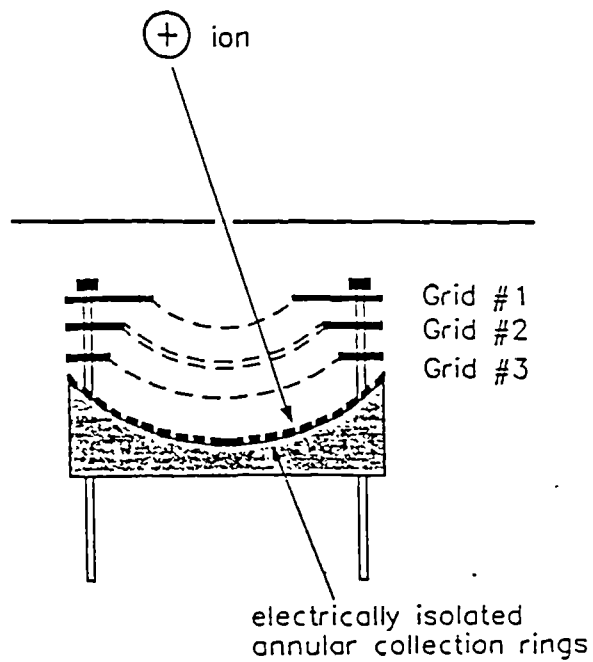
**Figure 1.18** Schematic view of RFA designed for measuring angularly resolved IEDs. After Liu et al[67]

the RF supply. The smaller electrode is then the grounded electrode. The field distribution in the plasma chamber does not depend on whether the RF signal is connected to the large or small electrode. Thus measurements at the grounded electrode are similar to measurements at a cathode in a reactor with ordinary geometry. The results of this experiment display IEDs up to hundreds of eV with charge exchange peaks being clearly visible at high pressures.

## 1.7.3 Theoretical Studies of IEDs

Attempts to understand the processes by which the measured IEDs arise has led to theoretical work to try and calculate IEDs. The first attempt at modelling ion trajectories in the sheath region was by Davis and Vanderslice[80]. They modelled Ar IEDs at the cathode in a DC discharge for high pressures, but only included charge exchange collisions. Tsui[81] was the first to model an IED in an RF reactor using a method of macroscopic energy balances. His results showed the double peaked distribution that has now become familiar. Later work[82-84] has used electrical component models of the discharge to correlate predictions of theory with measurements values. Typically, the sheath, where there is a low concentration of electrons, is modelled as a capacitor while the bulk plasma, with highly mobile electrons, is a conductor and is modelled with an impedance. Zarowin[83,84] used this method to estimate average quantities for the directed and random energies of ions passing through a sheath with many collisions. This method assumes that the distributions are fully developed i.e. the overall IED is not affected by further collisions, and thus these results are limited to high pressures. Also, Zarowin only included charge exchange collisions in the model, further limiting its usefulness.

Another approach to discharge modelling has been to use Monte Carlo methods to simulate the transport of ions through the sheath. Kushner[85] modelled $Ar^+$ trajectories for different plasma conditions, investigating the effect of increasing the pressure. However he only included charge exchange collisions. Kushner also investigated the effect on the IED of using either a sinusoid or a rectified sinusoid form of the plasma potential. Thompson et al[86] developed Kushner's approach to

include momentum transfer scattering in addition to charge exchange collisions. They modelled both DC and RF discharges and used both linear and uniform electric fields. Liu et al[67] used Thompson's program to simulate IEDs at the anode to compare with measured IEDs. Their model does not include an expression for the floating potential and uses a uniform field approximation for the sheath region, which is not an accurate description of reality. Their results show an overall qualitative resemblance to the measured IEDs at low pressures, but at higher pressures the peak positions are not accurately reproduced.

All the Monte Carlo methods above have either only included charge exchange collisions or have used a form of the sheath electric field (uniform or linear) that is unrealistic. Expressions for the fundamental potentials in the discharge have been developed by Song et al[28] (see section 1.4.6). May et al[30,87] have used these expressions to perform calculations at the cathode of an RF discharge operating at RIE pressures. Their model incorporates a realistic description of the time-varying fields in the discharge as well as an adequate model of the collisions occurring. Excellent agreement with Kuypers' $Ar^+$ cathode IEDs has been obtained. Their program is used in our study to determine the limits of its applicability. The model has been described in detail by May[12] but since we use the model in this work a description of the methods used is now included.

The model uses Monte Carlo methods to follow ion trajectories as they move through the oscillating sheath from a *plane of origin*, defined as the maximum extent of the sheath, to the electrode surface. Ions enter the sheath region with random initial velocities in the x, y and z directions consistent with a Maxwell-Boltzmann distribution. The distribution is chosen to have a temperature of $\sim 0.05$ eV, which is typical for an RIE system. Ions entering the sheath receive energy in successive bursts as the sheath expands and contracts about them. Thus the ions are alternately accelerated and then have a period of constant velocity according to whether they are in the sheath or not. When the ion strikes the electrode its energy and angle of impact is recorded. Collisions may occur as the ion traverses the sheath. Elastic scattering is treated via a hard sphere model with an energy dependent cross section. Charge

exchange is included, also with an energy dependent cross section. A new ion formed by charge exchange is assumed to be moving, initially, with x,y and z velocities as determined by the Maxwell-Boltzmann distribution. Typically, $10^5$ ion trajectories are required to produce simulations with a good signal to noise ratio.

Snijkers[59] has recently developed an expression for the sheath potential based on a solution to the Poisson equation. Time dependence has been included in order to simulate IEDs. Both charge exchange and momentum transfer collisions have been included. Snijkers only shows limited results of his simulations but appears to get good agreement with experimentally determined IEDs.

The whole subject of low pressure gas discharge modelling has been addressed in a recent review by Lister[88]. This review covers DC, RF and microwave discharges together with a summary of the most frequently used modelling techniques.

# CHAPTER 2

# EXPERIMENTAL

## 2.1 INTRODUCTION.

This study has been concerned with the measurement of ion energy distributions at the anode of a reactive ion etcher. In order to make these measurements a retarding field analyser (RFA) has been constructed together with a pumping system and a data acquisition system. Each of these components will be discussed in turn in the following sections. Finally we will discuss the experimental method followed throughout these experiments.

## 2.2 THE 'MINSTREL' REACTIVE ION ETCHER.

### 2.2.1 The Vacuum Chamber.

The etcher used in these experiments was a 'Minstrel' reactive ion etcher built by Electrotech Special Research Systems, Thornbury, Avon. It is a modified version of the etcher used by Wade[89] and May[12] and consequently only the modified parts are considered in detail here. Figure 2.1 shows the etcher.

The lower electrode assembly consists of a Duralumin pedestal on to which electrode plates may be attached. A standard size plate is provided by Electrotech and is used for the majority of the experiments described here. It is made from aluminium that has been anodised and is 10.0 cm diameter, giving an electrode area of 78.5 cm$^2$. For investigations into the effect of relative electrode areas on IEDs other electrode plates were made, also from anodised aluminium. The dimensions and relative areas are shown in Table 2.1.

The lower electrode is connected to the radio frequency power supply and electrically isolated from the chamber via a PTFE collar 1 cm wide. The chamber assembly is connected to earth through the matching network earth connection.

The upper electrode assembly, or lid, has been adapted to accept a specially built gas showerhead and analyser assembly (see section 2.3.3). This is the main modification from the description of the etcher in Wade. The showerhead and upper chamber assembly bolt together in such a way that a planar surface results on the inside of the chamber. This is the same as in an Electrotech 'Omega' etcher - an updated model of the 'Minstrel'. As a result of the original showerhead assembly

59
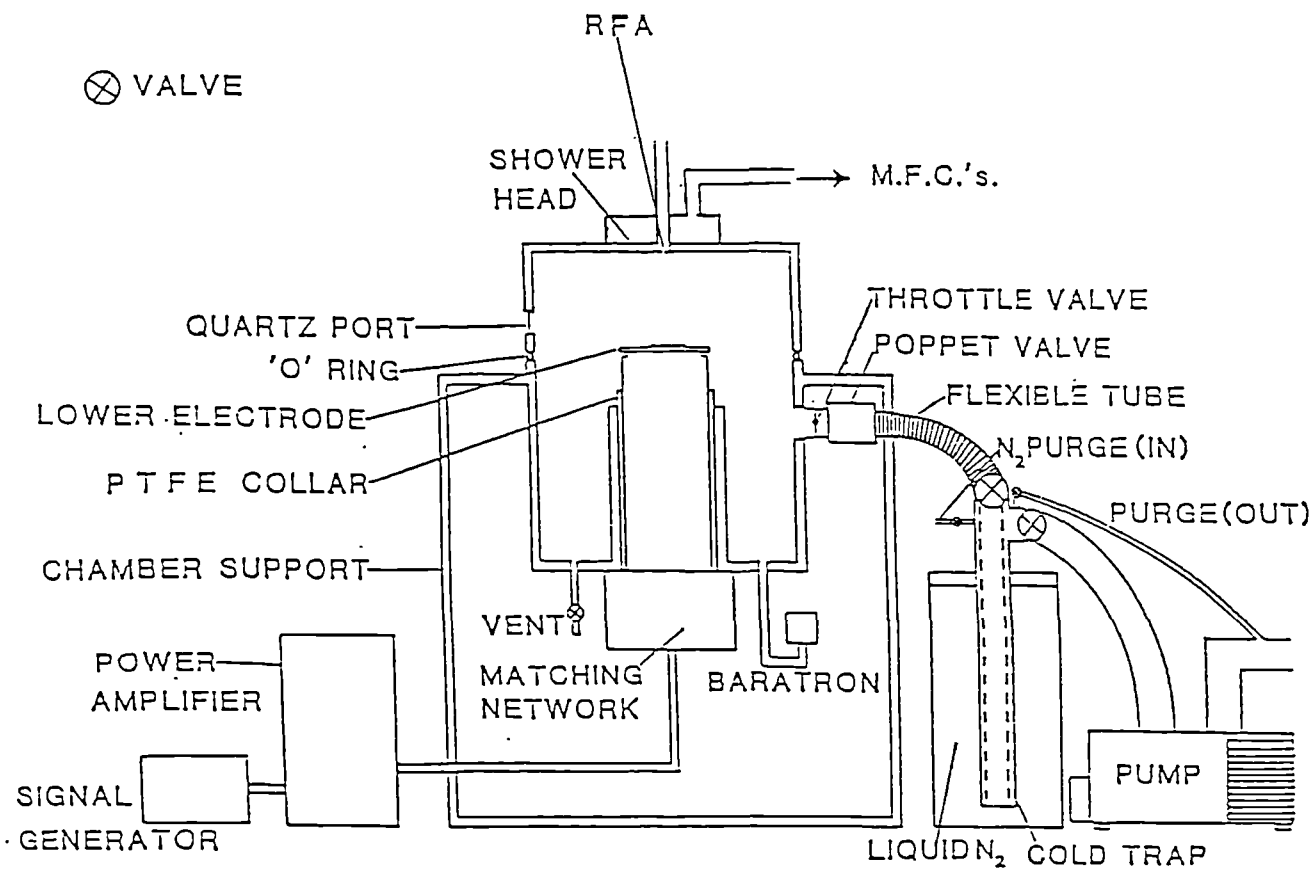
**Figure 2.1** Schematic representation of the 'Minstrel' reactive ion etcher. After Wade[89]

being replaced the pneumatic hoist gear became redundant. The only way to gain access to the chamber was to separate the pumping lines from the retarding field analyser and lift the upper chamber assembly clear by hand. No wafer etching was carried out during this study and so access to the chamber was only required for RFA maintenance.

| Radius / cm | Area / cm$^2$ | Relative Area |
|-------------|---------------|---------------|
| 5.0 | 78.5 | 1.0 |
| 7.06 | 157 | 2.0 |
| 8.66 | 235.5 | 3.0 |

**Table 2.1** Electrode areas for various lower electrode plates used on the 'Minstrel' reactive ion etcher.

## 2.2.2 The Pumping System

The chamber was pumped by a two stage rotary pump (Edwards, E2M80) which gave a base pressure of ~ 5 mTorr. The pumping speed, and thus chamber pressure, could be varied by adjusting two throttle valves situated between the chamber pumping port and the pump. The chamber could be isolated from the pump by means of a pneumatically operated 'poppet' valve. The chamber could then be vented using dry nitrogen from a cylinder. A liquid nitrogen cold trap was situated between the pump and the chamber . This served two purposes. Firstly it prevented any chlorinated species from reaching the pump and causing corrosion. Any contaminants trapped in this way were removed by isolating the trap and allowing it to warm to room temperature whilst flushing through with nitrogen. The nitrogen cold trap served a second purpose which was to prevent any back streaming of oil vapour from the pump to the chamber and consequently to the retarding field analyser. Thin films of oil in the analyser were found to be capable of causing serious problems with

analyser operation (see section 2.6.1).

## 2.2.3 Gas Handling Lines.

Flows of the process gases into the chamber were regulated using mass flow controllers (MFCs) (Tylan, type FC 260). Controllers were available for flows of 0 - 100 standard cubic centimetres per minute (sccm) and 0 - 20 sccm. However, the controllers were calibrated for use with nitrogen and so a correction factor[90] was required for other gases in order to measure flow rates accurately. Some of the gases used were supplied as liquid sources and were contained in a Pyrex flask attached to the MFC inlet. The vapour pressure of gases introduced in this way was sufficient to provide a flow of gas into the chamber. The gases used in the study were all of high purity and were bought from commercial suppliers. Details of the gases used together with the appropriate mass flow controller correction factors are shown in Table 2.2.

Gas pressure in the chamber was measured using a Baratron capacitance manometer (MKS, type 127A). This allowed pressures of less than a mTorr up to one Torr to be measured.

## 2.2.4 RF Power Supply

Two radio frequency power supplies were employed in this study. The first was a fixed frequency combined generator and amplifier (ENI, type HF-300) with a built in power meter. This generator also includes a filter designed to attenuate all harmonics of 13.56 MHz[91]. The circuit was useful in that it decreased the RF interference detected by the data acquisition system. Also available was a signal generator (Marconi Instruments, type TF144H) that supplies a small RF voltage at frequencies of 10 kHz to 72 MHz. This signal passes to an amplifier (ENI, type A-500) capable of delivering up to 500W to the discharge at frequencies of 0.3 to 30 MHz. This option was used for work at frequencies other than 13.56 MHz.

| Gas | State | Container | Supplier | Grade | Mfc factor |
|---|---|---|---|---|---|
| Ar | gas | cylinder | BOC | Zero | 1.42 |
| He | gas | cylinder | BOC | N4.5 | 1.42 |
| Xe | gas | flask | BOC | N4.3 | 1.42 |
| $H_2$ | gas | cylinder | BOC | CHP | 1.01 |
| $SF_6$ | gas | cylinder | Argo | 99.9% pure | 0.26 |
| $N_2$ | gas | cylinder | BOC | White spot | 1.00 |
| $CF_4/O_2$ | gas | cylinder | BOC | Electra II 99.7 % | 0.42 |
| $CCl_4$ | liquid | reservoir | BDH | Analar | 0.31 |
| $CO_2$ | gas | cylinder | Distillers | 99.9% pure | 0.74 |

**Table 2.2** Details of sources of the process gases used and the MFC correction factors.

The generators were connected to a matching network that consists of two variable air capacitors and an inductor. Varying the capacitance made it possible to tune the combined impedance of the matching network and the plasma to match the output impedance of the generator. When these impedances match the maximum power transfer occurs. The matching network was optimised for use at 13.56 MHz but can also be used at nearby frequencies, although the range over which we can measure IEDs is limited by its ability to supply sufficient power to sustain the plasma. As the frequency is increased above 13.56 MHz it becomes more difficult to match

the plasma and load since the 'window' over which the circuit will tune becomes increasingly narrow. Any reflected power however is negligible. Eventually however it becomes impossible to tune the circuit with sufficient precision and an unacceptable portion if the input power is reflected back to the generator. As the frequency is decreased below 13.56 MHz the range over which the circuit will match increases, but the efficiency with which it does so decreases. Eventually this too prevents IEDs from being measured due to too little power being supplied to the plasma. In practice it was found that below ~8 MHz and above ~20 MHz it was impossible to initiate a discharge and so this limited our range of IED measurements to between these frequencies. Other frequencies would only have been accessible by rebuilding the network - a discussion of this is covered in Wade[89].

Power supplied to the network was measured using the integral power meter on the HF-300 and a Wattmeter (Bird, Thruline) for the variable frequency A-500 system.

## 2.2.5 Measurement of Voltages and Area Ratio

A DC bias probe[89] was attached to the live electrode which allowed measurement of the DC bias, $V_{dc}$, and the applied peak to peak voltage, $V_{pp}$, when attached to a digital voltmeter. This probe was found to work very well at low powers but at higher powers ($> 100$ W) some fluctuation in the readings was observed.

The measured DC bias and applied voltage, $V_0$ (half the peak to peak voltage), were used to calculate the electrode area ratio as detailed in reference 28. The geometrical electrode area is about 0.4, but this is an estimate based upon the area of the top electrode. In reality, we cannot know how much of the top electrode is in contact with the plasma and so the *effective area ratio* must be calculated (see equation 1.5). This value is used in our computer simulation of IEDs. We note however that the DC bias probe circuitry consists of resistors and capacitors rated at only $\pm$ 20% accuracy leaving the value for the area ratio similarly uncertain.

## 2.3 THE RETARDING FIELD ANALYSER

### 2.3.1 Overview.

The retarding field analyser (RFA) used in this study is a development of a similar instrument used in fusion plasma studies[92]. Differentially pumped, it consists of an arrangement of grids and a collector housed in a specially built flange that forms part of the upper electrode, or anode. Ions and electrons enter the analyser from the plasma through a slit in the anode and by a suitable choice of grid voltages the energy distribution of the ions is obtained.

### 2.3.2 General Description of the RFA.

The arrangement of grids, collector and slit that form the RFA is shown in figure 2.2. Ions, electrons and neutrals enter the analyser via a defining slit in the anode. The slit (Graticules Ltd) has dimensions 25 $\mu$m wide x 30 $\mu$m deep x 5 mm long. It is made by the deposition of a layer of nickel on to an electrically biassed substrate which is later removed. The slit is attached to the anode by means of silver loaded epoxy resin (RS Components Ltd). This has excellent electrical conductivity (500 $\mu\Omega$ cm$^{-1}$) and ensures that the slit is at earth in common with the rest of the anode. Additionally, the epoxy serves to vacuum seal the analyser from the plasma chamber. The grids of the analyser are made from woven stainless steel (Bedford, Steer, End & Co. Ltd.) and are 81% transparent. They are held in position by soldering to stainless steel rings 18 mm o.d., 11 mm i.d.. The collector is a disc of aluminium 1 mm thick. 16 holes of 2 mm diameter situated around the periphery together with 4 x 1 mm diameter holes near the centre of the collector provide for pumping of the analyser. A third grid, 92.4% transparent, is situated behind the collector.

The grids and collector are held in place using machined PTFE rings that serve to insulate the components from each other and from the wall. The spacing between the first grid (G1) and the slit is 2 mm. G1 and the second grid (G2) are also 2 mm apart with the collector a further ~ 3 mm behind G2. The third grid (G3) is ~1.5 mm behind the collector. The PTFE rings stack together and slide into an aluminium
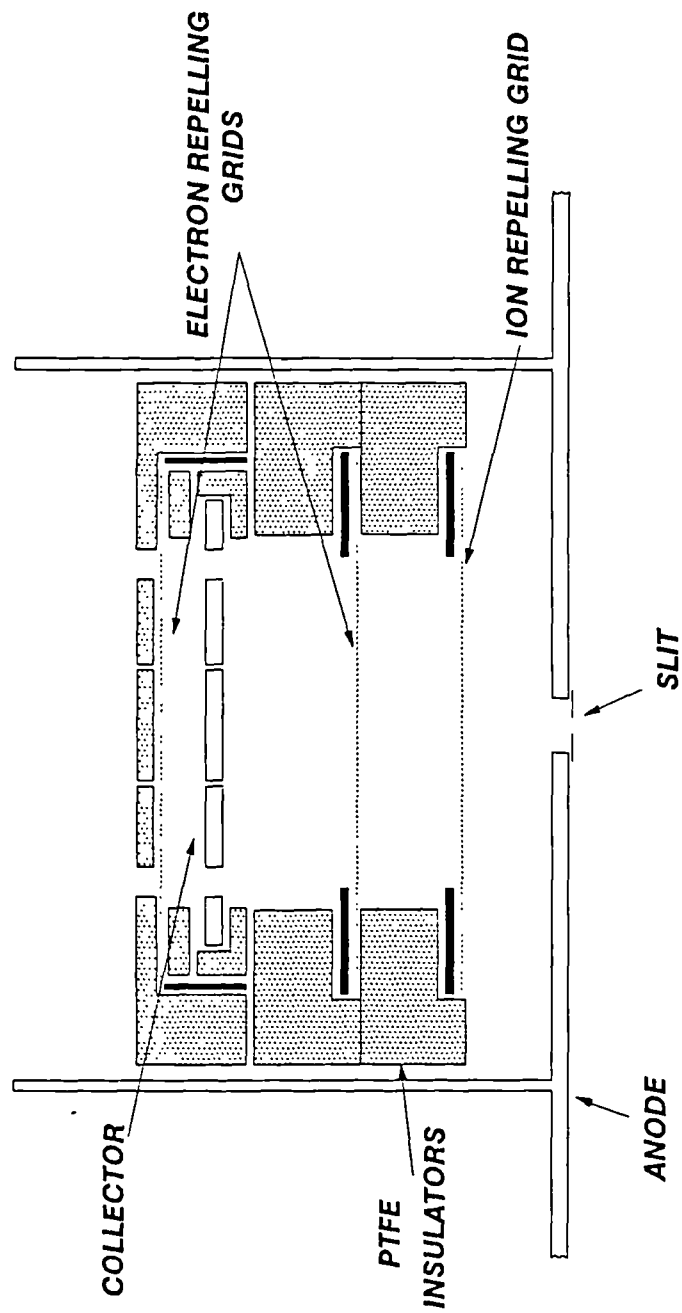
**Figure 2.2** Schematic diagram of Retarding Field Analyser.

tube (i.d. 24 mm) that forms the analyser housing.

Electrical connections are made by soldering wires to the grid mounting rings and the collector. These wires lead through specially machined channels in the PTFE to the vacuum feedthroughs that form part of the analyser mounting assembly.

## 2.3.3 RFA Mounting and Pumping.

The RFA is contained inside an 24 mm i.d. tube that forms part of a specially made flange depicted in figure 2.3. The flange assembly is made in two parts. The main body of the flange (130 mm diameter) consists of the tube containing the RFA, a gas mixing chamber and an outer ring containing 6 x 6 mm holes for mounting to the chamber. The gas line enters the mixing chamber via a compression coupling. The mounting is completed by a plate that fits across the front of the gas mixing chamber and analyser housing. The plate has an array of 1.5 mm diameter holes arranged in showerhead pattern that serves to distribute the gas into the chamber. Three 4 mm screws (not shown) connect through the showerhead plate into the main body of the flange. A Viton elastomer 'O' ring between the main body and showerhead plate seals the gas mixing chamber from the analyser. The entire flange assembly is attached to the chamber lid by 6 x 6 mm screws. These also allow for good electrical connection between the chamber and flange. A Viton 'O' ring provides vacuum sealing. Access to the analyser is obtained by removal of the flange assembly from the chamber followed by removal of the showerhead plate.

The analyser mounting terminates in a clamp flange (i.d. 24 mm). Connected to this is a four way cross piece that provides for electrical connections to the RFA via vacuum feedthroughs and for pumping of the analyser. The general scheme of this is shown in figure 2.4. One port from the cross piece holds a flange consisting of seven vacuum feedthroughs. Two of these are used for the biassing of the ion and electron retarding grids in the analyser. A second port on the cross piece holds a triaxial vacuum feedthrough. The inner core of this is connected to the collector while the centre connects to the third grid situated behind the collector.

The third port of the cross piece provides for pumping out the analyser. This

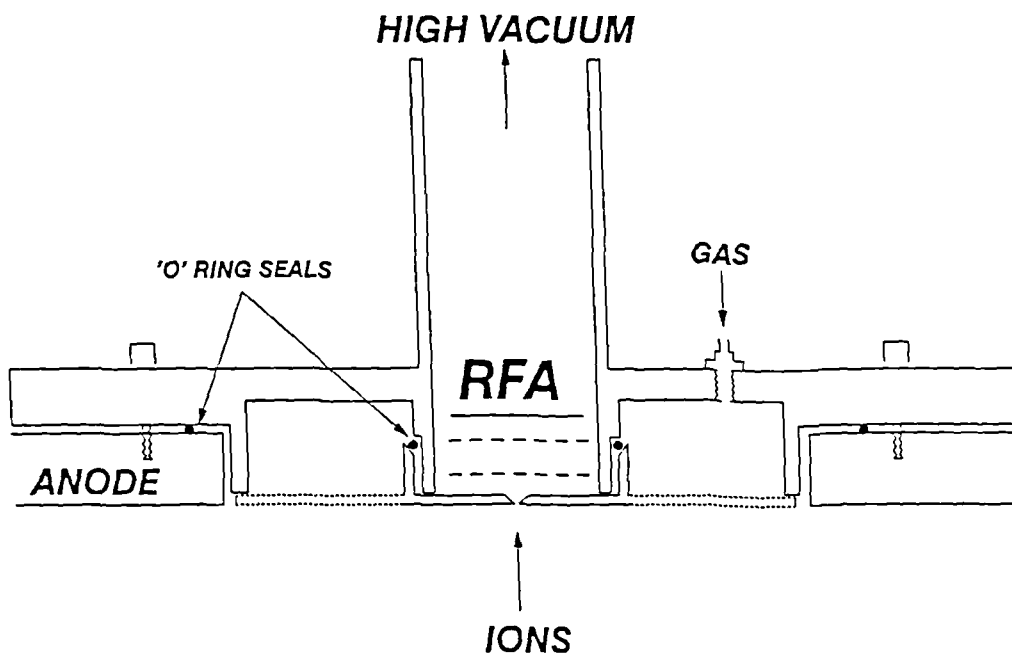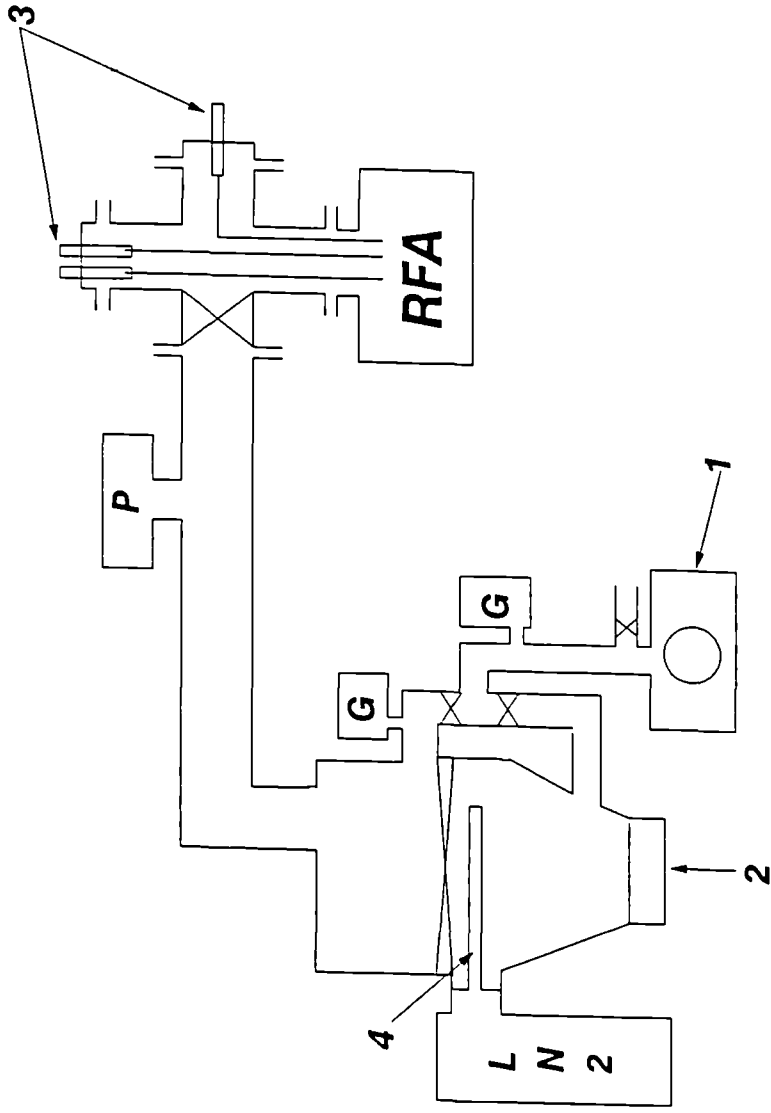**Figure 2.3** Schematic representation of RFA mounting flange.

**Figure 2.4** Schematic representation of RFA pumping system.

P - PENNING GAUGE
G - PIRANI GAUGE
1 - ROTARY PUMP
2 - DIFFUSION PUMP

3 - VACUUM FEEDTHROUGHS
4 - LIQUID N2 COLD FINGER
X - VALVE

is achieved using a water cooled diffusion pump (Edwards, 100M-LN2) backed by a rotary pump (Edwards, E2M8). A liquid nitrogen cold finger in the mouth of the pump reduces back streaming of diffusion pump oil to the analyser where films of oil limit operational life. Pirani gauges are fitted on the pump fore line and in the high vacuum line to indicate the system pressure all the time the pump is in use. A high vacuum gate valve across the mouth of the pump provides isolation from the rest of the system. Connection between the pump and the analyser mount was made by short length of 40 mm i.d. tube, a reducing piece to 25 mm i.d. tube and finally a second gate valve to isolate the entire high vacuum system from the analyser. A Penning ionization gauge is fitted in the final section of tubing to indicate the pressure in the high vacuum line. Typically, with the gate valve at the analyser shut the pressure in the vacuum system was $< 7.5 \times 10^{-2}$ mTorr. With the gate valve open and the chamber at base pressure ($\sim 5$ mTorr) the pressure in the vacuum line was $\leq 7.5 \times 10^{-1}$ mTorr.

## 2.3.4 Theory of Operation

Figure 2.5 shows the typical potentials on each of the components within the analyser together with the fates of particles entering the analyser. Ions and electrons leave the plasma with an energy that depends upon the plasma potential. They enter the analyser via the defining slit in the chamber anode, which is at earth. G1 is scanned between 0 and, typically, 30 V. At 0 V all ions will pass through the grid and continue on to the collector. At 30 V all ions will be repelled by the field between the grid and the slit and consequently do not reach the collector. At intermediate values only ions whose *perpendicular* component of energy exceeds the value of the potential on G1 will be able to pass the grid and be collected. For example, if the grid is at 15 V only ions with energy greater than 15 eV perpendicular to G1 will be able to pass the grid.

Electrons can cross the sheath when it is near the minimum potential and enter the analyser. The geometry of this etcher means that this is for a large part of the RF cycle (see section 1.4.6). In order that these electrons do not reach the collector and
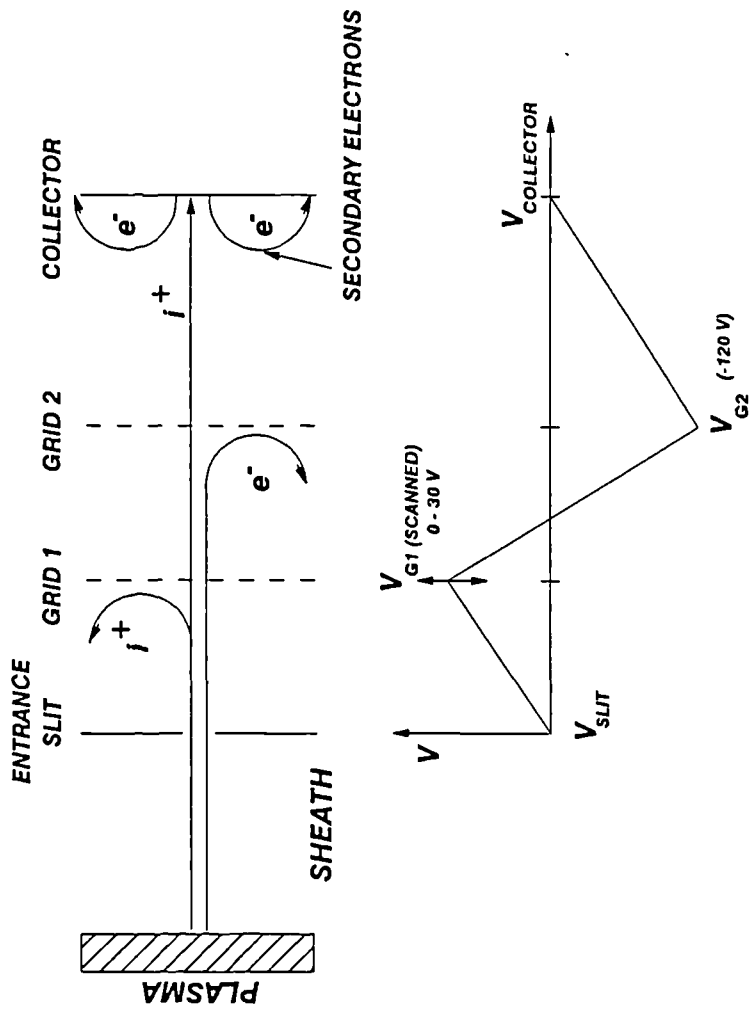
70

**Figure 2.5** Theory of operation of the RFA. Note that the electron repelling grid behind the collector is not shown.

71

affect the measured current they must be repelled. This is achieved by applying a negative bias to G2, typically - 120 V. This grid also returns any secondary electrons ejected by ion impact upon the collector back to the collector. This is necessary since an electron leaving the collector produces the same effect at the detector as an ion arriving and leads to an apparent current reading higher than the true ion current. Secondary electron emission effects of this type have been observed in an analyser that did not have a negatively biassed grid in front of the collector[71].

Behind the collector a third grid is situated. Most RFA designs have no need for a grid here and it is only necessary as a consequence of the geometry of this system. The collector consists of a plate with many holes in it to allow for vacuum pumping. Ions will impinge upon the collector and the sides of the pumping holes causing secondary electron emission. This emission can therefore spread back beyond the holes. It was found that effects due to loss of secondary electrons from the collector were observable in the measured current trace unless a third grid was inserted to counter this. The effect is manifest as an apparent rising current at the collector as the ion retarding voltage is increased. Typically $\sim$ - 20 V was sufficient to suppress this effect. This is a well known phenomenon and has been discussed by Simpson[93].

With all potentials correctly adjusted only an ion current will reach the collector. The current collected is measured as a function of the potential on G1. This produces a falling trace, as shown in figure 2.6a, that corresponds to the ion current being gradually reduced. The proportion of ions, dI, repelled as the grid voltage increments, dV, is obtained by differentiation. Thus differentiation of the entire trace produces the IED, an example of which is illustrated in figure 2.6b.

## 2.3.5 Sampling Considerations

The extraction of ions through an orifice into a low pressure analyser is a technique widely used to study processes in discharges. We must, however, be aware of the limitations of this technique and of the possible errors that may be introduced into the measured energy distribution by the orifice itself. The presence of an orifice

current / A



0                    grid voltage / V                    **30**

**Figure   2.6a**   Typical   I-V   trace   obtained   during
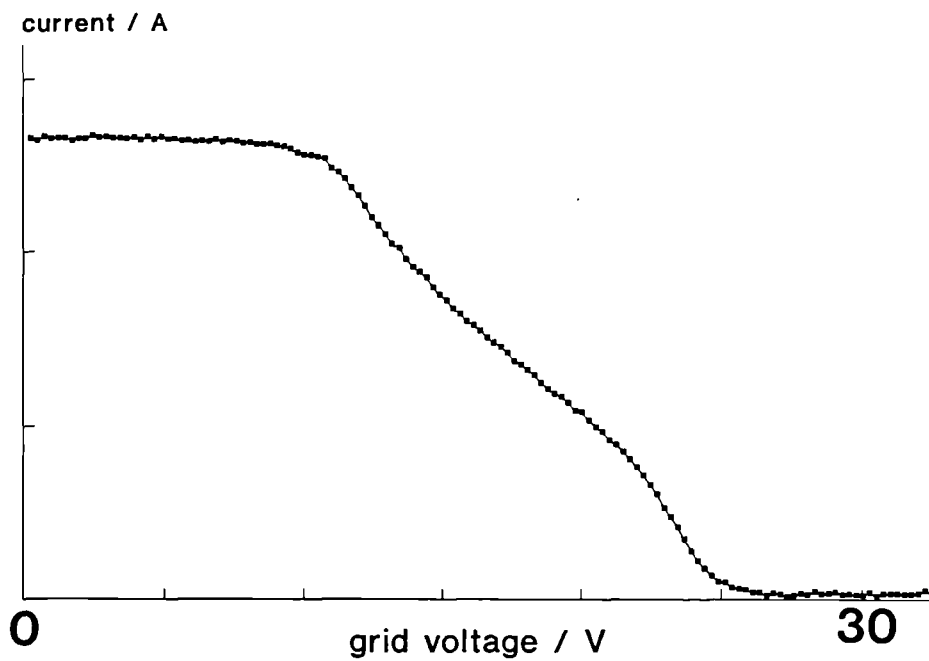experimentation.

dI/dV



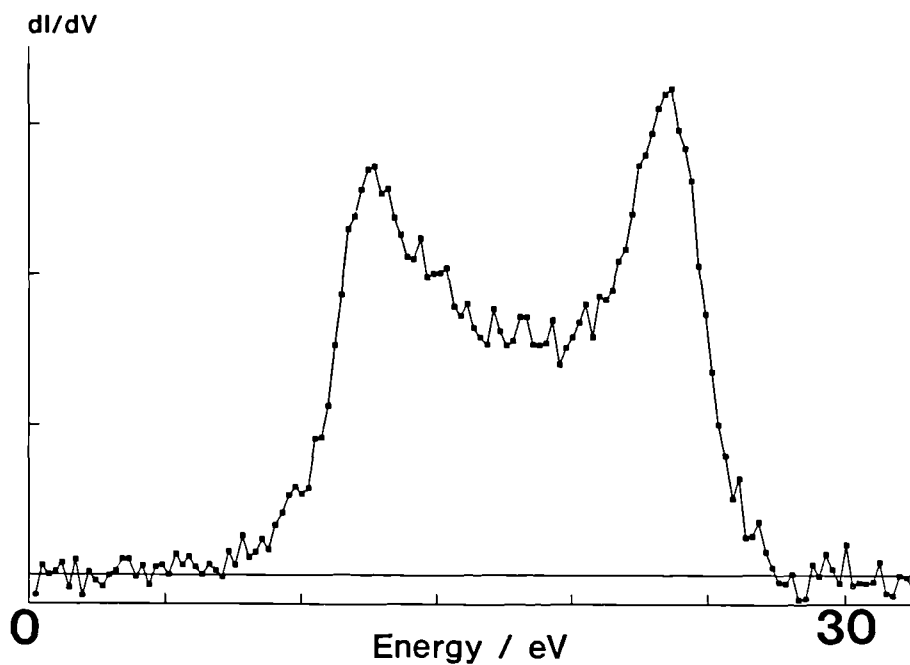0                    Energy / eV                    **30**

**Figure   2.6b**   Ion   energy   distribution   produced   by
differentiation of the I-V trace in figure 2.6a).

73

will have the following effects:

a) Neutrals will effuse from the high pressure region of the chamber to the lower pressure region of the analyser. This will cause a significant density of molecules in the region of the analyser immediately below the orifice.

b) The sheath electric field will be disturbed by the orifice and will deviate from the planar nature of the field above a flat electrode.

c) The sheath region above the orifice will be depleted in secondary electrons compared to the sheath above a continuous electrode.

We have used a slit as the entrance aperture to the analyser rather than the circular orifice favoured by other workers since it allows a large sampling area in the electrode and yet the narrowness of the slit ensures minimal disturbance to the sheath region. However, the disadvantage of the slit is that the large total area leads to significant neutral effusion through the orifice and into the analyser. Thus, this analyser is particularly suited to studies at low pressures.

We now consider some of the effects listed above in more detail.


## 2.3.5.1 Pressure Effects

The pressure differential between the plasma chamber and the analyser would ideally change as a step function at the orifice. Inevitably this is not the case. The region is in fact one of transition from the high pressure region of the chamber to the much lower pressure of the analyser.. Coburn and Kay[94] and Thompson et al[71] have studied the effect of this region upon collisions and molecular density variations about the orifice. In the low pressure region immediately below the orifice there is a significant density of molecules due to neutrals effusing through the orifice and consequently there is an increased chance of an ion - molecule collision occurring. Thompson, however, has shown that this effect is somewhat offset by a corresponding decrease in pressure immediately above the orifice. Liu et al[67] have discussed the possible fates of ions that do undergo a collision in the analyser and their effect upon the IED. Charge exchange collisions will rarely result in the creation of an ion oriented such that it would reach the collecting plate. The potentials within the

analyser will ensure that the new ion is lost from the beam of incoming ions and is not detected. Ions that undergo an elastic collision will generally be scattered away from the collector since we only sample ions with near surface normal incidence on the slit. Any scattered ions that reach the collector will be detected as a low energy tail in the IED due to a reduction in the component of velocity perpendicular to the electric field. In fact we find that we observe few ions scattered to low energies. Coburn and Kay have concluded that any ion that undergoes a collision in the analyser is lost from the beam and does not contribute to the measured ion current. Our observations support this.

In order to quantify the effects of collisions, and examine the effect on the attenuation of the ion current, we have calculated the pressure in the analyser for various chamber pressures. Our calculation was based upon the pumping speed of the diffusion pump, quoted by the manufacturer, and the calculation of the conductances of the various components of the system from standard vacuum theory[95]. Calculations were performed for both hydrogen and nitrogen. For nitrogen we find that the mean free path in the analyser approaches the analyser length when the chamber pressure is 50 mTorr. Thus we expect all ions to undergo a collision at this pressure. Experiment shows that nitrogen IEDs can be measured up to 50 mTorr but not beyond. This loss of detectable current is consistent with the assumption that once an ion collides it is lost from the beam and is not detected. Our calculations for hydrogen reveal that we should be able to detect current up to ~ 90 mTorr. In fact we can only measure IEDs up to 65 mTorr. The discrepancy here is probably due to the diffusion pump not pumping hydrogen as fast as is quoted by the manufacturer. This leads to an overestimate of the analyser pressure range. However the loss of detectable current would again appear to support the assumption that ions lost from the beam are not collected.

## 2.3.5.2 Electric Field Perturbations

Perturbations to the electric field in the region of the orifice can cause errors in the measured energy distributions. In the region above the slit the sheath will be

continuous provided that the slit half-width is much less than the minimum sheath dimension. With a slit half-width of 12.5 $\mu$m and sheath dimensions of the order of 1 mm we expect no gap in the sheath above the slit.

On a flat electrode the electric field lines will be parallel to the electrode. However, since an aperture exists in the electrode the electric field lines will penetrate in to the orifice as shown in figure 2.7. Thus, as ions pass through the orifice and travel to the collector their energies and direction of travel may be altered. The energy distribution measured at the collector may then become unrepresentative of the distribution at the electrode surface - the region of interest. The effect of this ion deflection in our system has been studied using the computer program SIMION (version 3.1)[96].

SIMION is a program that has been developed for the design and analysis of electrostatic lenses. Briefly, an array of up to 16,000 points can be created in computer memory and electrodes and grids assigned to positions in the array. Values are given to the electrodes and/or grids by the user and SIMION calculates the electric fields at each point in the array. Once the electric field gradients have been calculated a study can be made of ion trajectories in the array. SIMION requires as inputs:

a) The mass to charge ratio of the ion.

b) Whether the ion is to be conserved, fragment or be neutralized.

c) The starting position of the ion within the array for the first trajectory to be followed and whether this position is to be changed in succeeding trajectories.

d) The initial ion energy for the first trajectory and whether this energy is to be changed in succeeding ion trajectories.

e) The initial trajectory angle, along which the energy is to be directed, and whether this angle is to be changed in succeeding ion trajectories.

f) The number of ion trajectories to be computed.

The parameters that can be changed from one trajectory to the next are very useful in studying the effect of one or more of the initial ion conditions on trajectories. For example, we could set an angle of 0°, the change in the angle for successive
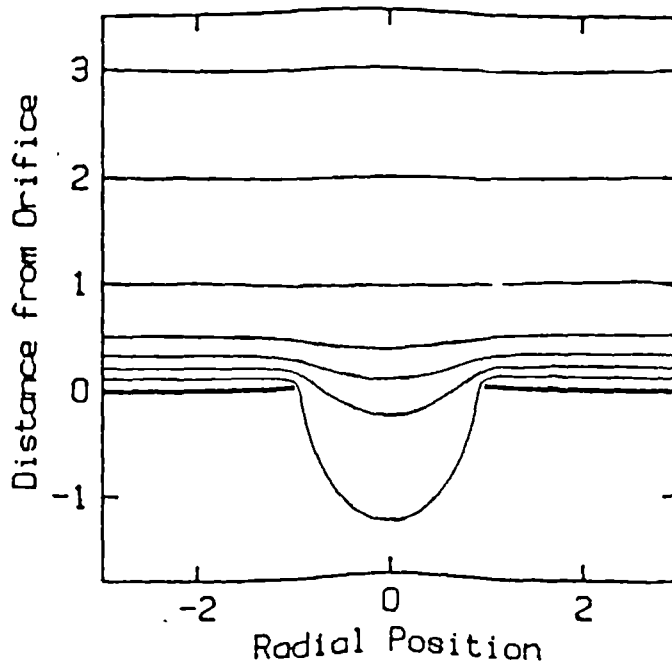
**Figure 2.7** Equipotential lines around an orifice. After Thompson et al [71].

trajectories of 2° and keep all other parameters constant. For 10 trajectories, say, we can observe the effect of changing the initial ion angle from 0° up to 18°.

Each ion trajectory is followed until the ion either hits an electrode or leaves the array at some other point. Output from SIMION gives the following for each ion trajectory followed:

a) Confirmation of the initial ion energy, angle, mass and start position in the array.

b) The final energy, angle and position in the array (or point where the ion left the array).

c) The speed of the ion at the time when the ion hit an electrode, or left the array, and the time of flight.

d) Information regarding the number of iterations performed during the trajectory and the accuracy of the calculation.

To study the effect of the slit on ion trajectories an array was created 260 points by 60 points. This represented a cross section through the sheath, slit and analyser as far as G1. We have no need to model the analyser to any further depth since we are only interested in errors caused by the slit and how this affects the measurement at G1.

The sheath was modelled as a plane placed 0.18 mm away from the slit. The rationale for this choice of distance was based upon modelling of energy distributions where the sheath thickness is a fitting parameter and this thickness successfully reproduced the measured distributions. The value of the sheath voltage was calculated from equation 1.11 and was set at 45 V. This represents the maximum voltage we may expect at the anode sheath. The sheath voltage oscillates between maximum and minimum potentials as described in section 1.4.6. We have chosen to model only the maximum as this will be a 'worst case' estimate for the degree of electric field penetration through the slit and therefore of errors in the IED.

To estimate the error in ion energies we have input ions into the array at a point remote from the slit where the field lines are parallel to the surface. This gives

us the energies of the ions at the surface in the absence of the slit. The same ion trajectories are then repeated in the region of the slit. Comparison of the two outputs from SIMION allows us to calculate the error introduced by the slit. Note that all references to energy here, and in the subsequent results tables, mean the component of ion energy that is *perpendicular* to G1. The retarding field generated by G1 is perpendicular to the grid plane so ions must have sufficient energy in this direction to overcome the field or they are retarded. We make no measure of energies parallel to the retarding field.

Within this study we have defined incident position '0' as the slit centre and incident position '1' as the slit edge as shown in figure 2.8. Since the field is symmetrical about the slit centre SIMION only calculates trajectories for one half of the slit. These results are then duplicated for the other half of the slit. Thus the following results may tabulate apparently 5 trajectories across the slit width but the graphical output will display 9 trajectories. (One trajectory will be at '0' and so there is no symmetric trajectory associated with it. Thus 9 trajectories arise and not 10). Ions incident at an angle to the surface are referred to in degrees from the surface normal. For all the cases we have studied here the mass / charge ratio of the ion has been held constant at 40, representing an argon ion with a single positive charge. Studies were carried out using an m/e ratio of 1, representing hydrogen ions, but the trajectories computed by SIMION were not sensitive to this change. We consider the results presented here to be representative for any ion being analysed.

The first case we have studied is for ions incident normal to the surface at energies of 25 eV, 10 eV and 2.5 eV. In order to do this we have placed an ion in the array with an initial energy and allowed it to accelerate across a section of the sheath towards the electrode, experiencing deflection as it accelerates. Ions with 25 eV at the surface were produced by starting an ion with 15 eV energy on the 10 V contour line, as defined by SIMION; 10 eV ions were started with 5 eV energy on the 5 V contour line; 2.5 eV ions were initially stationary on the 2.5 V contour line. We have considered ions incident at positions across the slit width i.e. '0' to '1' - see figure 2.8.
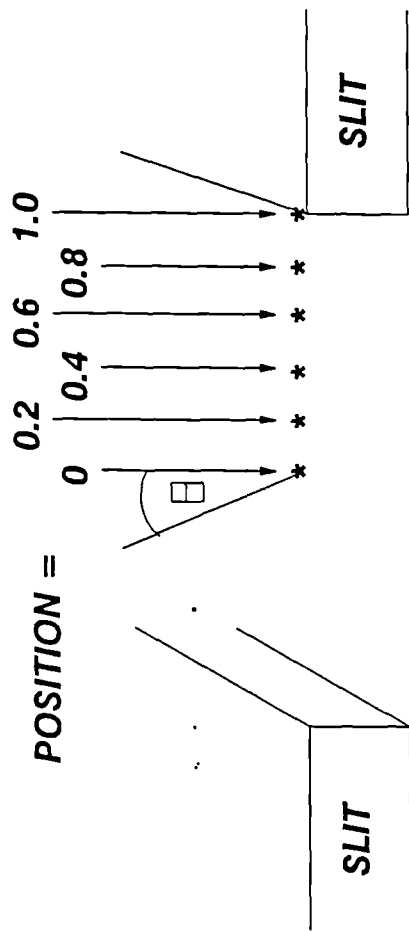
**Figure 2.8** Schematic representation of cross section of RFA entrance slit. Positions marked indicate the input positions for SIMION trajectories.

| Incident Position | Impact Energy (no slit) / eV | Detected Energy / eV | Final Angle / deg | Error / % |
|---|---|---|---|---|
| 0 | 25.00 | 25 | 0 | 0 |
| 0.2 | 25.00 | 24.99 | 0.77 | < 0.1 |
| 0.4 | 25.00 | 24.99 | 1.54 | < 0.1 |
| 0.6 | 25.00 | 24.99 | 1.77 | < 0.1 |
| 0.8 | 25.00 | 24.99 | 1.64 | < 0.1 |
| 0 | 10.00 | 10.00 | 0 | 0 |
| 0.2 | 10.00 | 9.98 | 2.35 | < 0.1 |
| 0.4 | 10.00 | 9.97 | 4.51 | < 0.3 |
| 0.6 | 10.00 | 9.97 | 4.79 | < 0.4 |
| 0.8 | 10.00 | 9.96 | 4.30 | < 0.4 |
| 0 | 2.50 | 2.50 | 0 | 0 |
| 0.1 | 2.50 | 2.43 | 6.69 | 2.8 |
| 0.2 | 2.50 | 2.38 | 12.70 | 4.8 |
| 0.3 | 2.50 | 2.35 | 17.34 | 6.0 |

**Table 2.3** SIMION results for 25, 10 and 5 eV ions incident at positions across the slit face. In all cases the ions are incident normal to the slit.

Results are shown in Table 2.3 with the corresponding trajectories in figure 2.9a - c. Clearly, energetic ions are not perturbed significantly by the presence of the slit. Ions that would impact the surface with 25 eV in the absence of the slit are found

to incur < 0.1% error in travelling through the slit. This is the case even for ions travelling near the slit edge where perturbation is greatest. As the ion energy decreases we observe an increase in the measurement error. 10 eV ions incident perpendicular to the slit show errors up to 0.4%, with the greatest error occurring for ions near the slit edge. As the ion energy drops still further, to 2.5 eV, we observe up to 6.0% error in the detected ions. Note that slow ions travelling near the slit wall are deviated so much that they impact on the side wall and are not transmitted.

We turn now to ions that impact the surface at an angle. For the conditions studied we do not expect many ions with large angles of incidence to be present[87]. Thus we have only considered ions a few degrees from normal. Ions have been input into the array with an initial energy directed 5° to the normal. The ions are again allowed to accelerate across the remaining sheath to the electrode. In order to produce ∼25 eV ions at the surface we started ions in the array on the 10 V contour line with an initial energy of 15 eV directed 5° to the normal. Similarly ∼10 eV ions were produced by starting 5 eV ions, at 5°, on the 5 V contour line and 3.5 eV ions by starting 1 eV ions, at 5°, on the 2.5 V contour line. The energies and angles of ions incident on the electrode in the absence of the slit are shown in columns 2 and 3 of Table 2.4. Although ions are initially directed 5° to the normal they are straightened towards normal, the exact amount depending on their energy and the distance they travel before striking the electrode. Results for ions incident at various positions across the slit are shown in columns 4 and 5. Energetic ions, i.e. ∼25 eV, are again found to be affected to only a small extent, < 1% for all the cases studied. Note that energetic ions that start from a position out of line to the slit, e.g. position = - 1.2, can still pass through the slit and be detected. This offsets to some extent the loss of detected ions on the other side of the slit from those ions that are directed away from the centre and impact on the slit sidewall. As the energy of the ions decreases, to ∼10 eV, the errors become larger and we also observe both increases and decreases in energy. Ions arriving at G1 with increased energy can arise from an ion at the edge of the slit travelling towards the centre. The effect of the field at the slit is to straighten the ions trajectory more than would have been the case if no slit were

| Position | Impact Energy (no slit) / eV | Impact Angle (no slit) / deg | Detected Energy / eV | Detected Angle / deg | Error in Energy / % |
|---|---|---|---|---|---|
| - 1.2 | 24.85 | 3.88 | 25.03 | 2.33 | + 0.7 |
| - 1.0 | 24.85 | 3.88 | 25.00 | 2.21 | + 0.6 |
| - 0.8 | 24.85 | 3.88 | 24.99 | 2.08 | + 0.6 |
| - 0.6 | 24.85 | 3.88 | 25.00 | 2.46 | + 0.6 |
| - 0.4 | 24.85 | 3.88 | 25.03 | 3.22 | + 0.7 |
| - 0.2 | 24.85 | 3.88 | 24.90 | 4.01 | + 0.2 |
| 0.0 | 24.85 | 3.88 | 24.86 | 4.79 | < + 0.1 |
| 0.2 | 24.85 | 3.88 | 24.87 | 5.50 | < + 0.1 |
| 0.4 | 24.85 | 3.88 | 24.87 | 5.63 | < + 0.1 |
| - 1.0 | 9.98 | 3.54 | 10.04 | 0.13 | + 0.6 |
| - 0.8 | 9.98 | 3.54 | 10.01 | 0.58 | + 0.3 |
| - 0.6 | 9.98 | 3.54 | 10.01 | 0.99 | + 0.3 |
| - 0.4 | 9.98 | 3.54 | 10.04 | 0.68 | + 0.6 |
| - 0.2 | 9.98 | 3.54 | 10.06 | 2.67 | + 0.8 |
| 0.0 | 9.98 | 3.54 | 9.93 | 4.71 | - 0.5 |
| 0.2 | 9.98 | 3.54 | 9.92 | 6.65 | - 0.6 |
| 0.4 | 9.98 | 3.54 | 9.91 | 8.00 | - 0.7 |
| 0.6 | 9.98 | 3.54 | 9.90 | 7.69 | - 0.8 |
| - 0.8 | 3.49 | 2.67 | 3.45 | 7.94 | - 1.3 |
| - 0.6 | 3.49 | 2.67 | 3.43 | 9.17 | - 1.9 |
| - 0.4 | 3.49 | 2.67 | 3.44 | 7.58 | - 1.6 |
| - 0.2 | 3.49 | 2.67 | 3.48 | 1.84 | - 0.3 |
| 0 | 3.49 | 2.67 | 3.42 | 4.28 | - 2.3 |
| 0.2 | 3.49 | 2.67 | 3.37 | 1.027 | - 3.7 |
| 0.4 | 3.49 | 2.67 | 3.36 | 14.48 | - 3.9 |

**Table 2.4** SIMION results for ions incident at 5° to the slit. Results are shown for ions incident at different positions across the slit.
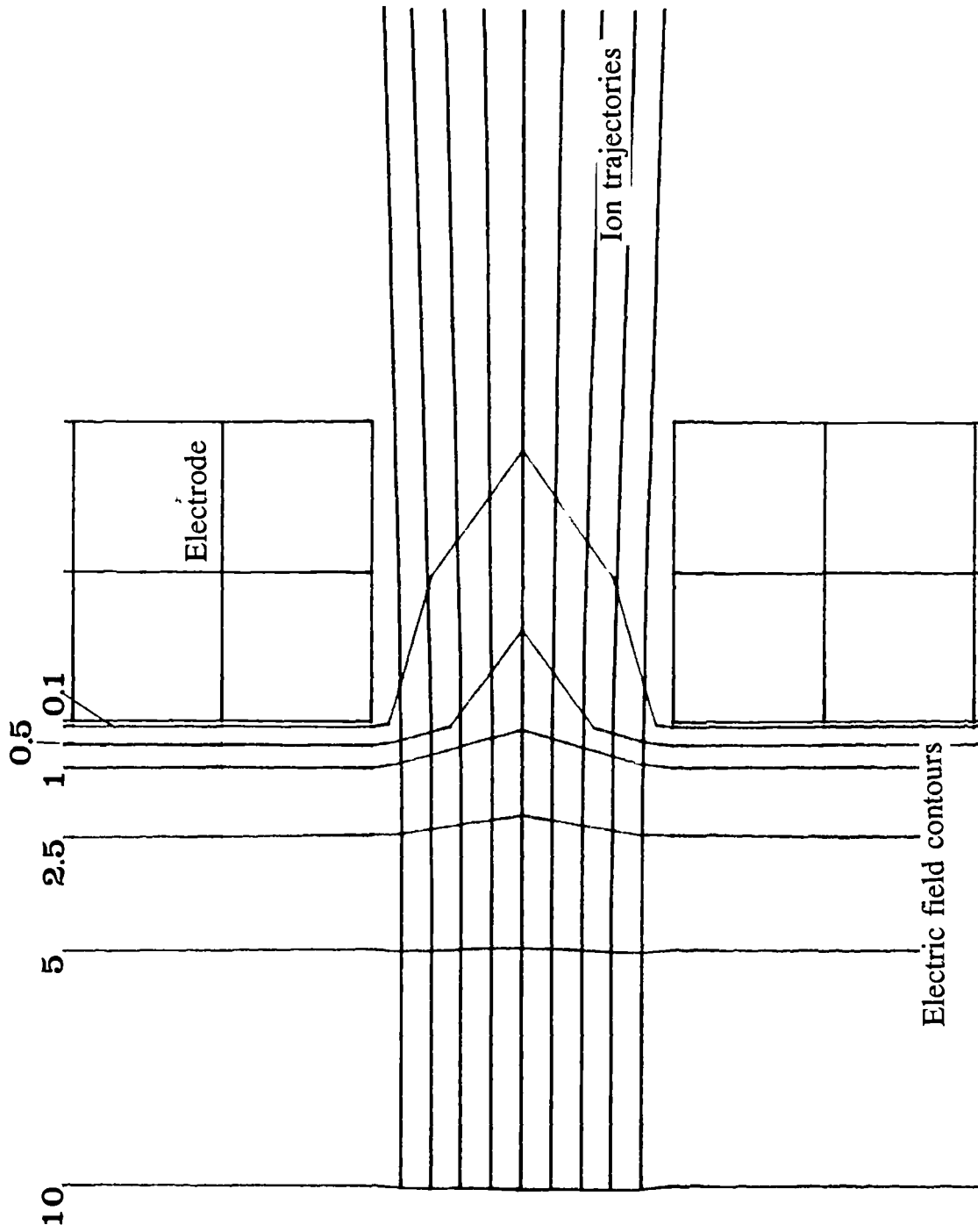
**Figure 2.9a** SIMION trajectories calculated for 25 eV argon ions. Electric field contours are in volts.
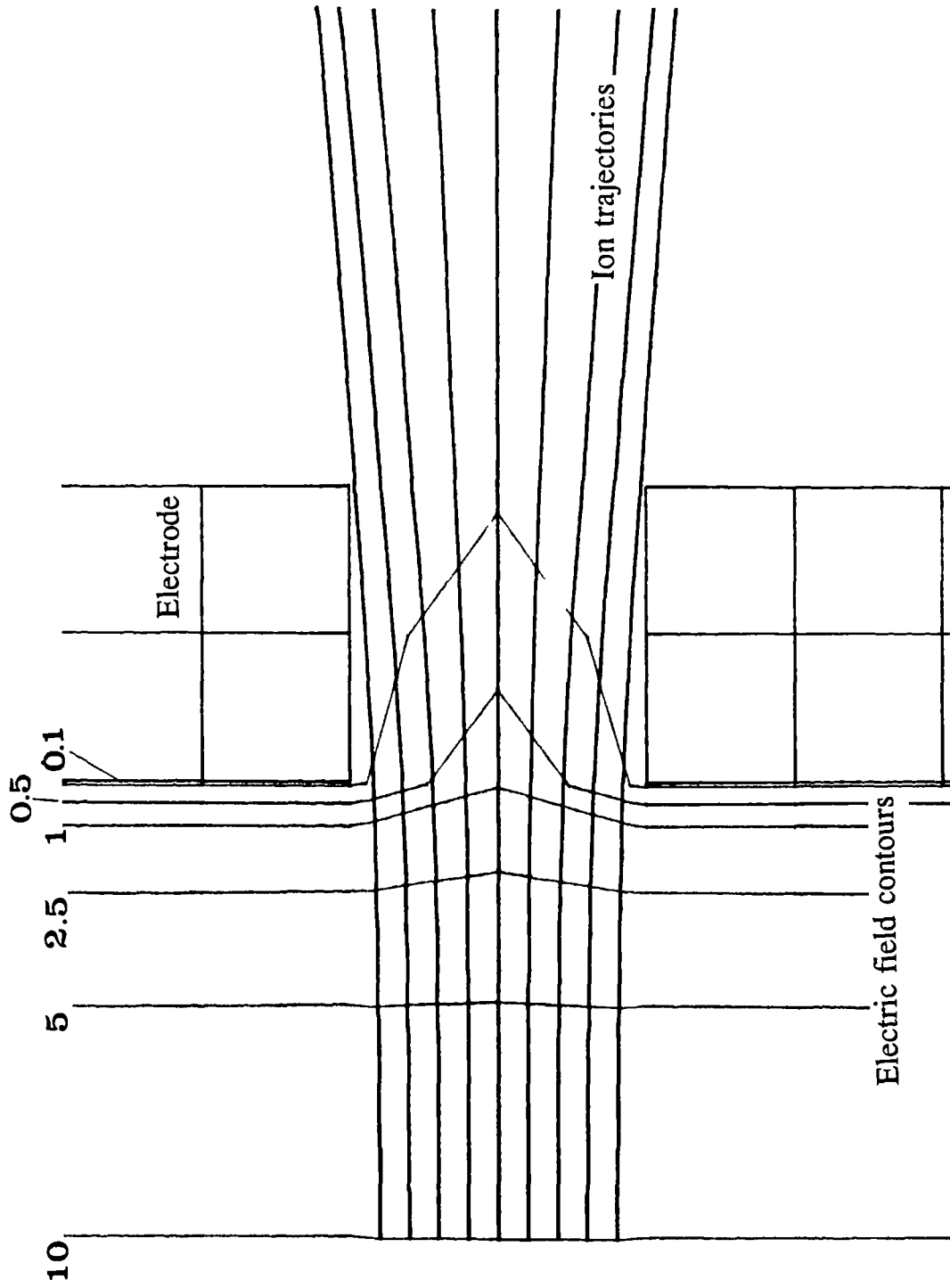
**Figure 2.9b** SIMION trajectories calculated for 10 eV argon ions. Electric field contours are in volts.
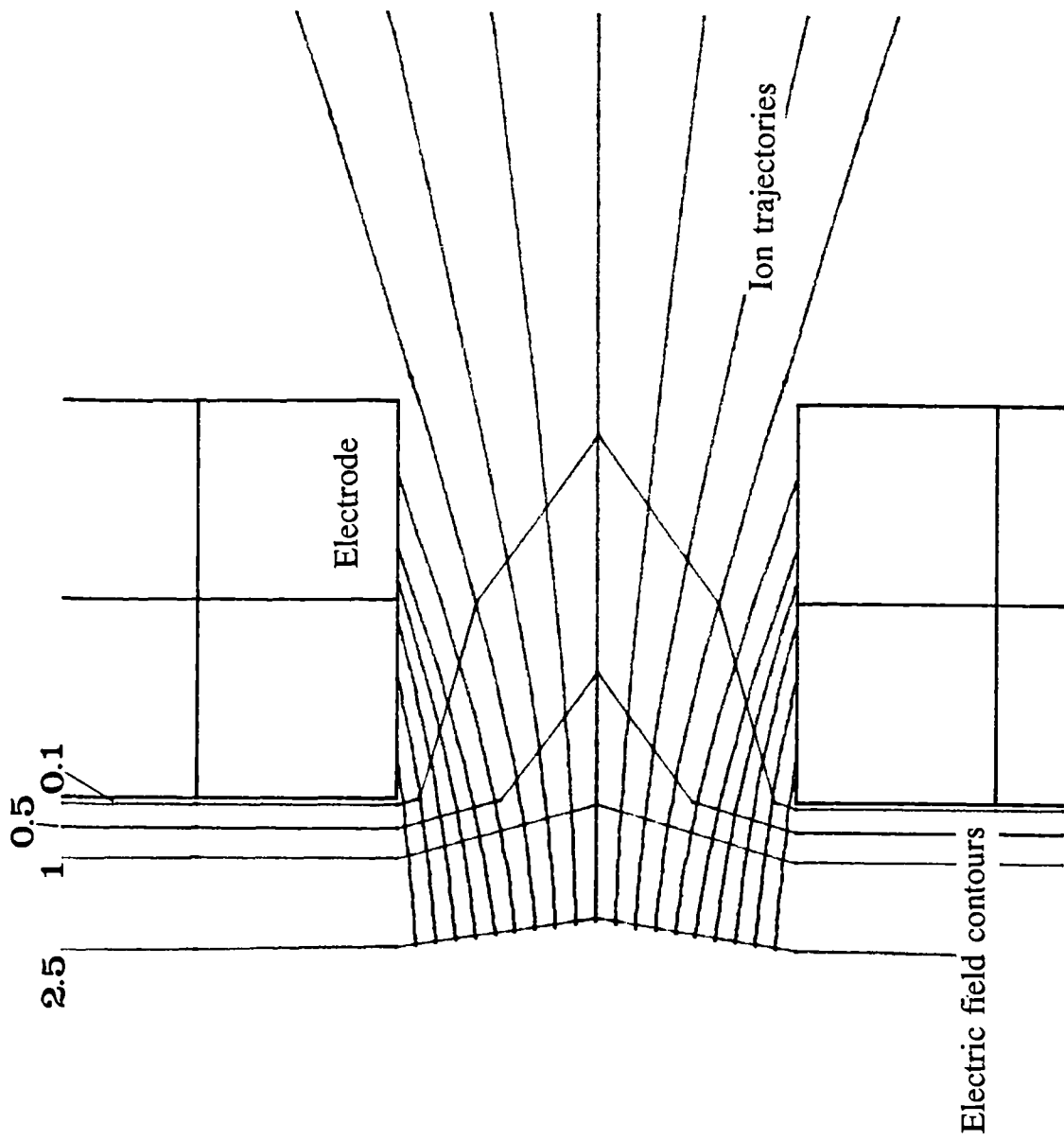
**Figure 2.9c** SIMION trajectories calculated for 2.5 eV argon ions. Electric field contours are in volts.

present. The ion then has more energy directed perpendicular to the retarding field and we observe a positive error. Ions that are travelling on a trajectory away from the slit centre are defocused and lose energy in the perpendicular direction. These give rise to negative errors. Ions moving relatively slowly, at $\sim 3.5$ eV, show a still larger error with up to 4% being found for the conditions studied here. All errors are now found to be decreases in energy due to the slow moving ions being strongly affected by the perturbed field.

In conclusion we find that slow moving ions are perturbed more than fast ions and the perturbation is greater for ions incident near the slit edge. Slow moving ions may not be transmitted at all due to the perturbed field directing them into the slit side wall. Thus the slit is effectively narrower for low energy ions. However, in order for slow ions to be present in the slit region they must be formed by a collision otherwise the ion would gain significantly more energy than this as it crossed the sheath. For the majority of pressures studied in this work we expect few collisions to take place and consequently little error in the measured IEDs. For higher pressures, however, we must be aware that some low energy ions, caused by collisions, may not be transmitted due to field deflection. For ions that are transmitted the slit appears to introduce little error. For the worst cases considered we find a 6% change in energy. This corresponds to an absolute error of only 0.21 eV - less than the voltage step used on G1.

## 2.4 ELECTRONICS AND DATA ACQUISITION

### 2.4.1 Overview

The control of grid voltages and measurement of collector current has been fully automated using a personal computer (Olivetti, M40). Details of the required ramp voltage are input into a file and a ramp created in the computer memory. This is passed via a digital to analogue converter to an amplifier and from there to the RFA. Detected current is amplified and passed to an analogue to digital converter and stored as a file on disk. A schematic of this system is shown in figure 2.10.
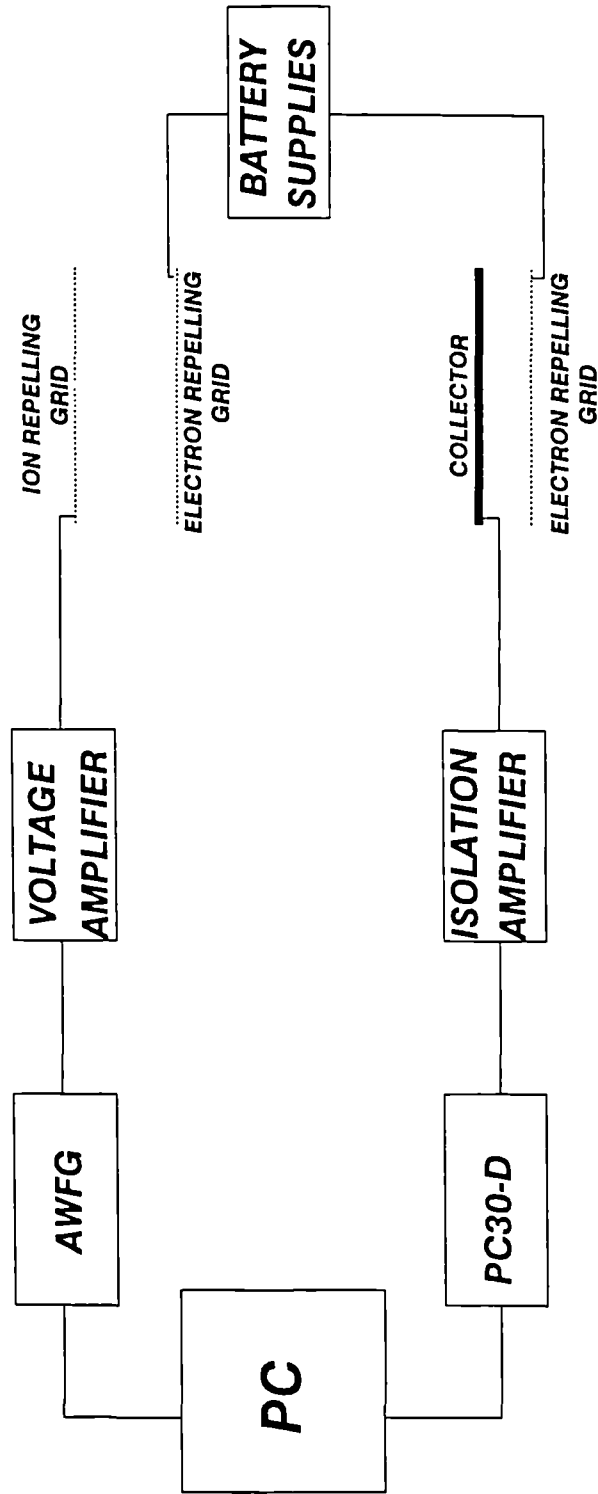
87

**Figure 2.10** Schematic representation of RFA voltage control and data acquisition systems.

## 2.4.2 Control of Grid Voltages

In order to analyse the ions coming into the RFA a smoothly varying positive voltage is required. This is achieved using an *Arbitrary Waveform Generator* (AWFG) (Keithley Instruments Inc.). This is in the form of a IBM PC compatible board that plugs directly into the PC. This instrument allows user defined digital waveforms to be generated in analogue form. The board can be controlled either directly using the keyboard or under control from an external program. The latter option was used in this work. The board can be configured to have a variety of full scale output voltages, these being +/- 10 V, +/- 5 V or 0 - 10 V. The +/- 5 V option was used. The update rate, i.e. how often the next point on the ramp could be generated and output, was variable according to the user manual[97] from 1 $\mu$s to 859 s. However, in reality an upper limit of 2 s was found, probably due to a software error. The accuracy of the outputs are to $\leq$ 0.01%. Further details of board specifications and configuring it for use in a PC are given in reference[97].

Output from the AWFG is fed to an amplifier (Kepco, BOP 1000M). This simply amplifies the generated waveform voltage by a factor of 100 and passes the voltage to the ion repelling grid. Generated waveforms from the computer must therefore be a factor of 100 less than is required at the repelling grid. Typical voltages required at the grid lie between 0 and 30 V. The AWFG was used to generate waveforms between 0 and 0.3 V. Care must be taken in producing the ramp voltage however. For reasons that are not clear the AWFG does not always produce a ramp with the output points set apart at equal voltage increments. Depending on the choice of conditions a ramp may be produced where five consecutive points, say, are at all the same voltage. A step to the next voltage increment follows where another five points are output at the same voltage. These steps in the ramp can then be detected in the measured current. Upon differentiation of the I-V trace spurious spikes are manifest in the energy distribution. In order to overcome the capricious behaviour of the AWFG two standard ramps were defined where output voltages incremented by an equal quantity with each data point. Details of these ramps are given in Table 2.5 in section 2.5.

The electron repelling grids in front and behind the collector need no variation during the course of the measurements. The grid in front of the collector is held at -120 V by a battery supply and similarly the grid behind the collector is biassed to -60 V .

## 2.4.3 Current Measurement

Two stages are employed in the measurement of collector current. The detected current is first amplified and then converted to digital form using an analogue to digital convertor. Amplification is carried out using an instrument, built by AEA Technology, Culham Laboratory, based on an isolation amplifier (Burr-Brown, ISO100 CP). The circuit acts as a current to voltage convertor. The ISO100 CP is an amplifier with input and output coupled by LEDs. Thus there is no ohmic connection between the input circuit and either the output circuit or the power supplies. The result of this is that current flowing due to ground loops is effectively eliminated thereby reducing interference in the system. In order to investigate the performance of the amplifier and be sure it produced a linear amplification a simple test was carried out. Nanoampere currents were fed into the amplifier and the output voltage monitored. The output voltages (0 - 400 mV) were found to be accurately linear over the range of input currents (0 - 40 nA). The amplifier was found to perform successfully even where low current is input. Measured I-V traces were therefore not corrupted by the amplifier.

The voltage output from the amplifier is passed to an analogue to digital convertor (Amplicon Liveline Ltd, PC30-D). This is in the form of an IBM PC board plugged directly into the computer. The PC30-D is capable of reading in up to 16 channels independently and converting them to 12 bit digital data with an accuracy of $\leq 0.003\%$. The board can be configured to accept input voltages in the range 0 to +10 V or +/- 5 V. The latter configuration was chosen for this work. The maximum throughput rate, i.e. how fast the board can convert data, is 200 kHz. Further details of the board specifications and connection to the PC are given in reference 98. Control of the board is via the external software that also drives the AWFG.

## 2.4.4 RF Interference.

The problems of interference from the radio frequency power supply with most of the components in the vacuum system can be overcome by screening the live surfaces with well-earthed copper mesh. Interference is usually noticeable as instabilities in the various LED displays and occasional erratic switching of the mass flow controllers. The problems are more evident at high RF powers (>100 W) and frequencies (e.g. 20 MHz). Adequate screening reduces the interference to these components to tolerable levels.

Of far more serious concern in this study was interference from signals induced in the wires carrying the low level signals to and from the analyser. These spurious signals were then introduced into the measured signal, distorting the IED. Noise of this type can often be introduced by *ground loops*[99]. Ground loops are electrical paths closed by the ground wires of the system and the ground plane as illustrated in figure 2.11. Current can be caused to flow in the loops by

a) Inductive pick up from stray RF and magnetic fields

and    b) Differences in potential between the points of the ground plane.

The ground plane in our system can be thought of as the etcher and diffusion pump / high vacuum line connected to the same earth as the PC. Connection of voltage control wires to the etcher and the grounding of the associated shields causes complete ground loops. In order to remove these loops, and reduce the interference caused by current flows in the earth line, the shields on the wires carrying the voltages to the grids were earthed only at the end nearest the PC. This effectively shields the wires from RF but breaks up the ohmic ground loop. Ground loops were not a problem in the collector and amplification circuit since the optically coupled isolation amplifier effectively breaks the connection.

Removal of ground loops in the data acquisition system succeeded in reducing the amount of interference detected. The complete removal of ground loops in the system was not possible. This is because the system is earthed at two points - through the mains connection supplying the PC, diffusion pump and various electrical components and also via the 3 phase supply connected to the vacuum pump on the
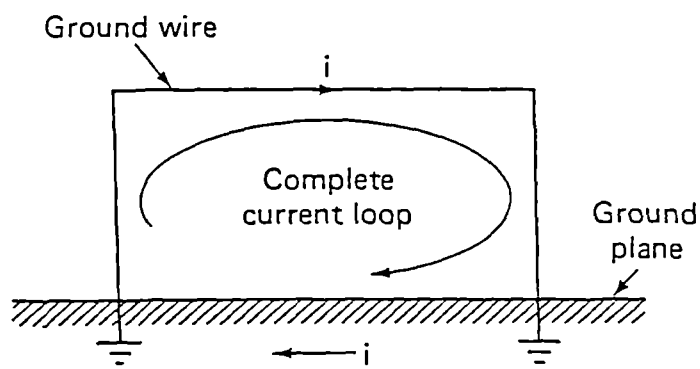
**Figure 2.11** Principle of the ground loop. After Wolf[99].

chamber. Any difference in potential between these two grounds will cause current to flow, introducing noise to the reference ground used for the measurements. Ideally all components of a system should be earthed at a single point to prevent any possibility of ground loops. Further details regarding the various types of noise present in a system and their elimination are given in references 99 and 100.

A junction box is located between the current amplifier and the PC. This simply converts the connection from a coaxial cable to a 'D' connector for input in to the PC. Further reduction in the noise level was effected by enclosing this junction box in an earthed metal box. The associated ribbon cable was encased in a copper shield earthed at one end only to prevent the establishment of ground loops.

## 2.5 EXPERIMENTAL PROCEDURE

IEDs were measured for a series of applied voltages and a series of discharge pressures. Each of these series consisted typically of 5 or 6 energy distributions at different conditions.

Before any discharge was initiated the chamber and analyser pumping lines were pumped to their base pressures. This usually took 30 to 45 minutes depending on how long the chamber had been open to the atmosphere and exposed to water vapour. Once the base pressures had been reached the process gas was introduced, usually at a low flow of $\sim 10$ sccm. The discharge was then initiated at the required voltage and the matching network adjusted for the minimum reflected power, typically $< 5$ W. The plasma was then left to stabilise for 15 minutes before measurements of IEDs began.

Measurements of the distributions have been fully automated. The upper and lower limits for the required voltage ramp, the number of points in the ramp and the number of scans required are entered in a file 'env.dat'. The control program, 'rfa.exe'[101], is then executed. 'Rfa.exe' creates a file, 'ramp.dat', that contains the required ramp in digital form together with the other parameters the AWFG requires such as the time increment between points. 'Ramp.dat' is passed to the AWFG which

can then generate the ramp at the output terminals. The ramp produced varies linearly from the upper ramp voltage to the lower voltage and back again. This allows us to perform two acquisition runs, one for the scan down the voltage ramp and one for the scan up. The two measured I-V traces can then be compared for hysteresis. Usually one of two possible ramps was used, the details of which are shown in Table 2.5.

| number of points | 124 | 247 |
|---|---|---|
| minimum awfg voltage / V | 0 | 0 |
| maximum awfg voltage / V | 0.3005 | 0.6005 |
| ramp update rate / ms | 1 | 1 |
| number of scans | ~2000 | ~2000 |

**Table 2.5** Details of the standard ramps used for waveform generation.

Each time the output ramp is updated (i.e. every 1 ms) the voltage change at the grid causes a change in detected current at the collector and a consequent change in the voltage fed into the PC-30D. Every time the control program updates the output ramp it also instructs the PC30-D to read the voltage at the input terminal. This is converted to digital form. At the end of the scan the entire digital trace is passed from the control program and stored in memory. Each subsequent scan is added to the existing data and averaged. The process of scanning, measuring and averaging continues until the full number of scans is complete, usually 2000 in order to acquire a good signal to noise ratio. At the completion of the scans the control program separates the sections of the data corresponding to the up and down parts of the scan and stores them on disk as 'dat1.tmp' and 'dat2.tmp' ready for manipulation.

Measured traces can be displayed and manipulated using the specially written program[102] 'test.exe'. This will read the file on disk currently named as 'dat.tmp' and display it in graphical form on screen. The trace can then be smoothed using a sliding

mean over a number of points, which can be defined by the user. Usually 5 point smoothing was used. In addition, differentiation of the trace to obtain the energy distribution is performed numerically by this program. The energy distribution can then be stored as a file or output to a plotter or printer.

## 2.5.1 Calibration of the Ion Energy Distribution

The measurements of the IEDs were complicated by a tendency for the measured traces to drift with time exposed to the plasma. A distribution measured at the start of an acquisition run and later repeated may appear to have shifted by up to 10 eV in energy. The IED is otherwise identical, i.e. peak heights and widths are unchanged. Whilst small changes in the plasma may be expected over the period of an entire acquisition run ($\sim 2$ hr), by cathode heating, this should not lead to the large effect as is observed. A calibration run was therefore established using an argon discharge at a pressure of 10 mTorr and 500 V applied voltage. The analyser was fitted with new grids and the entire vacuum system cleaned before making the calibration run. This run was then repeated to check for drift in the analyser measurements over the course of the acquisition run.

It was also found that if the analyser was set up and left pumping overnight without a liquid nitrogen cold trap on the chamber pump then sometimes the calibration run would be offset along the energy scale. Clearly this was not a phenomenon associated with the plasma. The most likely explanation for this observed offset is the formation of an insulating film upon the retarding grids of the analyser by pump oil back streaming and / or by the process gases during the course of the acquisition run. A similar effect has been observed by Ehlemann et al[103] in a study of a heated Langmuir probe system. They observed that when the probe was not heated the build up of an insulating layer with time required that greater voltages needed to be applied, in order to penetrate these layers, and enable measurements of plasma parameters. When the probe was heated layers were prevented from forming and measurements could proceed unhindered.

In order to overcome this effect of drift a number of methods were used to

ensure that the amount of drift was limited and known. As already stated, an argon calibration run was used as the first and last run of any series to check for drift over time. Additionally, a series of IED measurements, such as is shown in figure 3.1, would not be acquired consecutively. The order of taking the measurements was randomized in order to distinguish between trends due to a deliberate change in plasma conditions and any that are manifest due to drifting with time. A final check on the data was made possible by comparing a series of varying pressure IEDs and a series of varying voltage IEDs. Typically, pressure series were acquired for a fixed voltage and voltage series for a fixed pressure. This meant that usually one distribution was duplicated in each series, allowing some degree of cross checking.

The most effective method of ensuring the measurements were not corrupted was to always be sure the grids were clean. Thus, at the end of each acquisition run the grids were discarded and new grids were soldered in place. This was not always an adequate method however and depended on what process gas was being used. Chlorine containing gases usually contaminated the grids quickly while $CH_4/H_2$ discharges proved to be unmeasurable due to the intolerance of the grids. The choice of grid material was important too, with stainless steel being found to be more stable than tungsten.

## 2.6 COMPUTER SIMULATION METHODS

Measured IEDs have been simulated using computer programs on an IBM 3090 mainframe computer. The programs used employ Monte Carlo methods and were written by May[12] who gives details of the programming procedures and means of implementing the programs on the IBM. The programs used were:

a) **IED**: A low pressure simulation program for the case of a collisionless sheath. IEDs can be calculated at either the anode or the cathode.

b) **NEDANOD**: A high pressure version of the IED simulation program that includes collisions (scattering and charge exchange) in the sheath. This program is in fact Mays' **NED** program with the potentials altered for the anode to make it applicable to the work studied here.

96

Modifications to these programs to take account of the Bohm criterion and for other possible sheath potentials have been made. These are discussed in chapter 4. A description of the simulation model is included in section 1.7.3.

# CHAPTER 3

# MEASUREMENT OF ION ENERGY DISTRIBUTIONS

## 3.1 INTRODUCTION

In this chapter we present experimental IEDs obtained for a variety of discharges using the retarding field analyser described in the preceding section. As well as examining the differences between IEDs for different gases the effect of changing the relative areas of anode and cathode on argon IEDs is explored. Finally we investigate the effect on argon IEDs of altering the frequency of the applied RF voltage.

In all the following IEDs the y-axis of the IEDs is presented as $dI/dV$. Strictly, this is correct[104] since the trace corresponds to the differential of the I-V curve produced by the analyser. However, for all purposes the reader should regard this as simply the intensity of the signal at any energy. For clarity the IEDs have been scaled to unity.

## 3.2 RESULTS

### 3.2.1 Argon IEDs

Experimental data are presented in figure 3.1 of IEDs from 10 mTorr argon plasmas in which the applied RF voltage, $V_0$, is varied from 200 V to 700 V. These data clearly show a double peaked distribution where the intensity of the high energy peak increases relative to the low energy peak as the applied voltage is increased. We also observe a decrease in the distribution width, $\Delta E$, as $V_0$ is increased. This trend is plotted in figure 3.2. The consequence of the change in $\Delta E$ is that the maximum ion energy that we observe at the anode is seen to decrease as the applied voltage increases. Figure 3.3 shows the experimentally measured values of $V_{dc}$ plotted against $V_0$. These values are used in the calculation of IEDs in chapter 4.

Figure 3.4 shows IEDs for argon discharges at $V_0 = 500$ V for pressures of 7.0 mTorr through to 17.1 mTorr. Here we again observe that the relative peak intensities depend upon discharge conditions. The intensity of the high energy peak is found to decrease relative to the low energy peak as the pressure is increased. We also find that $\Delta E$ increases as the pressure rises and consequently that the maximum observed ion energy increases with pressure. The change in $\Delta E$ with pressure is
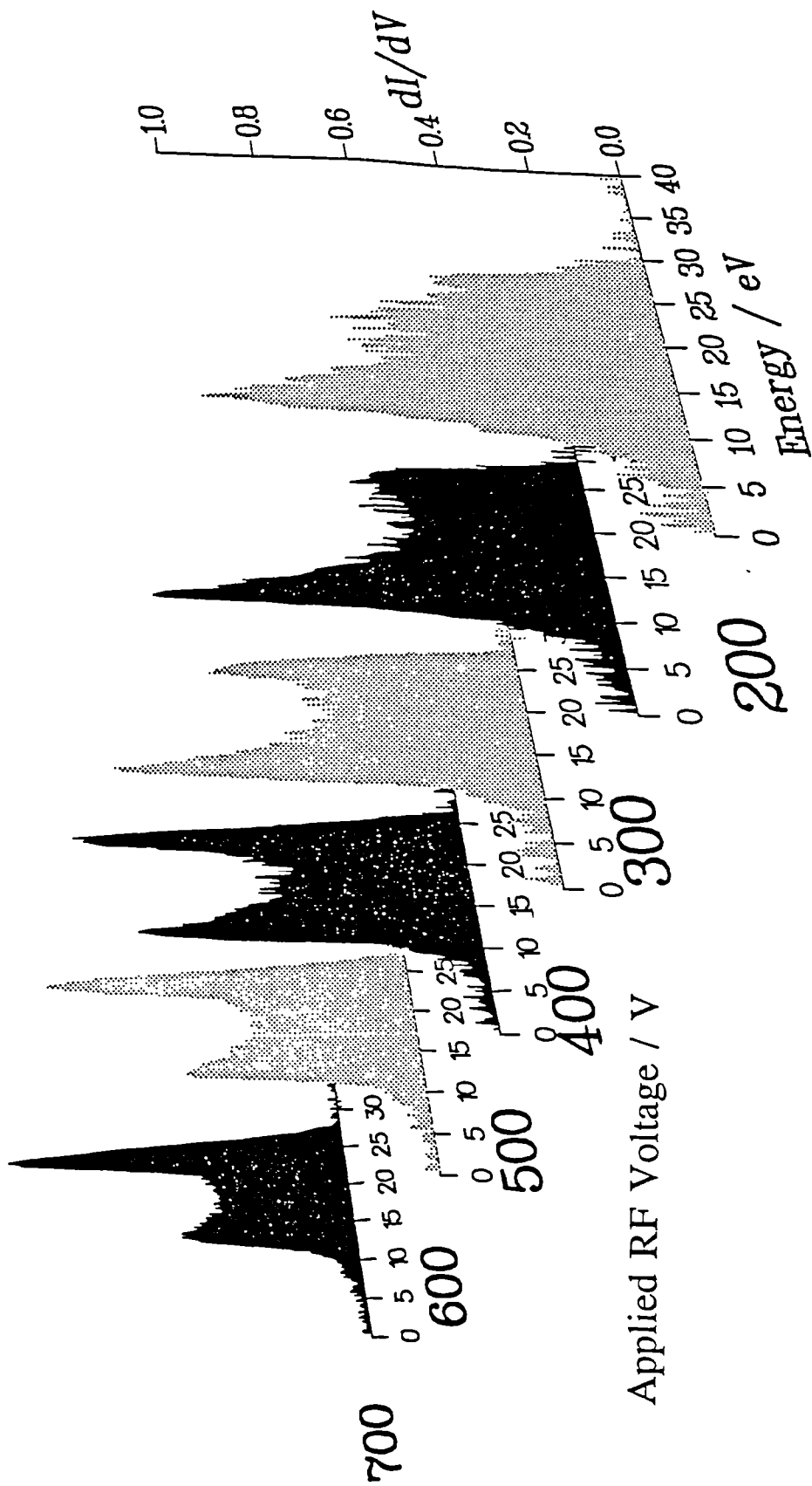
Figure 3.1 Argon IEDs measured at 10 mTorr for different applied RF voltages.
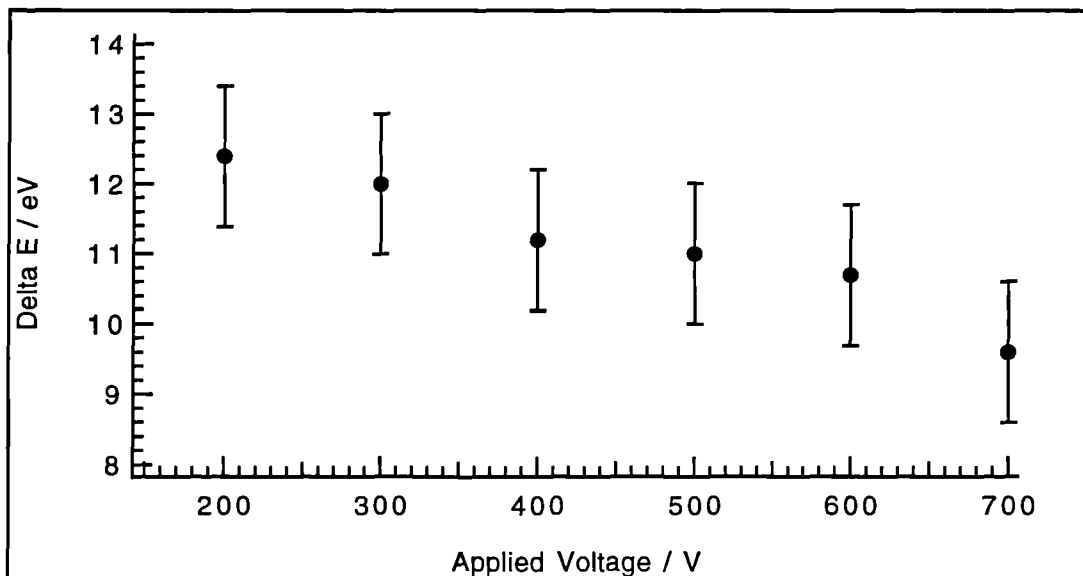
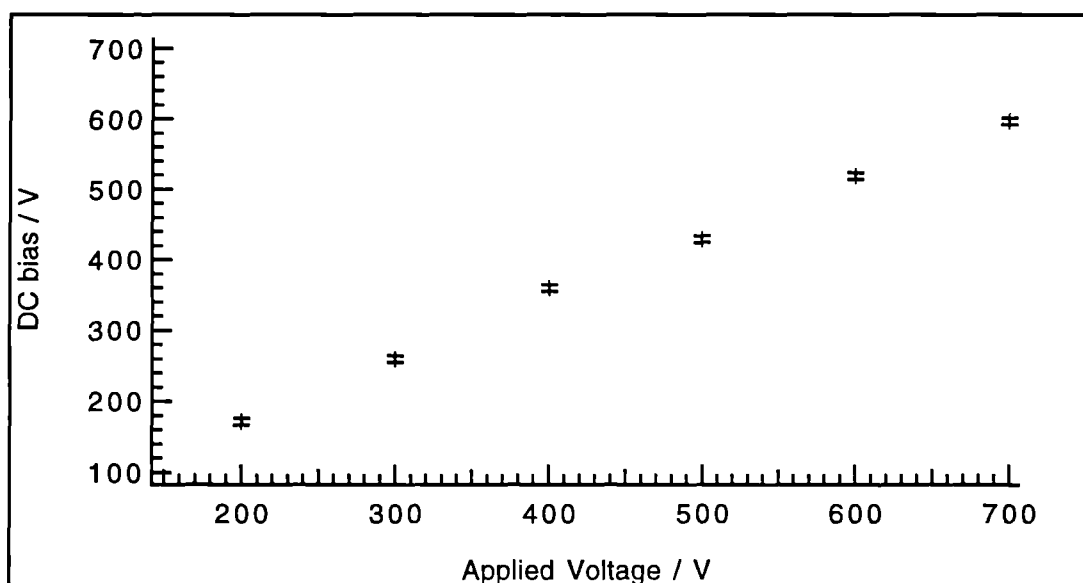**Figure 3.2** Distribution width versus applied RF voltage
for argon IEDs in figure 3.1



**Figure 3.3** DC bias versus applied RF voltage for each of the
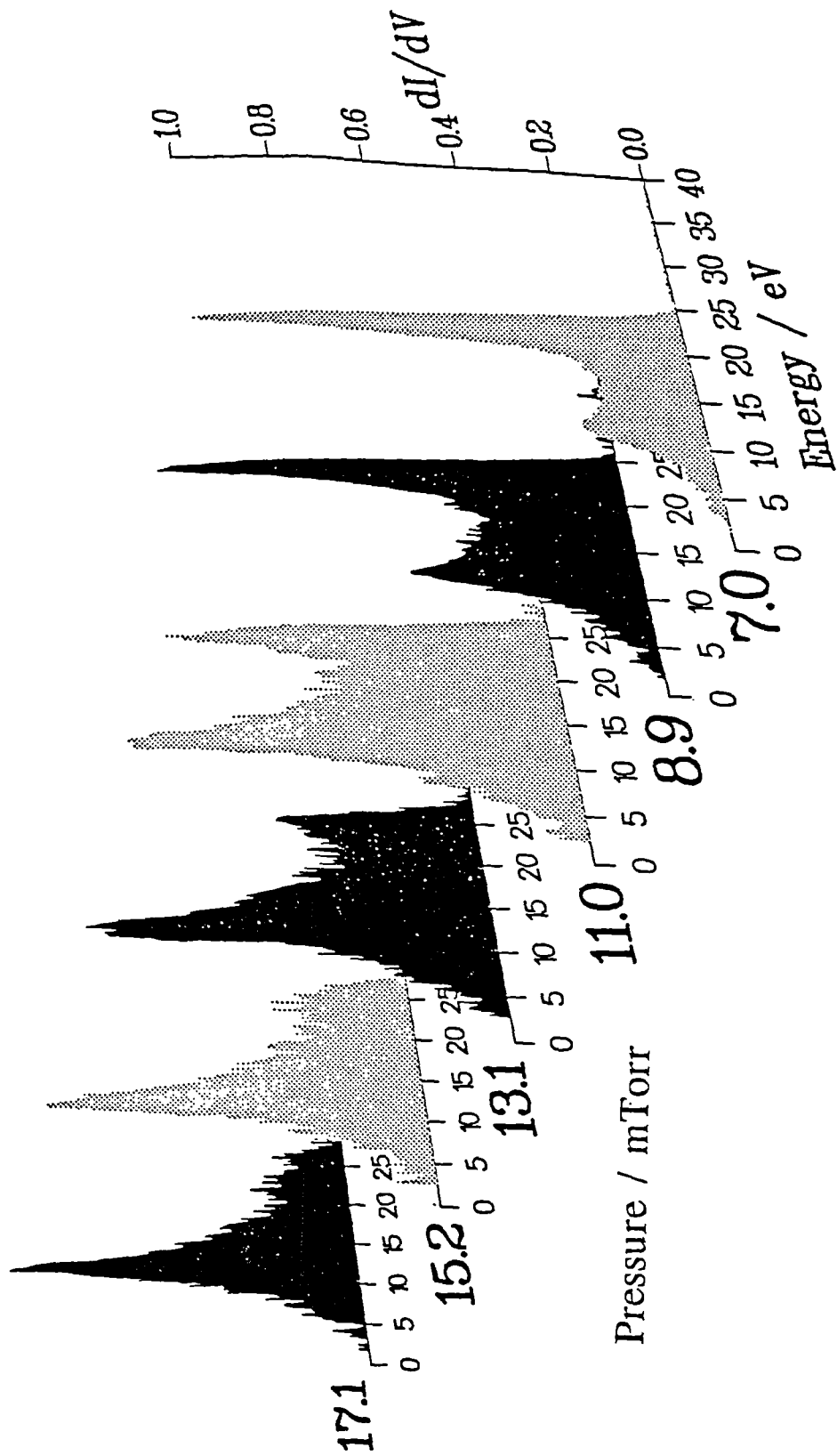argon IEDs in figure 3.1.

101

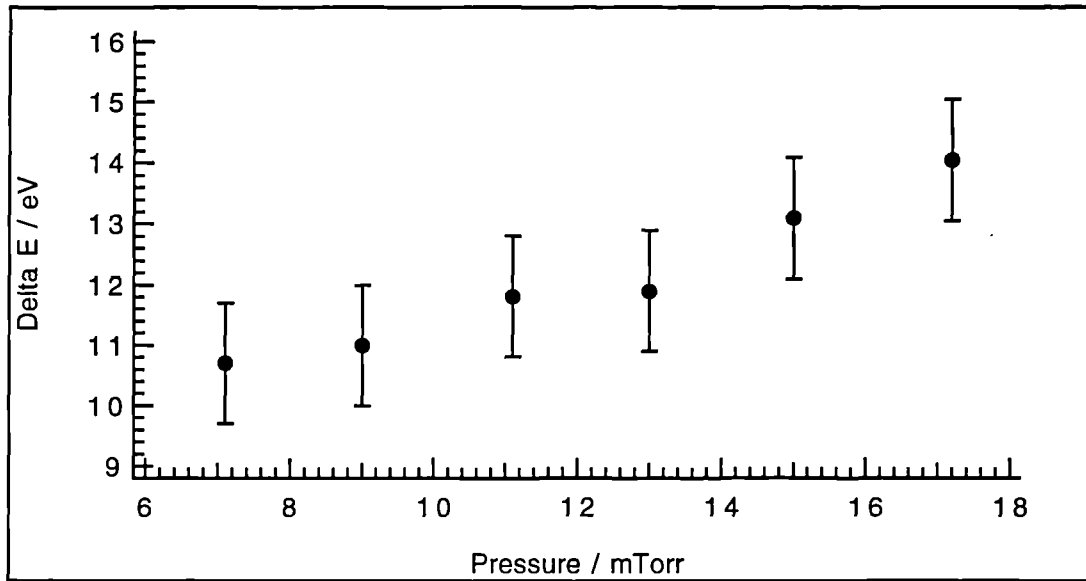**Figure 3.4** Argon IEDs measured at $V_0$ = 500 V for different chamber pressures.

**Figure 3.5** Distribution width versus chamber pressure for argon IEDs in figure 3.4.
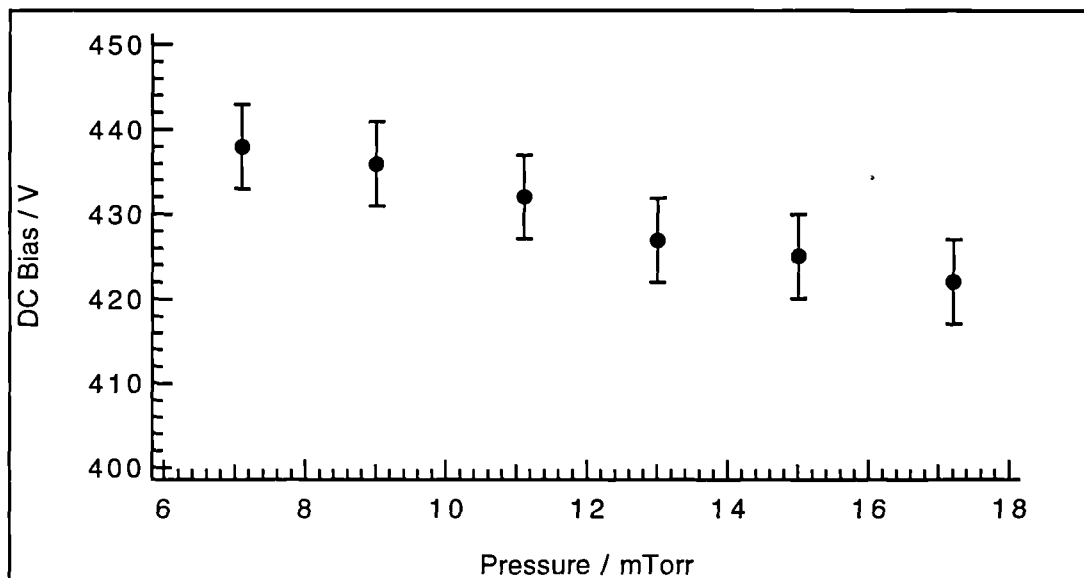


**Figure 3.6** DC bias versus chamber pressure for the argon IEDs in figure 3.4.

shown in figure 3.5. In figure 3.6 we show the change in DC bias as the pressure is increased.

The ions that we expect to observe in an argon discharge are $Ar^+$ and small amounts of $Ar^{2+}$. The doubly charged species would be expected to be evident in the IED at energies approximately twice that of the singly charged ions. We did not observe any peaks outside of the main body of the IED and therefore conclude that $Ar^{2+}$ either does not reach the detector or is present in such small quantities such that it is not identifiable above the residual noise levels. Mass resolved IEDs from argon plasmas[59] indicate that $ArH^+$, $H_3O^+$, $H_2O^+$, and $H_3^+$ can also be expected to be present in the chamber in small amounts due to residual water vapour. The contribution to the total IED due to these ions is expected to be small. The significant species in the IED is therefore only $Ar^+$.

The double peak distribution observed in all these data originates from the influence of the RF voltage on the sheath potential as discussed in section 1.4.8. If the ion transit time across the time varying sheath is short the ion will experience the instantaneous sheath potential and a double peaked distribution arises. The IED is then said to be RF modulated. Where the ion transit time is more than a few RF periods the distribution that develops is related to the time averaged sheath potential.

The degree of RF modulation of the IED is indicated by the amount of splitting between the peaks in the IED. Equation 1.13 shows the dependence of this splitting, $\Delta E$, on discharge parameters. For the system under study here (single mass, fixed frequency) the only parameters that can vary are $V_{pe,max}$, the maximum sheath potential and $l_{max}$, the maximum sheath thickness. We can calculate the increase in the anode sheath potential for the IEDs in figure 3.1 as the RF voltage is increased using equation 1.11. For this purpose we calculate values for the effective electrode area ratio from experiment using equation 1.5. We also adopt an electron temperature of 2 eV which is a typical value found in similar reactors by other workers[37]. The anode sheath potential is then found to increase from 42.9 V at $V_0 = 200$ V to 109.9 V at $V_0 = 700$ V. Note however that these are <u>maximum</u> sheath potentials and an ion can only attain the maximum energy if it crosses the entire sheath during one expansion.

The increase in sheath potential as the applied RF voltage increases will have the effect of broadening the distribution since the ion transit time is decreased. However, we actually observe a decrease in $\Delta E$. Since $V_{pe,max}$ has, as just shown, increased with voltage we conclude that for equation 1.13 to hold there must also be an increase in $l_{max}$ to produce the observed decrease in $\Delta E$. This change in $l_{max}$ must be sufficient to offset the broadening of the IED by the increased sheath potential. This would then account for the apparent anomalous observation of a decrease in maximum ion energy when the applied voltage increases.

The hypothesis that the sheath thickness must increase with applied RF voltage in our reactor could not be verified experimentally due to the position of the viewing window. Theoretical studies of the sheath do, however, confirm that this should be the case. Recently, Snijkers[59] has developed a high frequency sheath model based on a self-consistent sheath solution derived for a DC discharge. His solution shows that the maximum sheath thickness is proportional to the maximum sheath potential.

Morgan[105] has derived a formula for the sheath thickness in high pressure systems. The theory is based on standard expressions for the space charge limited current through a sheath derived using Poisson's equation. The equation given by Morgan has been empirically modified by May[12,87] after comparing results of the equation with measurements of the sheath thickness for three experimental systems. Strictly, Morgan's theory applies only to high pressure systems but May has shown that the equation successfully reproduces experimentally observed trends in the sheath thickness where the discharge pressure is varied from 10 to 500 mTorr. May's modified version of Morgan's equation is:

$$l_{max} = 2.12 \times 10^{-5} \left\{ \frac{0.5\,e}{3.5 \times 10^{-19}\,p\,m_i\,\sigma_{max}} \right\}^{\frac{1}{5}} V_{pe,max}^{\frac{3}{5}} \qquad (3.1)$$

Where $V_{pe,max}$ is the maximum sheath potential calculated using equations 1.9 or 1.11, $p$ is the pressure / mTorr, $m_i$ is the mass of the ion / kg and $\sigma_{max}$ is the collision cross section / $\mathring{A}^2$. The sheath thickness is then given in m.

Importantly, equation 3.1 shows that the sheath thickness is expected to increase

with the sheath potential and therefore also with the applied RF voltage. This agrees with our conclusion from the evidence of the IED measurements.

There have been studies by several workers to measure the sheath thickness by a variety of methods. These include a visual estimate of the sheath dark space, optical emission studies and studies with electrical probes. It is not clear that a simple visual estimate of the dark space by eye will necessarily reveal the full extent of the influence of the sheath electric field. As discussed by May the dark space may not be synonymous with the sheath but only a secondary effect. Given the correct input phase electrons can cross the sheath region from the plane of origin to the cathode whilst the sheath is near its minimum thickness[106]. During their transit some electrons will excite $Ar \rightarrow Ar^*$. Thus we only expect the sheath region to be actually dark for the portion of the RF cycle where the sheath is greater than its minimum value - about 4/5 cycle in our system. Simple visual inspection of the sheath will therefore give a time-averaged value for the thickness and not a measure of the *maximum* extent of the sheath.

Liu et al[67] used a method of visual inspection and found no change in sheath thickness with applied RF voltage within ± 0.5 mm, their estimated accuracy of measurement. However, any small change in the maximum sheath thickness may not be detected due to the accuracy and the fact that a time averaged thickness is probably being monitored. Kuypers[73], who inferred sheath thicknesses in his reactor from the splitting of IED peaks, found a small increase in sheath thickness from 4 to 5 mm when the RF power was varied from 100 W to 400 W. This corresponds to the regime of our experiments. Bisschops[72] has used optical emission spectroscopy to study the sheath region. The sheath is a region of electron depletion and so by monitoring emission intensities of species excited by electrons an indication of the spatial extent of the electric field, i.e. sheath, can be obtained. The emission is shown not to end abruptly but to decay over a few mm. For a 50 mTorr $CF_4$ plasma Bisschops data show that the region of decay increases slightly with increased power, and therefore voltage, supplied to the plasma. The sheath thus expands a small amount with increased voltage, in agreement with our conclusions from experiment. In agreement

with Bisschops, Langmuir probe studies[107,108] also show a decay of the sheath near the electrode.

The most striking effect of the varying voltage on the IED is in the peak intensities. The relative heights of peaks in the IED depends upon the ion transit time across the sheath. An increase in the ion transit time (i.e. a thicker sheath) means that more ions experience relatively more time within the sheath. Thus it would be expected that more high energy ions would occur. This is in fact the effect we see as the voltage rises - thereby indicating the presence of an increasing sheath thickness.

The data in figure 3.4 for varying discharge pressures can also be analysed with reference to equation 1.13. The RF voltage to the plasma was kept constant at 500 V for each IED measurement and so the maximum sheath potential will vary only slightly. The DC bias was found to change progressively from -438 V at 7.0 mTorr to -423 V at 17.0 mTorr. There was also a small progressive change in the effective electrode area ratio from 0.19 at 7.0 mTorr to 0.22 at 17.0 mTorr. Using these values in equation 1.11 we can calculate the sheath potential we expect at the anode, assuming $kT_e$ = 2 eV. We find that the anode sheath potential will increase from 68.9 V at 7.0 mTorr to 83.9 V a 17.0 mTorr. As before, these are calculated *maximum* sheath potentials and an ion will only gain, say, 83.9 V if it crosses the entire sheath width during one expanded phase of the sheath. Equation 1.13 shows that the small increase in sheath potential with pressure will cause $\Delta E$ to increase also, since the ion transit time will decrease provided the sheath thickness remains constant. This is in agreement with the trend in $\Delta E$ that we observe (see figure 4.5). However, there is general agreement amongst workers that the sheath thickness does not remain constant but instead decreases with increasing pressure. This has been observed by Liu et al[67] and also by Wild and Koidl[79] amongst others. The sheath thickness is found to vary most in the region 0 - 50 mTorr where a rapid decrease with increasing pressure is found. Equation 3.1 shows that the sheath thickness is expected to be proportional to $p^{-1/5}$. As a result, at pressures greater than ~20 mTorr the sheath thickness is less sensitive to changes in plasma conditions and will remain relatively constant. This is observed experimentally[67]. If the sheath thickness does decrease, as seems likely, then

this will also cause $\Delta E$ to increase. Thus, the observed increase in $\Delta E$ as the pressure rises can be attributed to both a small increase in the sheath potential and a decrease in the sheath thickness.

The peak intensities in the IEDs offer further qualitative support for the behaviour of the sheath thickness. At lower pressures we find that there are more high energy ions than low energy ones, as indicated by the peak intensities. As the pressure is increased there are less high energy ions. This simply corresponds to proportionally less ions being able to attain a high energy, thereby indicating the sheath thickness is decreasing with pressure.

The effect of the experimental parameters on the shape of the IED is quite striking. The distribution is evidently highly sensitive to experimental conditions. Other workers have observed small changes in peak intensities over larger pressure ranges[74] together with an increase in $\Delta E$. However the large effect on the peak intensities over the small pressure range used has not, to the authors knowledge, been previously reported. Also, the effect of the applied RF voltage on the IEDs observed by other workers is usually different to that seen here. Typically, the peak intensities are not found to vary so much as seen in this work and the distribution width is found to increase due to the increased sheath potential.

Although the sensitivity of the IEDs to these parameters has not been observed Thompson et al[86] have in fact predicted it. They have simulated ion transport through RF discharge sheaths using Monte Carlo methods. Their model uses a spatially uniform field of the form $E = E_0(1 - \sin\omega t)$ - a combination of DC and RF fields. This form is not applicable to all RF cases[85] but it does allow observation of the effects of the RF component of the field. Calculations in Thompson et al were performed for collisional and collisionless sheaths. For the pressures under study here we can consider the collisionless case. The prediction of Thompson for collisionless sheaths is shown in figure 3.7. The value of M alongside the IEDs is a scaling parameter introduced by Thompson. As $M \to \infty$ the distribution will only be affected by the DC field and as $M \to 0$ the distribution should depend mainly on the instantaneous electric
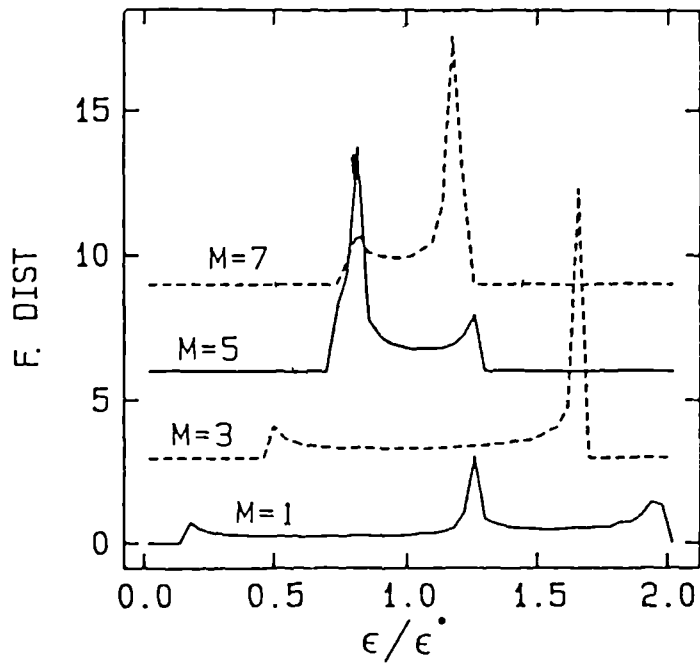
**Figure 3.7** Predictions of ion energy distributions by Thompson et al[86]. A large M corresponds to the physical case of a thick sheath or high frequency while small M represents a thinner sheath or a low frequency.

field. Thus a large M corresponds to the physical case of a thick sheath or a high frequency discharge while small M refers to thinner sheaths or lower frequencies. The calculations show that as M varies from 5 to 7, i.e. the sheath thickness is increased, the relative peak intensities are interchanged and the distribution narrows slightly. This prediction is exactly in accordance with our experimental observations and conclusions of the sheath behaviour with both voltage and pressure. The regimes corresponding to M = 1 and M = 3 were presumably not accessible in our reactor. Thompson et al noted that although the effects of the RF field have been quantified, the sensitivity of the IEDs to discharge parameters had not been observed. Our data would appear to be the first such observations and confirm the findings of Thompson et al.

### 3.2.2 Helium IEDs

We turn now to IED measurements for helium discharges. Figure 3.8 shows data for 20 mTorr helium discharges where the applied voltage has been varied from 200 V to 600 V. These data show a double peaked distribution at lower voltages, with the distribution almost coalescing into a single peak when $V_0$ = 600 V. As in the case of Ar, the distribution width, $\Delta E$, is found to decrease as $V_0$ increases. This effect is plotted in figure 3.9. The contraction of the distribution causes the maximum observed energy in the IED to decrease with increasing applied voltage. In figure 3.10 the variation of $V_{dc}$ with $V_0$ is shown.

Figure 3.11 displays IEDs measured in helium discharges at pressures from 9 to 57 mTorr. In all cases $V_0$ = 400 V. The form of the IED is found to be strongly dependent on the pressure. At low pressure the IED is found to consist of a single peak, whilst at higher pressure a double peaked distribution develops. Note that in the data labelled as '16 mTorr' there is some interference present from an unidentified external source. The distribution width is found to increase as the pressure rises and this trend is plotted in figure 3.12. Figure 3.13 shows the effect of increasing pressure on the DC bias when the applied voltage is kept constant at 400 V.

In a helium discharge the major species expected to be present is $He^+$[109]. We do not expect any other species, including water vapour, to be present in quantities
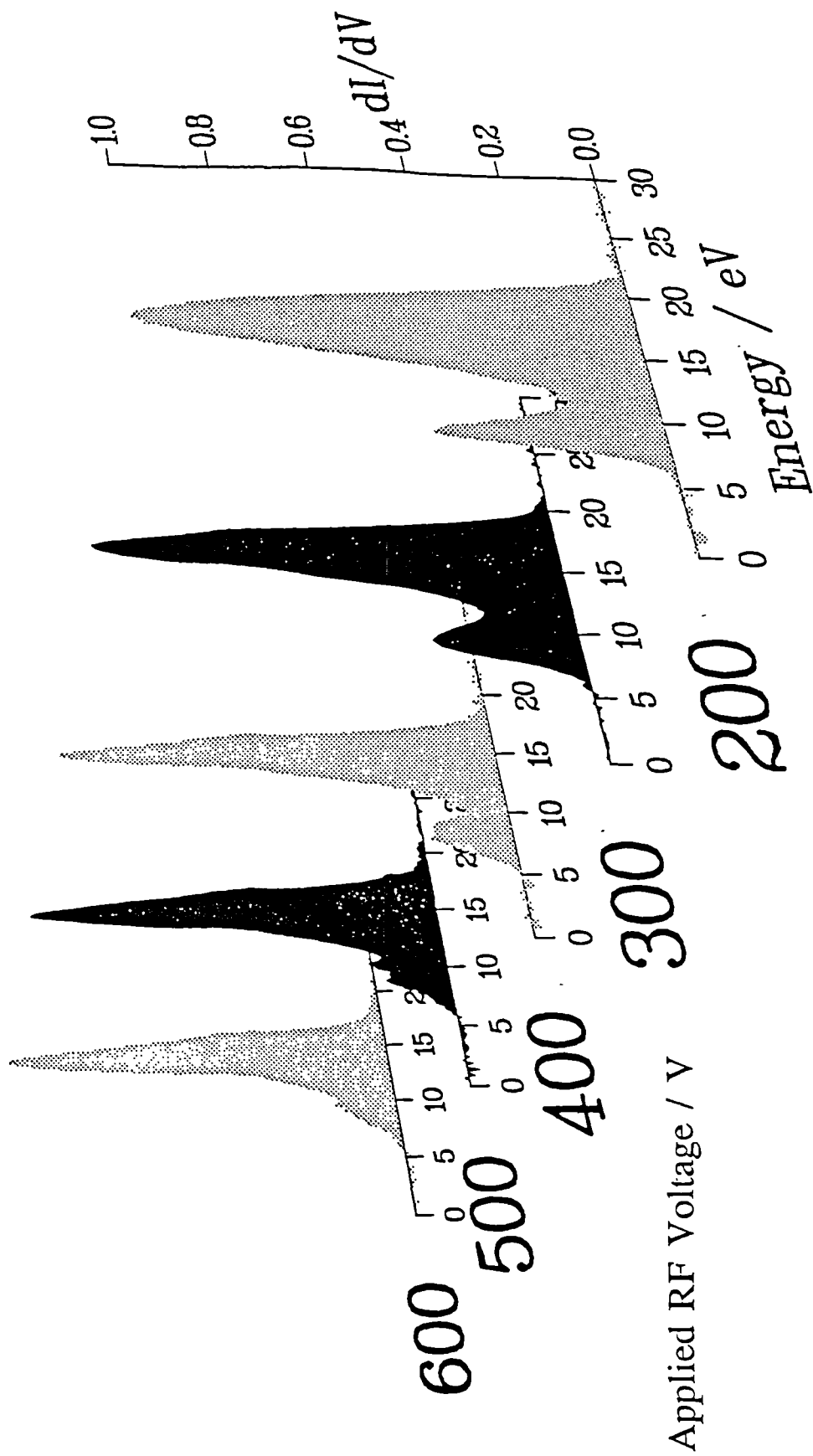
110

**Figure 3.8** Helium IEDs measured at 20 mTorr for different applied RF voltages.
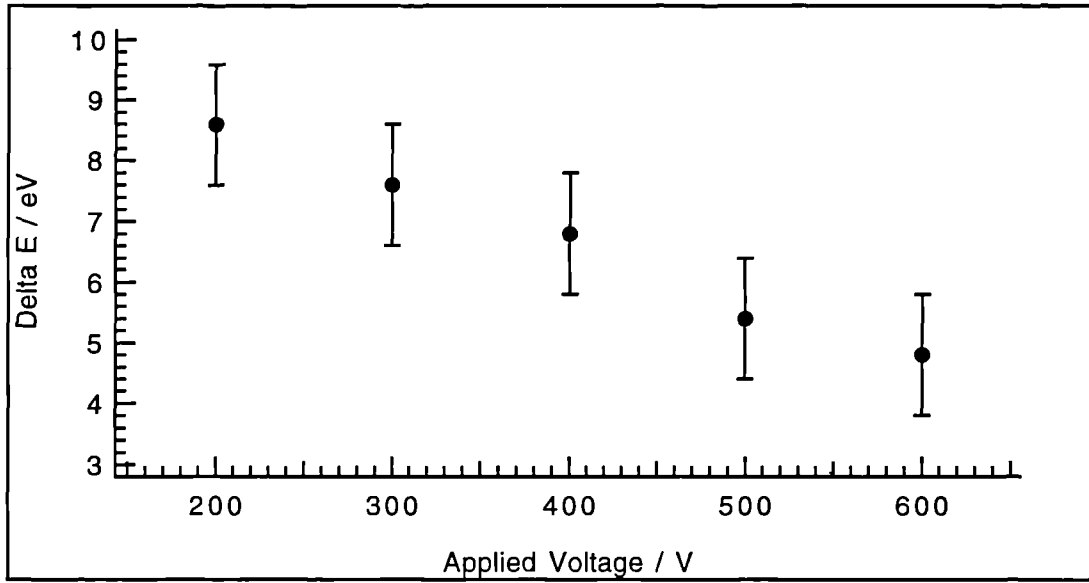
**Figure 3.9** Distribution width versus applied RF voltage for helium IEDs in figure 3.8.
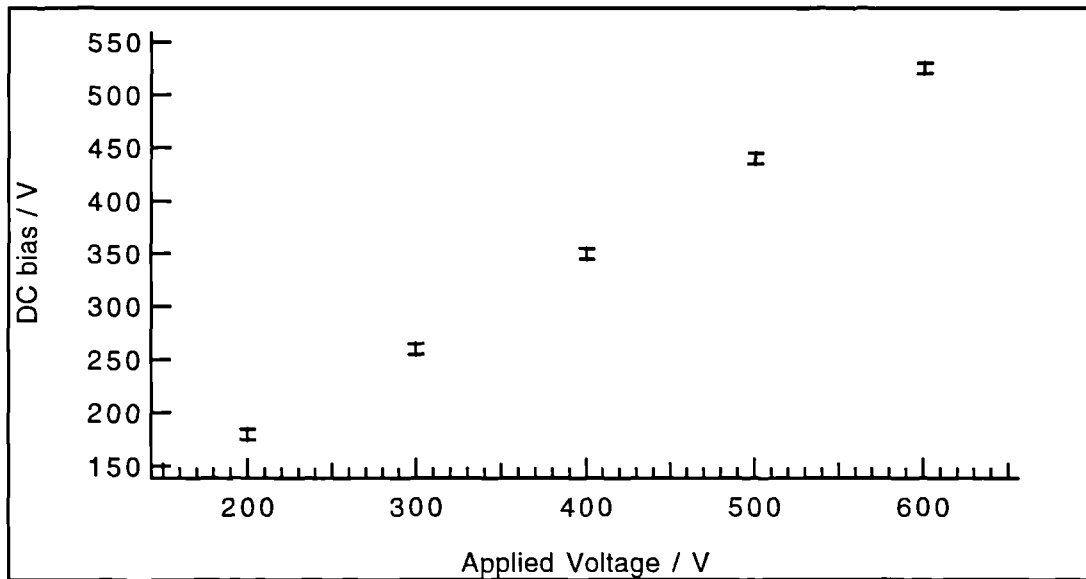


**Figure 3.10** DC bias versus applied RF voltage for each of the helium IEDs in figure 3.8.
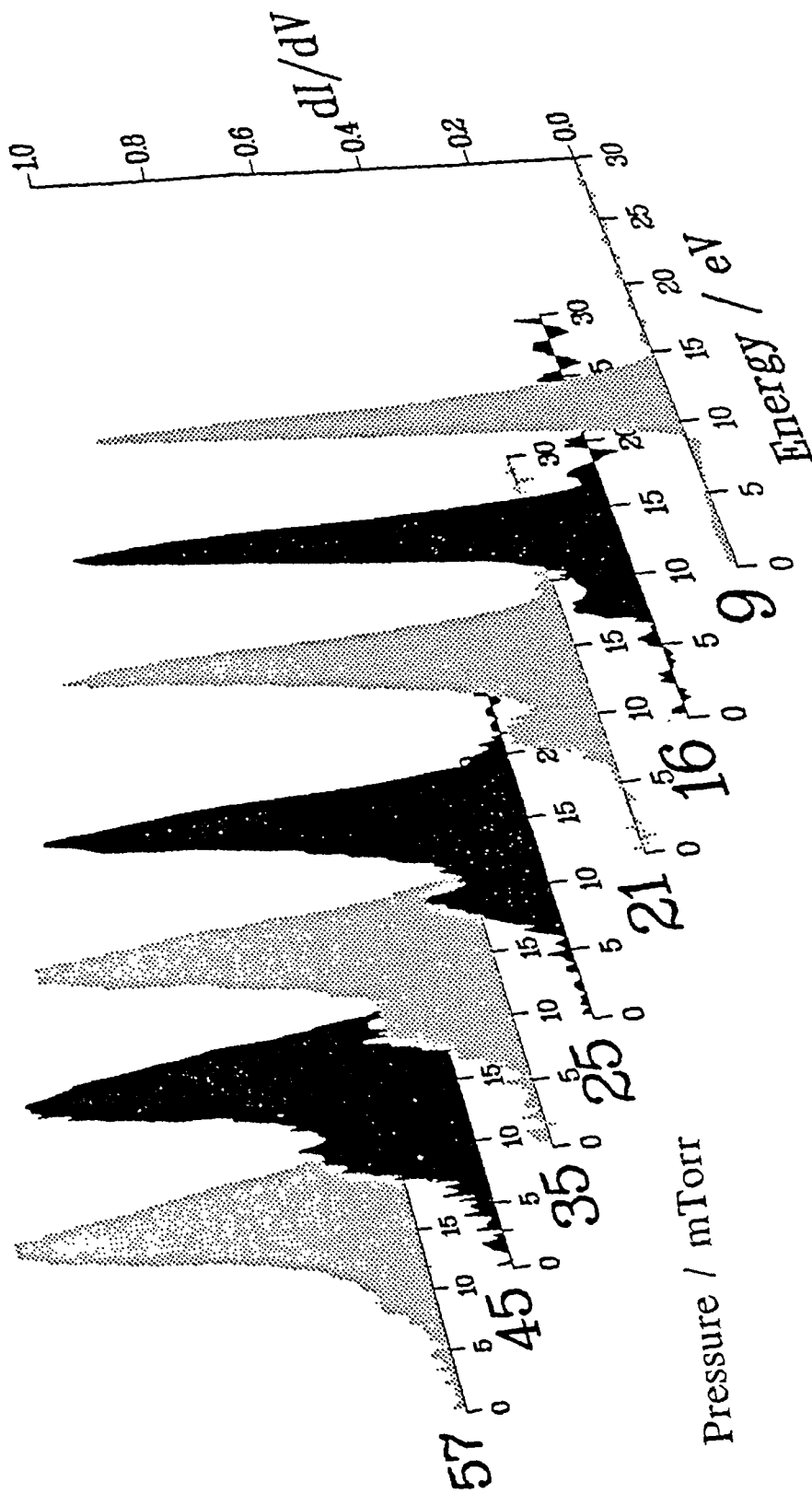
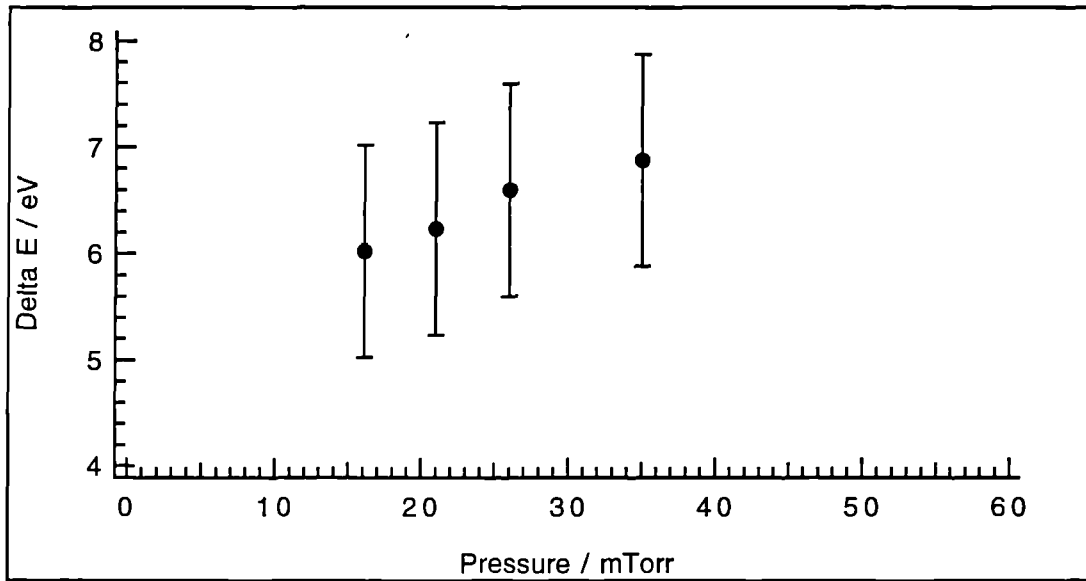**Figure 3.11** Helium IEDs measured at $V_0 = 400$ V for different chamber pressures.

**Figure 3.12** Distribution width versus chamber pressure for helium IEDs in figure 3.11.
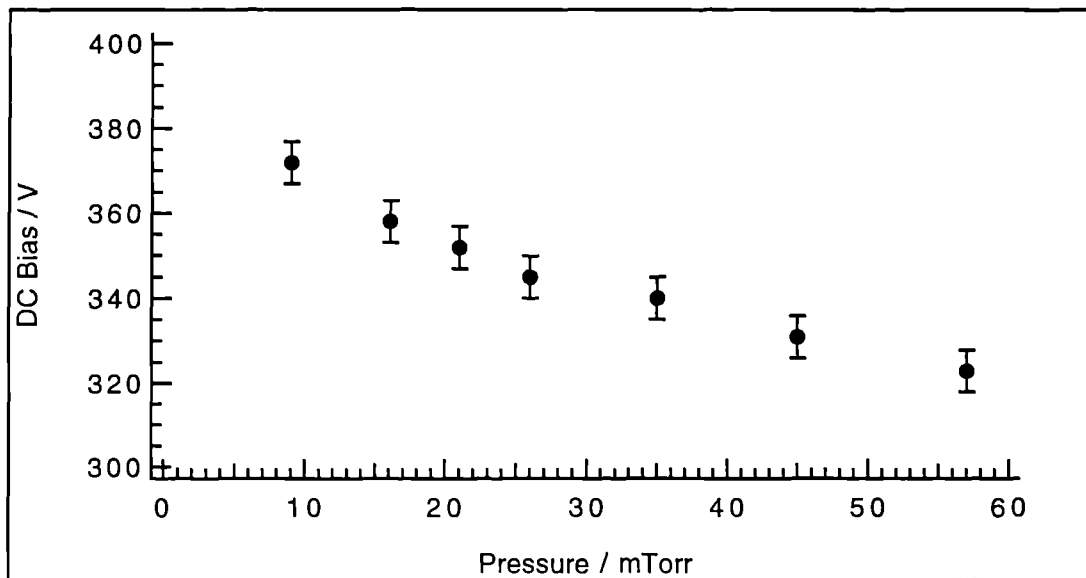


**Figure 3.13** DC bias versus chamber pressure for the helium IEDs in figure 3.11.

114

significant enough to be observed in the IED. Thus, the IEDs measured are solely due to $He^+$.

These measurements of helium IEDs are, at first sight, very different to the argon IEDs presented in the previous section. However, there are similarities that lead us to conclude that the same mechanisms are operating in both discharges. Firstly, in the voltage series presented for both Ar and He discharges, the low energy peak decreases in intensity relative to the high energy peak as the applied voltage is increased. Also for both sets of data there is a contraction of the IED as $V_0$ increases. Similarly, in the pressure data we find that for both discharges the low energy peak increases in intensity as the pressure rises together with a broadening of the distribution.

The double peaked distributions that we observe in these data we again attribute to the influence of the RF component of the sheath potential. It may be that the low energy peak, being considerably less intense than the high energy peak, could be due to a collision phenomenon i.e. charge exchange. Discrete peaks have been observed in IEDs which correspond to ions being formed within the sheath region by a neutral colliding with an ion that is being accelerated[79]. An electron is transferred between the particles, resulting in a fast moving neutral and ion moving with thermal velocity. The newly formed ion is then accelerated by the sheath electric field. However, it cannot gain as much energy as an ion that is accelerated across the full sheath and so peaks at energies lower than that of the main body of the IED are seen.       We can show that this is not the case for the data here. Let us consider the pressure data presented in figure 3.11 and the peak positions of these IEDs. At low pressure the distribution is very narrow and consists of a single peak with no hint of a second peak. At a pressure of 16 mTorr a second peak does begin to appear. If this were a charge exchange peak we would expect that the major peak in the IED to be in the same place as at lower pressures. This is in fact not the case and we observe that the peaks in the distribution split away from a central position as the pressure rises. Thus there is a consequent increase in the maximum observed energy, albeit slight. This effect

could not be caused by charge exchange processes. Additionally, if the low energy peak were to be due to charge exchange we would expect to see some indication of a third peak at yet lower energy due to further charge exchange processes. At no point is a third peak observed. Furthermore, the collision cross section for $He^+$ on He is approximately half of that of $Ar^+$ on $Ar^{110,111}$. Since we do not observe any charge exchange phenomena in the Ar IEDs, we are unlikely to observe any in the He IEDs at similar pressures. Instead, what we appear to be observing is the onset of RF modulation broadening as the ion transit time across the sheath is decreased. We would suggest, based on other workers' observations already presented in the previous section, that the cause of the decrease in the ion transit time is a decrease in the sheath thickness as the pressure rises. We do observe some scattering of the ions as indicated by the smearing of the distribution to low energies at the highest pressures, with a consequent loss of a discrete low energy peak.

The voltage series displayed in figure 3.8 also shows the effect of RF modulation broadening. Here, the movement of the peaks is more distinct than in the pressure series. As the voltage increases the low energy peak moves up in energy while the high energy peak moves down, eventually almost coalescing into a single peak at an intermediate energy. This can also only be attributed to the effect of RF modulation rather than charge exchange phenomenon. Again, if charge exchange were to be the mechanism responsible for the IED features we would expect some indication of a third peak, especially in the 200 V IED where the low energy peak is quite intense. None is observed which suggests that this low energy peak is not due to charge exchange. The observed change in the degree of RF modulation is again interpreted in terms of the ion transit time across the sheath.

We conclude, as with the Ar data, that as the voltage increases the ion transit time must also increase in order to account for the observed contraction. Since the maximum sheath potential must increase with applied RF voltage, and this would cause the distribution to spread out (see equation 1.13), there must be some other factor causing the IED to contract with increasing applied voltage. Equation 1.13 leads us to suggest that this can only be an increase in the sheath thickness with voltage.

116

The evidence for increasing sheath thickness with increasing applied voltage has already been discussed in the previous section concerning Ar IEDs.

The observed onset of RF modulation by changing the discharge parameters is very unusual. Other workers have demonstrated that very different IEDs can be obtained depending on the frequency of the applied voltage. Köhler et al[69] have shown that at 100 kHz well separated peaks are observed in the IED of $ArH^+$. This corresponds to a "low frequency regime", where the ions cross the sheath in a fraction of an RF cycle and so their transit time is very short. At 13.56 MHz Köhler et al show that an $Ar_2^+$ IED is a single peak. This is a "high frequency regime" where the ion experiences many cycles in its passage across the sheath and the transit time is quite long. However, in our data we appear to be observing a transition from the high frequency regime, where there is a single peak, towards the low frequency regime. The author knows of no other study where the onset of RF modulation has been observed simply by changing easily adjustable process parameters such as pressure and voltage. This may have important consequences for etch processes if the effect is replicated at the cathode since, as these results clearly show, increasing the voltage does not necessarily increase the maximum ion energy. We discuss cathode IEDs further in section 4.3.1.

Although we have drawn attention to the similarities of these helium IEDs and the argon IEDs of the previous section there is one striking difference between them. The helium IEDs are found to be generally much narrower than the argon case. This is an indication that the sheath thickness in the helium discharge is likely to be much thicker than in a corresponding argon discharge since the IED splitting is expected to be proportional to $M^{-1/2}$ where M = ion mass[31]. Thus, if all other parameters were invariant we would expect the helium IED to be far more spread out than argon. We shall discuss sheath thickness and ion mass further (section 3.2.4) after presentation of some xenon IEDs.


## 3.2.3 Xenon IEDs

We turn now to consider IEDs for a xenon discharge. However, we only

present IEDs from a low pressure discharge for a series of varying applied RF voltages. This is because the pumping capabilities of the retarding field analyser did not allow us to measure IEDs at pressures much above the lowest attainable pressure of $\sim 7$ mTorr. The effects of varying pressure on Xe IEDs was not, therefore, measurable. Figure 3.14 shows IEDs from a Xe discharge for varying applied voltages between 400 V and 800 V. The species that we would expect to be present in a xenon discharge at this pressure are only $Xe^+$ and, possibly, $XeH^+$ formed by reaction with water vapour[112]. However, the latter is probably present in small quantities and, since its mass is nearly the same as $Xe^+$ the analyser would not resolve the separate species. Thus we consider that the observed IED is due only to $Xe^+$ ions.

The trends that we observe in the xenon IEDs are similar to those seen previously in the argon and helium discharges. We find that as $V_0$ increases there is an interchange in intensity of the two peak heights, with the high energy peak developing at higher voltages. We also find that the IEDs contract slightly as the voltage increases, in common with our observations in the Ar and He discharges. The change in $\Delta E$ with applied voltage is plotted in figure 3.15. The relationship between $V_0$ and $V_{dc}$ for the xenon discharges is plotted in figure 3.16.

Our interpretation of this data is the same as for the argon and helium discharges, i.e. there is a change in the degree of RF modulation, caused by a change in the ion transit time across the sheath. This is most likely to be due to an increase in the sheath thickness, although this could not be verified unequivocally in our reactor.

## 3.2.4 Effect Of Ion Mass On IEDs

At this stage it is convenient to consider the influence of the ion mass on the IED. We have, up until now, presented IEDs for helium, argon and xenon discharges. The mass of each of these ions is, respectively, 4, 40 and 131 amu. We have already noted in the previous section that the splitting, $\Delta E$, of the helium IEDs is less than that of the argon IEDs, while we now see that the Xe IEDs are comparable to the argon IEDs. We now consider the splitting of the IEDs for each species when $V_0 = 500$ V.
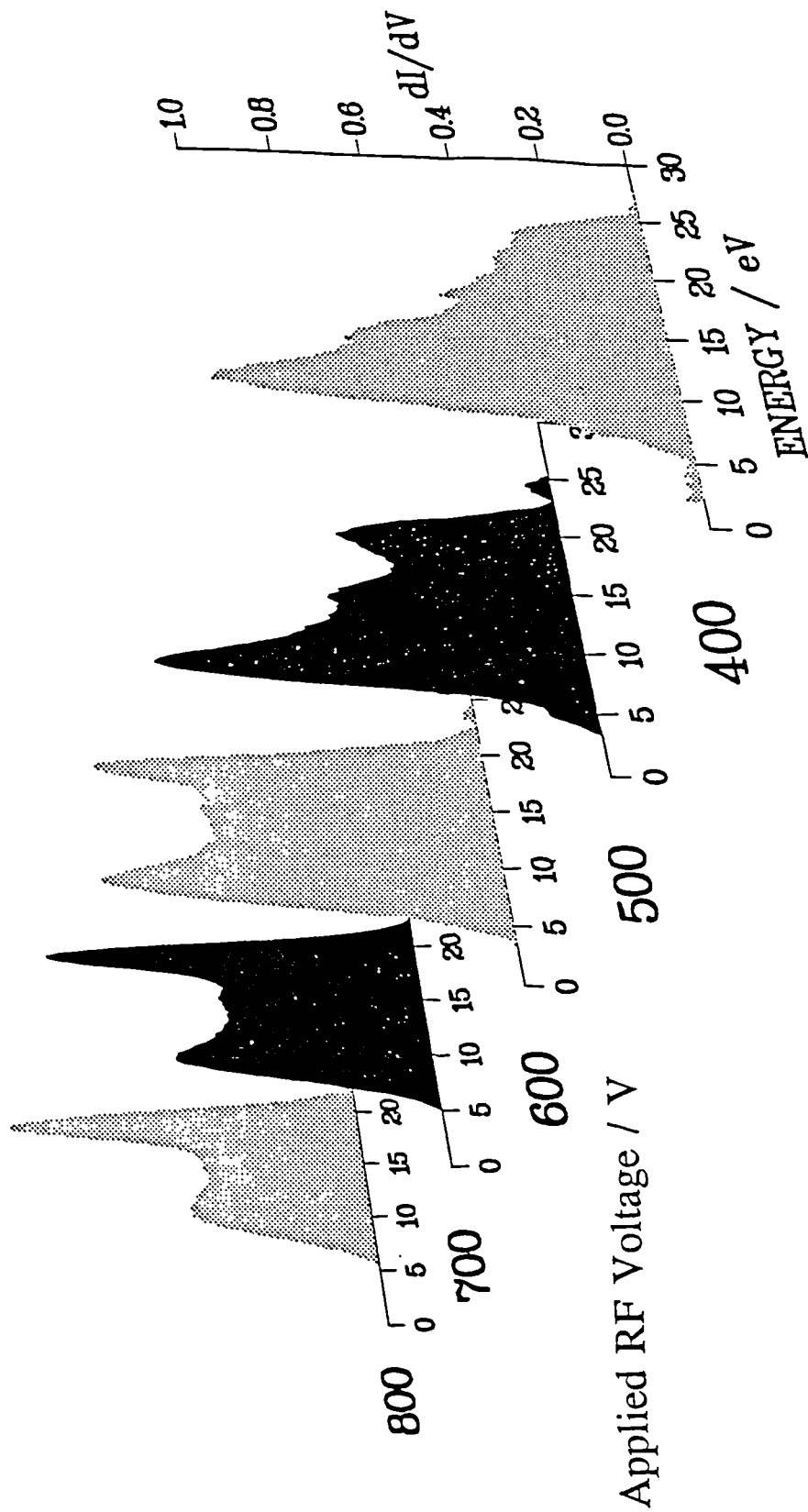
118

**Figure 3.14** Xenon IEDs measured at 7.5 mTorr for different applied RF voltages.
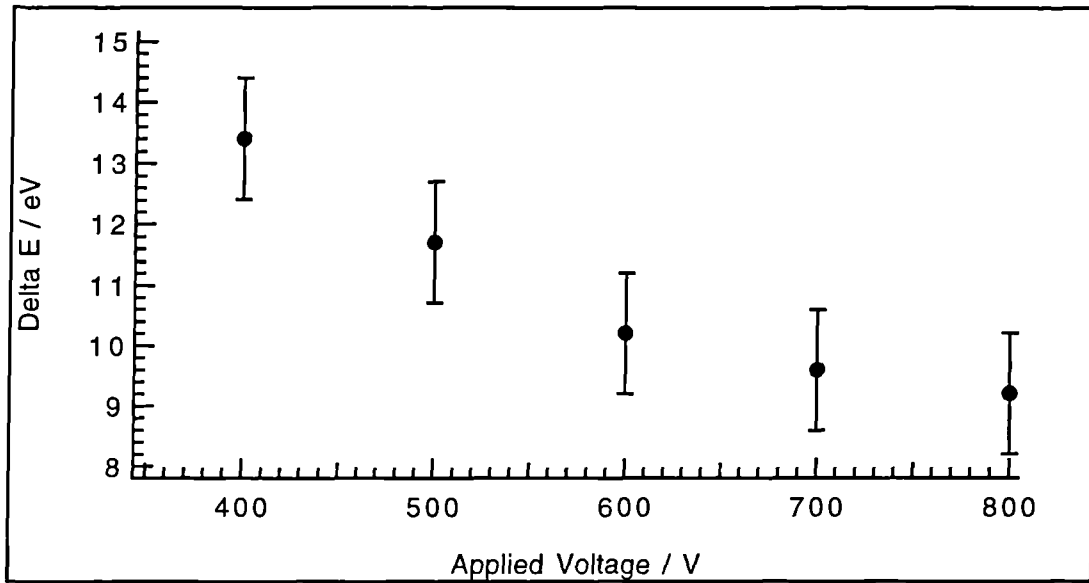
119

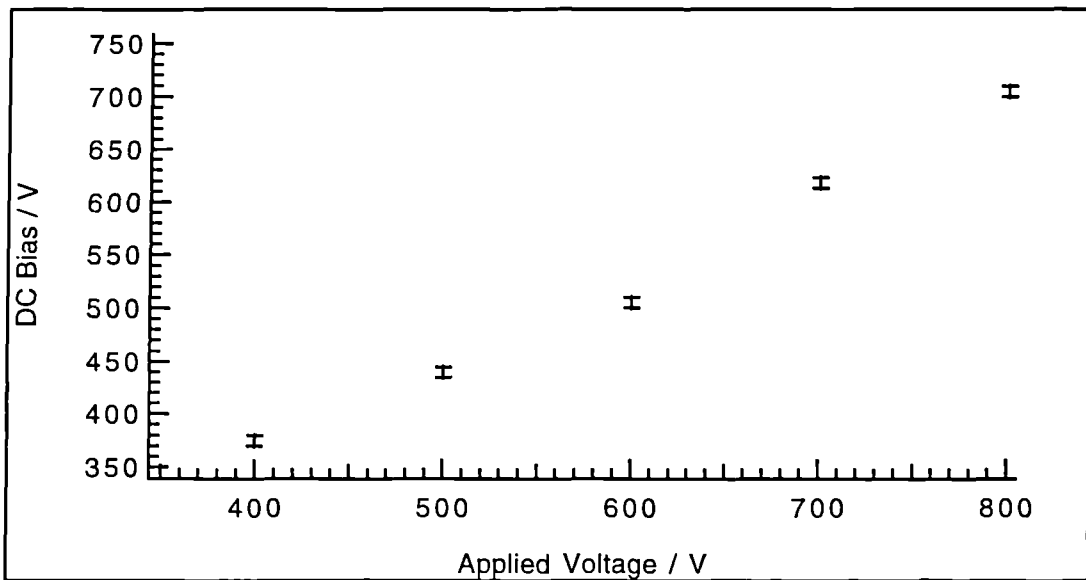**Figure 3.15** Distribution width versus applied RF voltage
for xenon IEDs in figure 3.14.



**Figure 3.16** DC bias versus applied RF voltage for each of the
xenon IEDs in figure 3.14.

We find the following:

| Discharge | Mass / amu | $\Delta E$ / eV |
|-----------|-----------|-----------------|
| He | 4 | 5.4 |
| Ar | 40 | 11.0 |
| Xe | 131 | 11.7 |

**Table 3.1** Splitting of peaks in the IEDs observed in helium, argon and xenon discharges when $V_0 = 500$ V.

Other workers have studied the effect of ion mass on the peak splitting in the IED. Coburn and Kay[31] have shown that $\Delta E$ is expected to be proportional to $M^{-1/2}$ where $M$ = ion mass. IEDs measured by them for $H_3^+$, $H_2O^+$ and $Eu^+$ are shown in figure 3.17. More recently Hope et al[43] have measured the dispersion of ions extracted from an $SiCl_4$ discharge during the etching of an indium containing gallium arsenide substrate. Their data is shown in figure 3.18. This clearly shows the dependence of $\Delta E$ on $M^{-1/2}$ as identified by Coburn and Kay. However both of these studies have measured different ions originating from the same discharge which therefore experience the same sheath potential and sheath thickness. For different discharges with similar external process parameters the sheath thicknesses and sheath potentials will almost certainly be different. Since the IED splittings observed in our data clearly do not obey the $M^{-1/2}$ dependence we conclude that the sheath potential and thickness must be different in each discharge.

Vallinga et al[33] have identified the parameters affecting the IED splitting (equation 1.13). This equation includes a term confirming the $M^{-1/2}$ dependence of the peak splitting. For the three IEDs under consideration in Table 3.1 many of the discharge parameters are identical and so Vallinga's equation reduces to:
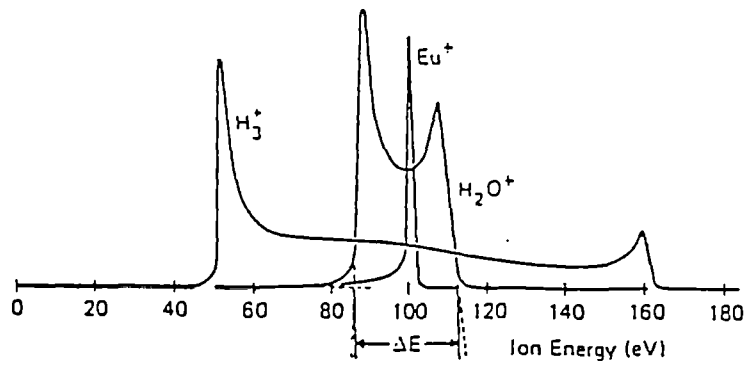
**Figure 3.17** $H_3^+$, $H_2O^+$ and $Eu^+$ IEDs measured from a 100 W, 75 mTorr discharge showing the different splitting for different mass ions. After Coburn and Kay .
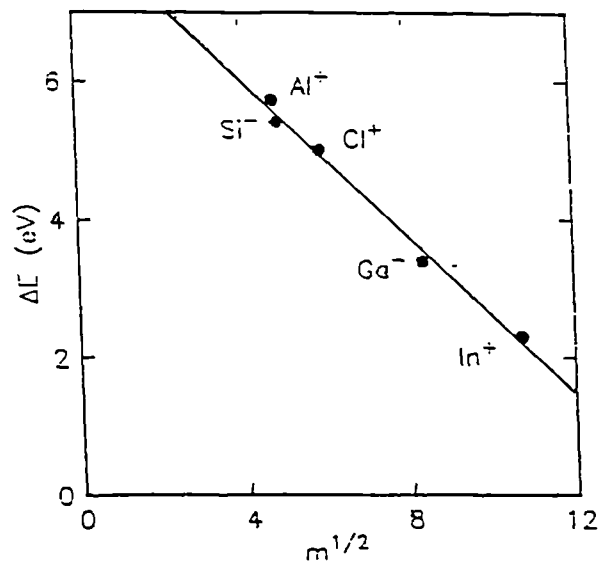


**Figure 3.18** Energy splittings of a variety of ions extracted from a SiCl$_4$ discharge during etching of a InGaAs layer. After Hope et al .

$$\Delta E = 8.35 \times 10^{-18} \frac{(V_{pe,max})^{3/2}}{l_{max}\sqrt{2\,m_i}} \qquad\qquad (3.2)$$

where $\Delta E$ = IED splitting / eV, $V_{pe,max}$ = maximum sheath potential / V, $l_{max}$ = maximum sheath thickness / m and $m_i$ = mass of ion / kg.

Using equation 1.11, based on the theory of Song et al[28], we can calculate values for $V_{pe,max}$ to use in equation 3.2. This requires an estimate for the electron temperature. We choose 2 eV as being a typical value for discharges of this type[37]. However, the exact value of the electron temperature is unimportant since its influence in the calculation of the sheath potentials is small. The experimental values required to calculate $V_{pe,max}$ are shown in Table 3.2, together with $V_{pe,max}$. The floating potential, $V_p^0$ is calculated using equation 1.4.

| Discharge | $V_0$ / V | $V_{dc}$ / V | $V_p^0$ / V | $A_e$ | $V_{pe,max}$ / V |
|-----------|-----------|--------------|-------------|-------|------------------|
| He        | 500       | -440         | -8.06       | 0.187 | 48.25            |
| Ar        | 500       | -436         | -10.36      | 0.205 | 50.05            |
| Xe        | 500       | -445         | -11.55      | 0.177 | 39.86            |

**Table 3.2** Calculated maximum sheath potentials and experimental parameters for 500 V He, Ar and Xe IEDs. $V_0$ = applied RF voltage, $V_{dc}$ = DC bias, $V_p^0$ = floating potential, $A_e$ = electrode area ratio and $V_{pe,max}$ = maximum sheath potential.

These calculated values can now be used in conjunction with equation 3.2 to derive estimates for the sheath thickness at the anode. We find that in the helium discharge the maximum sheath thickness is 4.5 mm, in argon the corresponding value is 0.7 mm while calculations for xenon yield a value of 0.3 mm. These values are consistent with observations of the sheath thickness being in the region of ~1 - 5

mm[67]. However, it is not clear why there should be such a thick sheath in the helium discharge in comparison to both the argon and xenon discharges. Clearly the results are correct or we would otherwise observe a large splitting in the helium IEDs. This difference is at present unresolved.

It should be noted that the IEDs we have chosen here are not strictly comparable due to small pressure differences between the discharges. Variations in pressure affect the value of the DC bias and consequently the calculated value of the maximum sheath potential. However, all the IEDs were measured at $14\pm7$ mTorr and so this effect is expected to be small.

### 3.2.5 Hydrogen IEDs

We now consider IEDs incident at the anode from a hydrogen plasma. Hydrogen is used in some commercial processes e.g. the $CH_4/H_2$ etching of indium phosphide and as such can be considered a 'real' process gas.

Figure 3.19 displays the IEDs measured for a hydrogen discharge at 20 mTorr where the applied RF voltage is varied from 200 V to 550 V. We find that at low voltages two peaks are present although at 200 V they appear to be unresolved. As the voltage is increased the peak separation decreases and the IED coalesces into a single peak. In figure 3.20 the distribution width for each IED at each applied RF voltage is shown. In the examination of IEDs in the previous sections it has been relatively easy to establish the positions of the peaks. Here, however, there is some ambiguity at applied voltages greater than 500 V due to the peaks merging. In order to overcome this we depart from the former method of measuring the $\Delta E$ from the positions of the peak centres. Instead we measure the entire distribution width at a point corresponding to one quarter of the maximum intensity of the IED. This is a far less satisfactory method than directly measuring the IED splitting but it does at least allow some observation of the effect of $V_0$ on the distribution width. In figure 3.21 we show the experimentally measured values of $V_{dc}$ at each value of $V_0$.

In figure 3.22 IEDs are shown, for $V_0 = 400$ V, and pressures up to 65 mTorr. At very low pressures the distribution is a single peak with only a slight indication of
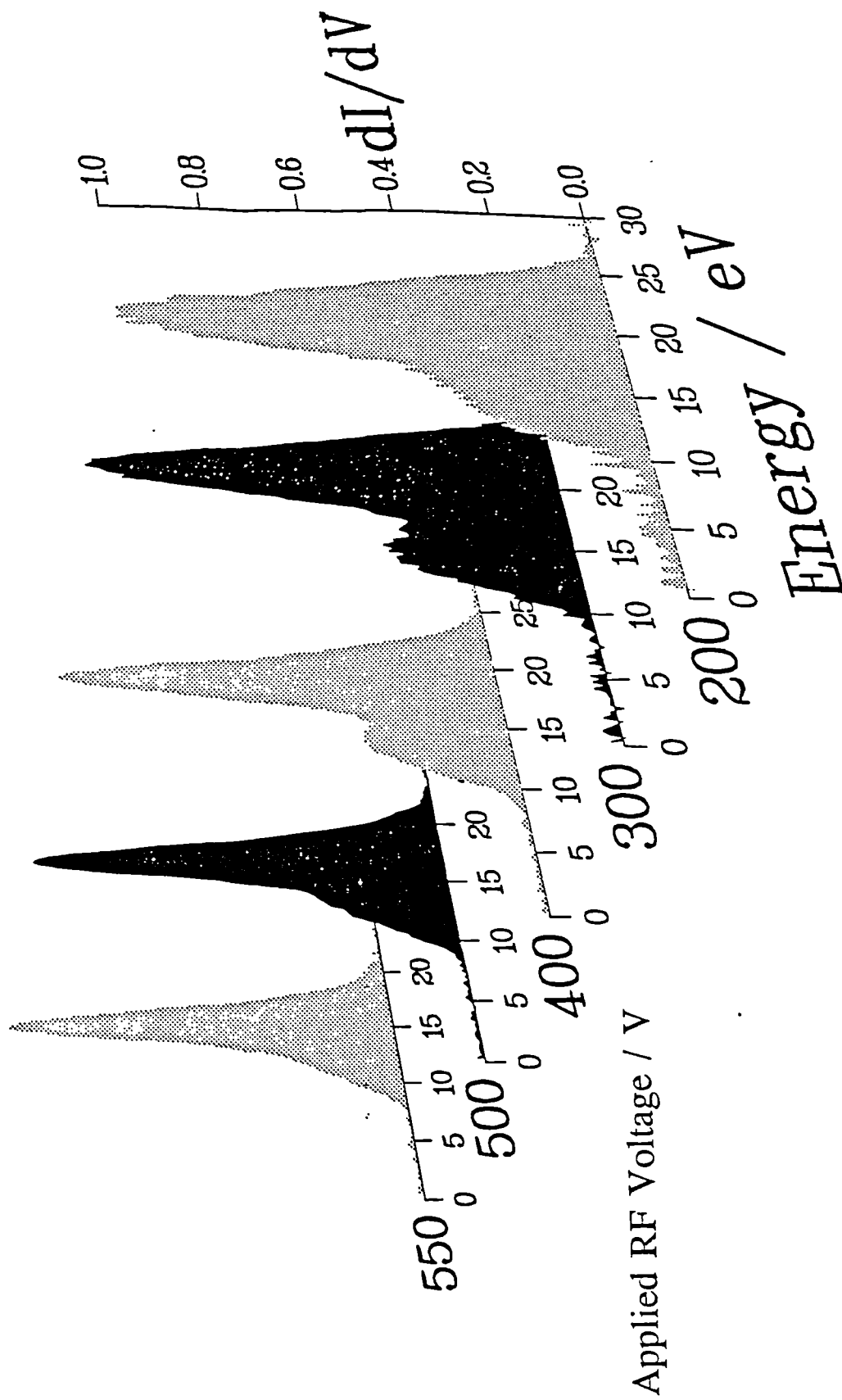
**Figure 3.19** Hydrogen IEDs measured at 20 mTorr for different applied RF voltages.
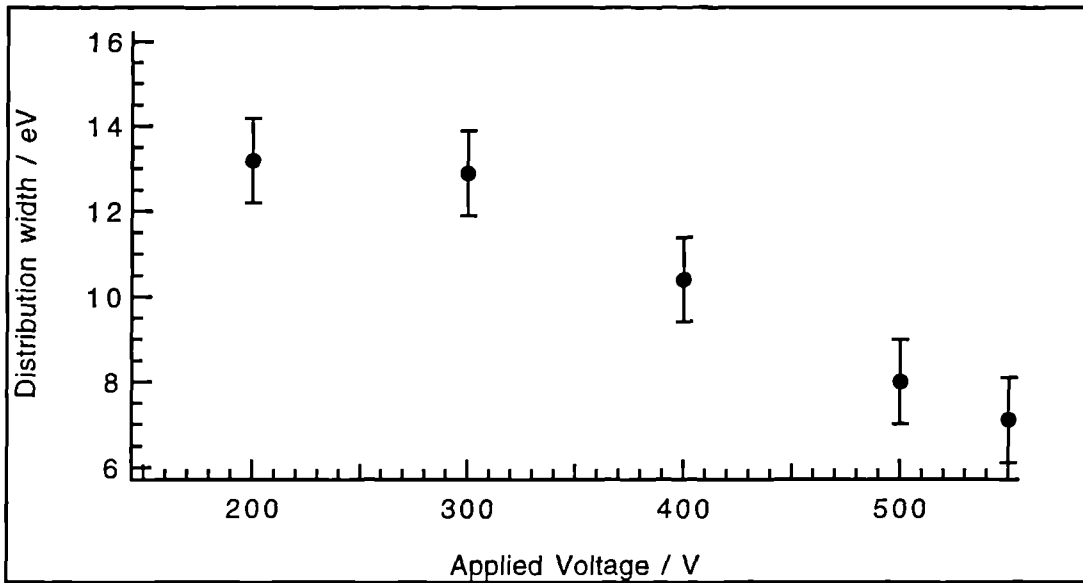
125

**Figure 3.20** Distribution width versus applied RF voltage for hydrogen IEDs in figure 3.19.
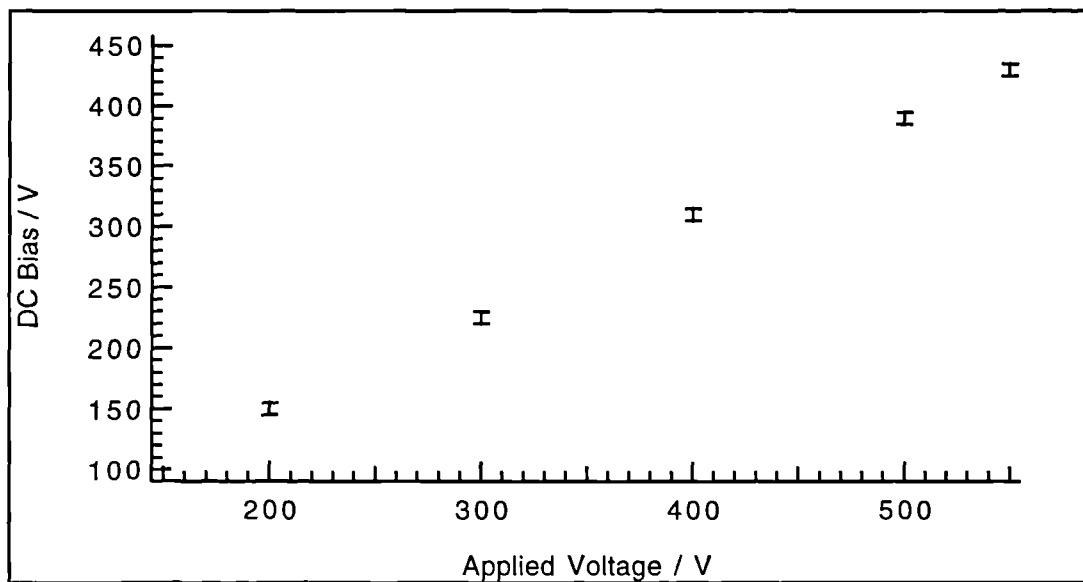


**Figure 3.21** DC bias versus applied RF voltage for each of the hydrogen IEDs in figure 3.19.

126

a second peak. As the pressure rises the distribution width increases and a second peak, at low energy, develops. At pressures above 27 mTorr the discrete nature of the second peak vanishes and the IED exhibits some smearing towards low energy. Additionally, at these higher pressures, the whole IED moves to lower energies. In figure 3.23 the distribution width at each discharge pressure is shown. We have again measured the width at the point corresponding to one quarter of the IED maximum intensity. We have omitted the two lowest pressure measurements from this figure since the intensity of the low energy peak is so diminished that it falls below the quarter intensity measurement point. Again, this method is less satisfactory than measuring directly the IED splitting from peak positions, but it does at least allow some measure of the distribution width. In figure 3.24 the measured values of $V_{dc}$ are shown at each pressure for which IED measurements were made.

In a hydrogen plasma the species that are expected to be present are $H^+$, $H_2^+$ and $H_3^+$. Due to water vapour there may also be some $H_2O^+$ present but this is expected to be negligible. The relative proportions of $H^+$, $H_2^+$ and $H_3^+$ in the discharge are unknown without further diagnostics e.g. mass spectrometry. We do not resolve peaks in the IED that are due to these individual species and so cannot gain any information on the proportions present by this means. Kuypers[107] measured IEDs for an $Ar/H_2$ mixture in a barrel etcher at 2 kW applied power. May's modelling of the distribution[30] showed that the relative proportions of $H^+$, $H_2^+$ and $H_3^+$ were 0.2 : 0.12 : 0.48 with the balance consisting of $Ar^+$. However in our etcher, with the absence of argon, these proportions are probably different.

Our interpretation of the data in these hydrogen IEDs is complicated by being unable to fully resolve the $\Delta E$ splitting, and thus the applicability of equation 1.13 is questionable. This equation only applies to the splitting of IEDs that originate from a collisionless sheath. However we are able to draw some general conclusions , partly by analogy to the helium IEDs in figures 3.8 and 3.11 which these hydrogen IEDs partially resemble.

In figure 3.19 we find that the distributions are RF modulated at low voltages. As the voltage rises the narrowing of the distribution is attributed to loss of this
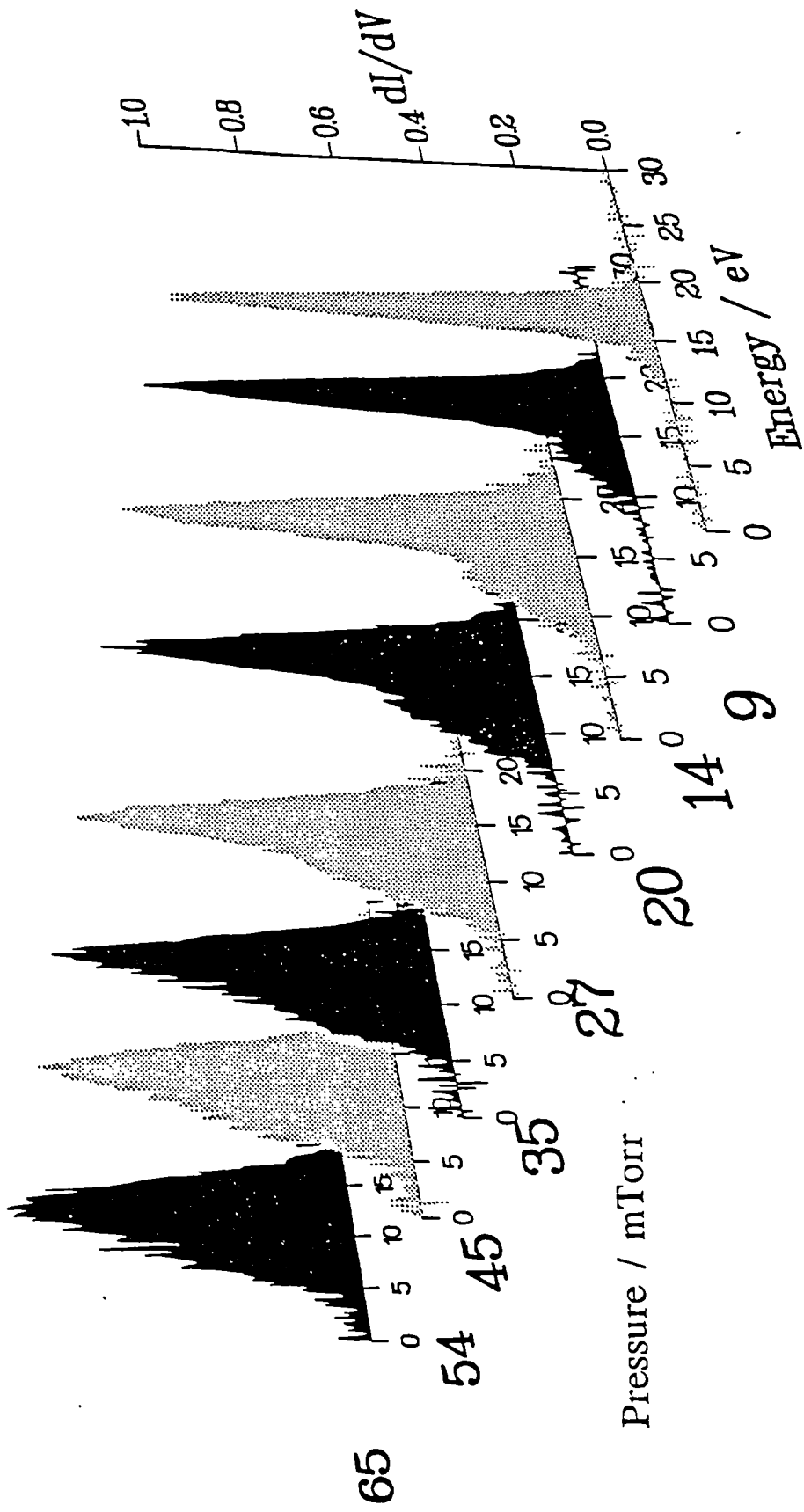
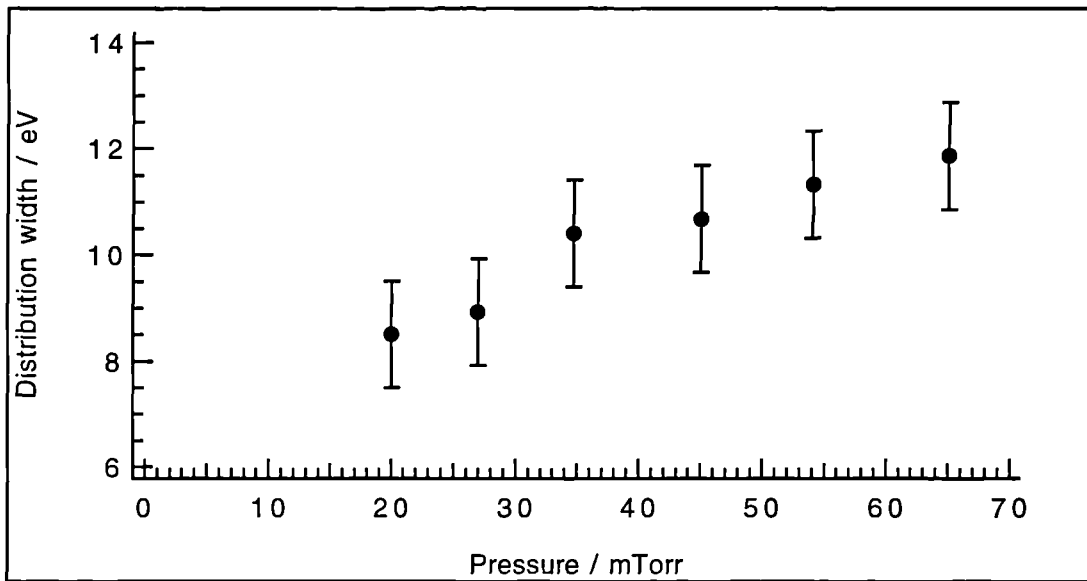**Figure 3.22** Hydrogen IEDs measured at $V_0 = 400$ V for different chamber pressures.

128

**Figure 3.23** Distribution width versus chamber pressure for hydrogen IEDs in figure 3.22.
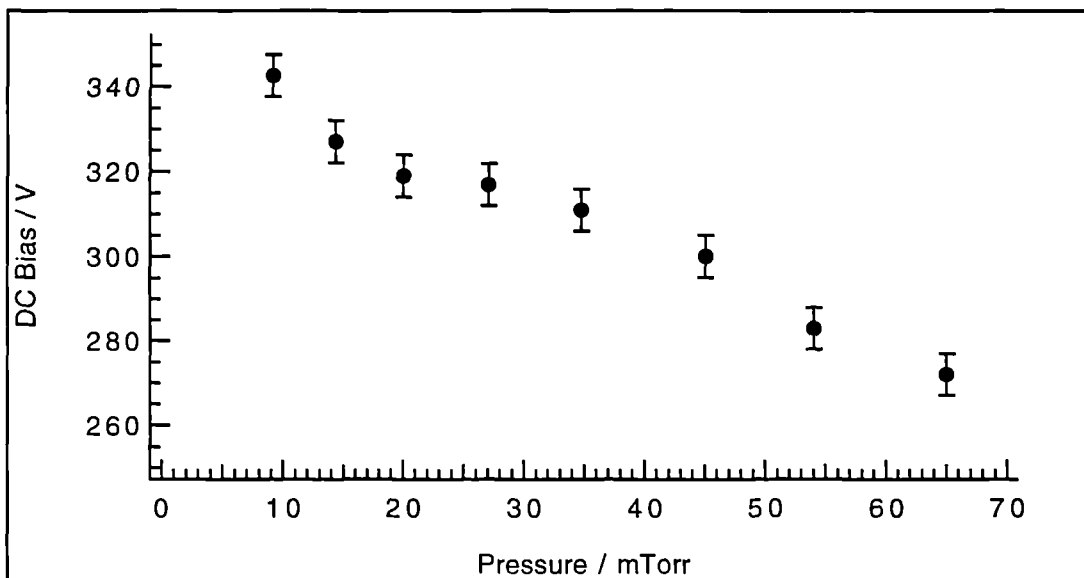


**Figure 3.24** DC bias versus chamber pressure for hydrogen IEDs in figure 3.22.

129

modulation and the IED reflects the time averaged sheath potential. In common with our previous observations we suggest this is due to an increase in the sheath thickness. At high voltages there is still some suggestion of RF modulation due to the low energy shoulder on the IED, although the analyser does not resolve the peak.

In figure 3.22 the distributions are also interpreted in terms of the RF modulation argument previously presented. At low pressures we observe a narrow distribution which, as the pressure rises, broadens. Comparison with He IEDs suggests that this is due to the sheath thickness decreasing and the onset of RF modulation broadening occurring. However, if we simply consider these hydrogen IEDs by themselves this argument is harder to sustain. The IEDs become smeared towards lower energies, due undoubtedly to collisions, and this masks the low energy peak of the IED. We cannot then resolve the splitting of the IED due to the RF modulation effect.

### 3.2.6 Nitrogen IEDs

Figure 3.25 displays IEDs from a 15 mTorr nitrogen discharge where the applied RF voltage has been varied from 400 V through to 700 V. The distribution is found to contract with increasing voltage and a high energy peak is observed to develop, forming a saddle shaped structure. In figure 3.26 the peak splitting, $\Delta E$, is plotted against $V_0$. The splitting for the 400 V IED has not been included since it is not possible to be certain of the high energy peak position due to its low intensity. Figure 3.27 shows the measured values of $V_{dc}$ plotted against $V_0$.

Figure 3.28 shows IEDs for nitrogen discharges at pressures of 8.0 mTorr to 30 mTorr where $V_0$ is kept constant at 500 V. The distribution is found to be narrow at low pressures and to broaden as the pressure rises, with a consequent increase in the maximum observed ion energy. Additionally, the peak intensities are seen to interchange as the low energy peak develops with increasing pressure. The distribution passes through the familiar saddle shaped form at a pressure of 16 mTorr. Figure 3.29 shows the distribution width plotted against pressure. We have only included the first four IEDs from figure 3.28 in this since it is not possible to fully discern the high
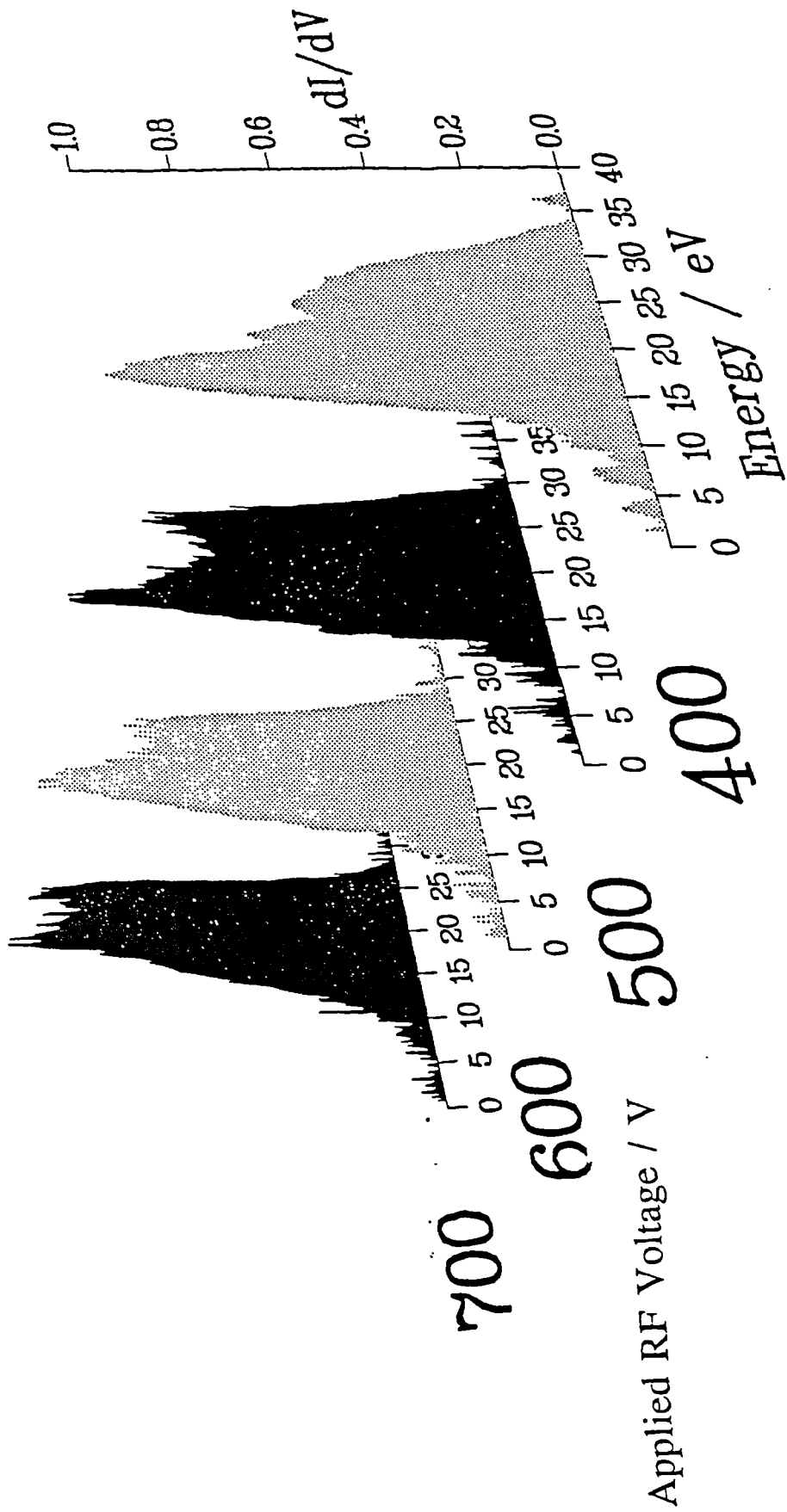
**Figure 3.25** Nitrogen IEDs measured at 15 mTorr for different applied RF voltages.

131
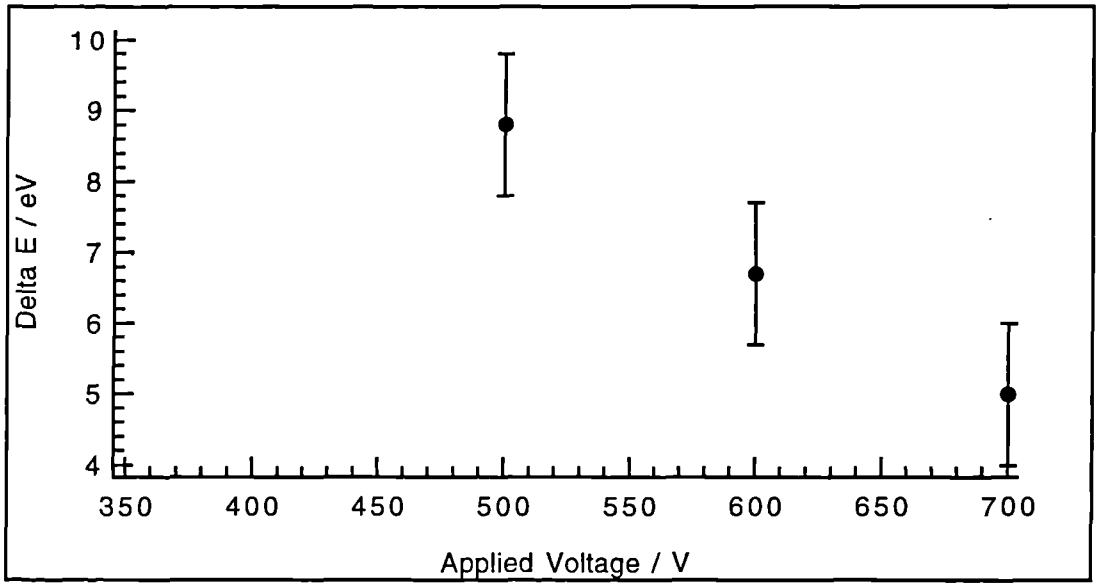
**Figure 3.26** Distribution width versus applied RF voltage for nitrogen IEDs in figure 3.25.



**Figure 3.27**DC bias versus applied RF voltage for each of the nitrogen IEDs in figure 3.25.

132

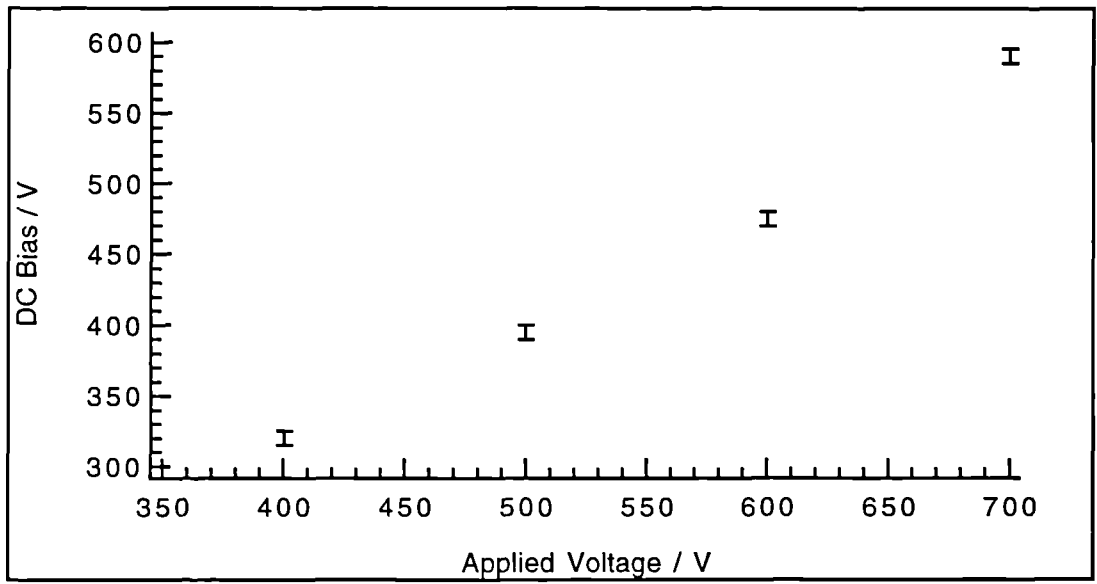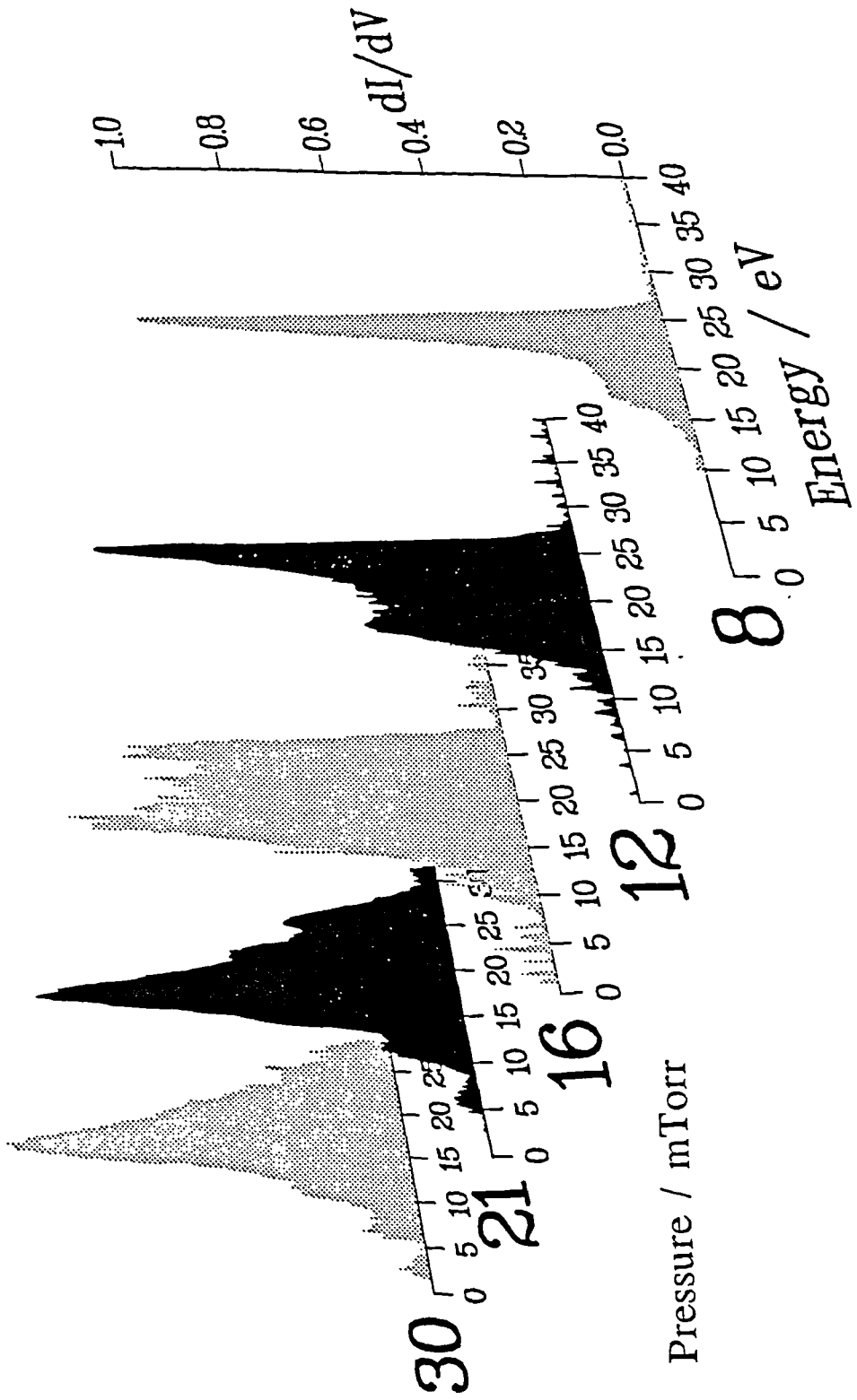**Figure 3.28** Nitrogen IEDs measured at $V_0 = 500$ V for different chamber pressures.
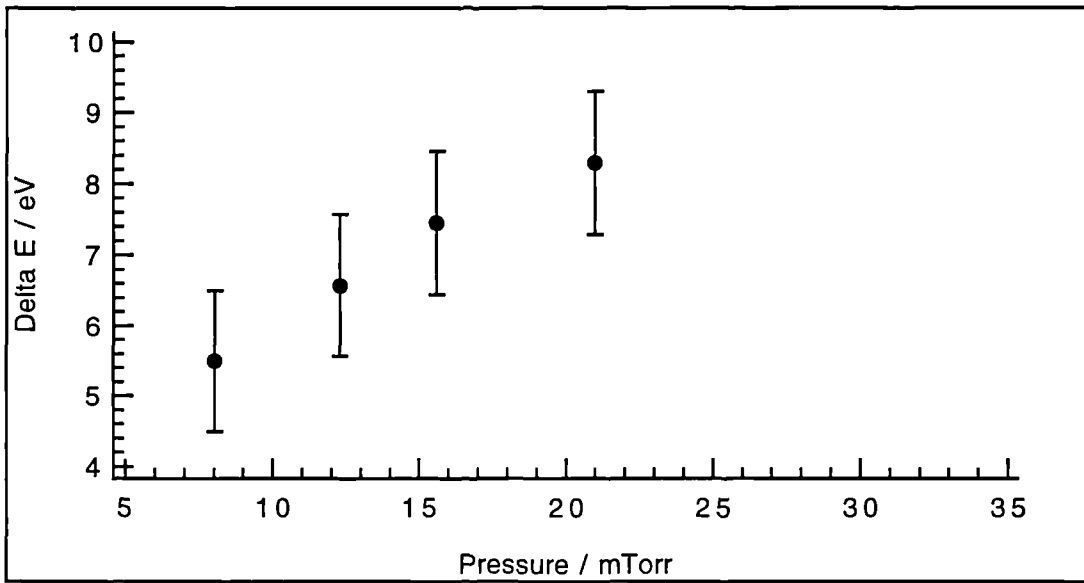
**Figure 3.29** Distribution width versus chamber pressure for nitrogen IEDs in figure 3.28.
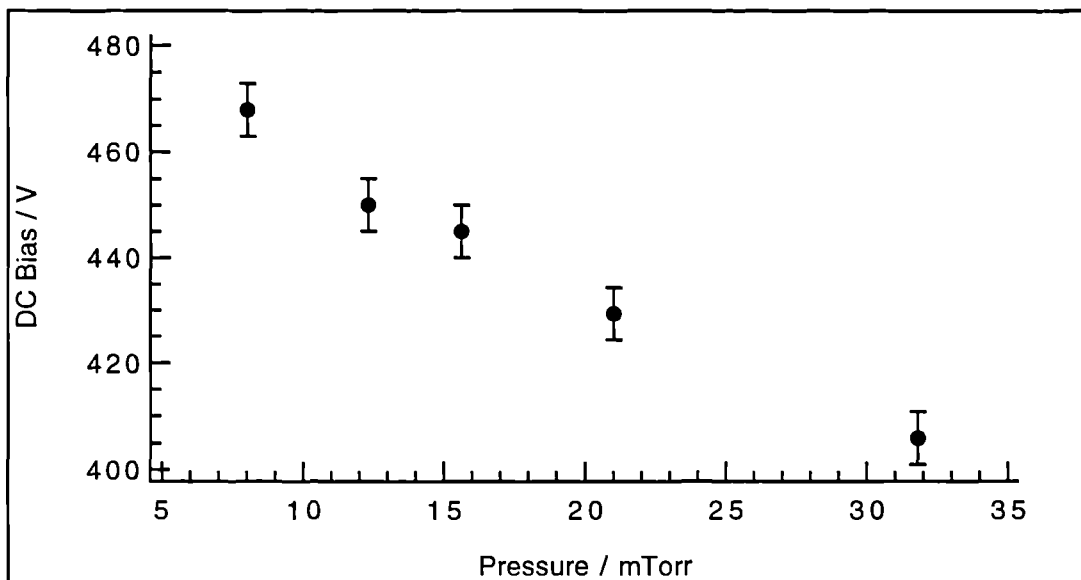


**Figure 3.30** DC bias versus chamber pressure for the nitrogen IEDs in figure 3.28.

energy peak position at 30 mTorr. In figure 3.30 the measured values of the DC bias are plotted against the discharge pressure.

Mass spectrometry of 13.56 MHz nitrogen discharges[59] shows that $N^+$, $N_2^+$ and $N_3^+$ ions are present. However, the proportion of $N_2^+$ has been shown to be greater than 90% of the discharge. Thus, it is this ion that will predominate in the IED and will obscure any contribution due to the other species.

The trends observed in these IEDs as the experimental conditions are varied are the same as has been previously observed in argon IEDs. We therefore conclude that the same mechanism operates as been described in preceding sections, i.e. a change in the degree of RF modulation also occurs in the nitrogen discharge.

Snijkers[59], in his study of nitrogen and argon IEDs, concludes that the sheath thickness in the nitrogen discharge is thicker, for ostensibly the same discharge conditions, than in the argon case. We can show that this is also the case in our reactor. Equation 3.2 shows that the IED splitting is expected to depend only on the sheath potential, the sheath thickness and ion mass. If we consider the nitrogen IED at a pressure of 12 mTorr and $V_0 = 500$ V we find that the measured DC bias is -450 V. This yields a maximum sheath potential (equation 1.11) of 56.1 V. The comparable argon IED, at 11 mTorr and 500 V, has a DC bias of -433 V. This leads to a maximum sheath potential of 73.78 V. Insertion of these values into equation 3.2 shows that:

$$l_{max}(N_2) = k.2.08 \times 10^{14}$$

while

$$l_{max}(Ar) = k.1.44 \times 10^{14}$$

where k = constant.

Thus, we conclude that the sheath thickness in the nitrogen discharge is $\sim$ 1.5 times thicker than in the argon discharge. This is in agreement with the conclusion of Snijkers.

## 3.2.7 Carbon Dioxide IEDs

Figure 3.31 displays IEDs measured from a $CO_2$ discharge, at 15 mTorr, for applied RF voltages of 500 V to 800 V. We find a double peaked distribution that narrows as the voltage increases. The heights of the peaks in the IED are observed to change their relative intensity with the high energy peak being most intense at high voltages while the low energy peak dominates at low voltages. In figure 3.32 the distribution width is plotted for each value of $V_0$. As was the case with the hydrogen IEDs discrete peaks in the IED are difficult to discern. To quantify the narrowing of the distribution we have chosen to measure the IED width at the half maximum point in this case. Figure 3.33 displays the measured DC bias at each value of $V_0$.

IEDs are presented in figure 3.34 from a $CO_2$ discharge at pressures up to 29 mTorr. The applied voltage is 600 V in each case. We observe that the distribution broadens with increasing pressure with a consequent increase in the maximum ion energy in the IED. The relative peak intensities once again depend strongly on the discharge conditions with the low energy peak dominating at high pressures while the high energy peak is most intense at low pressures. The distribution is found to broaden quite significantly as the pressure rises. However it is not a simple matter to measure the distribution width since the exact peak positions cannot be established. Neither can we measure the half maximum value (or indeed the quarter maximum) for all the distributions due to the large variation in the peak intensities. Instead, to demonstrate the expansion of the IED at these pressures we choose to plot, in figure 3.35, the maximum ion energy for each pressure. In figure 3.36 the value of the DC bias is also plotted for each pressure.

In a $CO_2$ discharge there are likely to be many different ionic species present that will reach the RFA. Mass spectrometry studies of RF discharges have not been found in the literature. However, studies of microwave discharges[114] indicate that the ions we can expect to find in a discharge are $CO_2^+$, $CO^+$, $C^+$, $O_2^+$, and $O^-$ although the proportions of $C^+$ and $O^-$ are small. The fact that the IED does not properly resolve into the familiar saddle shaped structure is consistent with the presence of several ions of different mass with each individual IED overlaid on each other.
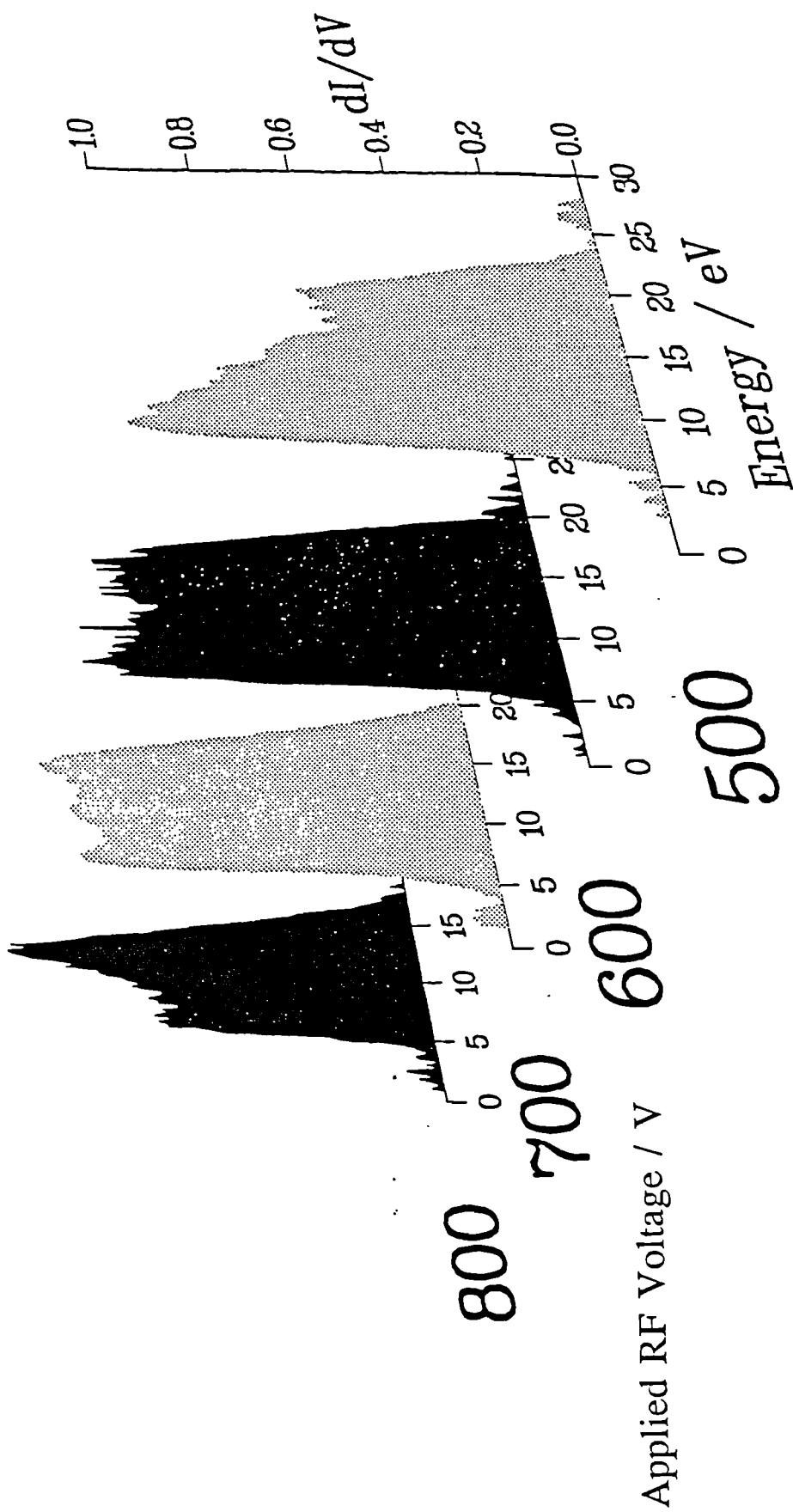
**Figure 3.31** Carbon dioxide IEDs measured at 15 mTorr for different applied RF voltages.
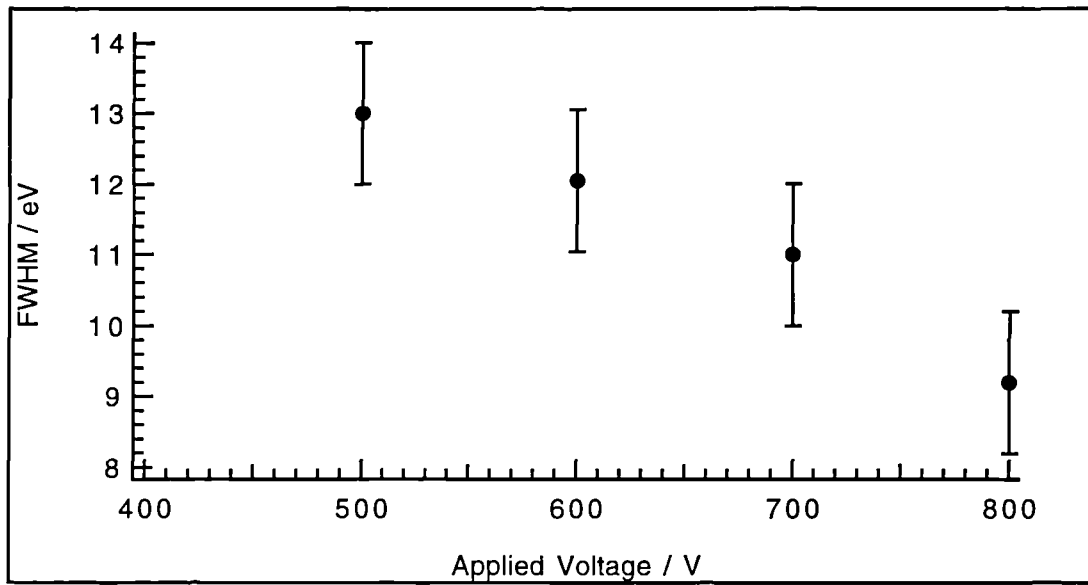
**Figure 3.32** Distribution width versus applied RF voltage for carbon dioxide IEDs in figure 3.31.



**Figure 3.33** DC bias versus applied RF voltage for each of the carbon dioxide IEDs in figure 3.31.
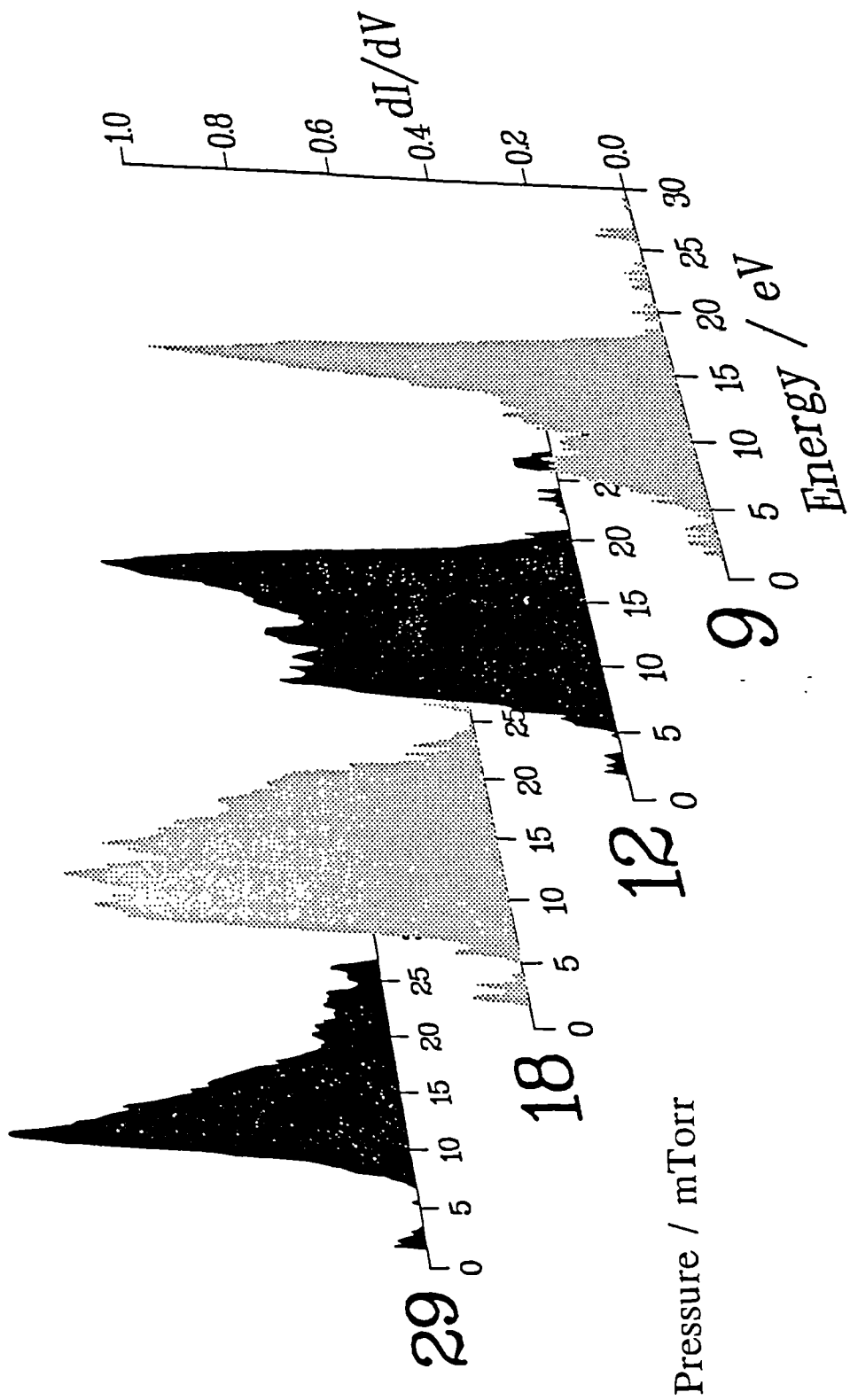
**Figure 3.34** Carbon dioxide IEDs measured at $V_0 = 600$ V for different chamber pressures.
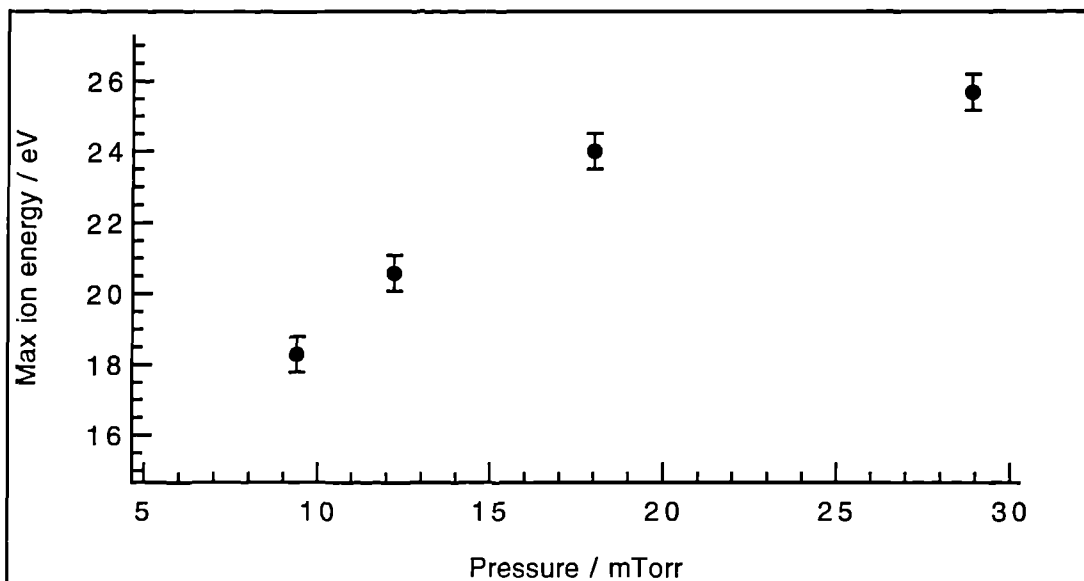
**Figure 3.35** Maximum ion energy versus chamber pressure for carbon dioxide IEDs in figure 3.34.
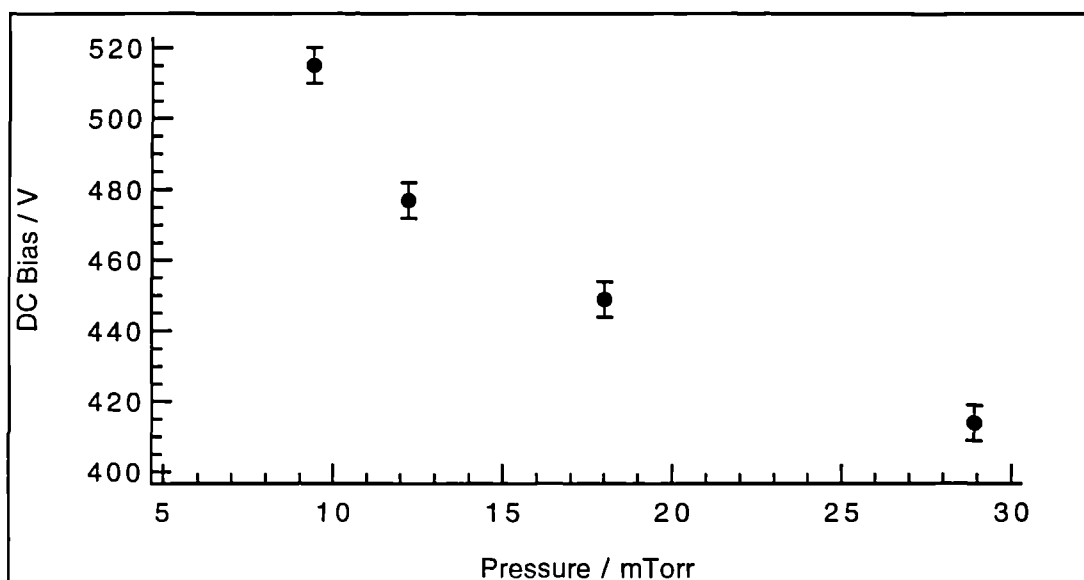


**Figure 3.36** DC bias versus chamber pressure for the carbon dioxide IEDs in figure 3.34.

The mechanism operating in this $CO_2$ discharge is, we believe, identical to that found previously (see section 3.2.1). Changes in the RF modulation of the IED causes a variation in the peak intensities and distribution widths.

## 3.2.8 Electronegative Gas Discharges.

We turn now to IEDs for plasmas where there are negative ions present. The first such discharge we consider is that of $CF_4$ / 8%$O_2$. As noted in section 1.5.2 this is not a truly electronegative gas since the proportion of negative ions formed does not reach the magnitude of that in, say, a $CCl_4$ plasma. There are, however, likely to be some negative ions present. $CF_4$ / 8%$O_2$ is a frequently used gas mixture in commercial etch processes. The function of the fluorine containing species is to etch the substrate while the presence of oxygen prevents the build up of carbonaceous deposits on the surface.

The ions we expect to be present in the discharge include $CF_n^+$ (n = 0 → 3), $O_2^+$, $O^+$, $O^-$, $CF_3^-$, $F^-$ as well as variously fluorinated $C_2$ species. The $CF_4$ / 8%$O_2$ discharge environment is therefore very complex and the concentrations of species that are present are interdependent. Chatfield has produced a reaction scheme for such a discharge[34]. His results show that the main species in the plasma is $CF_4$ and so we expect that $CF_n^+$ (n = 1 to 3) will make up the majority of ions reaching the surface. However this is only an assumption based on Chatfield's results where sampling from the bulk plasma was undertaken. Kuypers[107] measured IEDs at the cathode of a reactor and resolved separate peaks due to $CF_n$ (n = 1 → 3) as well as small amounts of C, F and also O due to a leak in his chamber. Despite the unintentional presence of oxygen in this experiment Kuypers did not observe any other species in the IED. We therefore conclude that the IEDs we present in the following section are due only to $CF_n$ where n = 1 → 3 with other species being negligible.

Figure 3.37 shows IEDs from a $CF_4$ / 8%$O_2$ plasma at 10 mTorr where the applied RF voltage has been varied from 300 V to 700 V. The IED is found to change very little in shape as the voltage is increased with the only effect being the high energy peak becoming relatively more intense. The position of this peak is found to

**Figure 3.37** IEDs measured at 10 mTorr from a carbon tetrafluoride / 8% oxygen discharge for different applied RF voltages.
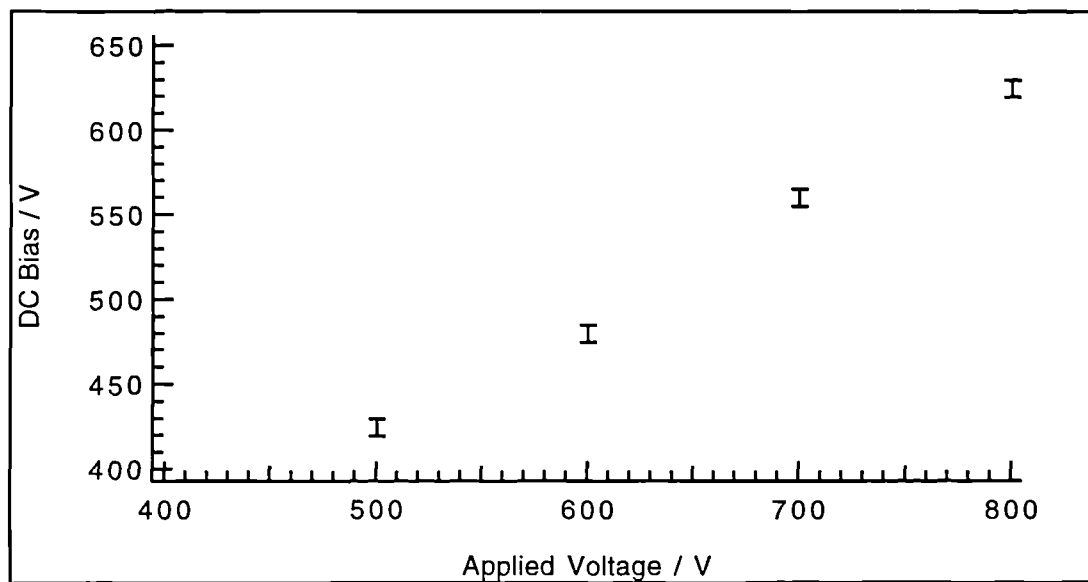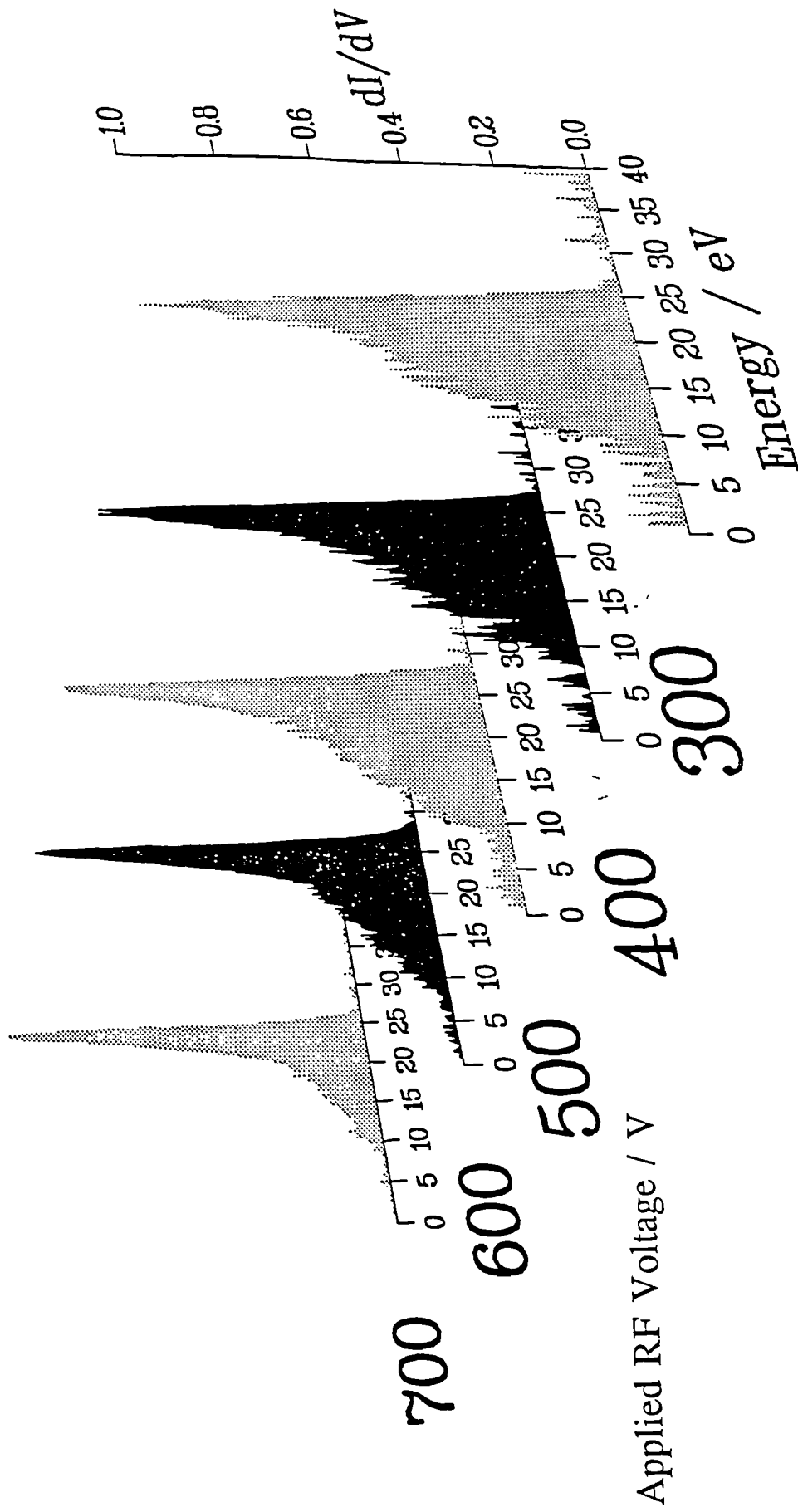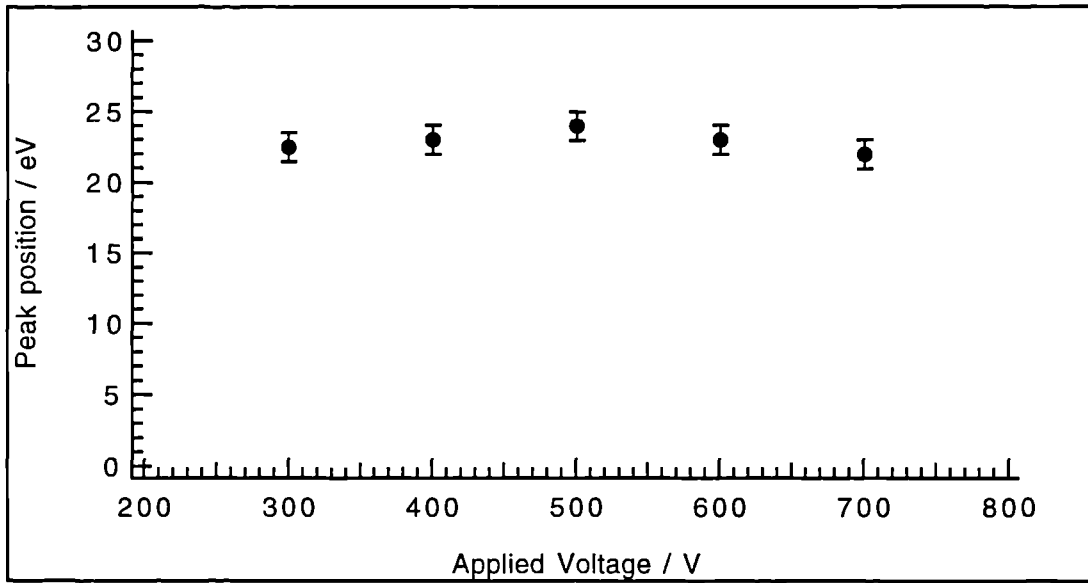
**Figure 3.38** Peak position versus applied RF voltage
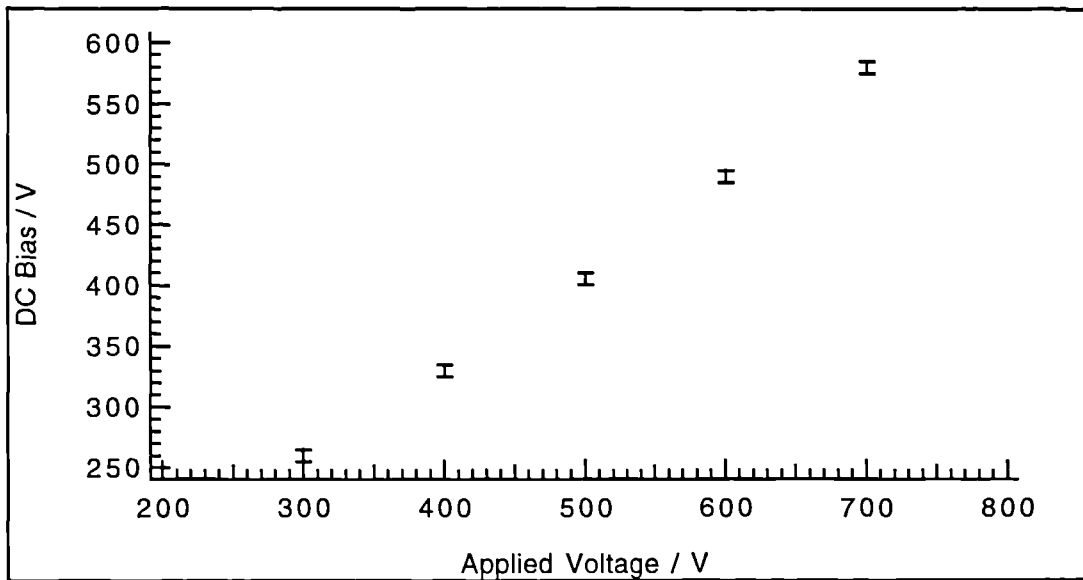for CF4/8% O2 IEDs in figure 3.37



**Figure 3.39** DC bias versus applied RF voltage for each of the
CF4/8%O2 IEDs in figure 3.37.

143

be almost constant at $23 \pm 1$ eV, with no trend with voltage change being discernible. This is shown in figure 3.38. The behaviour of these IEDs is in contrast to that found in an more electropositive plasma e.g. the argon IEDs in figure 3.1. It was found there that the distribution contracted with increasing voltage and the peak intensities varied considerably. Neither of these effects is observed in the $CF_4$ / 8%$O_2$ discharge. Janes[77] has measured mass resolved IEDs at the cathode for a $CF_4$ plasma at 10 mTorr. For a varying DC bias from -250 to -350 V little change in the IED shape or position was observed. Our results for the anode are in agreement with this. The DC bias value measured in each case is shown in figure 3.39.

Figure 3.40 shows IEDs from an $SF_6$ discharge for varying applied voltages from 150 V to 350 V. $SF_6$ has been used as a process gas for dry etch procedures chiefly because it is an excellent source of reactive F atoms. It offers high selectivity of Si to $SiO_2$ etching together with a good Si etch rate. Additionally, no carbonaceous deposits are formed on the surface as can occur with, for example, $CF_4$ / 8%$O_2$. The main neutral molecules occurring in this discharge are $SF_6$, $SF_4$ and $F_2$. These give rise to, mainly, $SF_3^+$, $SF_5^+$, $SF_3^-$, $SF_5^-$ ions in the discharge. Small amounts of $F^-$ and $S_2F_7^-$ are also found.[115]

Figure 3.40 shows that the $SF_6$ IEDs, in common with $CF_4$ / 8%$O_2$, do not exhibit any pronounced change in peak intensities as was observed with more electropositive plasmas. However, we do find that the $SF_6$ IEDs shift to higher energies as the voltage increases. To illustrate this the position of the high energy peak for each IED is plotted in figure 3.41. The width of the distribution is not found to alter significantly as the discharge conditions vary. In figure 3.42 the DC bias measured for each IED is plotted.

$SF_6$ discharges are highly electronegative with an electron attachment cross section $\sim 100$ times that of $CF_4$ [12]. The consequence of this is that the number of electrons present in the plasma is much reduced and there is a significant presence of negative ions. The plasma appears relatively dim due to a decrease in electron excitation. The sheath thickness is also expected to be thinner[116]. These effects are also expected to occur in a $CF_4$ plasma, although to a lesser extent.
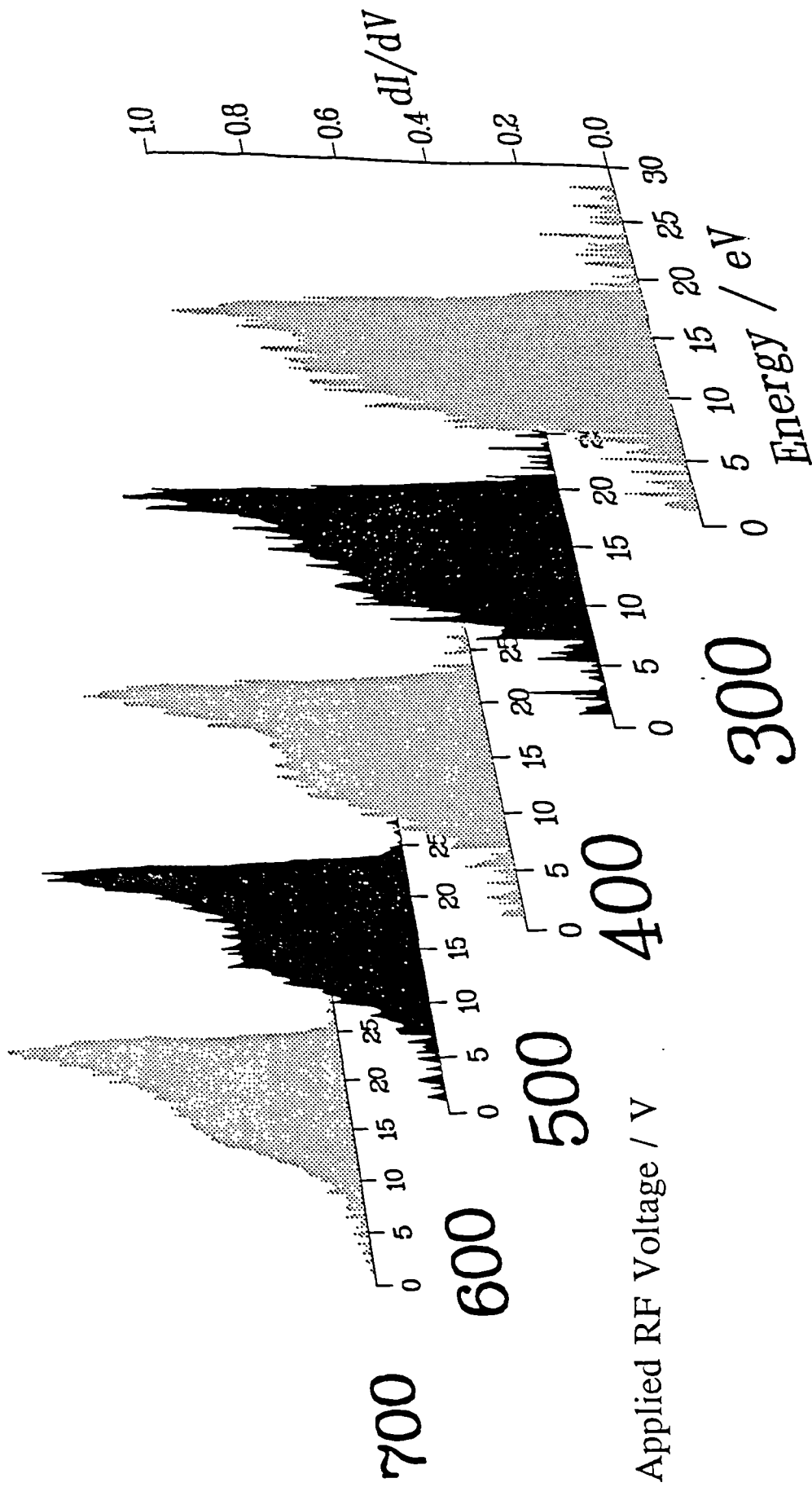
**Figure 3.40** IEDs measured at at 10 mTorr from a sulphur hexafluoride discharge for different applied RF voltages.
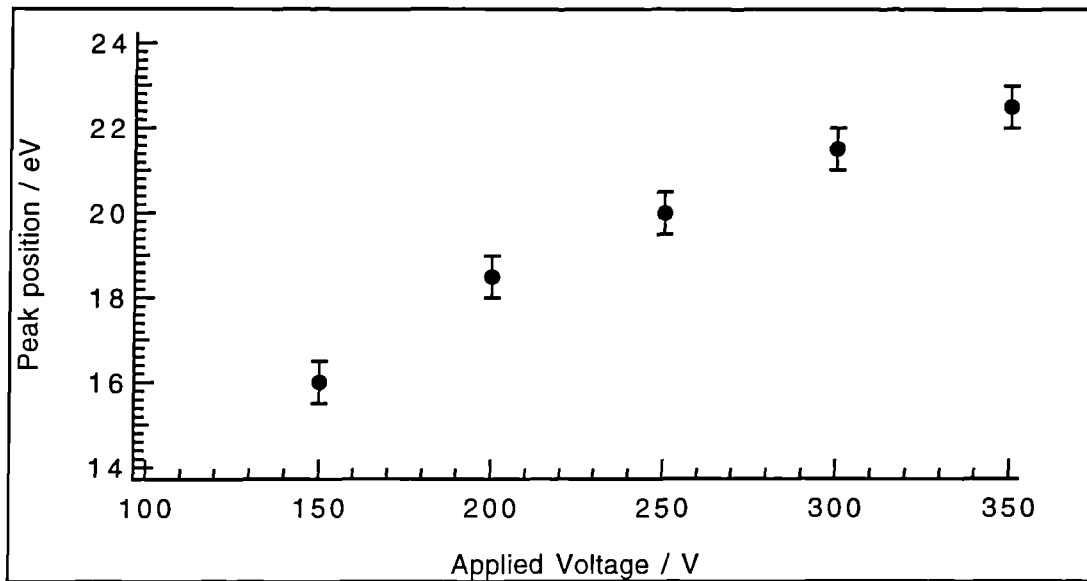
145

**Figure 3.41** Peak position versus applied RF voltage for SF6 IEDs in figure 3.40.
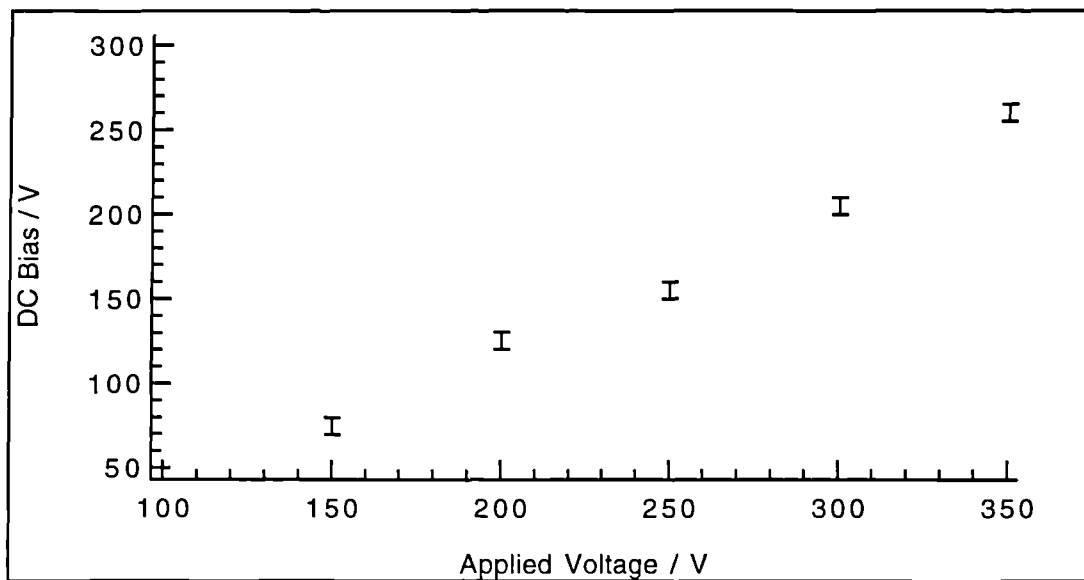


**Figure 3.42** DC bias versus applied RF voltage for each of the SF6 IEDs in figure 3.40.

There is a fundamental difference observed between the IEDs from electropositive and electronegative plasmas in that the peak intensities are evidently not strongly dependent on discharge conditions in electronegative plasmas. It is not certain why this should be so. A possible reason lies in the extent that the sheath thickness depends on discharge conditions in each case. The sheath thickness is one of the parameters that affects how long an ion takes to cross the sheath (the ion transit time) - see section 1.4.8. This in turn affects the relative peak heights. The sheath thickness scales with Debye length:[117,118]

$$\lambda_D = \left( \frac{\epsilon_0 \, T_e}{n \, e^2} \right)^{\frac{1}{2}} \qquad (3.3)$$

where $\epsilon_0$ = permittivity of free space, $T_e$ = electron temperature / eV, n = charge density in the plasma.

Thompson et al[71] state that electronegative plasmas are expected to better confined, i.e. not spread away from between the electrodes, than is the case with electropositive plasmas. Presumably the reason for this lies in the reduced numbers of highly mobile electrons present in the plasma. Our highly asymmetric 'top-hat' design of reactor, with a large spacing between the electrodes, is not well designed for confining plasmas. Let us now consider what happens to the Debye length, and therefore sheath thickness, in confined and unconfined discharges. In an unconfined (or ill-confined) discharge, e.g. Ar, as the power to the plasma is increased, $T_e$ will rise; this is due to the increase in the fields in the plasma from which electrons gain their energy. There should, therefore, be a concomitant increase in sheath thickness. However n - the charge density - may also be expected to increase with power due to the increased ionization of the gas. If, however, the plasma simultaneously becomes less confined this may mean that n does not increase or that n increases only weakly. In a confined (or better confined) discharge, however, $T_e$ will increase with power, as will the charge density which will offset the effect of $T_e$ on the sheath thickness to some extent. This may then explain why the sheath thickness may vary with voltage

in an electropositive discharge but not in an electronegative one.

It should be noted however that the time varying form of the sheath potential is also important in determining peak heights - as our modelling in the following chapter shows - since this too can influence how much of the sheath potential an ion experiences. Electronegative discharges have been shown to form double layers of charge in the sheath region[116]. Here layers of positive and negative charge density exist adjacent to one another. These effects have only been observed in low frequency plasmas (50 kHz) and are expected to be difficult to form above ~ 3 MHz. However, there are clearly some very different effects occurring in electronegative plasmas that are not observed in electropositive discharges. We should not therefore discount the possibility that the differences we observe in the IEDs are due to some modification of the sheath field.

We conclude this section with the presentation of two IEDs measured for chlorine containing discharges. Figure 3.43 shows an IED measured from an 8 mTorr $CCl_4$ plasma where the applied voltage was 200 V. The measured DC bias in this experiment was only -8 V; this is an indication of the exceptional electronegativity of this gas. Figure 3.44 shows an IED from a $CFCl_3$ discharge at 10 mTorr where the applied voltage was 500 V. The corresponding DC bias was -410 V. There has been no extensive measurement of IEDs from either of these discharges containing chlorine. The tendency of the RFA grids to become corroded caused the measurement of IEDs in these gases to be exceptionally problematic.

## 3.2.9 Effect Of Area Ratio

We now consider the effect on IEDs of altering the effective area ratio, i.e. the area of the cathode to the anode. This can be simply accomplished in the 'Minstrel' reactor since the cathode plate is bolted on to the pedestal to which the power is supplied. The cathode plate can be replaced with a larger one thereby altering the effective area ratio. Two larger cathode plates were made; their sizes have been detailed in Table 2.1. They were made such that their areas are two and three times the area of the standard plate that was used for the rest of the experiments. In the
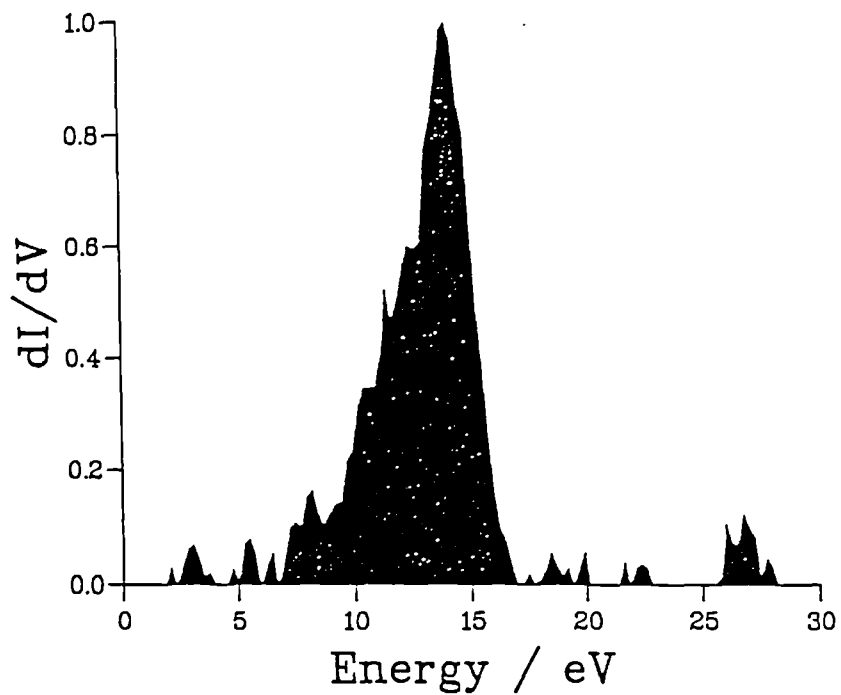
**Figure 3.43** Carbon tetrachloride IED measured at $V_0$ = 200 V with a chamber pressure of 8 mTorr.
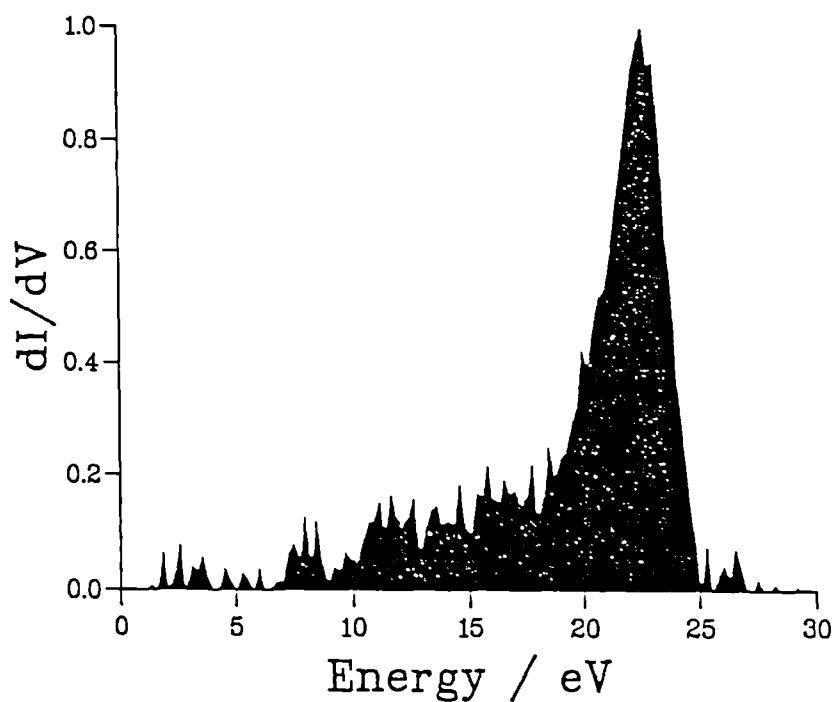


**Figure 3.44** $CFCl_3$ IED measured at $V_0$ = 500 V with a chamber pressure of 10 mTorr.

149

following discussion each different sized cathode will be referred to as $A = 1$, $A = 2$ or $A = 3$.

Theory predicts that the effect of increasing the area ratio should cause the DC bias to decrease, i.e. become less negative. Equation 1.5 demonstrates this: in the limit where the areas of anode and cathode are equal and $A_e = 1$, and the equation yields $V_{dc} = 0$. In this case the form of $V_0$ in figure 1.10 would be symmetrical about the t axis. The effect of increasing the area ratio is to make the anode electrically more like the cathode. The sheath potential at the anode increases while at the cathode it decreases - as demonstrated by equations 1.9 and 1.11.

To study the effect of area ratio variation we have measured IEDs for varying applied voltages and for varying discharge pressures. We have restricted these measurements to argon discharges only. The results for the case of $A = 1$ have already been presented in figures 3.1 and 3.4 for varying voltage and pressure respectively. In figures 3.45 and 3.46 IEDs for varying voltage and pressure are presented for $A = 2$. The experimental conditions in this case are the same as for the $A = 1$ results. The discharge pressure was held at 10 mTorr when the voltage was varied. The applied voltage was adjusted to a constant 500 V when the pressure was varied. Similarly, figures 3.47 and 3.48 show Ar IEDs for the same conditions but with $A = 3$.

Figures 3.49 to 3.54 show various discharge parameters and IED measurements for all the different areas. Figure 3.49 and 3.50 show the effect on the DC bias of varying voltage and pressure respectively when different sized cathodes are used. Both of these figures confirm that the DC bias is indeed less where the cathode area is larger. The relative change in DC bias as the pressure increases for each different area is approximately the same. As the applied voltage is changed the relative increase in DC bias is similar for $A = 1$ and $A = 2$. Where $A = 3$ it is found that the DC bias does not increase as rapidly.

The effective area ratio for each discharge, calculated using equation 1.5 and using $V_0$ and $V_{dc}$ from experiment, is plotted in figures 3.51 and 3.52 for varying voltage and pressure respectively. In the pressure data the relative change in area ratio
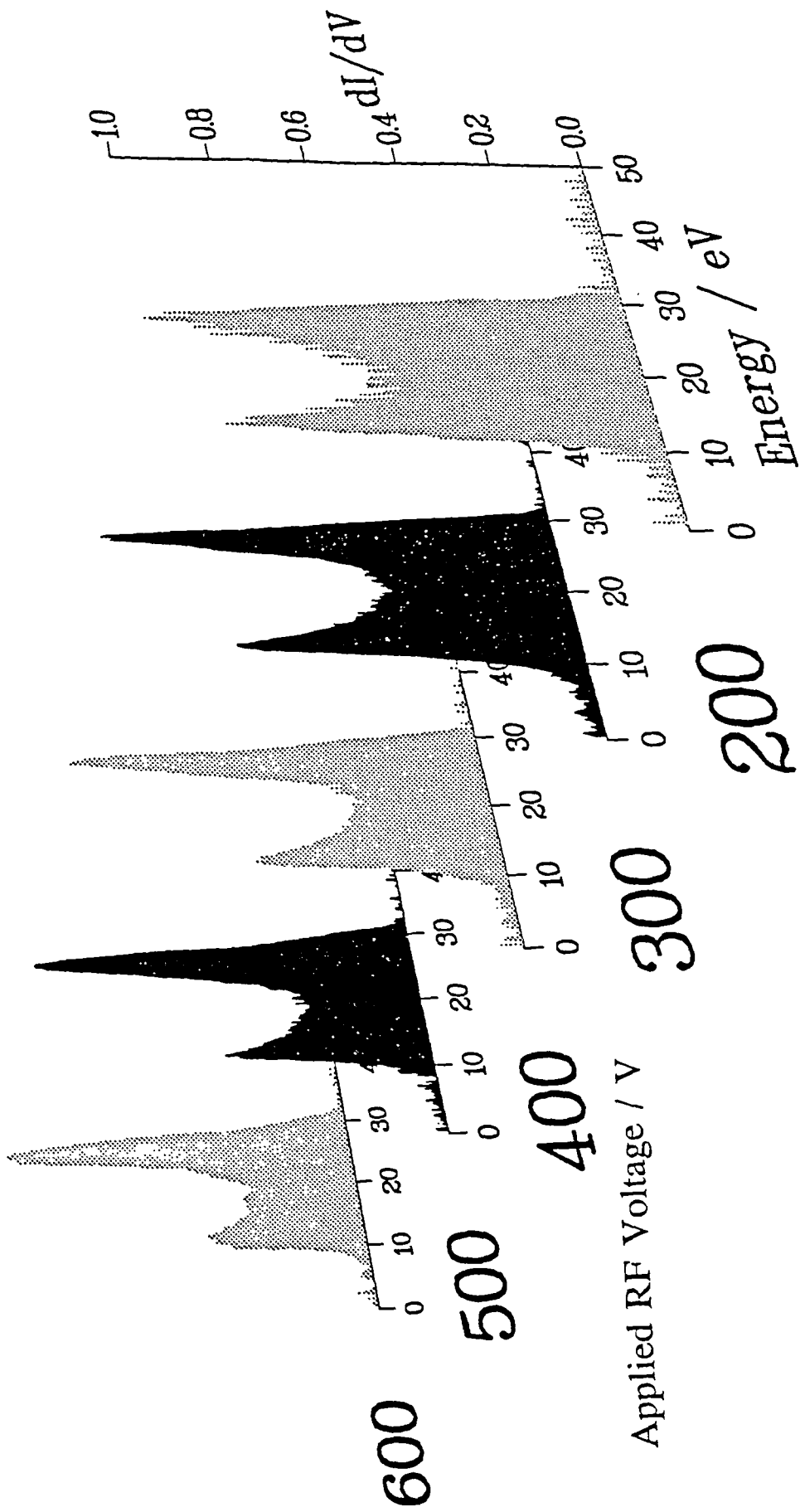
**Figure 3.45** Argon IEDs measured at 10 mTorr for different applied RF voltages. Cathode area was twice that used in obtaining the corresponding IEDs in figure 3.1.

151
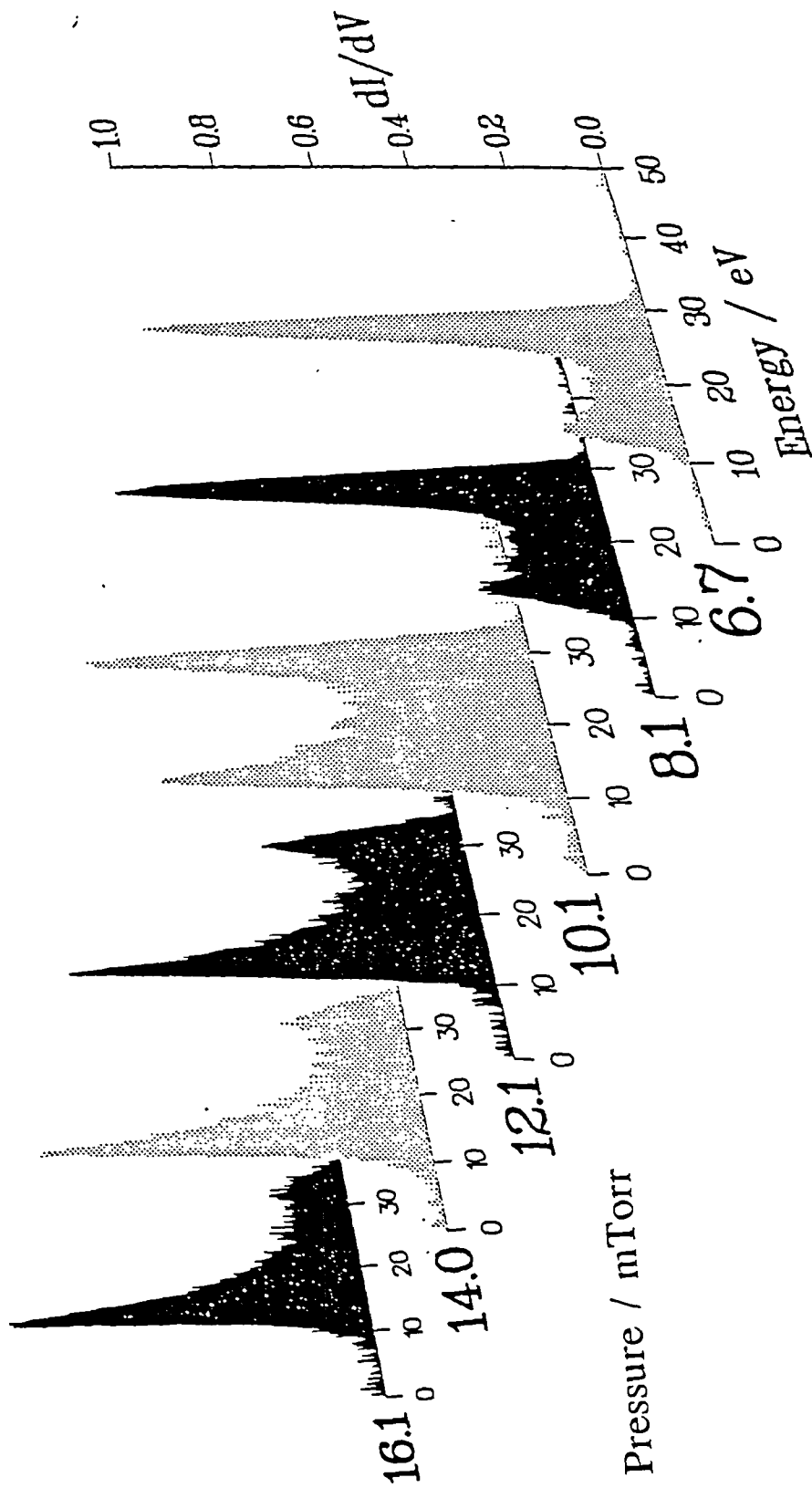
**Figure 3.46** Argon IEDs measured at $V_o = 500$ V for different chamber pressures. Cathode area was twice that used in obtaining the corresponding IEDs in figure 3.4.

152
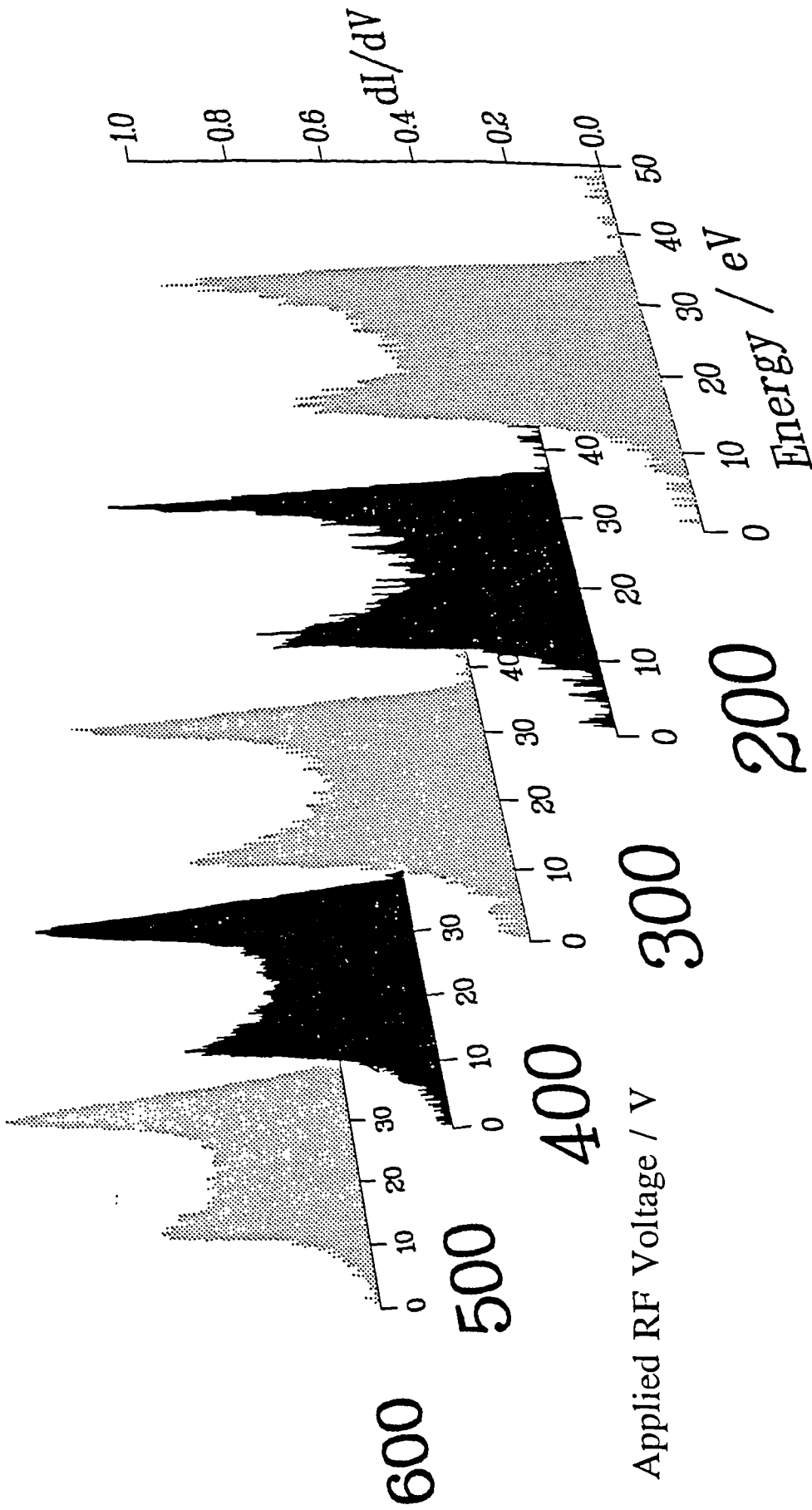
**Figure 3.47** Argon IEDs measured at 10 mTorr for different applied RF voltages. Cathode area was three times that used in obtaining the corresponding IEDs in figure 3.1.
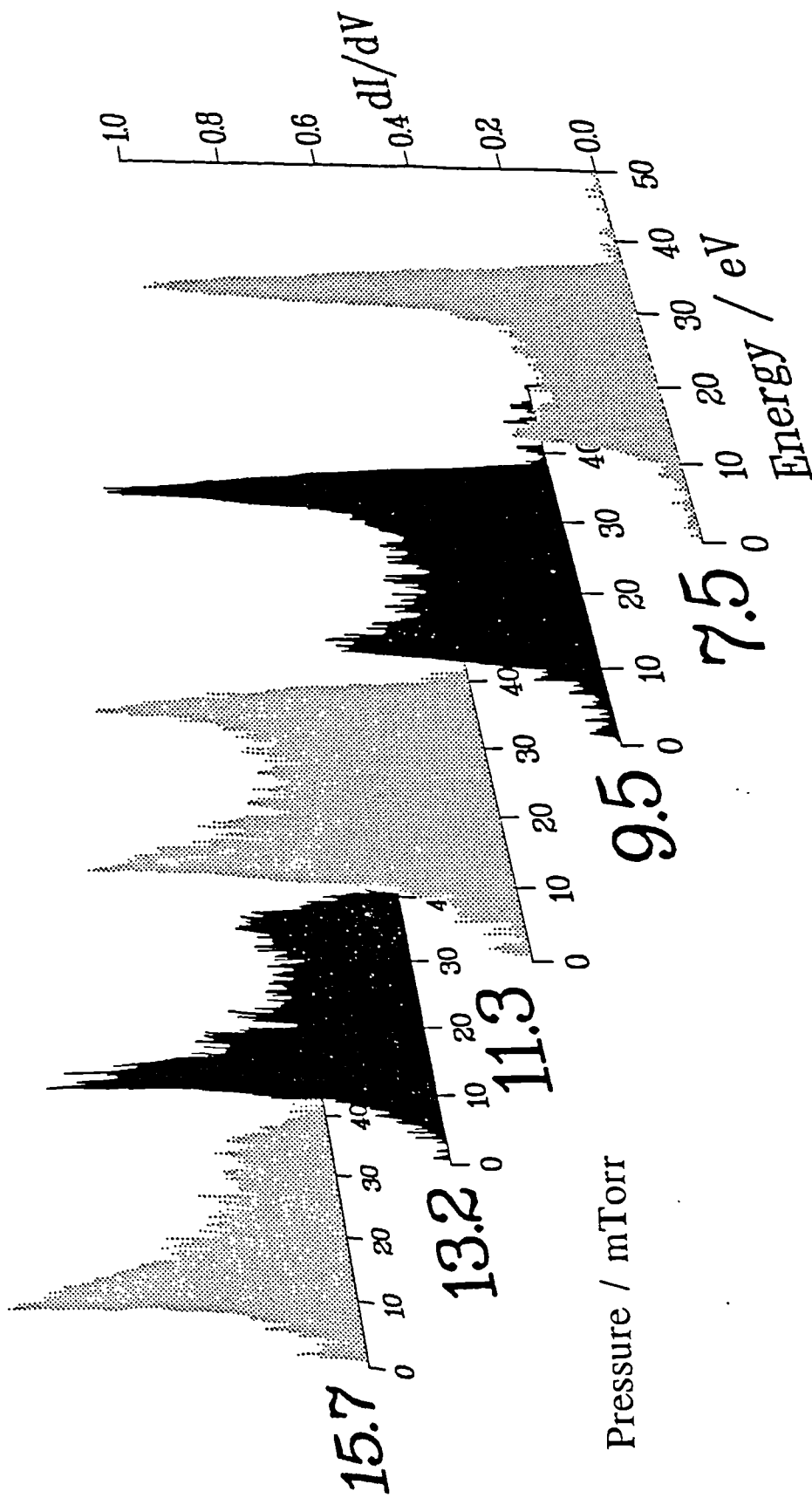
**Figure 3.48** Argon IEDs measured at $V_0 = 500$ V for different chamber pressures. Cathode area was three times that used in obtaining the corresponding IEDs in figure 3.4.

154
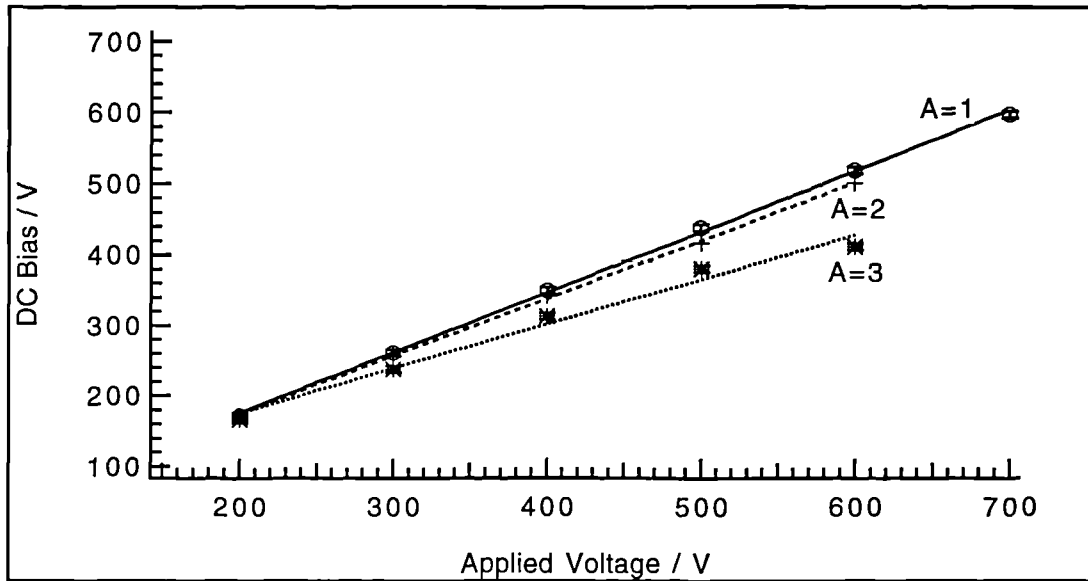
**Figure 3.49** DC Bias versus applied RF voltage for argon IEDs in figures 3.1, 3.45 and 3.47. Straight lines are drawn to draw attention to the trends with different sized electrodes.
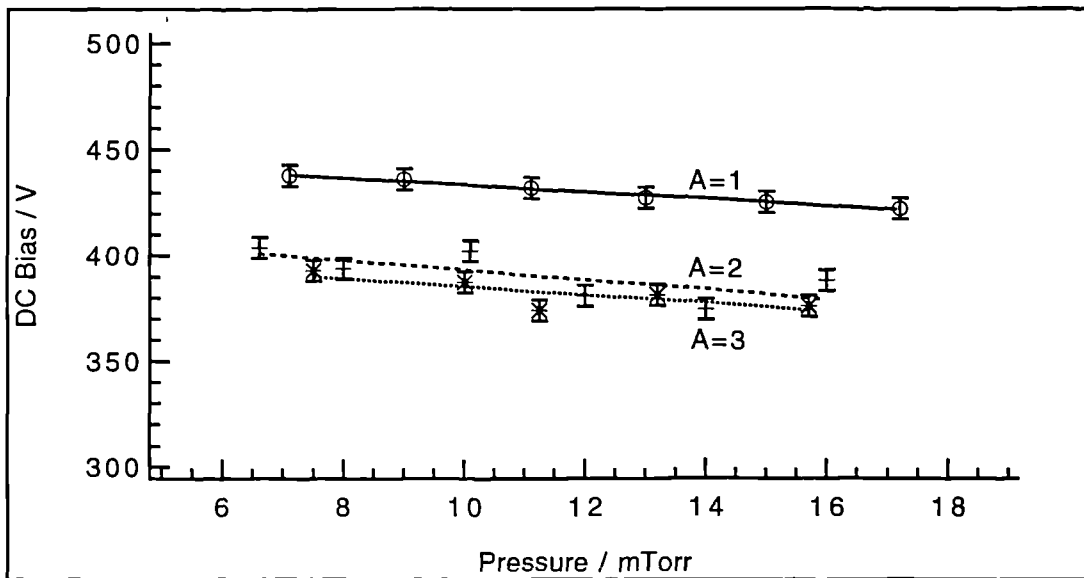


**Figure 3.50** DC bias versus chamber pressure for the argon IEDs in figures 3.4, 3.46 and 3.48. Straight lines are drawn to draw attention to the trends with different sized electrodes.
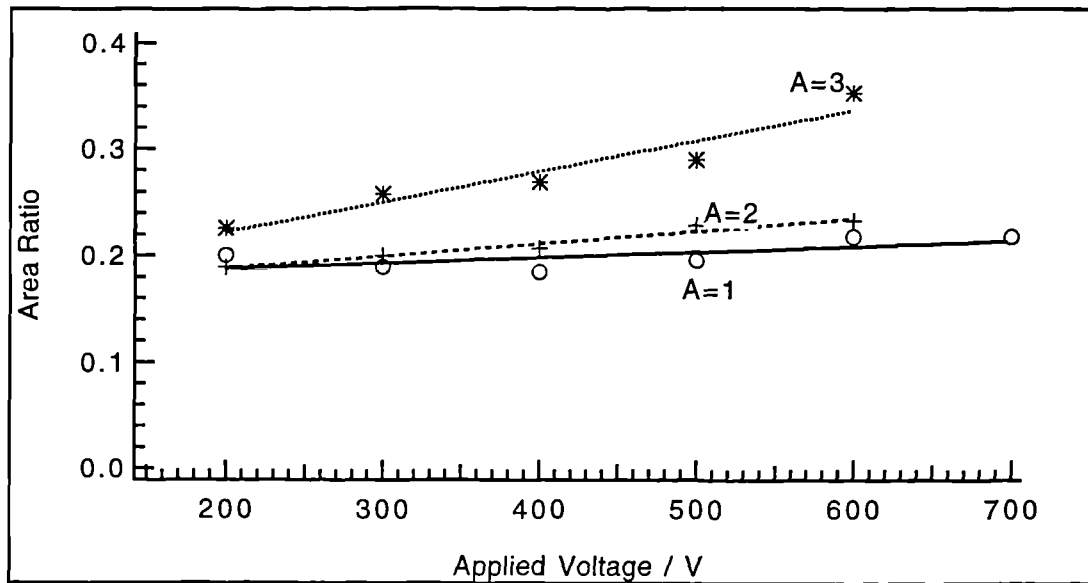
**Figure 3.51** Area ratio versus applied RF voltage for argon IEDs in figures 3.1, 3.45 and 3.47. Straight lines are drawn to draw attention to the trends with different sized electrodes.
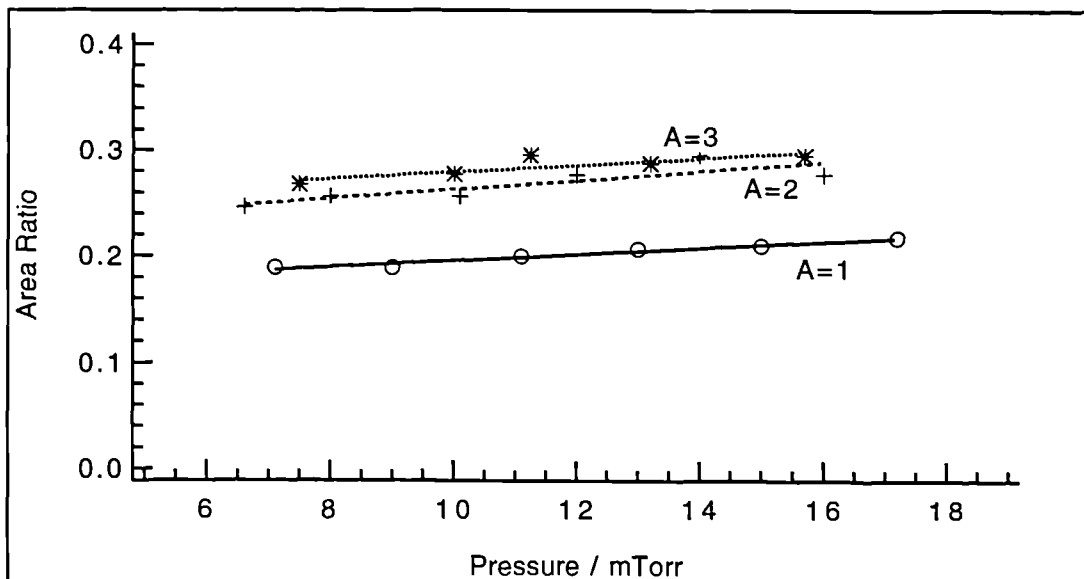


**Figure 3.52** Area ratio versus chamber pressure for the argon IEDs in figures 3.4, 3.46 and 3.48. Straight lines are drawn to draw attention to the trends with different sized electrodes.
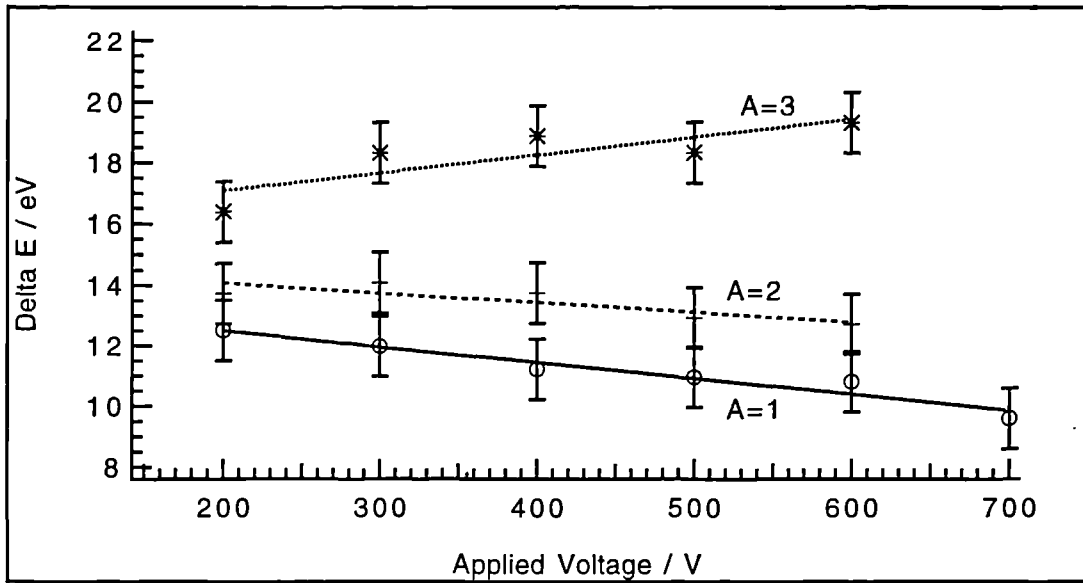
**Figure 3.53** Distribution width versus applied RF voltage for argon IEDs in figures 3.1, 3.45 and 3.47. Straight lines are drawn to draw attention to the trends with different sized electrodes.
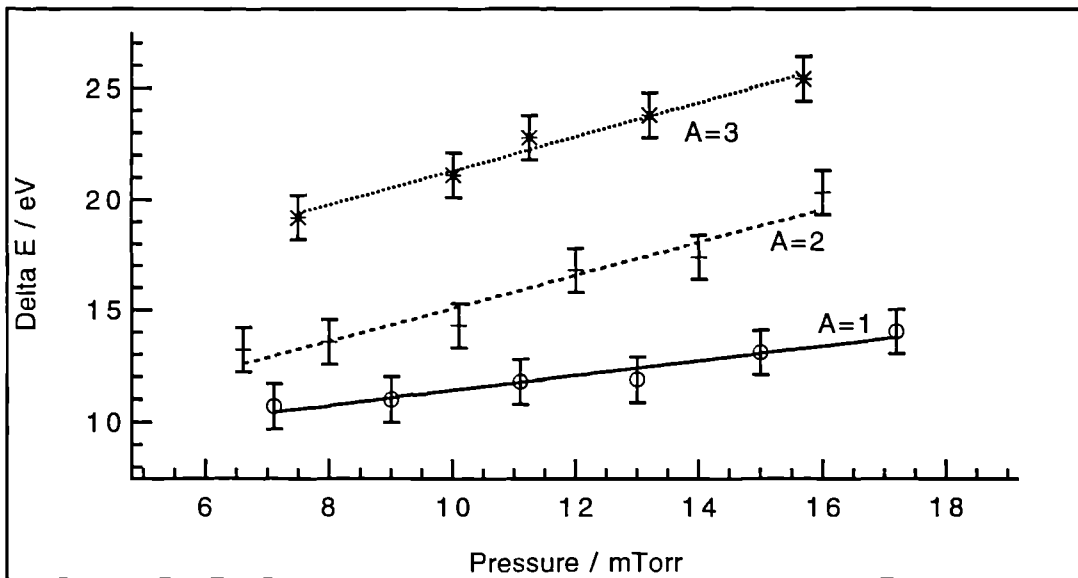


**Figure 3.54** Distribution width versus chamber pressure for the argon IEDs in figures 3.4, 3.46 and 3.48. Straight lines are drawn to draw attention to the trends with different sized electrodes.

is independent of which cathode is used. In the case of varying applied voltage the effective electrode area ratio changes little when A = 1 but for A = 3 there is a large variation, with $A_e$ increasing significantly as $V_0$ increases.

Figures 3.53 and 3.54 show the IED width, $\Delta E$, for each of the three cathode areas, for varying applied voltage and pressure respectively. In all cases the distribution width is found to be greater when the cathode area is greater. This corresponds to the concept of the anode becoming more 'cathodic' in nature and higher energies arising. More quantitatively, it corresponds to an increase in $V_{pe,max}$ in equation 1.13, repeated here for convenience, causing $\Delta E$ to increase.

$$\Delta E = 0.889 \frac{[eV_{pe,max}]^{\frac{3}{2}}}{\pi\, e\, \omega\, l_{max}\sqrt{2\, m_i}} \tag{1.13}$$

The relative change in $\Delta E$ for each case of A=1,2 and 3 when the pressure is varied is approximately the same; the distribution width is found to increase in each case as the pressure is increased, the rate of increase being slightly greater for A = 2 and 3 than for A = 1. For the variation of applied voltage however there is a more striking difference. The small contraction found when A = 1 also occurs when A = 2. For A = 3, however, the distribution width is found to increase as the voltage increases. This can be attributed to the $V_{pe,max}$ term in equation 1.13 becoming relatively more important than the $l_{max}$ term due to the increased sheath potential.

The most noticeable effect of varying discharge conditions on the IEDs is in the relative peak intensities. Exactly the same effect is found whether A = 1,2 or 3 when the pressure is increased. The high energy peak diminishes in intensity and the low energy peak becomes relatively stronger. The peak intensities when A = 1 in the varying voltage series are found to exhibit similar strong changes in intensity. However when A = 2 the relative change is less and when A = 3 there is still less variation. We now seek to explain why this may be so. The origin of the ion energy distribution has been detailed in section 1.4.8. The relative heights of the peaks in the

158

discharge will depend upon the ion transit time across the sheath. More specifically the energy an ion can attain depends on the time an ion spends being accelerated inside the sheath. Since an ion takes, typically, a few RF cycles to cross the sheath it will experience periods of constant velocity followed by periods of acceleration. The peak heights will therefore mainly depend on the frequency and sheath thickness since these govern how many RF cycles an ion experiences. Other factors such as voltage and form of the sheath potential also have a lesser influence. Since the frequency is fixed in this case we shall concentrate on the sheath thickness. It is the variation of this parameter that was used to explain the changes in distribution widths earlier.

The sheath thickness, as mentioned earlier, scales with Debye length. An equation governing the behaviour of $\lambda_d$ was also given earlier (equation 3.3). We find that $\lambda_d$ depends on i) the electron temperature, $T_e$ and ii) the charge density, n. As $T_e$ rises with voltage we can expect $\lambda_d$, and therefore the sheath thickness, to rise also. However any change in $T_e$ will be similar for all cases of A = 1,2 and 3 since the discharge conditions are the same. This could not therefore be the cause of any difference in the behaviour of the sheath thickness, and thus peak intensities, for the different cathodes.

If we now consider the charge density we must consider what effect the increased electrode area will have. It would be expected that the plasma will be better confined with a larger electrode since there is less opportunity for it to 'leak out' from between the electrodes, especially considering the design of the 'Minstrel' reactor (see figure 2.1). A change in the area ratio can be inferred as a change in the degree of confinement. For example, in the case of A = 3 the effective area ratio is 0.23 when $V_0$ = 200 V and 0.35 when $V_0$ = 700 V. This evidently means that either the effective area of the cathode increases or the anode decreases or a combination of both. Considering the geometry of the chamber it would seem likely that the effective anode area decreases. Thus as $V_0$ increases, for the case of A = 3, the plasma will become increasingly confined. For A = 1 and 2 the plasma does not appear to become appreciably more confined. The charge density, n, will increase when the voltage is increased. It may then be expected to increase more when the plasma is also becoming

159

confined. Thus, n will vary more, as the voltage is increased, for A = 3, than A = 2 which in turn will vary more than A = 1. Since $T_e$ also increases as the voltage increases what then will be the overall effect on $\lambda_d$, and sheath thickness, as the voltage increases? $T_e$ and n both increase when A = 3 with the effect that they will offset one another to some extent. When A = 1 the change in n is less and $\lambda_d$ will increase more due to the rise in $T_e$. Thus, the sheath thickness varies less where the plasma is well confined but could increase markedly where it is not.

The experimental data are consistent with this mechanism. Where the sheath thickness increases (A = 1) the peak heights do vary and the increase is sufficient to cause a contraction in the distribution width. Where there is expected to be little variation the peak heights do not vary as much and the effect of $l_{max}$ in equation 1.13 governing the distribution width is diminished, allowing $V_{pe,max}$ to dominate and $\Delta E$ to increase. In the pressure data there is no indication from the changes in the area ratio that the degree of confinement is different for any of the electrodes. The changes in the charge density will be the same in each case as the pressure changes. The applied voltage is constant and so the effect of $T_e$ will be the same throughout all three cases of A = 1, 2 and 3. Thus any change in $l_{max}$ will be the same whatever cathode is used. The effect on the IED is therefore the same.

This is a complex argument, but plasmas are complex environments where many parameters are interdependent. It does, however, appear to resolve an apparent anomaly in our experimental data. Whilst our conclusion, from the A = 1 data, that the sheath thickness decreases with pressure is well supported in the literature from many sources, our conclusion of an increasing sheath thickness with voltage (section 3.1) is less well documented. There is some evidence that it may do so but also some to show that it is expected to be constant[67]. Also, the contraction in IED width with increasing voltage that we found when A = 1 is a very abnormal observation. Other workers have shown that the distribution width increases as $V_0$ increases. This effect is only observed in our reactor when a larger area of cathode is used, at which point we conclude that the sheath thickness is varying less - which agrees with other measurements of the sheath thickness. The lack of variation of the peak intensities

where the plasma is expected to be confined agrees with the IEDs measured in electronegative plasmas. Here the plasma is also expected to be confined and no change in the peak intensities with varying applied voltage was found.

### 3.2.10 Effect of Frequency

In figure 3.55 IEDs are presented for argon discharges for a range of frequencies of the applied voltage between 8 and 20 MHz. The discharge pressure in all cases was 10 mTorr. The applied RF voltage was 500 V for all cases except 20 MHz where the maximum voltage the system could operate at was 313 V. For this reason this IED is not truly comparable with the rest of the series. It is omitted from the discussion that follows.

The IEDs exhibit the double peaked structure that is characteristic of RF modulation. The intensity of the high energy peak is found to increase as the frequency is increased from 8 MHz. At 13.56 MHz the intensities of the two peaks are equal; at still higher frequencies the high energy peak increases in intensity still further. The width of the IED, ΔE, in each case is plotted against frequency in figure 3.56. ΔE is found to increase as the frequency increases from 8 to 13.56 MHz; it then decreases slightly as the frequency rises still further. The DC bias measured in each case is plotted in figure 3.57. No reading was possible at 8 MHz due to the interference of the RF with the probe circuit and so no stable value of the DC bias could be attained. The DC bias shows no obvious trend with frequency.

Theory predicts (section 1.4.8) that as the frequency increases the distribution width should decrease. Eventually at sufficiently high frequencies the IED becomes a single spike. This is because the ions experience an increasing number of RF cycles in their transit across the sheath. The tendency of the IED to be RF modulated is therefore reduced and the IED reflects the average sheath potential. At very low frequencies the IED is, by contrast, very spread out since the ions can cross the sheath in < 1 RF cycle and can gain energies that correspond to them having experienced the full sheath potential or, alternatively the least sheath potential. However, the frequency range between these two
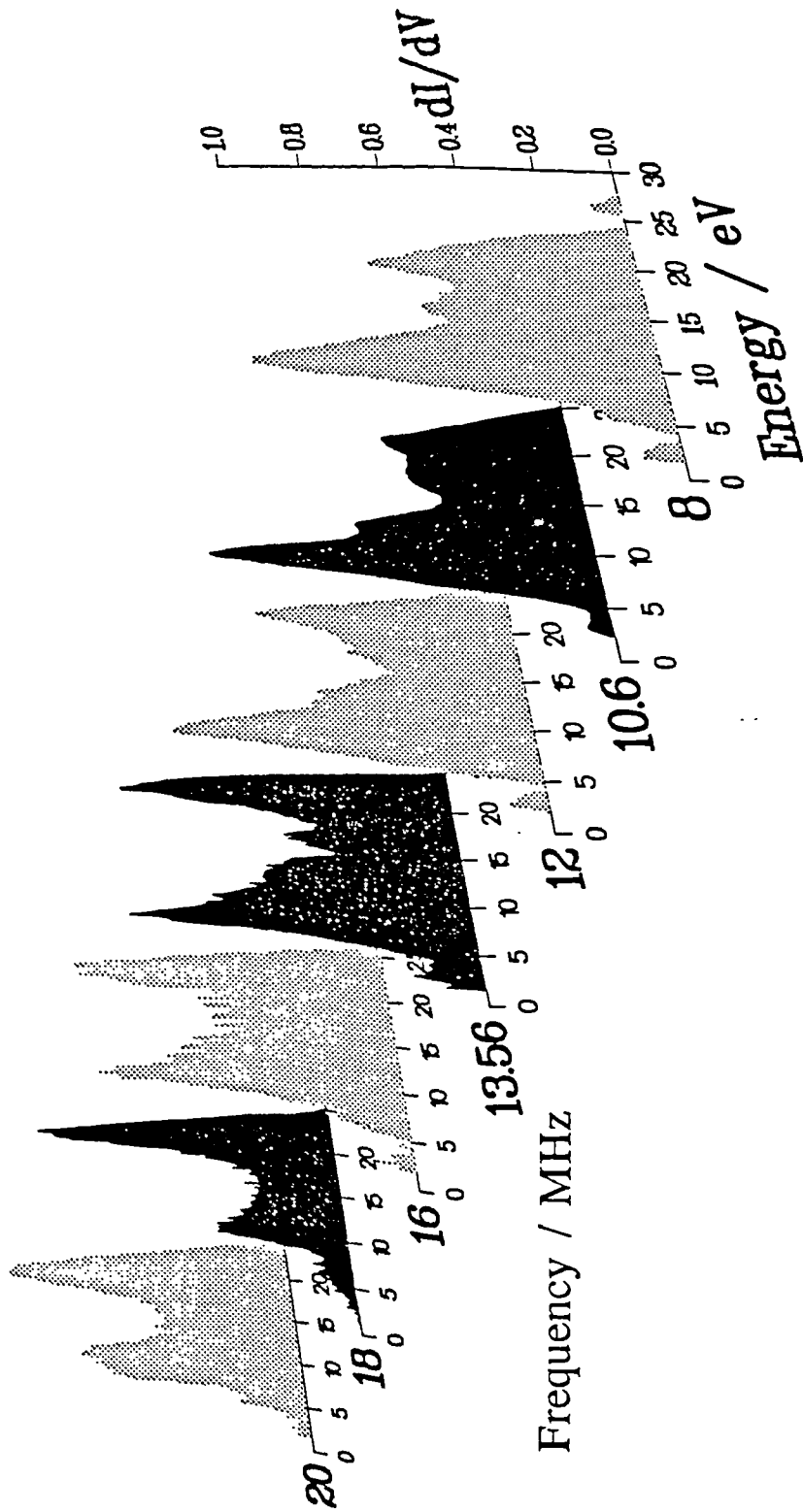
**Figure 3.55** Argon IEDs measured at 10 mTorr for different frequencies of the applied RF voltage. $V_0$ = 500 V, except the 20 MHz IED where $V_0$ = 313 V.
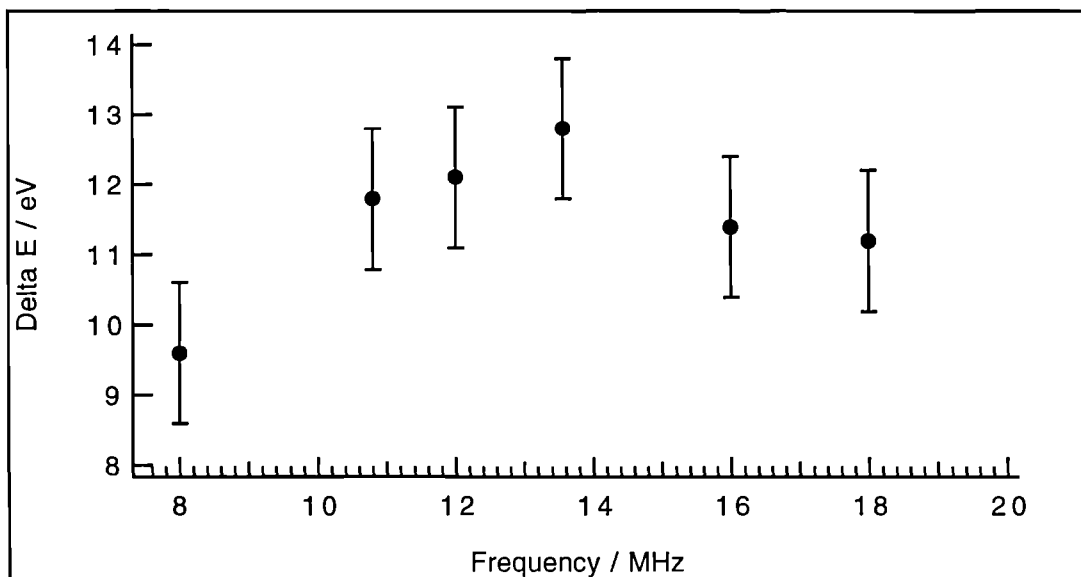
**Figure 3.56** Distribution width versus frequency of applied voltage for argon IEDs in figure 3.55.
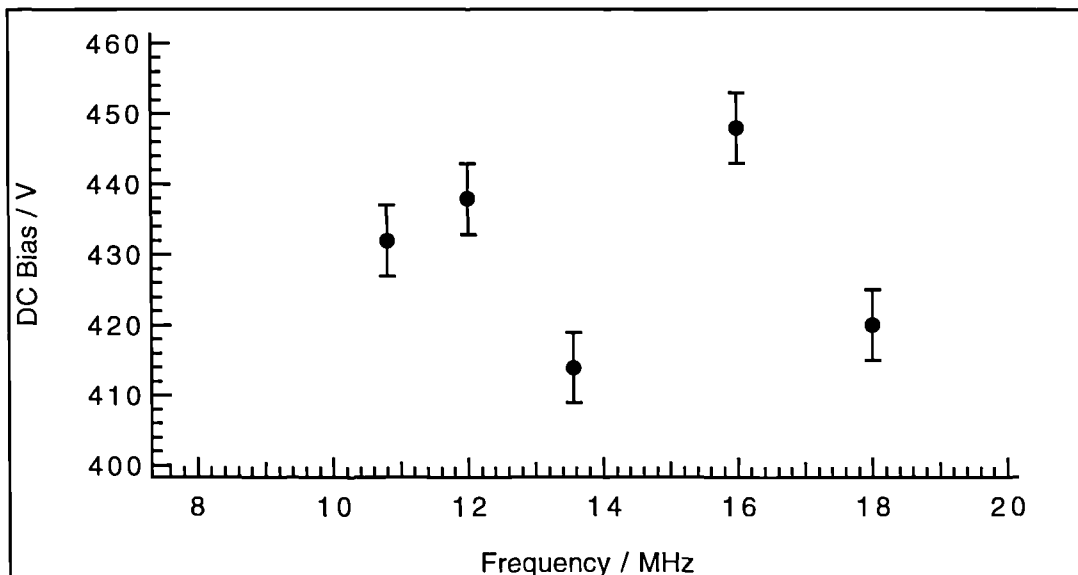


**Figure 3.57** DC bias versus frequency of applied voltage for each of the argon IEDs in figure 3.55.

163

extremes is large. May[12] , in his simulation of argon on the cathode, shows that the IED begins to contract when the frequency is ~ 100 kHz. When the frequency is 100 MHz the IED is still split by some 10 eV. Between 5 and 20 MHz, the closest comparison to our frequency range, May shows that for the conditions specified the cathode IED should contract from ~160 eV to ~35 eV. However, in these simulations other factors such as the sheath thickness and area ratio have been kept constant. This is unrealistic and Gottscho[116] has shown that as the frequency rises from 50 kHz to 10 MHz there is a concomitant rise in sheath thickness. Thus, while the simulations show the effect of frequency solely, any real system should be expected to have these effects modified by other factors. This must be borne in mind in the interpretation of our experimental data. Additionally, changes at the anode will be much smaller than those at the cathode due to the smaller sheath potential that is present.

There is thus no clear picture of what is occurring as the frequency is varied in our reactor. The initial increase in $\Delta E$ as the frequency is increased from 8 to 13.56 MHz is counter to the trend expected from theoretical studies. However the increase in frequency in this experiment is only small and any contraction due to frequency effects could easily be offset by other factors, such as a small change in sheath thickness. The data of figures 3.1 and 3.4 demonstrate that a small change in sheath thickness can have a large effect on the IED. As the frequency increases still further from 13.56 to 18 MHz the IED contracts. This may be due to the effect of frequency dominating over any change that is occurring in the sheath thickness. Note however that from 10.8 MHz to 18 MHz $\Delta E$ can be regarded as being constant at ~12 eV within experimental error. Thus although we are only expecting small changes in $\Delta E$, since we are measuring at the anode, the observed changes are too small to be conclusive of any trends with frequency.

We note here that the effects we observe may be due to the matching network system. As we have already noted in section 2.4.4 the matching network is optimised for use at 13.56 MHz. Above this frequency it is possible to match the generator and load, but the window over which this is possible is reduced. Below 13.56 MHz the tuning window increases but the efficiency of matching is

decreased. In the frequency range below 13.56 MHz which we have studied typically 15 - 20 % power was reflected. Thus the portion of the graph in which we observe an increase in ΔE, i.e. up to 13.56 MHz, could be due to external factors. If the full 500 V applied voltage does not reach the cathode in this frequency range then the plasma from which we measure IEDs will not be comparable to those of 13.56 MHz and above, where the matching network is operating efficiently. The rather scattered data of the DC bias measurements offers no further indication of what is happening to the voltages in the system.

There is a clear trend discernible in the behaviour of the peak intensities as the frequency is varied. As we noted above, as the frequency increases so does the intensity of the high energy peak in the IED. Previously, this has been indicative of a progressive change in the sheath thickness and has always been supported by a concurrent change of ΔE. There is no such consistency in these frequency dependent data.

One aspect that could affect the IED and should not be overlooked is the influence of the sheath potential. A sine wave, such as is applied to the matching network, is not necessarily preserved as a sine wave at the cathode. Thus, the specific form of the sheath potential is unknown. As the matching network efficiency decreases below 13.56 MHz the form of the sheath potential may well vary and modify the IED. In the following chapter we demonstrate that the exact form of the sheath potential is crucial in determining the form of the IED. Without more sophisticated equipment, e.g. an improved matching network and a method of determining the sheath thickness, it is impossible to draw any conclusions of the effect of frequency over this narrow range. A much larger frequency range should be investigated. This entails building a new matching network designed for operation at specific frequencies.

## 3.3 SUMMARY OF CONCLUSIONS

Ion energy distributions have been measured at the anode of a 'Minstrel ' reactive ion etcher for the following discharges: argon, helium, xenon, hydrogen, nitrogen, carbon dioxide, carbon tetrafluoride with 8% oxygen and sulphur hexafluoride. The IEDs have been measured as a function of gas pressure and applied RF voltage.

In all cases the IEDs exhibit, to a greater or lesser extent, a degree of RF modulation as characterized by a double peaked distribution. For electropositive gas discharges the degree of RF modulation, as evidenced by the splitting, $\Delta E$, between the IED peaks, is found to depend upon discharge conditions. As the applied voltage to the discharge is increased $\Delta E$ is found to decrease. Consequently, the maximum ion energy observed in the IED also decreases despite the sheath potential having increased. This is attributed to an increase in the sheath thickness which must be of sufficient magnitude to cause a reduction in $\Delta E$ despite the accompanying rise in sheath potential. Support for this hypothesis is found by reference to the heights of the peaks in the IED. They are found to be strongly dependent on the applied voltage with a relatively more intense high energy peak present at high voltages. Since the height of the peaks is known to depend on the ion transit time across the sheath the increased intensity of the high energy peak is consistent with a sheath thickness that increases with voltage.

The discharge pressure is also found to have a large influence on IEDs in electropositive discharges. At low pressures the high energy peak in the discharge dominates. As the pressure rises a few mTorr the intensity of the peaks is found to interchange and the width of the IED to expand. Thus, at higher pressures a higher maximum ion energy is observed. This phenomenon is also attributed to a changing sheath thickness. The thickness is proposed to decrease as the pressure rises. This, in turn, causes an increase in the degree of RF modulation and a consequent expansion of the IED. The relative peak intensities are also accounted for with this mechanism.

The IEDs found from electronegative discharges are found to exhibit a degree of RF modulation, but with the high energy peak being dominant irrespective of

166

discharge voltage. For very electronegative discharges (e.g. $SF_6$) the IED is found to expand as the applied voltage, and therefore sheath potential, increases. It is proposed that in electronegative discharges the sheath thickness does not vary appreciably since the plasma is better confined between the electrodes. Thus, in the absence of the influence of a varying sheath thickness the relative peak intensities do not vary and the contraction of the IED found for electropositive discharges as the applied voltage rises is absent.

IEDs have also been measured for Ar discharges where the ratio of anode to cathode area has been varied. Where the area ratio is large and the applied voltage is varied the variation of relative peak intensities that was previously observed is removed. Similarly the contraction of the IEDs with increasing voltage is absent. This is again attributed to the presence of a sheath thickness that is relatively constant due to the plasma being better confined by a larger electrode. The IEDs found when the pressure is varied are found to behave in a similar manner independent of the area ratio. Thus, the influence of pressure on the sheath thickness would appear to be independent of any change in the degree of confinement of the plasma.

# CHAPTER 4

# CALCULATION OF ION ENERGY DISTRIBUTIONS

## 4.1 INTRODUCTION

One of the main aims of this work is to simulate ion energy distributions using parameters taken from experiment and compare them to the corresponding measured IEDs. In doing this we seek to examine the validity of our model and, if necessary, to refine it. To do this we have chosen to model, almost exclusively, the argon IEDs in figures 3.1 and 3.4. Our rationale for this is that choosing to model other gases only changes the mass of the ion in the calculation. Since we seek to test the expressions for the potentials used in the model by detailed comparison of experiment and theory, this would not provide any further information as to the validity of our expressions. Additionally, obtaining best fit distributions is an iterative computer intensive procedure which realistically reduces the scope for performing numerous calculations. We do however report some simulations of hydrogen IEDs, recently performed by Hedgecock using a development of the model.

## 4.2 INITIAL SIMULATIONS

The model that we have used is that of May[12] which is based on the potentials derived by Song et al. This has been used to successfully model cathode IEDs from Kuypers experiments. Details of the model have been outlined in section 1.7.3. References 28 and 30 provide fuller explanations of the theory. Inputs required for the model are as follows: applied voltage $V_0$, effective area ratio $A_e$, ion temperature $T_i$ and electron temperature $T_e$, pressure n, sheath thickness $l_{max}$, and ion mass $m_i$. Of these the voltage, area ratio, pressure and ion mass are provided from experiment. Ion and electron temperatures are chosen as typical values for an RIE reactor. Their influence on the simulated IED is small, being restricted to their contribution to the floating potential. The main effect is to shift the IED by fractions of an eV up or down the energy scale. The sheath thickness is therefore the main parameter used to fit the simulated IEDs to experiment.

Figure 4.1 shows some of the best fit IEDs obtainable using the model. We find that it is impossible to achieve a full fit of these simulations to the data in some cases. The way we get a close approximation is to use simulated resolutions of 0.5 to 1 eV,

169
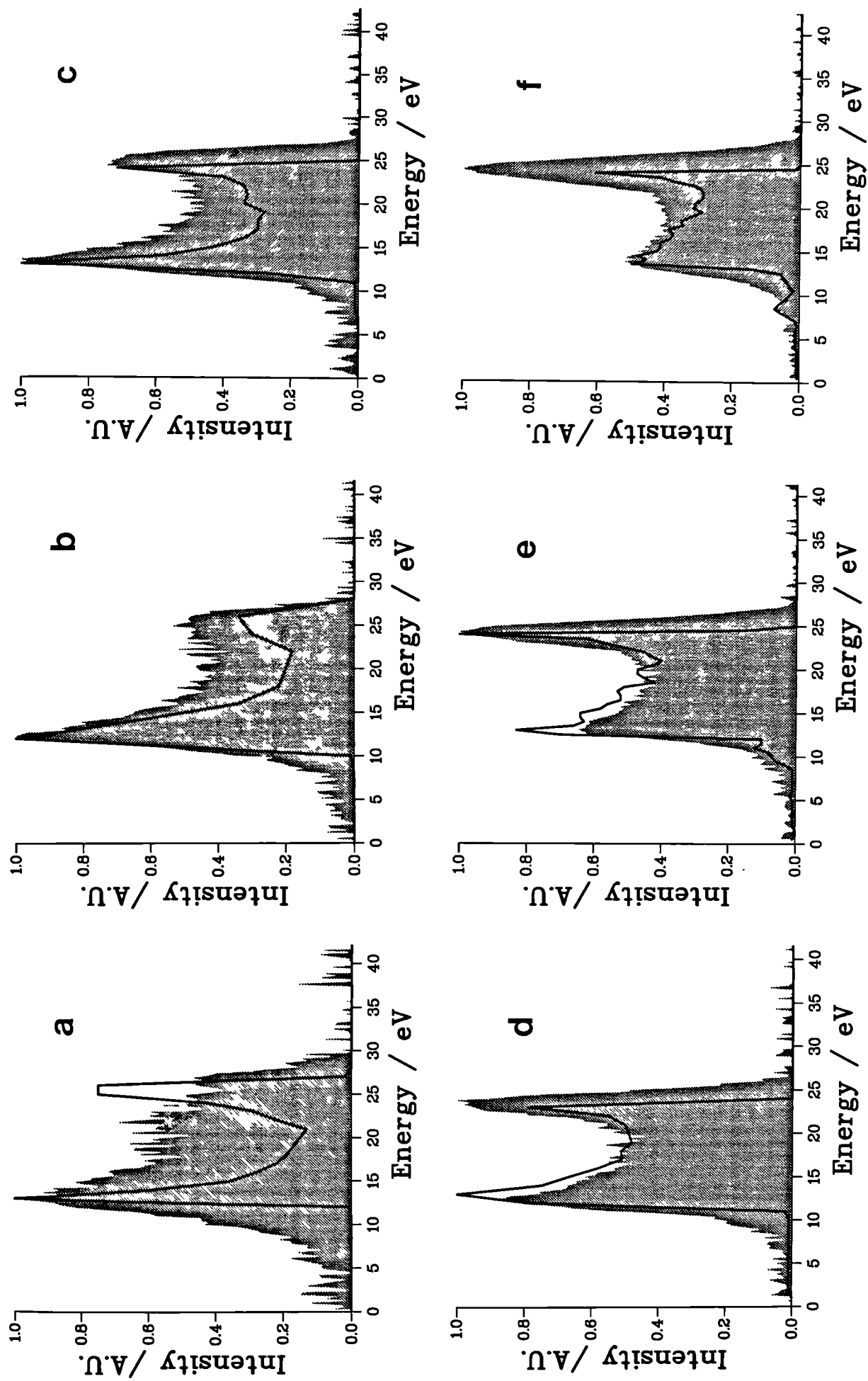
**Figure 4.1** Monte Carlo simulations of argon IEDs in figure 3.1 using the model of May et al[30]. Shading = experimental data, envelope = simulation. Applied RF voltage a) 200 b) 300 c) 400 d) 500 e) 600 and f) 700 V.

170

below that of the estimated experimental resolution of 2.5 eV. The most serious problem in these simulations is the failure to fully replicate the high energy peak in the high voltage data. The peak that is produced is too narrow and of too low an intensity. Clearly, the model in this form does not reproduce the data well.

May[12], however, has found that the model was sufficiently accurate for the simulation of IEDs measured by Kuypers[73]. The reason for this apparent discrepancy lies in the fact that Kuypers' measurements were carried out at the cathode of the reactor rather than at the anode as in our experiments. If we consider the factors governing the cathode sheath potential (equation 1.9) we find that it is dominated by the applied voltage and the DC bias. The contribution of the other terms is relatively small. $V_0$ and $V_{dc}$ are relatively easy to measure accurately and, moreover, the temporal variation of $V_0$ is known. Thus we expect the expression for the cathode sheath potential to be a good description of the actual potential. If we now consider the terms in the corresponding anode equation (1.11) we find the sheath potential depends on the difference between $V_0$ and $V_{dc}$. In a highly asymmetric reactor, such as was used in these experiments, these two voltages can approach one another in magnitude. Consequently the other terms in the equation become significant. These terms are less accurately defined than $V_0$ and $V_{dc}$. The expression included for the floating potential depends on whether the Bohm criterion is held to be valid or not. Additionally, the temporal variation of the plasma potential ($\cong$ anode sheath potential) has been proposed in many publications to be either sinusoidal or a rectified sinusoid[69]. We note that the form of the plasma potential in the theory of Song et al[28] describes a rectified sinusoid. However, in the original derivation of the fundamental expressions, on which the model is based, Song et al emphasise this rectified sinusoid form of the potential should be regarded only as approximate. Thus, unless the form chosen is rather precisely correct we can only realistically hope to get approximate *anode* IEDs from the simulation.

In the following sections we shall examine the effect on the IEDs of inserting the Bohm criterion and of altering the temporal variation of the sheath potential. We shall also demonstrate the importance of the spatial dependence of the sheath potential

with distance from the electrode.

## 4.3 EFFECT OF THE BOHM CRITERION

The Bohm criterion has already been mentioned briefly in section 1.4.5 under the discussion of the floating potential. It is associated with the interface of the sheath and the bulk plasma. The criterion proposes that the sheath does not end abruptly at the limit of the positive space charge but that a transition region exists where ions must undergo a small pre-acceleration before they enter the sheath. Many discussions of the Bohm criterion are restricted to stationary sheaths in DC discharges. It can be shown[119] that for such a stationary sheath to exist the Bohm criterion is a necessary condition that must be met. However, the requirement or otherwise for the Bohm criterion in an RF discharge has been the subject of some recent debate[26,27] since the assumptions under which it is derived are not necessarily valid. Briefly, these assumptions are:

a) Monoenergetic cold ions. That is, all ions are of equal energy. This is in fact not the case in an RF discharge and ions are well described by a Maxwell - Boltzmann distribution of energies with a temperature of $\sim 0.04$ eV.

b) Collisionless sheath. This is valid for pressures of $\sim 5$ mTorr and below and so will be applicable to many of our measured argon IEDs. However at higher pressures the sheath is clearly not collisionless and thus the Bohm criterion may be invalid.

c) Maxwell-Boltzmann distribution of electron speeds. Whilst the EED is often approximated by a Maxwell-Boltzmann distribution[106] some workers have reported that the high energy tail will be depleted. The exact form is dependent on discharge conditions and so the assumption used for the Bohm criterion may be invalid.

Furthermore, in an RF discharge the oscillation in space of the sheath may cause the ion pre-acceleration in the quasi-neutral region not to have time to take place before being enveloped by the expanding sheath front. All of these factors combined

make the subject of the Bohm criterion in RF discharges contentious.

In his modelling of Kuypers data, May[12] chose to ignore the contribution of the Bohm criterion. The difference between the 'Bohm' and 'non-Bohm' IEDs was found to be very small. Figure 4.1 shows that our simulations without the Bohm criterion lack accuracy when compared to experimental data. Thus, we have amended the program to account for the Bohm criterion to try and resolve this. The amendments necessary are:

a) The initial thermal x, y and z velocities of the ion are chosen as before. The velocity in the x direction then has an additional $kT_e/2$ added to it before it enters the sheath. This is the amount of energy the Bohm criterion predicts an ion should gain in the quasi-neutral region.

b) The expression for the floating potential is modified to become

$$V_p^0 = (kT_e/2)\ln(m_i/2.3m_e).$$

This altered program was then used to calculate best fit simulations for the argon data in figures 3.1 and 3.4. Figure 4.2 shows the best fit simulations for the distributions in figure 3.1. Table 4.1 shows the experimental parameters on which the simulations are based together with the actual parameters used to fit the data.

| $V_0$exp /V | $V_0$sim /V | $V_{dc}$exp /V | $V_{dc}$sim /V | $A_e$exp | $A_e$sim | $l_{max}$ /mm | $kT_e$ /eV | $kT_i$ /eV |
|---|---|---|---|---|---|---|---|---|
| 200 | 200 | -173 | -168 | 0.20 | 0.22 | 0.15 | 2.00 | 0.05 |
| 300 | 300 | -262 | -263 | 0.19 | 0.19 | 0.16 | 1.95 | 0.05 |
| 400 | 400 | -352 | -355 | 0.19 | 0.18 | 0.18 | 1.90 | 0.05 |
| 500 | 500 | -436 | -451 | 0.20 | 0.17 | 0.18 | 1.80 | 0.05 |
| 600 | 600 | -517 | -554 | 0.21 | 0.17 | 0.23 | 1.90 | 0.05 |
| 700 | 700 | -597 | -648 | 0.22 | 0.15 | 0.24 | 1.95 | 0.05 |

Table 4.1 Experimental parameters for data in figure 3.1 together with best fit parameters used in the simulated IEDs shown in figure 4.2.

**Figure 4.2** Monte Carlo simulations of argon IEDs in figure 3.1 using the model of May et al[30] adapted to take account of the Bohm criterion. Shading = experimental data, envelope = simulation. Applied RF voltage a) 200 b) 300 c) 400 d) 500 e) 600 and f) 700 V. Other conditions as specified in Table 4.1.

174

The values for $V_0$, $V_{dc}$ and $A_e$ (Area$_{cathode}$/Area$_{anode}$) are linked via equation 1.5. During experiment $V_0$ and $V_{dc}$ are measured which leads to a value for $A_e$. As noted in section 2.2.5 the components comprising the voltage probe are only rated at $\pm$ 20% tolerance of their values. For our simulations the philosophy adopted was to keep $V_0$ constant at the experimental applied voltage and allow $A_e$ to vary within the limits of the known accuracy of the measurements. In fact we find that the values used in our best fit simulations are very close to experimentally observed values except at high voltages (600 and 700 V). This may be attributed to errors in the measurement probe and also to RF interference which is more noticeable at higher powers.

We can calculate a value for the sheath thickness to use in the simulation using equation 1.13 if we first calculate the sheath voltage we expect using equation 1.11. If we do this we find that the sheath thickness for the IEDs in figures 3.1 and 3.4, depending on the exact discharge conditions, should be in the region 1.5 to 2.0 mm. However, using this value in our simulations typically produces IEDs with a single spike, i.e. no RF modulation is observed. This indicates that the thickness used is too large. The sheath thickness was therefore treated as an entirely free parameter and was adjusted to fit the data.

We find that the simulated IEDs fit the experimental data well. The best fit parameters used even predict an increase in $l_{max}$ with voltage in accordance with our conclusions from experiment. It is important to stress however that these values for $l_{max}$ should not be regarded as a measure of the sheath thickness in our reactor, but simply that the trend predicted by theory is in agreement with conclusions from experiment. Our simulations fit the experimental data well in terms of the peak positions as well as the peak heights except in the extreme case of the data when $V_0$ = 700 V. Here the peak positions are well modelled but the intensity of the high energy peak is underestimated. No amount of parameter adjustment can resolve this. The signal-to-noise ratio here in the experimental data is very good and so we cannot attribute the discrepancy to experimental error. We conclude that the model is not sufficiently accurate and requires further adjustment (see section 4.6).

Figure 4.3 shows the Monte Carlo simulations of the data in figure 3.4. The
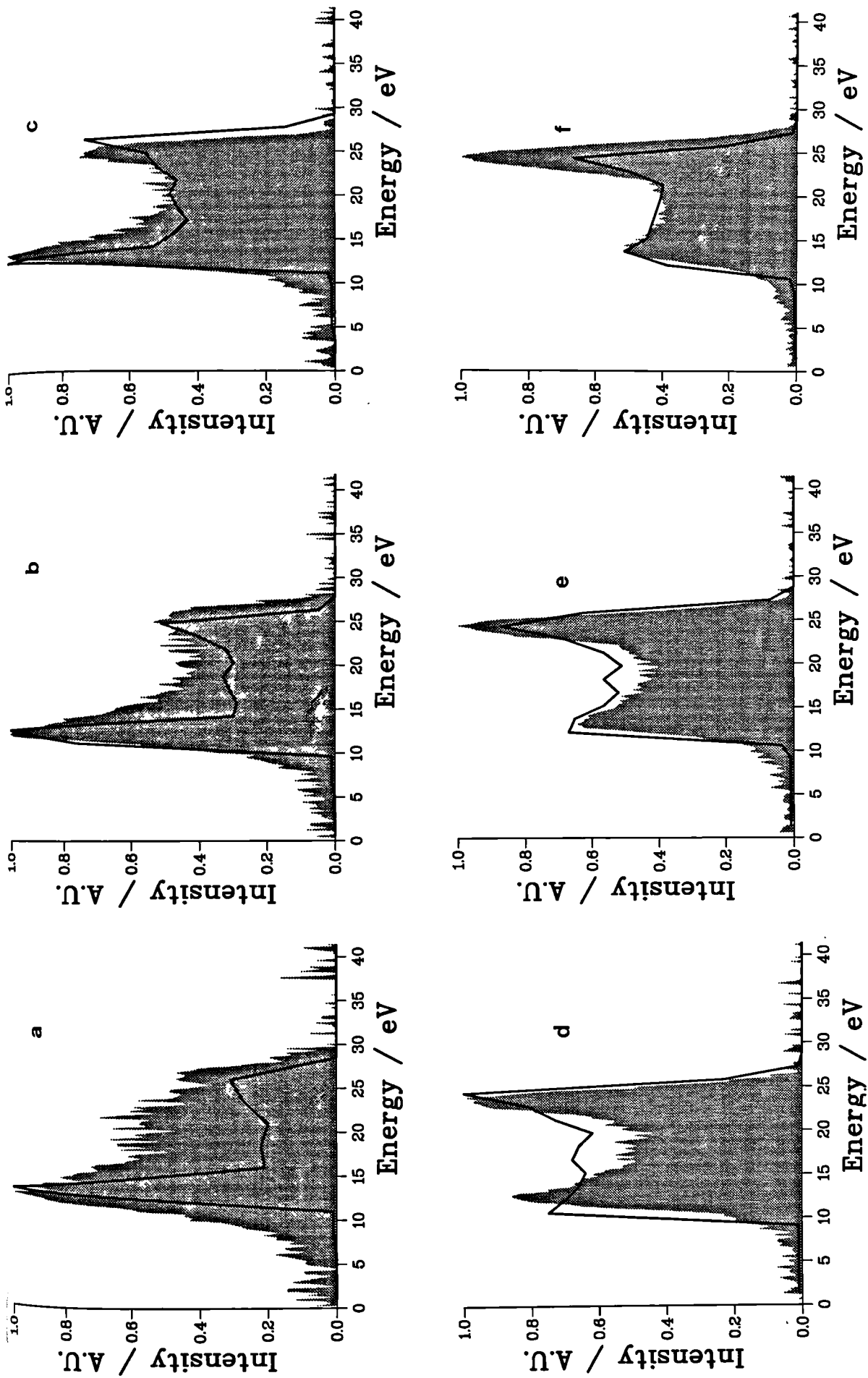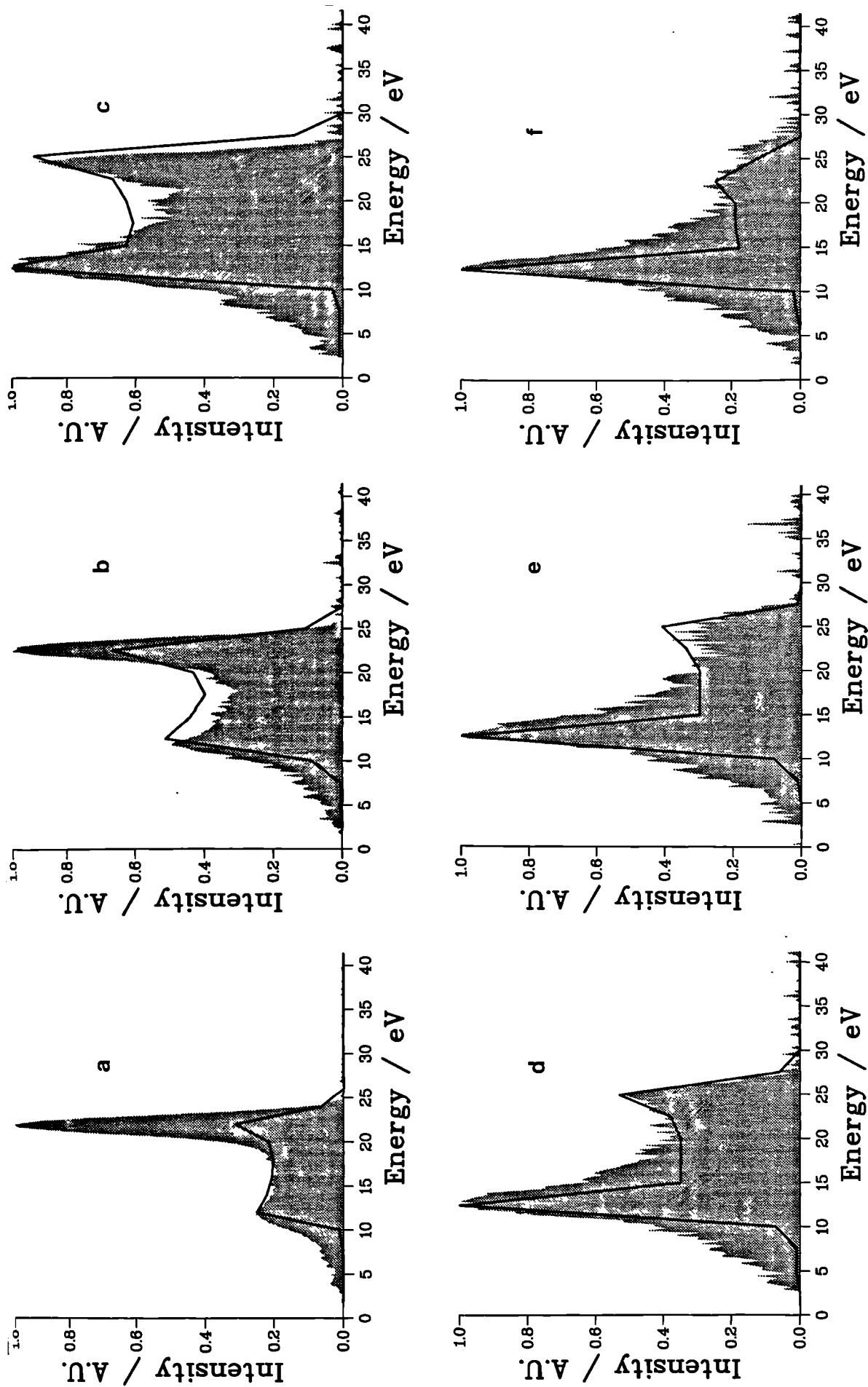
**Figure 4.3** Monte Carlo simulations of argon IEDs in figure 3.4 using the model of May et al[30] adapted to take account of the Bohm criterion. Shading = experimental data, envelope = simulation. Pressure = a) 7.0 b) 9.0 c) 11.1 d) 13.1 e) 15.0 and f) 17.2 mTorr. Other conditions as specified in Table 4.2.

parameters used for the simulation, together with the experimental parameters where appropriate, are shown in Table 4.2.

| Pressure /mTorr | $V_{dc}exp$ /V | $V_{dc}sim$ /V | $A_e exp$ | $A_e sim$ | $l_{max}$ /mm | $kT_e$ /eV | $kT_i$ /eV |
|---|---|---|---|---|---|---|---|
| 7.0 | -438 | -446 | 0.19 | 0.18 | 0.24 | 1.80 | 0.05 |
| 9.0 | -436 | -446 | 0.17 | 0.18 | 0.23 | 1.80 | 0.05 |
| 11.1 | -433 | -451 | 0.21 | 0.17 | 0.18 | 2.00 | 0.05 |
| 13.1 | -429 | -456 | 0.21 | 0.15 | 0.15 | 2.00 | 0.05 |
| 15.0 | -426 | -458 | 0.21 | 0.15 | 0.14 | 2.00 | 0.05 |
| 17.2 | -423 | -465 | 0.21 | 0.13 | 0.11 | 2.00 | 0.05 |

**Table 4.2** Experimental parameters for the data in figure 3.4 together with the best fit parameters used for the simulated IEDs in figure 4.3. In all cases $V_0 = 500$ V.

As before, we have allowed $V_{dc}$ and $A_e$ to vary within the limits defined by the accuracy of the voltage probe in the experiment. The parameters $kT_e$ and $kT_i$ have again been kept at values close to those observed in similar reactors and $l_{max}$ is a free fitting parameter. Once again we find that for our best fit simulations the value of $l_{max}$ agrees with our conclusions from experiment i.e. that it should decrease with rising pressure.

The simulations fit the experimental data acceptably except at the lower pressures. Here we find that we underestimate the intensity of the high energy peak by some magnitude. This is the same problem as we encountered in the simulation of the data in figure 3.1. Again, since no amount of parameter adjustment enables the simulation to fit the data exactly we conclude that the model still does not reflect the physical case accurately enough and further refinements are necessary (see section 4.6).

## 4.3.1 Prediction of Cathode IEDs

Up until now we have considered IEDs at the anode of the etcher. However since etching of substrates takes place at the cathode it is the IEDs here that are of interest for any technological application of our work. Experimental measurements of IEDs at the cathode are complex[73] and are rarely performed due to the presence of the large rapidly oscillating applied voltage. The theory of Song et al[28] as described in section 1.4.6 develops expressions for all the potentials in the discharge. It is these potentials that are used in our simulation program. Consequently, once an anode IED has been modelled it is a simple matter to apply the theory to the cathode and predict the IED that will be present there. Our simulations of the anode IEDs are sufficiently good to allow us now to predict cathode IEDs. To do this we use all the parameters $(kT_e, kT_i, A_e, V_0)$ that were found to fit the anode IED. The only parameter for which we need an estimate is the maximum sheath thickness, $l_{max}$. This can be found by applying equation 3.1 to both the anode and cathode sheaths, resulting in:

$$l_{max}^{cath} = \frac{V_{pe,max}^{cath}{}^{\frac{3}{5}}}{V_{pe,max}^{anode}{}^{\frac{3}{5}}} l_{max}^{anode} \qquad (4.1)$$

$V_{pe,max}$ is calculated as before using equations 1.9 and 1.11. Using the value of $l_{max}^{anode}$ that we found to fit our data we can then get a value for $l_{max}^{cathode}$. Our predictions for the cathode IEDs corresponding to the experimental data in figure 3.1 are shown in figure 4.4. The sheath thicknesses used in these simulations are shown in Table 4.3. We mention here, in passing, that figure 4.4 is an interim prediction: the best predictions we can make will be presented later in section 4.6.3.

178

**Figure 4.4** Predicted argon IEDs at the cathode using the model of May et al[30] adapted to take account of the Bohm criterion. Applied voltage a) 200 b) 300 c) 400 d) 500 e) 600 and f) 700 V. Other conditions as specified in Tables 4.1 and 4.3.

179

| $V_0$ / V | Anode $l_{max}$ / mm | Cathode $l_{max}$ / mm |
|---|---|---|
| 200 | 0.15 | 0.56 |
| 300 | 0.16 | 0.73 |
| 400 | 0.18 | 0.90 |
| 500 | 0.18 | 1.00 |
| 600 | 0.23 | 1.30 |
| 700 | 0.24 | 1.45 |

**Table 4.3** Sheath thicknesses calculated for the cathode IED simulations in figure 4.4 together with the corresponding anode sheath thicknesses for comparison.

Figure 4.4 shows that at the cathode we expect the maximum ion energy to increase with the applied RF voltage. When $V_0$ = 200 V the maximum observed ion energy is ~340 V while when $V_0$ = 700 V we find the maximum energy is ~1100 V. We also predict there to be little change in the relative peak intensities as $V_0$ varies. Thus, the trends we observed at the anode are not mirrored at the cathode. This can be understood with reference to the equations 1.9 and 1.11. $V_{pe,max}$ at the anode is relatively small due to the term ($V_0$ - $V_{dc}$). $V_{pe,max}$ at the cathode is by contrast much larger since the corresponding term is ($V_0$ + $V_{dc}$). Thus the effect of the voltage on $\Delta E$, the peak splitting, is far more important than any change in $l_{max}$. These predictions of the IED behaviour are in agreement with observations by other workers of the trends found by varying $V_0$[58]. In particular the general form of the predicted argon IED agrees with an IED measured at the cathode by Kuypers and reproduced in figure 4.16a.

Figure 4.5 shows the IEDs we predict to be present at the cathode for pressures of 7.0 mTorr to 17.0 mTorr. These correspond to the measured anode IEDs shown
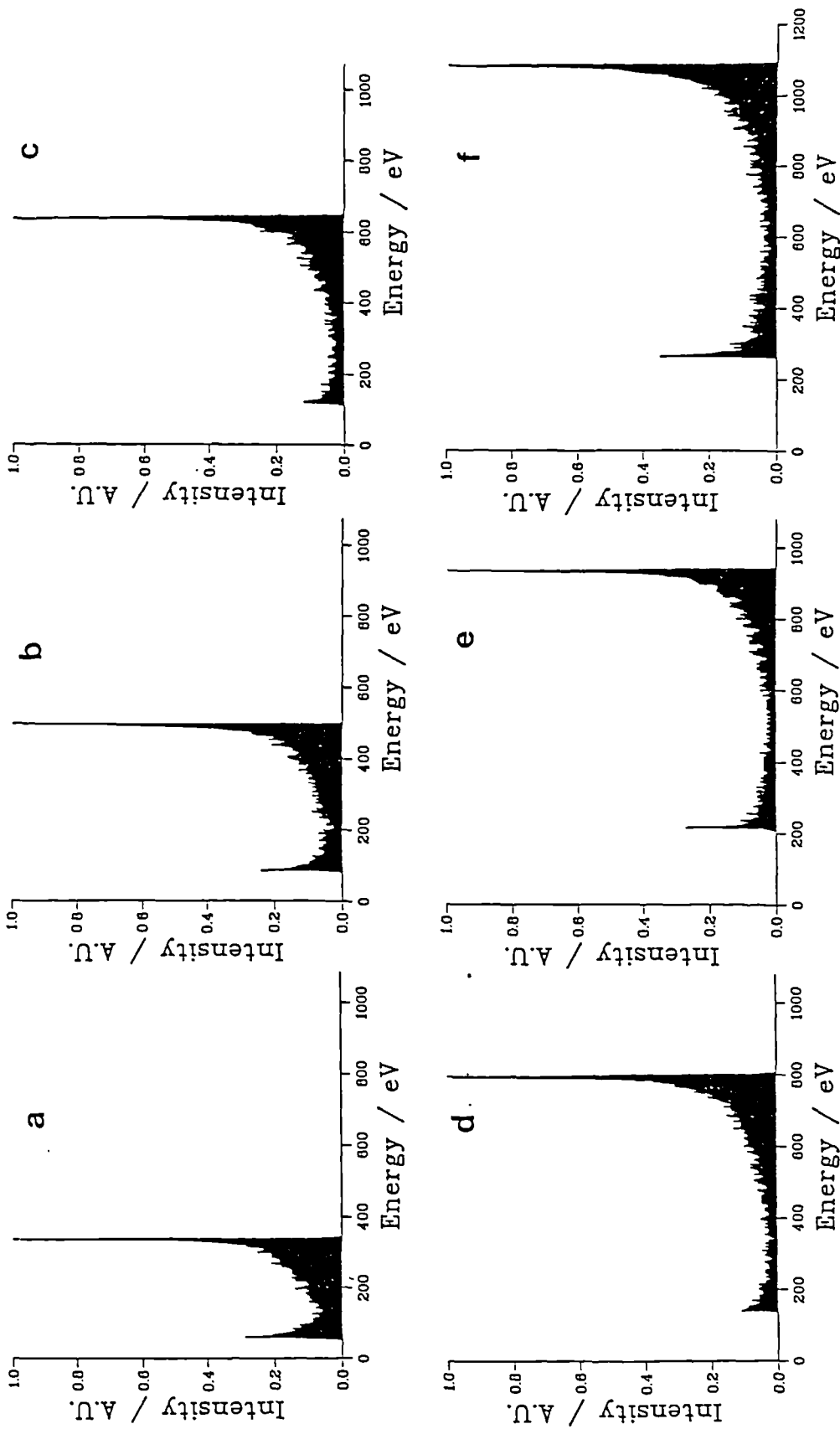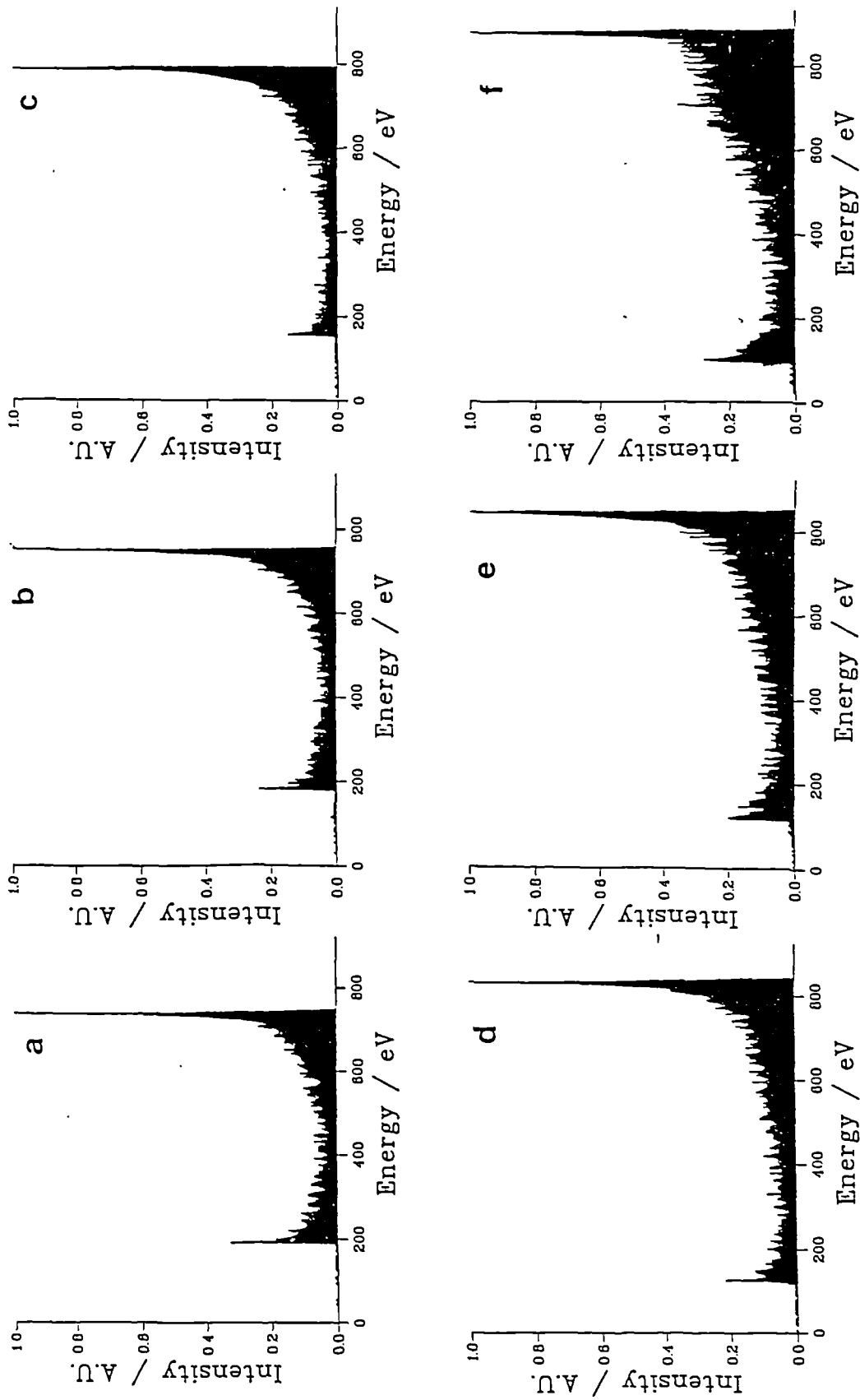
**Figure 4.5** Predicted argon IEDs at the cathode using the model of May et al[30] adapted to take account of the Bohm criterion. Pressure = a) 7.0 b) 9.0 c) 11.1 d) 13.1 e) 15.0 and f) 17.2 mTorr. Other conditions as specified in Tables 4.2 and 4.4.

181

in figure 3.4. The values of the cathode maximum sheath thickness used in the simulation and calculated via equation 4.1 are shown in Table 4.4.

| Pressure / mTorr | Anode $l_{max}$ / mm | Cathode $l_{max}$ / mm |
|---|---|---|
| 7.0 | 0.24 | 1.27 |
| 9.0 | 0.23 | 1.21 |
| 11.1 | 0.18 | 1.06 |
| 13.1 | 0.15 | 0.88 |
| 15.0 | 0.14 | 0.85 |
| 17.2 | 0.11 | 0.74 |

**Table 4.4** Sheath thicknesses calculated for cathode IED simulations in figure 4.5 together with corresponding anode sheath thicknesses for comparison.

The form of the IED is not found to vary greatly as the pressure is increased. The width of the IED is found to increase only very slightly, even though we predict $l_{max}$ to decrease. Again it would seem that the large sheath voltage present at the cathode is more important than the sheath thickness in determining the distribution width.

## 4.4 EFFECT OF A LINEAR SHEATH POTENTIAL

The spatial variation of the sheath potential with distance x into the sheath is uncertain. All of the simulations up to now have been performed using the collisionless Child-Langmuir potential as derived in Chapman[11]. Other sheath potentials have been reported as being more closely approximate to the actual sheath potential, in particular a linear variation has been suggested[120].

In his development of the model May[12] found that cathode IEDs were

**Figure 4.6** Monte Carlo simulations of argon IEDs using the model of May et al[30] adapted to include a linear sheath potential. Applied RF voltage a) 200 b) 300 c) 400 d) 500 e) 600 and f) 700 V. Other conditions are as specified in Table 4.1.

183

approximately the same whether the Child-Langmuir potential or a linear potential was used to describe the sheath potential. By adjustment of the simulation parameters by a few percent the I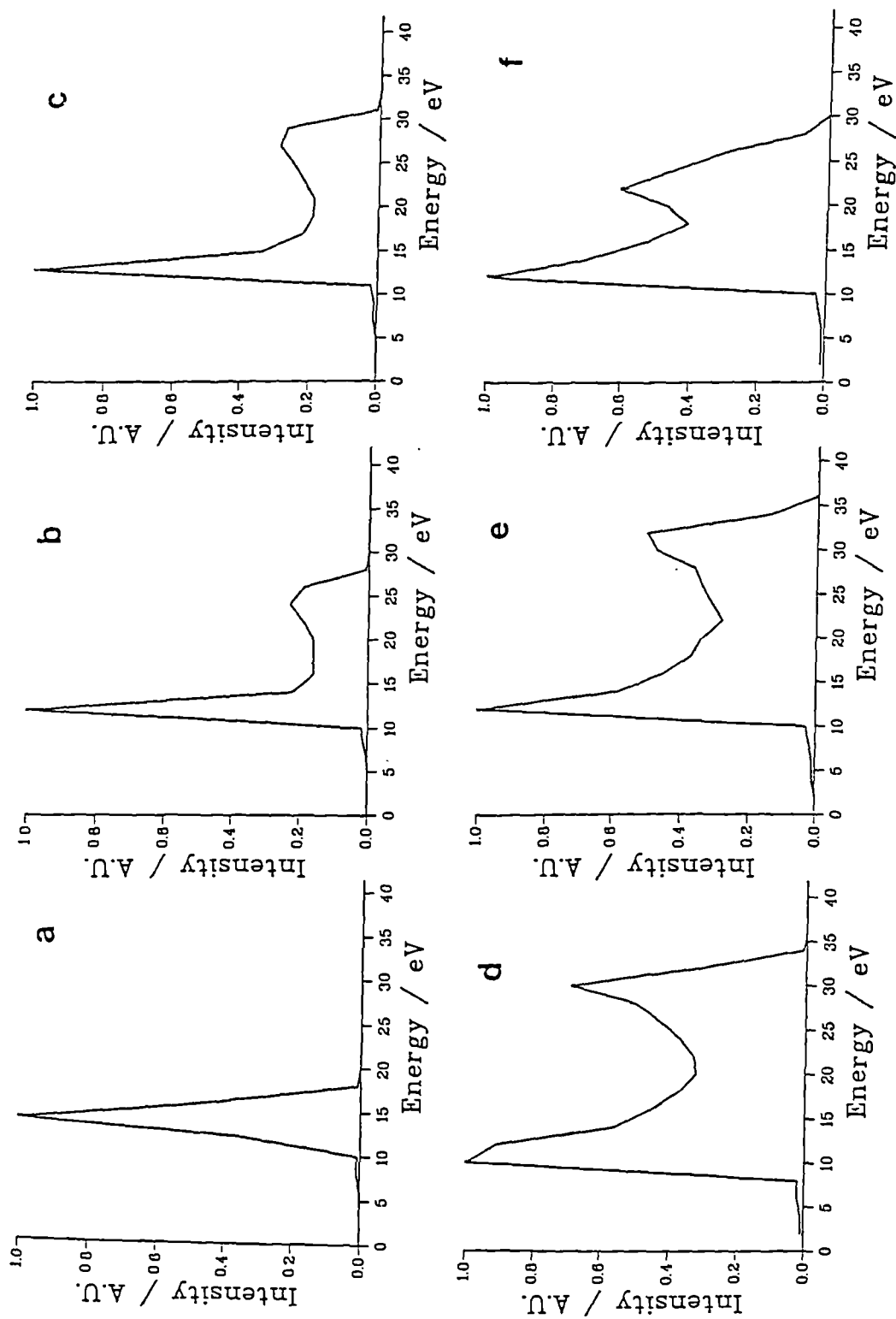EDs using each potential could be made identical. We now consider whether the form of the potential is important at the anode. For this to be done adjustments to the model, as detailed by May, were performed. The best fit parameters that were found to model the IEDs in figure 3.1, when a Child Langmuir potential was used, were input into the model. The resulting IEDs are shown in figure 4.6. Comparison of this figure with 4.2 reveals that the IEDs are substantially different. We cannot regain the same IEDs by adjusting parameters by 'a few percent' as May found. Evidently the exact form of the potential is crucial to obtaining accurate simulations of anode IEDs using realistic input parameters.

No exhaustive attempt has been made to reproduce experimental IEDs using a linear sheath since, as Field at al point out[30], this potential violates flux conservation and the use of a linear sheath should be avoided. A Child-Langmuir potential therefore serves as our best approximation for IED simulations. However, unless the real potential actually obeys this form then attempts to model IEDs will be frustrated. Once again we note that uncertainties in the small potential at the anode are of more consequence in the IED than, according to May's work, small uncertainties at the cathode.

## 4.5 SIMULATIONS OF HYDROGEN IEDs

We have demonstrated up to now that the simulation model using a Child-Langmuir potential, with the Bohm criterion accounted for, reproduces experimental data very well. This version of the model has been used in our laboratory by Hedgecock[40] to model the hydrogen IEDs in figures 3.19 and 3.22. Hedgecock has then extrapolated these results to the cathode with the ultimate aim of predicting etch profiles in indium phosphide substrates and comparing the results to experiment. Hedgecock has made further adaptions to the model to include expressions that account for the scattering and charge exchange collisions that all the various hydrogen containing ions in the discharge can be expected to undergo. To further demonstrate

the accuracy of the model we reproduce some of the simulations obtained by Hedgecock here.

Figure 4.7 shows a selection of three hydrogen IEDs taken from figure 3.19 together with the best fit envelopes as found by Hedgecock. The fitting parameters in these data are the electron temperature and the sheath thickness (see figure caption). The sheath thickness is found to increase with applied RF voltage in agreement with our conclusions from experiment. The electron temperature required to fit the data is found to decrease with voltage, contrary to experimental evidence, and is thought by Hedgecock to be due to remaining inadequacies in the model. Similarly, the value used for the area ratio is significantly different from the experimentally derived value; again this is attributed to residual inaccuracies in the model. We note here that it may also be due to errors in the measurement of $V_0$ and $V_{dc}$ leading to erroneous estimates of the area ratios.

Figure 4.8 displays some simulated hydrogen IEDs corresponding to the data in figure 3.22. The simulations here predict that the electron temperature will decrease with rising pressure. This is to be expected since the mean free path decreases and so energy loss through collision will increase. However the value for the sheath thickness increases with increasing pressure. This is contrary to both our own conclusions from experiment and other workers' direct measurements[67].

The modelling of these hydrogen IED series has highlighted some further inadequacies in the model. In modelling the voltage series the trend of electron temperatures behaves contrary to experimental evidence while in the pressure series it behaves as expected. The sheath thickness, by contrast, is well behaved in the voltage series but fails to reflect experimental trends in the modelling of the pressure series. The value for the area ratio adopted in fitting both series deviates from that found in experiment.

Clearly, if these parameters are ever going to be more than just fitting parameters they need to reflect experimental trends more closely than at present. One reason that they do not may be the interdependence of several parameters on the same feature of the IED. The sheath thickness, electron temperature and area ratio all affect

**Figure 4.7** Monte Carlo simulations of hydrogen IEDs selected from figure 3.19. Shading = experimental data, envelope = simulation. Pressure = 20 mTorr. Applied RF voltage = a) 200 b) 400 and c) 500 V. Fitting parameters: sheath thicknesses a) 3.75 mm, b) 4.00 mm and c)4.50mm; electron temperatures a) 1.6 eV b) 1.5 eV and c) 1.3 eV.

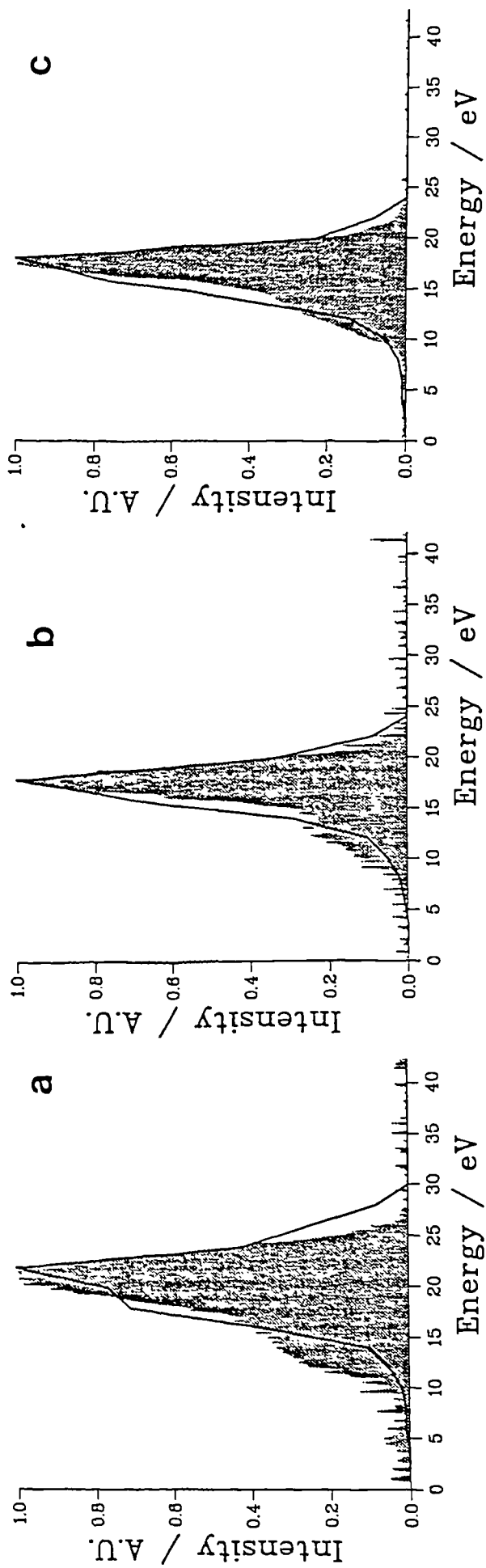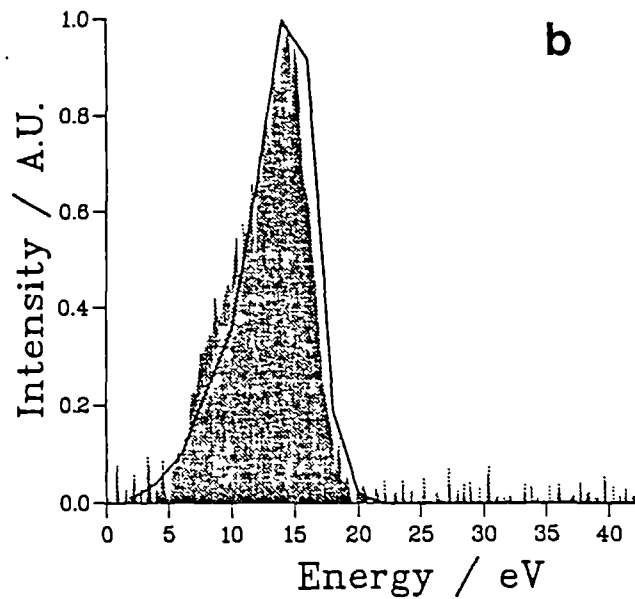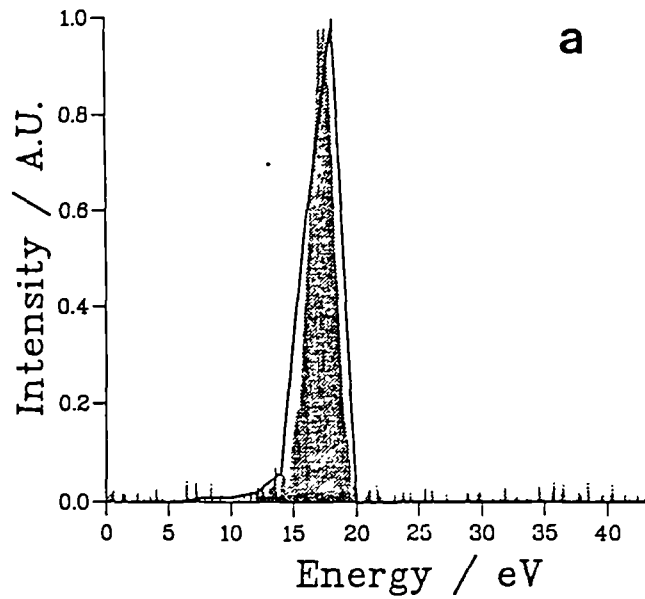**Figure 4.8** Monte Carlo simulations of hydrogen IEDs selected from figure 3.22. Shading = experimental data, envelope = simulation. Applied RF voltage = 400 V. Pressure = a) 9 and b) 45 mTorr. Fitting parameters: sheath thicknesses a) 5.00 mm, and b) 5.50 mm; electron temperatures a) 2.0 eV and b) 0.75 eV.

the width of the IED, the latter in a rather complex way[12]; the area ratio and the electron temperature both also influence the mean of the distribution.

The IEDs simulated by Hedgecock are close to the experimental IEDs and, in general, fit better than the argon simulations in figure 4.2 and 4.3. This is because the sheath that is used in these hydrogen simulations is considerably thicker and so the IEDs depend <u>mainly</u> on the average sheath potential. The exact spatial and time dependence of the potential is less important than where the sheath is thin. To refine the model and make it more accurate for cases such as argon a further amendment to the model has been made. Before discussing this we note that Hedgecock found that the presence or absence of the Bohm criterion preacceleration made only an insignificant difference to the simulated IEDs. This is due, again, to the relatively thick sheath making a small preacceleration negligible in the final ion energy.

## 4.6 TEMPORAL VARIATION OF THE SHEATH POTENTIAL

As noted in earlier sections the temporal variation of the plasma potential is uncertain. Opinion in the literature[26,27] is divided as to whether a sinusoidally varying potential or one of more rectified appearance is correct. Song et al[28] have developed an expression describing a rectified sinusoid but emphasise that this is only an approximation. This form is used in the model so far and we now consider whether altering the form of the plasma potential to instead include a sinusoidal time dependence allows for greater accuracy in modelling experimental data.

### 4.6.1 Adjustments to the model

To include a sinusoidal form of the plasma potential the expression for $V_p(t)$ in the model (equation 1.7) must be rewritten. Figure 4.9 shows the form of the potential as used by Song et al, and in our simulations up to now, and the sinusoidal potential we require an expression for. An intermediate case as suggested by Köhler et al[69] is also shown. The model of Song et al develops an expression for $V_{pe,max}$ at the anode. To obtain an expression for a sinusoidally varying potential we simply subtract the contribution of the floating potential from $V_{pe,max}$ and use the resulting value to
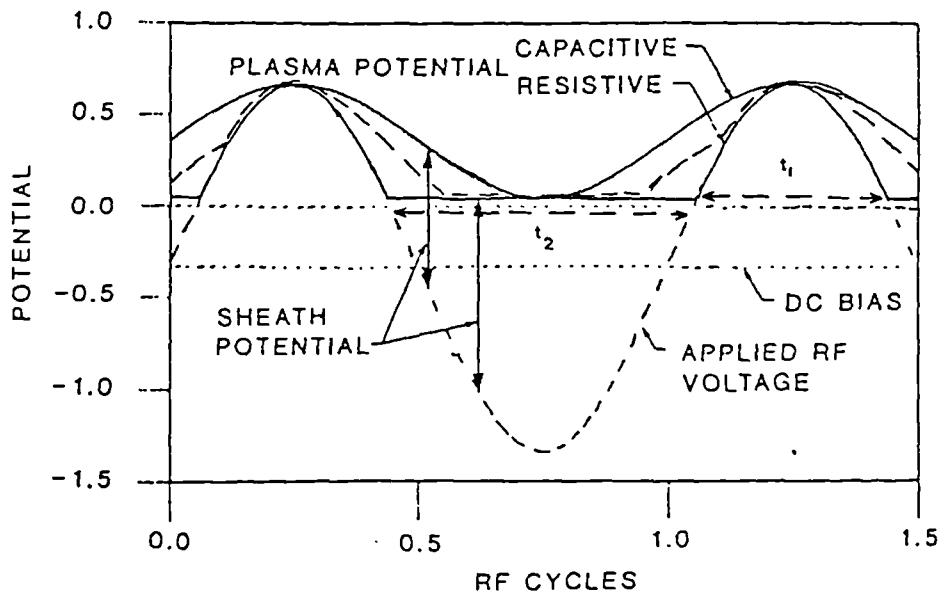
**Figure 4.9** Schematic of the plasma potentials for sheaths displaying dominantly capacitive and resistive characteristics. The instantaneous sheath potential is the difference between the potential of the electrode and the plasma potential. An intermediate case for the plasma potential (dashed line) is also shown. After Kushner[85] and Kohler et al[69].

189

calculate the sinusoidal dependence. In the program all that is required is to replace the expression for $V_p(t)$ with

$$V_p(t) = \frac{V_{pe,max} - V_p^0}{2} (1 + \sin \omega t) + V_p^0 \qquad (4.2)$$

where $V_{pe,max}$ = maximum sheath voltage, $V_p^0$ = floating potential, $\omega$ = RF frequency.

Equation 4.2 describes a simple sine wave tacked on to the floating potential. This is similar to the models used by Kushner[85] and Thompson[80].

One of the effects of having the area ratio in the model of Song et al is to determine the ratio of the time that $V_p(t)$ is at its minimum value to the time that it is expanded i.e. $t_1 / t_2$ in the figure 4.9. This now becomes unnecessary in this development of the model. Additionally the program inputs have been altered to allow the direct input of $V_{dc}$ rather than calculating it using the area ratio and $V_0$. The influence of the area ratio is now only to be found in its contribution to $V_{pe,max}$.

## 4.6.2 Modelling Results

The altered program has been used to calculate best fit simulations to the argon data in figures 3.1 and 3.4. Figure 4.10 shows the best fit simulations to the data of figure 3.1. The experimental parameters together with the fitting parameters used are shown in Table 4.5.

The best fit simulations using this version of the model are, in general, better than the corresponding simulated IEDs using a rectified form of the plasma potential (figure 4.2). In particular it is possible to reproduce the intense high energy peak that is observed at high voltages. This was not possible using a rectified sinusoid as the plasma potential. Although it is not clear exactly why this is so, it is believed to be due to the extended time ions spend in the sheath region, allowing a greater proportion to gain a higher energy. The values of the parameters used in the simulation are close to those found in experiment. At higher voltages there is some deviation, although all

190

**Figure 4.10** Monte Carlo simulations of argon IEDs in figure 3.1 using the model of May et al[30] adapted to take account of a sinusoidally time dependent plasma potential. Shading = experimental data, envelope = simulation. Applied RF voltage a) 200 b) 300 c) 400 d) 500 e) 600 and f) 700 V. Other conditions as specified in Table 4.5.

the values are within the 20% accuracy of the voltage probe. The sheath thickness is found to increase with voltage in agreement with our conclusions from experiment (although this effect is slight). More apparent is the increase in electron temperature with voltage from 0.25 eV at $V_0$ = 200 V to 0.8 eV at 700 V. This trend is in agreement with experimental observations[37].

| $V_0$exp / V | $V_0$sim / V | $V_{dc}$exp / V | $V_{dc}$sim / V | $A_e$exp | $A_e$sim | $l_{max}$ / mm | $kT_e$ / eV | $kT_i$ / eV |
|---|---|---|---|---|---|---|---|---|
| 200 | 203 | -173 | -169 | 0.20 | 0.20 | 0.30 | 0.25 | 0.05 |
| 300 | 297 | -262 | -263 | 0.19 | 0.19 | 0.32 | 0.35 | 0.05 |
| 400 | 393 | -352 | -359 | 0.19 | 0.19 | 0.33 | 0.40 | 0.05 |
| 500 | 482 | -436 | -451 | 0.20 | 0.20 | 0.30 | 0.50 | 0.05 |
| 600 | 572 | -517 | -540 | 0.21 | 0.21 | 0.33 | 0.55 | 0.05 |
| 700 | 670 | -597 | -637 | 0.22 | 0.22 | 0.35 | 0.80 | 0.05 |

**Table 4.5** Experimental parameters for the data in figure 3.1 together with the best fit parameters used in the simulated IEDs in figure 4.10.

Figure 4.11 shows the best fit simulations to the data of figure 3.4. The experimental parameters with the corresponding best fit parameters are shown in Table 4.6.

These simulations are again very close to the experimental IEDs. In particular we find that the intense high energy peak present in some of the data can easily be modelled using the sinusoidally varying plasma potential. The fitting parameters used in the simulation are again close to those in experiment. The main deviation appears to be in the simulation value of $V_{dc}$ which is not required to vary as much in our simulations as experiment shows. The simulation value for $kT_e$ drops as the pressure increases, in accordance with the observations of other workers. However we find that
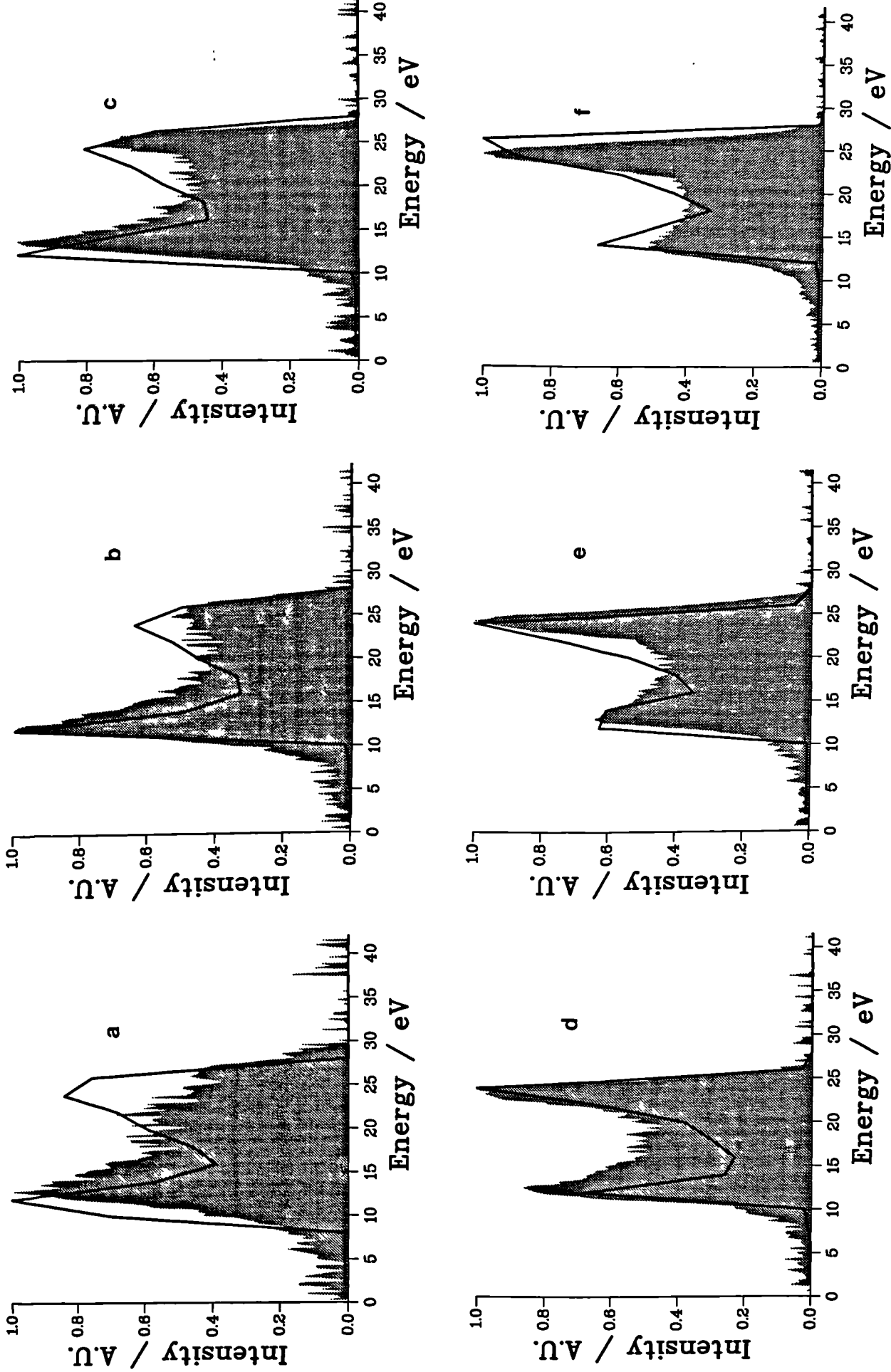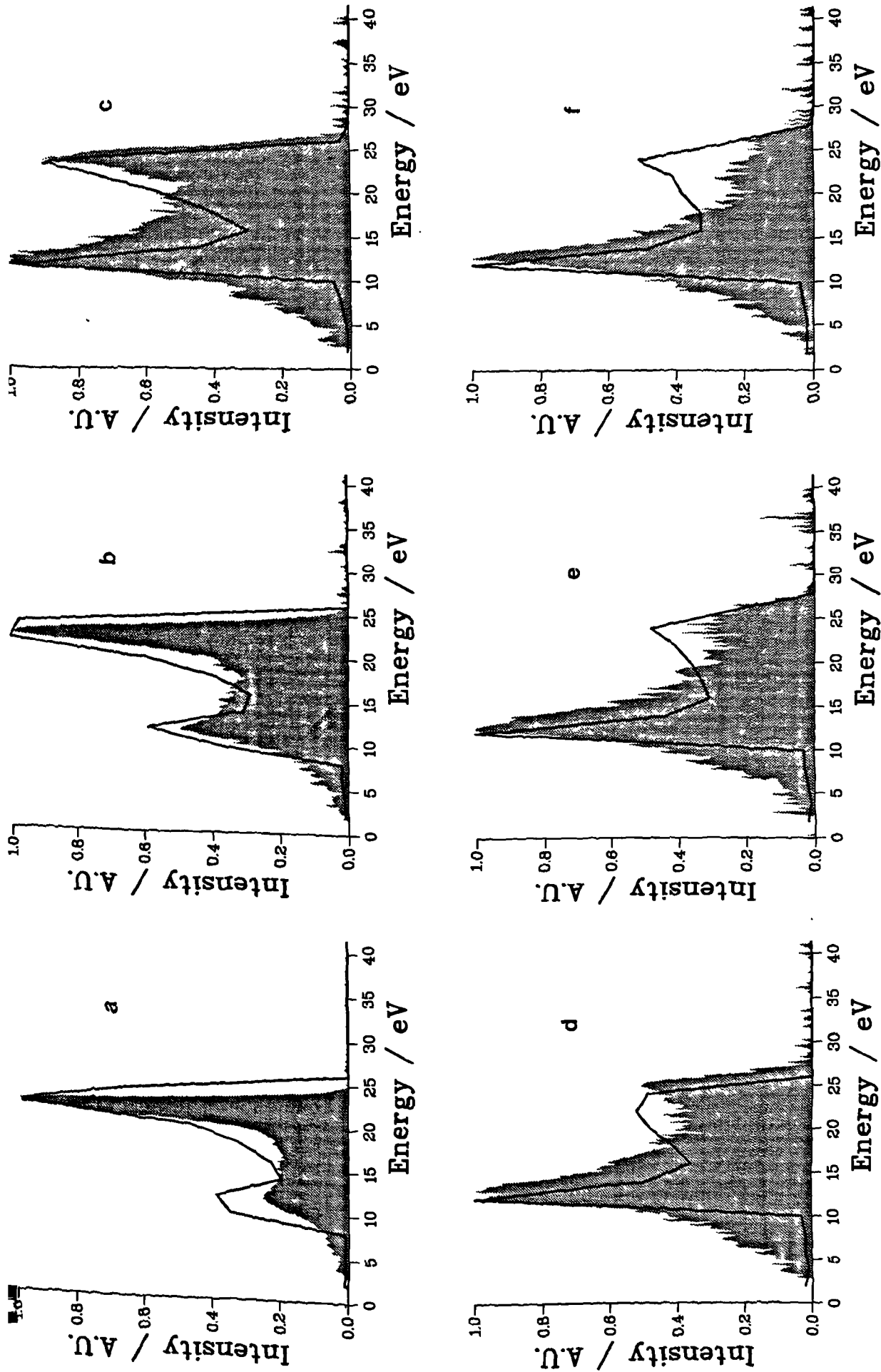
**Figure 4.11** Monte Carlo simulations of argon IEDs in figure 3.4 using the model of May et al[30] adapted to take account of a sinusoidally time dependent plasma potential. Shading = experimental data, envelope = simulation. Pressure = a) 7.0 b) 9.0 c) 11.1 d) 13.1 e) 15.0 and f) 17.2 mTorr. Other conditions as specified in Table 4.6.

193

to successfully fit the experimental data we must include a small increase in the sheath thickness as the pressure increases. This is contrary to both our conclusions from experiment and observation. At present we can offer no explanation for this.

| Pressure / mTorr | $V_0$sim/ V | $V_{dc}$exp/ V | $V_{dc}$sim/ V | $A_e e$ | $A_e s$ | $l_{max}$ | $kT_e$ | $kT_i$ |
|---|---|---|---|---|---|---|---|---|
| 7.0 | 481 | -438 | -452 | 0.19 | 0.19 | 0.28 | 0.50 | 0.05 |
| 9.0 | 481 | -436 | -451 | 0.17 | 0.17 | 0.29 | 0.47 | 0.05 |
| 11.1 | 483 | -433 | -451 | 0.21 | 0.21 | 0.31 | 0.40 | 0.05 |
| 13.1 | 483 | -429 | -451 | 0.21 | 0.21 | 0.33 | 0.37 | 0.05 |
| 15.0 | 483 | -426 | -449 | 0.21 | 0.21 | 0.33 | 0.28 | 0.05 |
| 17.2 | 483 | -423 | -449 | 0.21 | 0.21 | 0.33 | 0.28 | 0.05 |

**Table 4.6** Experimental parameters for data in figure 3.4 together with the best fit parameters used in the simulated IEDs in figure 4.11. In all cases the applied voltage in the experiment was 500 V.

One of the most striking effects of the model is revealed in this set of simulations. For quite small changes in simulation parameters large changes can be seen in the IED. Comparison of the first and last rows of data in Table 4.6 reveals that the values for the voltages have changed only very slightly - a combined total for $V_0$ and $V_{dc}$ of only 5 V. The sheath thickness alters by only 0.05 mm. The biggest change is found in the value used for $kT_e$ - almost halved from 0.5 eV to 0.28 eV. However these changes are enough to cause the intensities of the two peaks in the discharge to interchange, as comparison of figures 4.11a and 4.11f reveals. This effect is, in fact, exactly that which we see in experiment. A small increase in pressure produces a large effect on the experimental IED. In this respect the model reproduces the experimental observation very well indeed.

### 4.6.3 Predictions of Cathode IEDs

We can again use our best fit parameters ( tables 4.5 and 4.6) to extend the application of the model to predict IEDs at the cathode. As before, we have predicted the sheath thickness required at the cathode using equation 4.1.

Predictions of cathode IEDs corresponding to the best fit anode IEDs in figure 4.10 are displayed in figure 4.12. The sheath thicknesses used for the simulation are shown in Table 4.7 together with the corresponding values of $l_{max}$ at the anode for reference.

| $V_0$ / V | Anode $l_{max}$ / mm | Cathode $l_{max}$ / mm |
|:---:|:---:|:---:|
| 200 | 0.30 | 1.27 |
| 300 | 0.32 | 1.75 |
| 400 | 0.33 | 2.15 |
| 500 | 0.30 | 2.36 |
| 600 | 0.33 | 2.77 |
| 700 | 0.35 | 3.29 |

**Table 4.7** Sheath thicknesses used for the simulations in figure 4.12 together with the corresponding anode sheath thicknesses for comparison.

These simulations can be compared directly to our previous predictions in figure 4.4 where the best fit simulations were found using a rectified sinusoidal form of the plasma potential. We find that there are some substantial differences. The mean of the IEDs is in approximately the same position, for comparable IEDs, but the width of the distribution is substantially less where the sinusoidal form of $V_p(t)$ is used. This is due to the larger sheath thickness that is predicted for this case - since the sheath thickness required to fit our anode data was larger than that where a rectified sinusoid

195

**Figure 4.12** Predicted argon IEDs at the cathode using the model of May et al[30] adapted to take account of a sinusoidally time dependent plasma potential. Applied RF voltage a) 203 b) 297 c) 393 d) 482 e) 572 and f) 670 V. Other conditions as specified in Tables 4.5 and 4.7.

potential was used. The cathode sheath thickness increases as the voltage increases and this should cause the distribution width, $\Delta E$, to decrease in accordance with equation 1.13. However, we find that since the sheath potential also increases, this effect dominates and the distribution spreads out as the voltage is increased. Note that in the simulations in figure 4.12 we have included collisions[12], as evidenced by the low energy tail of the IED. Collisions were not included in the simulations in figure 4.4 but will not affect our comparison of IED means and widths since the proportion of collisions is so low.

We have also predicted cathode IEDs corresponding to the best fit simulations in figure 4.11. These are shown in figure 4.13. The sheath thicknesses used for the simulation are shown in Table 4.8.

| Pressure / mTorr | Anode $l_{max}$ / mm | Cathode $l_{max}$ / mm |
|---|---|---|
| 7.0 | 0.28 | 2.30 |
| 9.0 | 0.29 | 2.33 |
| 11.1 | 0.31 | 2.39 |
| 13.1 | 0.33 | 2.53 |
| 15.0 | 0.33 | 2.43 |
| 17.2 | 0.33 | 2.43 |

**Table 4.8** Sheath thicknesses for the simulations in figure 4.13 together with anode sheath thicknesses for comparison.

We can compare these predicted IEDs to those in figure 4.5 where a rectified sinusoid was used. It is found that the IEDs in figure 4.13 are much narrower than in the previous corresponding set of predictions. This is, as before, due to the thicker sheath that is now predicted to be present when a sinusoidally varying plasma potential is used. The effect of the increasing pressure can be seen in figure 4.13 where increased smearing of the IED to low energies is observed.
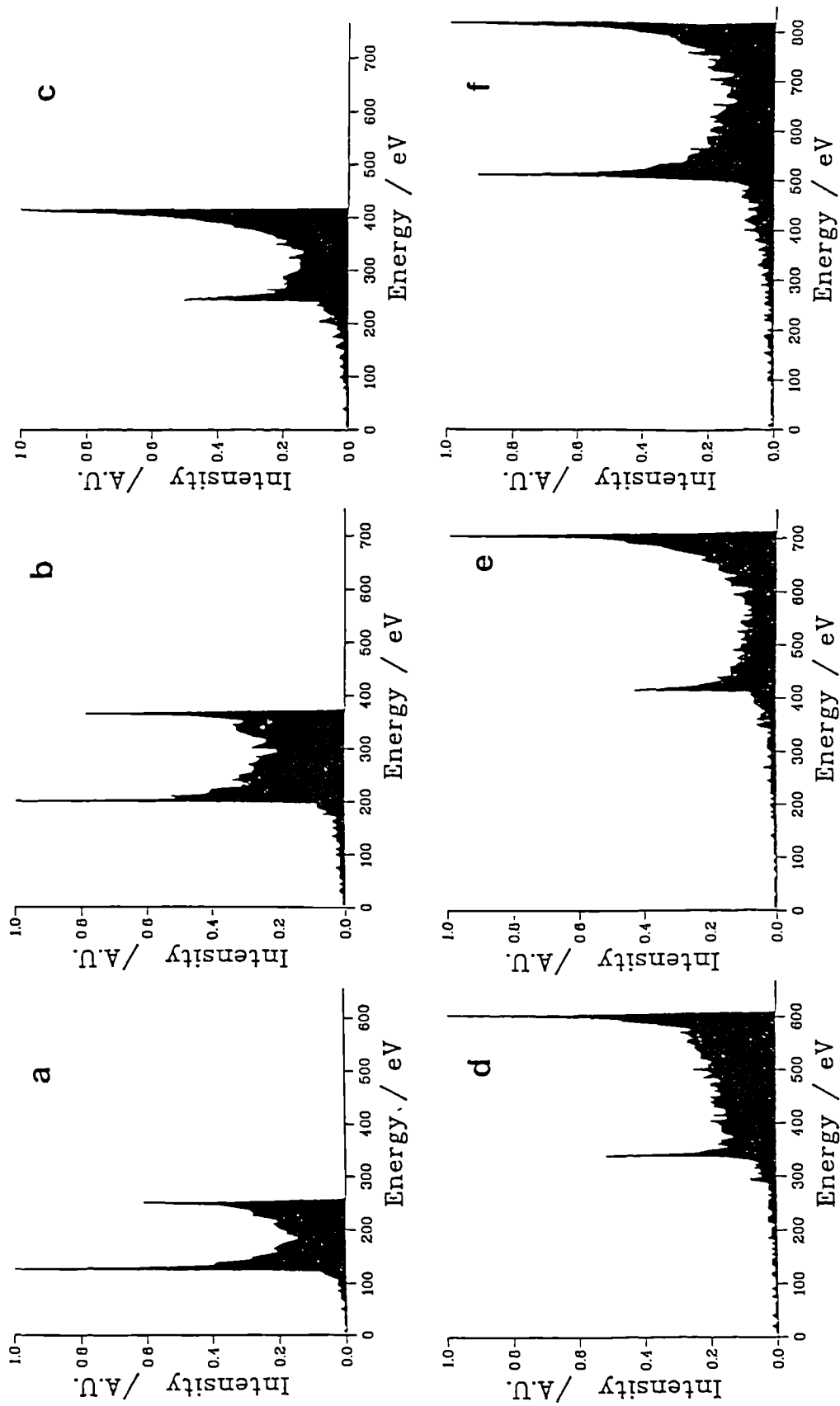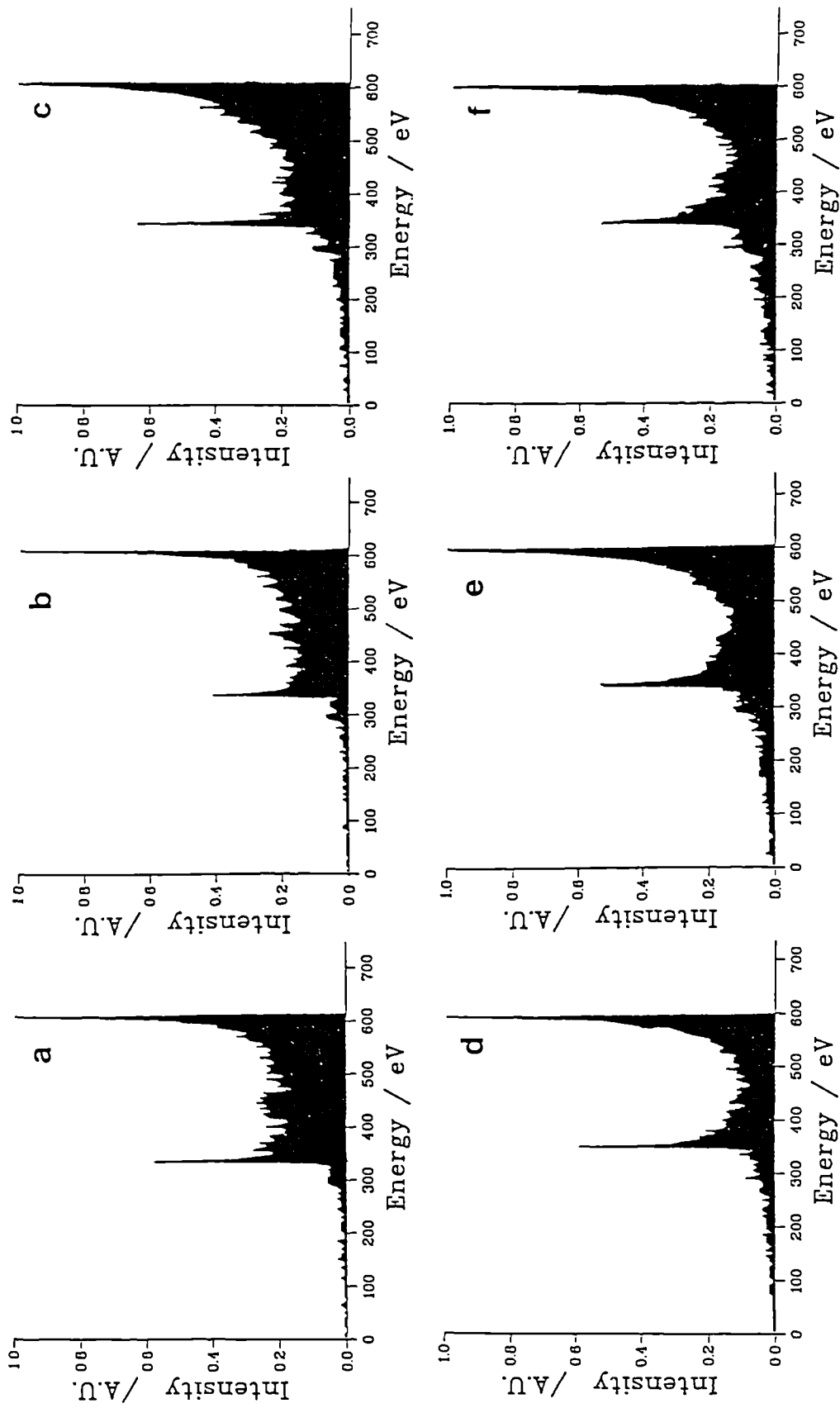
**Figure 4.13** Predicted argon IEDs at the cathode using the model of May et al[30] adapted to take account of a sinusoidally time dependent plasma potential. Pressure = a) 7.0 b) 9.0 c) 11.1 d) 13.1 e) 15.0 and f) 17.2 mTorr. Other conditions as specified in Tables 4.6 and 4.8.

# 4.7 EXTENDED DISCUSSION OF MODELLING RESULTS

## 4.7.1 Sources of Inaccuracy

The controversy over the form of the plasma potential has arisen from the use of equivalent circuits to model RF discharges. In this method a circuit comprising resistors, capacitors and diodes is designed to represent the discharge chamber. The behaviour of macroscopic discharge parameters e.g. $V_0$ and $V_{dc}$ is then modelled using this circuit and conclusions are drawn about the nature of the system. A typical equivalent circuit is shown in figure 4.14.[69]

In this model the diodes represent electron motion, resistors represent ion current and the capacitors represent the electrical properties of the sheaths and their enclosed charge. The nature of the sheath in RF discharges was first recognized to be capacitive by Gould[121]. Thus models of discharges that employ equivalent circuits have assumed that the resistive components of the circuit are negligible i.e. $R_e$ and $R_w \rightarrow \infty$ and $R_p \rightarrow 0$. A purely capacitive sheath leads to the derivation, in more sophisticated models, of a plasma potential that is sinusoidally varying while a purely resistive sheath gives a rectified sinusoid form of the potential. These two extremes were shown in figure 4.9 together with an intermediate case , which represents some degree of both capacitive and resistive behaviour. Thus our modelling of the argon IEDs has effectively encompassed both "capacitive" and "resistive" models of the sheath behaviour.

Our results show unequivocally that the Ar IEDs can be more closely modelled using a sinusoidally varying plasma potential. In particular, the intense high energy peak in our data that could not be modelled in the "resistive" model is successfully reproduced in the "capacitive" model. However, although our simulations are accurate, some of the distributions are not exact and we now offer the following explanations as to why this may be.

a) As shown in figure 4.9 the plasma potential need not be either a sinusoid or a rectified sinusoid: an intermediate case does exist. Indeed why should the sheath be
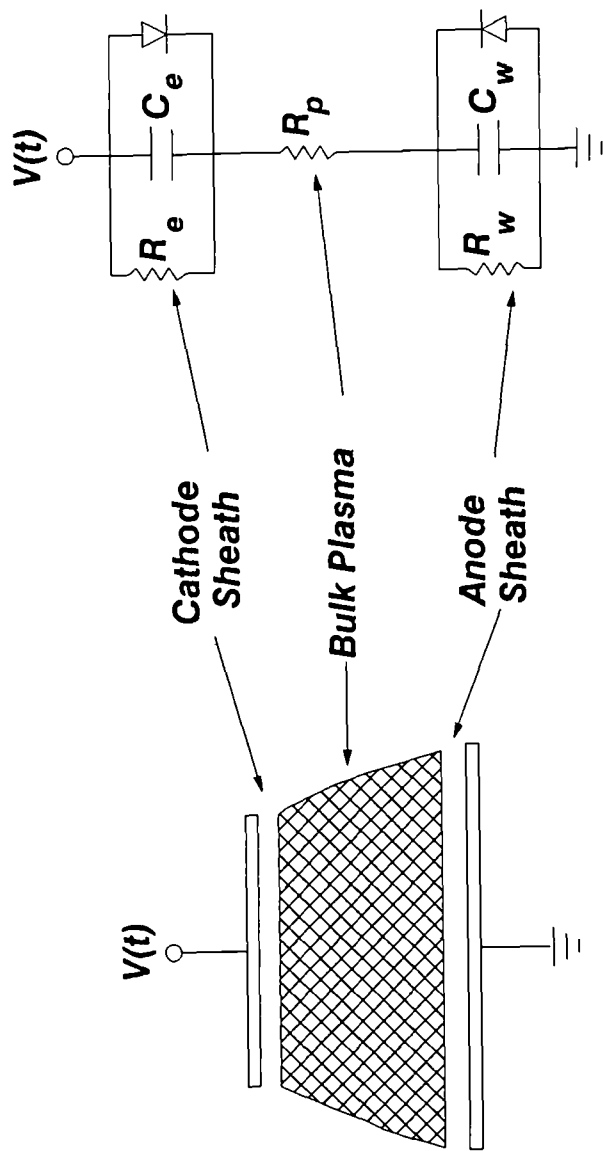
**Figure 4.14** Equivalent circuit model of an RF discharge. After Köhler et al[69].

200

modelled solely by either a resistance or a capacitance ? It is quite plausible that it could bear characteristics of each. It may be that, although our data are modelled <u>more</u> closely by a "capacitive" sheath, some intermediate case will be more accurate. Köhler et al[69] drew similar conclusions in their modelling using equivalent circuits. They found that a purely capacitive model was invalid and both resistance and capacitance would be required to reproduce their experimental observations.

b) The form of the plasma potential need not be the same for all discharge conditions. Some authors have already recognized that the sheath is resistive at low frequencies and capacitive at high frequencies. Thus, at some frequencies an intermediate case must exist. Köhler et al found that a capacitive model gave better results at low power levels while a resistive model was more appropriate for higher power levels. It is possible that the nature of the sheath may change when discharge conditions change. This will affect ion transport across the sheath and therefore the form of the IED at the electrode.

c) The form of the applied RF voltage, assumed to be a sine wave, will not exactly be so. This is due to smoothing of the wave by the inductance in the matching network. This will in turn smooth out the plasma potential, again giving rise to an intermediate form.

d) We have shown in section 4.4 that the form of the sheath potential is important in determining the form of the IED at the anode. Any residual inaccuracies in the form used in the model will cause errors in the simulated IEDs. Furthermore, the sheath potential may vary with the discharge conditions, cf. b) above.

e) It has been assumed throughout these simulations that the RF components of the sheath thickness and sheath potential are in phase, i.e. as the potential increases the sheath expands in space. Kushner[85] has demonstrated that where the components become out of phase dramatic changes in peak intensities, such as were found in our
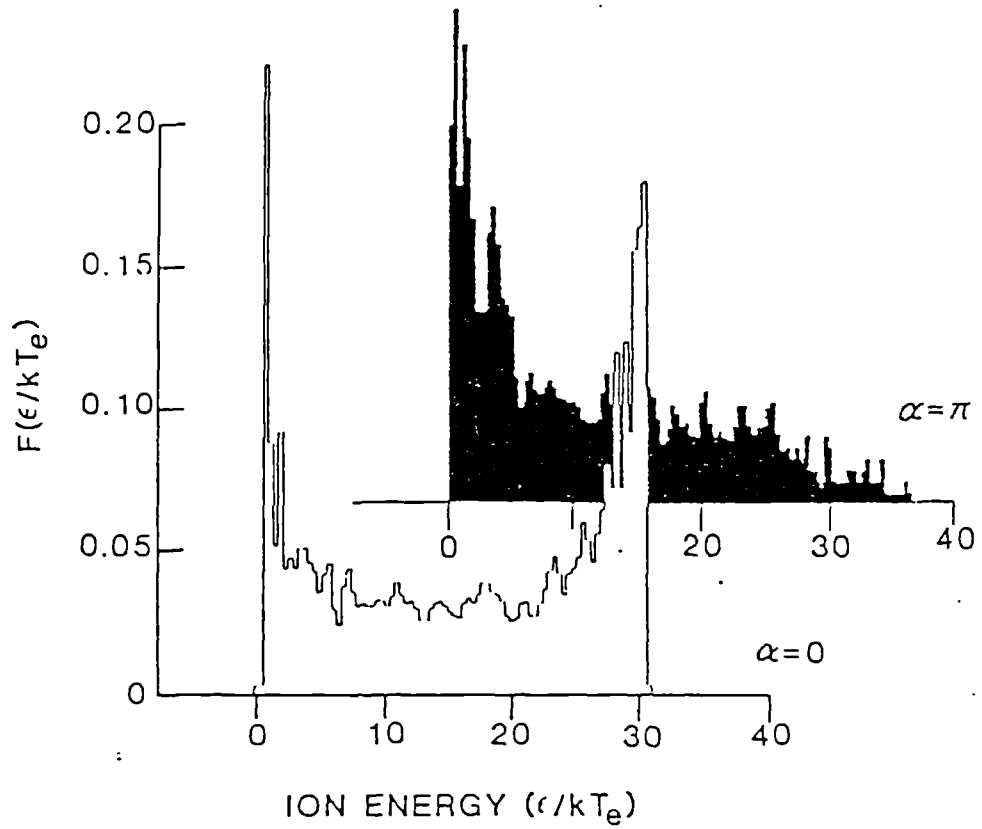
**Figure 4.15** Ion energy distributions for an argon ion in phase, $\alpha = 0$, and out of phase, $\alpha = \pi$, oscillation between the sheath potential and sheath thickness. After Kushner[85].

data, can be observed. Kushner's result is shown in figure 4.15. Although there is no experimental evidence that the sheath thickness and potential do become out of phase we should be aware that effects, similar to those observed in our experiments, can be reproduced by this mechanism.

## 4.7.2 A Comparison with Kuypers' Measurements

Our discussion up to this point has centred upon the form of the plasma potential and the effect on IEDs at the anode. We have also found, however, that at the cathode the predicted IED depends, substantially, upon which potential is used. This is because the form of the potential affects the value of the sheath thickness used to simulate the anode data, which in turn influences the cathode sheath thickness, and thus the form of the IED. This is, however, a rather indirect method of assessing the effect of the form of the plasma potential on cathode IEDs. As a method of assessing the effect we have modelled an argon cathode IED measured by Kuypers[73].

The parameters we have used for this simulation are the same as were found by May[30] to fit Kuypers' IED where a rectified sinusoid was used as the plasma potential. Kuypers measured IED and Mays' simulation are shown in figure 4.16a and 4.16b. Our simulation of this work using a sinusoidal plasma potential is shown in figure 4.16c. It is found that the resulting IED has both a higher mean energy, $<E>$, and a narrower peak separation, $\Delta E$, than the simulation of May. This is despite the maximum sheath voltage and sheath thickness being identical in each simulation. However, the evident differences would appear to be consistent with both a greater sheath voltage, thus causing an increased $<E>$, and a thicker sheath thereby decreasing $\Delta E$.

To explain these differences in the simulations we have to consider exactly what is meant by the sheath potential. At each instant the potential is defined by the difference between the plasma potential and the electrode potential. At the anode the sheath is then simply the same as the plasma potential, but at the cathode it is more complex due to the time varying electrode voltage. The sheath potential arising in each case is labelled in figure 4.9. In altering the form of the plasma potential the cathode
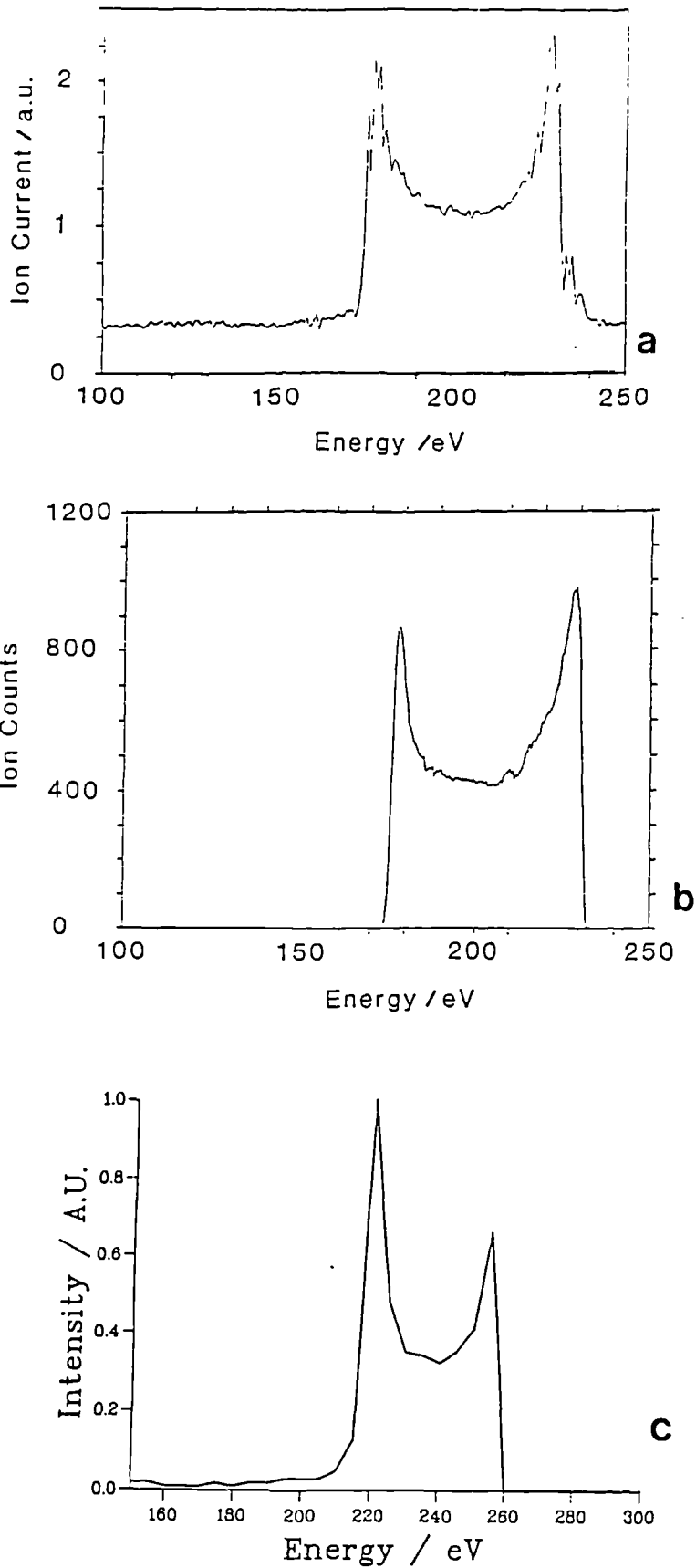
**Figure 4.16 a)** Argon cathode IED measured by Kuypers[73]. **b)** May et al[30] simulation of a) and **c)** simulation of this work using the parameters of b) but with a sinusoidally time dependent plasma potential.

sheath potential has a small extra increment added to it. Thus, although the *maximum* potential reached is the same in each case, for a large part of the cycle the sheath potential where a sinusoidal plasma potential is used is greater than where a rectified potential is employed. This leads to ions attaining higher energies as they travel through the sheath - as shown by the increased $<E>$ where a sinusoidal plasma potential is used. Moreover, since the sheath thickness is assumed to be in phase with the voltage, for most of the cycle the sheath will actually be thicker than if a rectified sine wave is used. An increased sheath thickness means that IEDs are less likely to be RF modulated i.e. they will be narrower, as in fact we observed.

No attempt has been be made to remodel Kuypers' data using the version of the model with a sinusoidal potential. The mean of the distribution could be adjusted by a decrease in the value of the electron temperature used in the simulation. Similarly the width of the distribution can be corrected by a decrease in $l_{max}$. Neither of these parameters was measured by Kuypers but were chosen by May to fit his IED. A reasonably close estimate of Kuypers' IED is almost certainly within the capabilities of the current model. However, modelling one IED in isolation will not increase our understanding of the factors affecting the IEDs. Indeed, it may even be that, as noted above, a rectified sinusoidal form may be more appropriate for the reactor and conditions used by Kuypers.

## 4.7.3 Some Practical Considerations

The comparison of the two models has demonstrated the need for an absolute value of $l_{max}$ in order to accurately predict IEDs. If an absolute $l_{max}$ were available the distribution width could no longer be fitted by adjustment of $l_{max}$ and the form of the plasma potential would govern the width. This could lead to a more certain form of the potential required. Similarly, a value for the electron temperature from experiment is required since this also affects the distribution width and energy mean. Thus, these parameters, measured in conjunction with IEDs, may allow a more precise form of the plasma potential to be found. Alternatively, since the plasma potential is the same as the anode sheath potential the form of $V_p(t)$ may be obtainable by some temporal

spectroscopic study of the anode sheath. Without this a trial and error method is required, involving modelling whole series of IEDs, to determine the best fit of the various potentials. Such an approach has been carried out in this work.

However, since we are capable of predicting IEDs with some accuracy, despite a poor knowledge of some of the parameters, we should ask ourselves whether it is in fact critical to know the IED any more precisely for any applications. The main aim of this work has been to produce IEDs that can then be used as inputs to a program that will model etch profiles in a semiconductor etch process. It may be that as long as 'ball-park' IEDs are available and the incoming particles - ions and neutrals - have enough energy to cause surface reactions and sputtering then etch profiles will be accurately modelled. Other factors such as side wall passivation and the ion angular distribution may be more important. To the authors' knowledge there has been no study of the effect of small changes in IEDs, e.g. the difference between IEDs in figures 4.16b and 4.16c, on sidewall profiles. However there has been some work on the sputter yield of silicon for argon ions of various energies. Figure 4.17 shows the sputter yield from an amorphous silicon surface when bombarded by argon ions of 200 eV and 250 eV. These yields have been calculated[40] using the program TRIM[122]. These two energies can be considered to be, approximately, the means of the IEDs in figures 4.16b and 4.16c respectively. The yields for the two ions are very similar and, indeed, the graph reveals that the sputter yield is strongly dependent on the ion incident angle. Thus, the etch profiles produced by each IED are likely to be the same if the angular distributions are the same. Kuypers measured his IED at 2.4 mTorr, so there are very few collisions of ions in the sheath. The angular distribution of ions will therefore be close to normal. The main difference between any etch profile calculated using the two simulated IEDs of figure 4.16 will be in the rate of the etch process. More ions will be required to produce the same etch profile using 200 eV ions than would be required with 250 eV ions due to the slightly lower sputter yield. Thus, from these data it would appear that the IEDs we can calculate will be sufficiently accurate to predict etch profiles. This will not necessarily be true at higher pressures however since the role of the ion angular distribution will become significant. Although we can
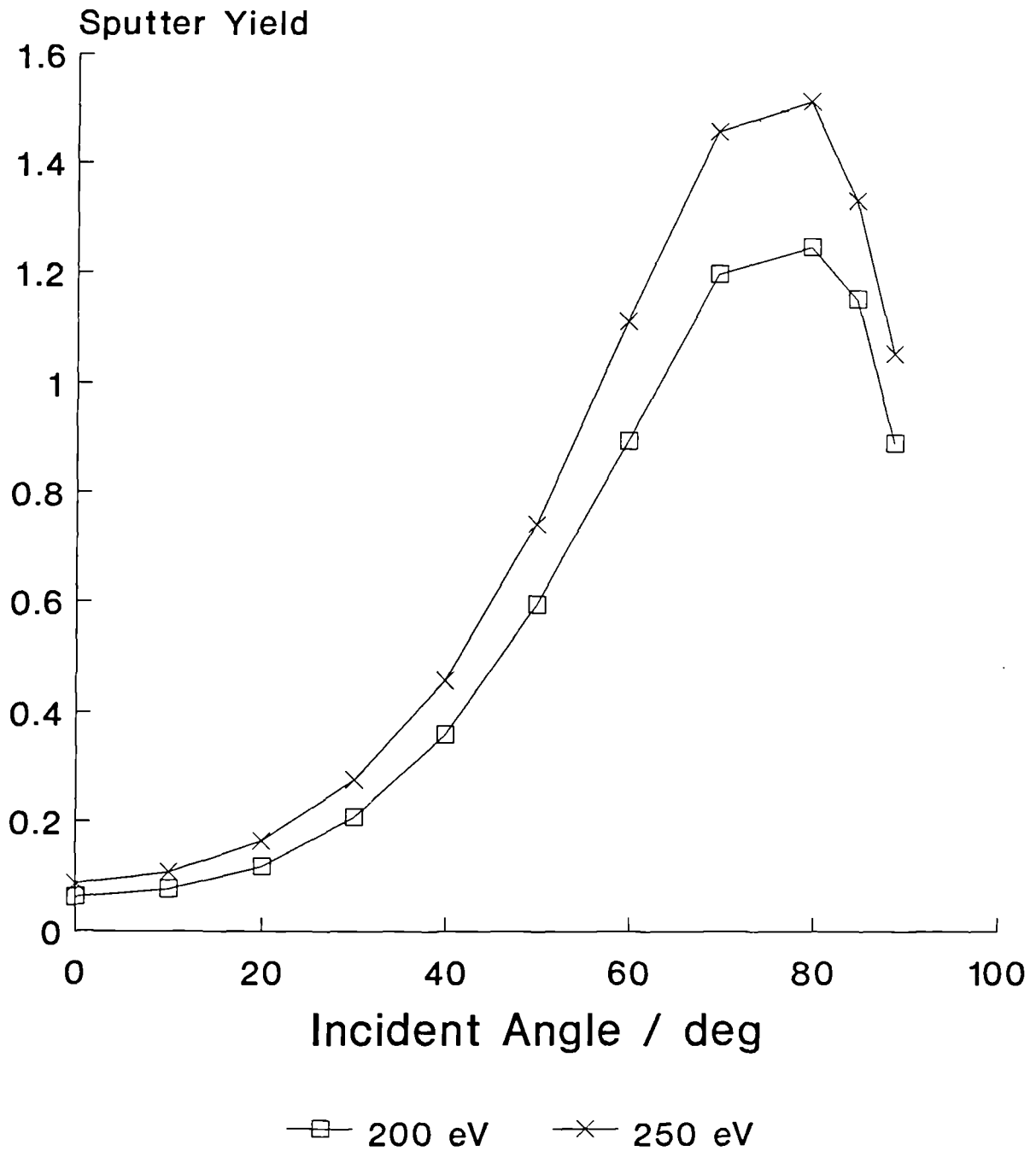
**Figure 4.17** Sputter yield from an amorphous silicon surface for 200 eV and 250 eV argon ions.

infer IADs from our IED calculations we have no means of checking the result experimentally with our current analyser.

## 4.8 SUMMARY OF CONCLUSIONS

Argon IEDs have been simulated using the model of May[30] with no modifications. The simulated IEDs do not fully reproduce the experimental data; in particular the high energy peak in the IED is underestimated. Only by using an unrealistic resolution for the simulated IED can the peak intensities be made to reproduce the trend in experimental data. In this case the high energy peak can be seen to be due to a single sharp spike.

To try and improve the agreement between experiment and theory the model has been adjusted to account for the Bohm acceleration that is expected to take place at the edge of the sheath region. The simulation of the data with this model is much better and a good fit is obtainable for most of the data using a more realistic resolution of 2 eV. However, at very high voltages and at very low pressures the experimental data has an intense high energy peak that still cannot be modelled.

Further modification of the model has been performed. The plasma potential (i.e. the anode sheath potential) was formerly described as a rectified sinusoid. This has now been replaced with a sinusoidal form of the plasma potential. Best fit distributions using this development of the model reproduce the experimental data extremely well. In particular the high energy peak in the distributions are reproducible. Whilst this is not conclusive proof of the form of the plasma potential, our work shows that a rectified sinusoidal form of the plasma potential is inaccurate and a sinusoid, or even an intermediate form, is more appropriate.

# CHAPTER 5

# CONCLUDING REMARKS AND FURTHER WORK

## 5.1 CONCLUDING REMARKS AND FURTHER WORK.

The main aim of this thesis has been to gain an increased understanding of the factors affecting ion energies at the electrode of an RF reactor. To achieve this a retarding field analyser has been constructed and IEDs measured at the anode of the reactor. The measured IEDs have been successfully simulated using a computer code.

Clearly, however, it is IEDs at the cathode that are required in any application to sidewall profile modelling. These can be obtained, as shown in the present work, by modelling or by constructing an analyser at the cathode and measuring them. Future possibilities for both of these options are now considered below.

### 5.1.1 Measurement of IEDs.

This section is primarily directed towards any future study that may consider building an RFA at the cathode although many of the comments are also valid for future anode studies.

The RFA used in this study is based on a design that has been used successfully in fusion plasma studies. As such it has simply been bolted on the analyser as an add on diagnostic and is not ideally optimised for this environment. We note the following concerning its use:

**a) Aperture** A narrow slit is employed to admit ions into the analyser. This allows an adequate current to be measured but minimizes disturbance to the plasma. At low pressures excellent IEDs can be measured. However, due to the relatively large collection area that exists there is significant neutral effusion into the analyser at higher pressures. Further work with the analyser should include replacing the slit with a circular orifice to reduce the collection area and allow an increased range of pressures to be measured. This will almost certainly reduce the signal to noise ratio and more measurement scans will be required to achieve acceptable IEDs.

**b) Pumping** The analyser is encased in a metal tube and pumping is achieved by an array of holes in the collector plate. The diameter and number of these holes is restricted due to the size of the collector. This therefore restricts the maximum operating pressure of the analyser. It would be preferable to increase the throughput of gas in the analyser, thus facilitating IED measurements at higher pressures than can

be achieved currently. This should involve designing the RFA chamber to be bigger and with less restrictions on the pumping line. This may not be possible however given the relatively restricted space available to mount the analyser. Perhaps the simplest and quickest method of improving the pressure in the analyser is to improve the pumping speed. This would be best achieved in the current set up by replacing the diffusion pump, situated some way downstream from the analyser, with a turbopump mounted directly behind the analyser. This would also alleviate the problem, occasionally experienced, of backstreaming of diffusion pump oil to the RFA grids.

Measuring IEDs at the cathode is a complex, but possible, experiment that could be achieved with the current analyser mounted in a suitably designed cathode. However the space currently available behind the cathode is extremely limited and it would be difficult to mount an RFA there. A better solution to the problem of measuring cathode IEDs would be to produce a complete integrated design of analyser and etcher that takes account of all the space required to mount and pump the RFA.

## 5.1.2 Modelling IEDs

The alternative to measuring IEDs is to predict them using a computer model. This work has shown that a major hindrance to predicting IEDs at the cathode is the lack of detailed knowledge of a few of the plasma parameters. These are now considered separately:

**a) Plasma Potential** The modelling of IEDs in this study has shown that the time variation of the plasma potential in our reactor is likely to be sinusoidal rather than a rectified sinusoid that has been otherwise suggested. Without knowing the exact form of this potential IEDs can be calculated that are in the right 'ball park' but lack detailed accuracy. Moreover, once a form of the potential is established for a given set of conditions it is not clear whether it will remain the same when the conditions such as the frequency of the applied voltage, power or identity of the process gas is altered. Clearly, studies into how the plasma potential alters under different process conditions would be most valuable. A few studies in this area have already begun[39,116]

using temporally and spatially resolved spectroscopic techniques to examine electric field strengths in the discharge. However, more work in this area is required to gain a full understanding of the plasma potential behaviour and remove one of the major unknown parameters in our model.

**b) Sheath Thickness** Without an unequivocal measure of the maximum extent of sheath at the cathode we can never be certain that predicted IEDs will be correct. The sheath thickness affects the width of the IED and is a parameter that it is therefore critical to know correctly. The elucidation of sheath thicknesses has usually been assessed by eye. This, however, would seem to give a time average rather than a true maximum value for the sheath thickness. Only by performing more sophisticated spectroscopic experiments, e.g. time resolved laser induced fluorescence, where the *maximum* extent of the sheath can be monitored can a true idea of the sheath thickness be gained and ambiguity in our IED predictions removed.

**c) Other Parameters** Other parameters used in our model, e.g. $kT_e$ and $kT_i$ have been derived from measurements in other reactors. As such, the values used are *typical* of those in RF discharges. However we would ideally like to input the exact value of these parameters to our program when predicting IEDs. This would require building and operating a Langmuir probe system to make the measurements. Similarly for gases where many species are expected to be present it is useful for accurate IED simulations to have a mass spectrometer available to identify the relative concentrations of species in the discharge. Whilst we can rely on other workers data to some extent to guidance for values to use for these parameters it is not clear that plasma conditions are the same for ostensibly similar machine parameters. One way round this is to build and operate a reactor with all the necessary diagnostics in place. A second and easier alternative is to restrict our modelling to a certain type of etcher where much data exists. The Gaseous Electronics Conference (GEC) reference cell[123] has recently been designed for use as a research reactor and results are now beginning to be published. To further refine our model it would be useful to model IEDs from this reactor and, using combinations of others experimental results, the number of free fitting parameters used to simulate an IED could be reduced.

# *REFERENCES*

213

1. P.A.Cox, *'The Electronic Structure and Chemistry of Solids'*, Oxford University Press, Oxford, 1987.

2. D.J.Elliott, *'Integrated Circuit Fabrication Technology'*, M$^c$Graw Hill, New York,1982.

3. I.Brodie and J.M.Murray,*'The Physics of Microfabrication'*,Plenum Press, London,1982.

4. S.J.Moss and A.Ledwith (eds), *'The Chemistry of the Semiconductor Industry'*, Blackie,London,1987.

5. SERC Vacation School Course Notes, Edinburgh Microfabrication Facility, 1991.

6. R.V.Stuart, *'Vacuum Technology, Thin Films and Sputtering'*, Academic Press, 1983.

7. P.Burggraaf, Semiconductor International, 16, 38, 1993.

8. Solid State Technol. 36, 25, 1993.

9. P.Slinger, Semiconductor International, 15, 52,1992.

10. A.J.van Roosmalen, J.A.G.Baggerman and S.J.H.Brader, *'Dry Etching for VLSI'*, Plenum Press, New York, 1991.

11. B.N.Chapman, *'Glow Discharge Processes'*, John Wiley, New York, 1980.

12. P.W.May, PhD.Thesis, University of Bristol, 1991.

13. F.F.Chen, *'Introduction to Plasma Physics'* Plenum Press, New York, 1977.

14. M.D.Gill, Vacuum, 34, 357, 1984.

15. M.J.Druvestyn and F.M.Penning, Rev.Mod.Phys., 12, 88, 1940.

16. W.L.Morgan and L.Vriens, J.Appl.Phys., 51, 5300, 1980.

17. J.Vlček and V.Pelikán, J.Phys D:Appl.Phys., 18, 347, 1985.

18. T.Holstein, Phys.Rev., 70, 367, 1946.

19. D.Barbiere, Phys.Rev., 84, 653, 1951.

20. D.Maundrill, J.Slatter, A.I.Spiers and C.C.Welch, J.Phys D:Appl.Phys., 20, 815, 1987.

21. V.A.Godyak, R.B.Piejak and B.M.Alexandrovich, Phys.Rev.Lett.,68, 40, 1992.

22. V.A.Godyak and S.N.Oks, Sov.Phys.Tech.Phys., 24, 1255, 1979.

23. T.I.Cox, V.G.I.Deshmukh, D.A.O.Hope, A.J.Hydes, N.S$^t$.J.Braithwaite and

N.M.P.Benjamin, J.Phys D:Appl.Phys.,20, 820, 1987.

24. V.A.Godyak, R.B.Piejak and B.M.Alexandrovich, Plas.Sources.Sci.Technol., 1, 36, 1992.

25. D.Bohm in 'The Characteristics of Electrical Discharges in Magnetic Fields', eds A.Guthry and R.K.Wakerling, p77, M$^c$Graw Hill, New York, 1949.

26. K-U.Riemann, Phys.Fluids, B4, 2693, 1992.

27. P.M.Meijer and W.J.Goedheer, Phys.Fluids, B3, 1804, 1991.

28. Y.P.Song, D.Field and D.F.Klemperer, J.Phys D:Appl.Phys., 23, 673,1990.

29. H.R.Koenig and L.I.Maissel, IBM J.Res.Dev., 14, 168, 1970.

30. D.Field, D.F.Klemperer, P.W.May and Y.P.Song, J.Appl.Phys., 70, 82, 1991.

31. J.W.Coburn and E.Kay, J.Appl.Phys., 43, 4965, 1972.

32. J.I.Ulacia F. and J.P.M$^c$Vittie, J.Appl.Phys., 65, 1484, 1989.

33. P.M.Vallinga, P.M.Meijer, H.Deutsch and F.J.de Hoog, Proc XVIII Intnl.Conf.Phen.Ion.Gases., Swansea, p814, 1987.

34. R.J.Chatfield, PhD.Thesis, University of Bristol, 1993.

35. H.V.Boenig, 'Fundamentals of Plasma Chemistry', Technonic, Lancaster, Penn, 1988.

36. D.L.Flamm, V.M.Donelly and D.E.Ibbotson, J.Vac.Sci.Technol., B1, 23, 1983.

37. C.C.Welch, MSc.Thesis, Thames Polytechnic, 1987.

38. O.Auciello and D.Flamm, eds.,'Plasma Diagnostics', Academic Press, London, 1989.

39. K.E.Greenberg and G.A.Hebner, Appl.Phys.Lett., 63, 3282, 1993.

40. I.M.Hedgecock, PhD.Thesis, University of Bristol, 1994.

41. R.M.A.Azzam and N.M.Bashara, 'Ellipsometry and Polarized Light', North Holland, 1987.

42. A.C.Dickenson, Project Report, University of Southampton, 1990.

43. A.M.Antoine and B.Drevillon, Mater.Res.Soc.Symp., 75, 333, 1987.

44. A.J.Hydes, PhD.Thesis, University of Bristol, 1985.

45. N.P.Johnson, A.P.Webb and D.J.Fabian, Mat.Res.Soc.Symp.Proc., 30, 1984.

46. J.W.Coburn, Rev.Sci.Instr., 41, 219, 1970.

47. J.W.Coburn and E.Kay, Solid State Technol., 22, 117, 1979.

48. G.Smolinsky and D.L.Flamm, J.Appl.Phys., 50, 4982, 1979.

49. D.J.Thomas, PhD.Thesis, University of Bristol, 1989.

50. P.E.Clarke, D.Field, A.J.Hydes, D.F.Klemperer and M.J.Seakins,
    J.Vac.Sci.Technol., B3, 1614, 1985.

51. D.J.Thomas, P.Southworth, M.C.Flowers and R.Greef,
    J.Vac.Sci.Technol., B8,   1044, 1990.

52. J.D.Swift and M.J.R.Schwar, 'Electrical Probes for Plasma Diagnostics', Iliffe,
    London, 1970.

53. M.J.Kushner, J.Appl.Phys., 53, 2939, 1982.

54. F.Bose, R.Patrick, S.Linder and H.P.Baltes, Contr.Papers, 'Highly Selective Dry
    Etching and Damage Control', Electrochemical Society Symposium, Honolulu,
    Hawaii, 1993.

55. R.A.Gottscho and V.M.Donelly, J.Appl.Phys., 56, 245, 1984.

56. K.H.Hurley, Solid State Technol., 30, 103, 1987.

57. C.J.Mogab, A.C.Adams and D.L.Flamm, J.Appl.Phys., 49, 3796, 1978.

58. A.Manenschijn, PhD.Thesis, Technische Universiteit van Delft, 1991.

59. R.J.M.M.Snijkers, PhD.Thesis, Technische Universiteit Eindhoven, 1993.

60. A.A.Goruppa, B.M.Annaratone and J.E.Allen, Proc XX Int.Conf.Phen.Ionized
    Gases, Contr.Papers 5, 1079, Pisa, 1991.

61. W.Steckelmacher, J.Phys.E.Sci.Instr., 6, 1061,1973.

62. W.M.Greene, M.A.Hartney, W.G.Oldham and D.W.Hess, J.Appl.Phys., 63,
    1367, 1988.

63. P.Briaud, G.Turbin and B.Grolleau, Mat.Res.Soc.Symp.Proc., 68, 109,1986.

64. R.J.M.M.Snijkers, M.J.M van Sambeek, G.M.W.Kroesen and F.J. de Hoog,
    Appl.Phys.Lett., 63, 308, 1993.

65. S.G.Ingram and N.St.J.Braithwaite, J.Phys.D:Appl.Phys., 21, 1496, 1988.

66. J.K.Olthoff, R.J.van Brunt and S.B.Radanov, J.Appl.Phys., 72, 4566, 1992.

67. J.Liu, G.L.Huppert and H.H.Sawin, J.Appl.Phys., 68, 3916, 1990.

68. K.Köhler, D.E.Horne and J.W.Coburn, J.Appl.Phys., 58, 3350, 1985.

69. K.Köhler, J.W.Coburn, D.E.Horne, E.Kay and J.H.Keller,
    J.Appl.Phys., 57, 59, 1985.

70. B.M.Annaratone, M.A.Skorik, A.A.Goruppa and J.E.Allen, Proc.Int.Conf.Plasma
    Phys., Contr.Papers III, 1977, Innsbruck, 1992.

71. B.E.Thompson, K.D.Allen, A.D.Richards and H.H.Sawin,
    J.Appl.Phys., 59, 1890, 1986.

72. T.H.J.Bisschops, PhD.Thesis, Technische Universiteit Eindhoven, 1987.

73. A.D.Kuypers and H.J.Hopman, J.Appl.Phys., 63, 1894, 1988.

74. A.Manenschijn, G.C.A.M Janssen, E. van der Drift and S.Radelaar,
    J.Appl.Phys., 69, 1253, 1991.

75. J.Janes and C.Huth, J.Vac.Sci.Technol., A10, 3086, 1992.

76. J.Janes and K.Bornig, J.Appl.Phys., 73, 2724, 1993.

77. J.Janes, J.Appl.Phys., 74, 659, 1993.

78. T.Otsubo and K.Ohara, Jap.J.Appl.Phys., 30, 1882, 1991.

79. C.Wild and P.Koidl, J.Appl.Phys., 69, 2909, 1991.

80. W.D.Davis and T.A.Vanderslice, Phys.Rev., B1, 219, 1963.

81. R.T.C.Tsui, Phys.Rev., 168, 107, 1968.

82. J.H.Keller and W.B.Pennebaker, IBM J.Res.Dev., 23, 3 1979.

83. C.B.Zarowin, J.Electrochem.Soc., 130, 1144, 1983.

84. C.B.Zarowin, J.Vac.Sci.Technol., A2, 1537, 1984.

85. M.J.Kushner, J.Appl.Phys., 58, 4031, 1985.

86. B.E.Thompson, H.H.Sawin and D.A.Fisher, J.Appl.Phys., 63, 2241, 1988.

87. P.W.May, D.Field and D.F.Klemperer, J.Appl.Phys., 71, 3721, 1992.

88. G.G.Lister, J.Phys.D:Appl.Phys., 25, 1649, 1992.

89. I.T.Wade, PhD.Thesis, University of Bristol, 1989.

90. Tylan Mass Flow Controller Reference Manual, Tylan (U.K.) Ltd., Swindon,
    U.K.

91. Operating and Service Instruction Manual, Model HF-300, ENI Power Systems
    Inc, Rochester ,NY, U.S.A.

92. R.A.Pitts, PhD.Thesis, University of London, 1991.

93. J.A.Simpson, Rev.Sci.Instr., 32, 1283, 1961.

94. J.W.Coburn and E.Kay, J.Vac.Sci.Technol., 8, 738, 1971.

95. G.S.Lewin, 'Fundamentals of Vacuum Science and Technology', M$^c$Graw-Hill, NY, 1965.

96. SIMION PC/PS2 Version 3.1 User Manual, D.A.Dal and J.E.Delmore, Idaho National Engineering Laboratory, EG+G Idaho Inc., U.S.A.

97. PCIP-AWFG User Manual, 1990, Keithly MetraByte Corporation, Taunton, Mass., U.S.A.

98. PC30-D User Manual, Amplicon Liveline Ltd., Brighton, U.K.

99. S.Wolf, 'Guide to Electronic Measurements and Laboratory Practice', Prentice-Hill, 1983.

100. 'Application Notes on Grounding', Advanced Energy Industries Inc., 1991.

101. G.F.Counsell, Culham Laboratory.

102. G.F.Counsell, Culham Laboratory.

103. U.Ehlemann, M.Petig, H.Sabadil and K.Wiesemann, Proc.11th Int.Symp.Plasma Chem., 1451, Loughborough, U.K. 1993.

104. J.E.Allen, J.Phys.D:Appl.Phys., 25, 1839, 1992.

105. R.A.Morgan, 'Plasma Etching in Semiconductor Manufacture', Elsevier, New York, 1985.

106. P.W.May, D.F.Klemperer and D.Field, J.Appl.Phys. 73, 1634, 1993.

107. A.D.Kuypers, PhD.Thesis, University of Utrecht, Netherlands, 1989.

108. H.Sabadil and S.Kagge, 17$^{th}$ Int.Conf.Phenom.Ioniz.Gases, 1, 333, 1985.

109. M.J.Vasile, J.Appl.Phys., 51, 2503, 1980.

110. W.H.Cramer and J.H.Simons, J.Chem.Phys., 26, 1272, 1957.

111. W.H.Cramer, J.Chem.Phys., 30, 641, 1959.

112. J.Dutta, K.Hasezaki, S.Mashima, P.J.M$^c$Elhany, A.Suzuki, G.Ganguly and A.Matsuda, Jpn.J.Appl.Phys., 31, L299, 1992.

113. D.A.O.Hope, G.J.Monnington, S.S.Gill, N.Borsing, J.A.Smith and J.A.Rees, Vacuum, 44, 245, 1993.

114. S.Grudzus and M.März, J.Phys.D:Appl.Phys., 26, 1980, 1993.

115. A.Picard, G.Turban and B.Grolleau, J.Phys.D:Appl.Phys., 19, 991, 1986.

116. R.A.Gottscho, Phys.Rev. A36, 2233, 1987.

117. R.N.Franklin, 'Plasma Phenomena in Gas Discharges', Clarendon, Oxford, 1976.

118. V.E.Golant, A.P.Zhilinsky and I.E.Sakharov, 'Fundamentals of Plasma Physics', Wiley, New York, 1977.

119. K-U.Riemann, J.Phys.D:Appl.Phys., 24, 493, 1991.

120. C.A.Moore, G.P.Davis and R.A.Gottscho, Phys.Rev.Lett., 52, 538, 1984.

121. R.W.Gould, Phys.Lett. 11, 236, 1964.

122. J.F.Ziegler, J.P.Biersack and V.Littmark, 'The Stopping Range of Ions In Solids' vol. 1 of 'The Stopping Range of Ions In Matter' ed. J.F.Ziegler, Pergamon Press, New York, 1985.

123. 1988 Workshop on the Design, Calibration and Modeling of Research RF Plasma Processing Systems, 41st Ann. Gaseous Electronics Conf. Oct 18-21 1988, (Minneapolis, U.S.A.) and following GEC Conferences.